UILU-ENG-78-2026

CIVIL ENGINEERING STUDIES

STRUCTURAL RESEARCH SERIES NO. 447

ORNL/SUB/4164/3
DIST. CATEGORY UC-77

AN ANALYTICAL MODEL FOR SHEAR STRENGTH OF END SLABS OF PRESTRESSED CONCRETE NUCLEAR REACTOR VESSELS

By

H. O. ABDULRAHMAN
M. A. SOZEN
W. C. SCHNOBRICH

HTGR BASE TECHNOLOGY PROGRAM
Prestressed Concrete Nuclear Pressure Vessel
Development (189a 01331)
Milestone 2b

Report prepared at Department of Civil Engineering, University of Illinois

for

OAK RIDGE NATIONAL LABORATORY
Oak Ridge, Tennessee 37830

operated by

UNION CARBIDE CORPORATION

for the

DEPARTMENT OF ENERGY
Contract No. W-7405-Eng 26

UNIVERSITY OF ILLINOIS
at URBANA-CHAMPAIGN
URBANA, ILLINOIS

APRIL 1979

UILU-ENG-78-2026

AN ANALYTICAL MODEL FOR SHEAR STRENGTH OF END SLABS OF PRESTRESSED CONCRETE NUCLEAR REACTOR VESSELS

by

H. O. Abdulrahman
M. A. Sozen
W. C. Schnobrich

Report prepared at
Department of Civil Engineering
University of Illinois
under subcontract number 4164

for

OAK RIDGE NATIONAL LABORATORY
Oak Ridge, Tennessee 37830
operated by
UNION CARBIDE CORPORATION
for the
DEPARTMENT OF ENERGY
Contract No. W-7405-Eng 26

UNIVERSITY OF ILLINOIS
at URBANA-CHAMPAIGN
URBANA, ILLINOIS
APRIL, 1979

Printed in the United States of America. Available from

National Technical Information Service

U.S. Department of Commerce

5285 Port Royal Road, Springfield, Virginia 22161

Price: Printed Copy $9.00 Microfiche $3.00

CONTENTS

TABLES

FIGURES

FIGURES (Continued)

FIGURES (Continued)

FIGURES (Continued)

FIGURES (Continued)

FIGURES (Continued)

FIGURES (Continued)

FIGURES (Continued)

FIGURES (Continued)

FOREWORD

This report is the culmination of an extensive experimental and analytical investigation of the loading response of PCRV head regions conducted by the University of Illinois under the Oak Ridge National Laboratory Program of Prestressed Concrete Nuclear Pressure Vessel Development (189a 01331). The studies undertaken under this task area were unique relative to other portions of the program owing to the complex geometries and states of stress encountered in the PCRV head region. The findings will be integrated into the other program task areas for analysis methods development and structural model testing.

Other reports published on the head failure studies include:

1. S. L. Paul, M. A. Sozen, W. C. Schnobrich, B. I. Karlsson, and Alan Zimmer, *Strength and Behavior of Prestressed Concrete Vessels and Nuclear Reactors, Volume I*, Structural Research Series No. 346, University of Illinois, Urbana, Illinois (July 1969).

2. S. L. Paul, A. Zimmer, H. L. Gotschall, R. H. Matson, B. I. Karlsson, B. Mohraz, M. A. Sozen, and W. C. Schnobrich, *Strength and Behavior of Prestressed Concrete Vessels for Nuclear Reactors, Volume II*, Structural Research Series No. 346, University of Illinois, Urbana, Illinois (July 1969).

3. R. Higashionna and W. C. Schnobrich, *Lumped-Parameter Analysis for Shear Failure in the End Slab of Cylindrical Prestressed Concrete Pressure Vessels*, Structural Research Series No. 363, University of Illinois, Urbana, Illinois (August 1970).

4. J. D. Reins, J. L. Quiros, Jr., W. C. Schnobrich, and M. A. Sozen, *Shear Strength of End Slabs of Prestressed Concrete Nuclear Reactor Vessels*, ORNL/Sub/4164-1, Oak Ridge National Laboratory (July 1976).

5. B. I. Karlsson and M. A. Sozen, *Shear Strength of End Slabs With and Without Penetrations in Prestressed Concrete Reactor Vessels*, UILU-ENG-71-2019, University of Illinois, Urbana, Illinois (July 1971).

1. INTRODUCTION

1.1 Object and Scope

This report describes the results of an investigation of the behavior and strength of flat end-slabs of cylindrical prestressed concrete nuclear reactor vessels. The investigation included tests of ten small-scale pressure vessels and development of a nonlinear finite-element model to simulate the deformation response and strength of the end slabs. Because earlier experimental studies (1,2) had shown that the flexural strength of the end slab could be calculated using intelligible procedures, the emphasis of this investigation was on shear strength.

The test specimens were designed to investigate the strength of flat end slabs (Fig. 1.1) of cylindrical vessels. The role of the side walls was primarily to provide proper boundary conditions.

The main experimental parameters were end slab thickness, size and distribution of penetrations (Fig. 1.1), and concrete strength. The outline of the experimental investigation is given in Chapter 2. Chapter 3 records observed behavioral characteristics of the test vessels.

The analytical model is two-dimensional (axisymmetric) and uses a simple set of rules for defining the material behavior of concrete. Its development and the method of numerical solution used are described in Chapter 4.

Analytical solutions for pressure-deflection and pressure-strain relationships are compared with experimental data in Chapter 5.

1.2 Acknowledgments

The work reported was carried out at the Structural Research Laboratory of the Civil Engineering Department, University of Illinois, Urbana, as part

of the prestressed concrete reactor vessel program of the Oak Ridge National Laboratory sponsored by the Department of Energy. The program is coordinated by Dr. J. P. Callahan of the Oak Ridge National Laboratory.
Laboratory.

Several graduate students in civil engineering who are part time research assistants contributed to the project. The experimental work was initiated by B. Oland, K. Clapp, and A. C. Stepneski and continued by J. D. Reins. J. L. Quiros was responsible for data reduction and analysis.

R. D. Metz, laboratory technician, should be credited for the development of the circular-prestressing equipment and the liner for the vessel. The success of the instrumentation was due to the careful work of G. H. Lafenhagen, J. H. Sterner and D. C. Hines. The experimental work was supported by the staff of the Civil Engineering Machine and Electrical Shops under the direction of Professor V. J. McDonald and Mr. O. H. Ray.

Acknowledgment is due Mrs. Pat Lane for her meticuluous work in collating and typing the manuscript.

All computational work for this report was carried out on the CDC CYBER 175 system of the Digital Computer Laboratory of the University of Illinois, Urbana.

The project was directed by W. C. Schnobrich and M. A. Sozen.

2. OUTLINE OF THE INVESTIGATION

The test specimens were small-scale cylindrical pressure vessels designed to investigate the influence of penetrations in the end slab on strength and behavior of the vessel. The overall dimensions of the ten test vessels described in this report were 40 by 40 in. round (1.02 by 1.02m) as shown in Fig. 1.1. The cavity, closed at one end by the test slab and at the other by a 4-in. (0.10m) steel plate, had a diameter of 25 in. (0.64m).

Circumferential prestressing was provided by five bands, each containing approximately 290 wraps of 0.08-in. (2mm) high strength wire at an effective prestress at time of test of approximately 120 ksi (830 MPa). Sixty Stressteel rods, uniformly distributed around the perimeter in two rows, were used to develop a total effective longitudinal prestress force of approximately 2700 kips (12×10^6 N).

The target concrete compressive strength was 5500 psi (37 MPa) for the first eight vessels. No reinforcing bars were used in the end slab. The bars in the skirt were placed to maintain integrity of the specimen during circumferential prestressing.

A composite liner made up of thin sheets of steel, copper, and neoprene was used for all specimens.

The three main variables in the experimental program were (1) the thickness of the end slab which was either 10 or 12.5 in. (0.25 or 0.32m) (2) the size and arrangement of the penetrations (Fig. 2.1), and (3) the concrete strength, which was reduced for the last two vessels (Table 1). The ten test vessels were distributed as indicated below with respect to the three variables. The two specimens with low concrete strength are identified by asterisks.

	Clear Span/Nominal Depth of Slab	
	2.5	2.0
Solid slab	PV26	PV28
Six penetrations, 5-in.	PV27	PV32,PV33,PV35*
Thirty-seven penetrations, 2 in.	PV29	PV30,PV31,PV34*

The five-in. (0.13m) penetrations (PV27, PV32, PV33, PV35) were arranged uniformly on an 8-in. (0.20m) radius. Locations of the two-in. (0.05m) penetrations (PV29, PV30, PV31, PV34), spaced at 3 in. (0.075m) center-to-center to each other, are shown in Fig. 1.1. No reinforcing sleeves were used in the penetrations. The penetrations were closed by steel plates on the pressurized surface of the slab.

The test vessels were first prestressed circumferentially. After installation of the liner, a 4-in. (0.10m) steel plate was placed at the open end and the longitudinal prestressing was applied. The vessel was then placed in the testing room and pressurized internally using oil, after the cavity was initially filled with water, to failure over a period of approximately three hours. In addition to the pressure, measurements included deflections of the end slab and the side wall, and strains in the concrete and the longitudinal rods, with the majority of the strain gages concentrated on the walls of the penetrations, if any.

The analytical model was developed with the objective of simulating the observed pressure-displacement relationships in all ranges of response. No emphasis was placed on generating crack trajectories, on the premise that the important issue was to locate the internal thrusts which influenced overall response directly.

The analytical model was used to calculate the entire range of response for each type of vessel tested. A particular study was also made of the sensitivity of the calculated strength to drastic changes in concrete quality.

3. BEHAVIOR OF THE TEST VESSELS

3.1 Pressure-Deflection Relationships

The measured relationships between deflection at the center of the slab and internal pressure for all eight vessels are shown in Fig. 3.1 and 3.2. The entire set of recorded pressure-deflection relationships are included in Appendix A. The deflections reported are the total deflections with respect to the initial position of the slab and include the small but finite extension of the side wall. In comparing the pressure-deflection curves, it must be considered that these refer to second-loadings for PV26, 28, 31, and 33. As recorded in Appendix B, the liner in some of the vessels leaked during initial pressurization at various levels (PV26, 80 psi; PV28, 3200 psi [22 MPa]; PV31, 1200 psi [8.3 MPa]; PV33, 1700 psi [11.7 MPa]). The liners for these vessels were repaired and they were subsequently loaded to failure. The curves in Fig. 3.1 and 3.2 refer to the tests in which structural failure was achieved and have not been modified to account for the initial loading.

The measured relationships between internal pressure and end-slab deflection provide a measure of the overall behavior of the test vessels. As would be expected, initial response was linear. Nonlinear response was introduced by development of cracks at the reentrant corner (intersection of interior surfaces of end slab and side wall) caused by tensile stresses in the radial plane and/or at the exterior surface of the end slab caused by circumferential tensile stresses. The initiation of some nonlinear response could be inferred from slab deflection measurements (Appendix A) at approximately 100 psi (7 MPa) internal pressure. The influence of the experimental parameters, such as concrete strength and presence of penetrations, could not be identified decisively from the deflection measurements.

Although a certain amount of ductility may be read into some of the pressure-deflection curves (they could be idealized using two straight lines, the slope of the second one being considerably less than that of the first), that would be a dubious definition of ductility considering that the maximum slab deflection observed at failure was less than half a percent of the clear span and less than one percent of the slab thickness.

In relation to the question of "ductility," it should be pointed out that, had the only available sensor during the test been the slab deflection at midspan, structural distress would have been signaled simply from comparing the changes in measured deflection in two consecutive load increments. Considering that the incremental stiffness of the slab in the linear range of response was estimated satisfactorily by elastic analysis, it would be possible to sense the initiation of nonlinear response well in advance of failure.

3.2 Failure Mode

In reference 1, failure modes of end slabs have been classified as flexural and shear failures depending primarily on the material providing the weaker link. If the strength of the end slab is limited by yielding or fracture of the reinforcement, the slab is said to have failed in flexure. If the strength is limited by distress in the concrete, the slab is said to have failed in shear. As in the case of slender beams, analysis of slab strength is simpler and more reliable for flexural failures. All ten vessels of this series failed in shear.

Despite the use of fluid for developing internal pressure, failure occurred explosively in every case. Chunks of slab concrete were ejected at failure. This phenomenon was attributed primarily to trapped gas in the pressurizing fluid.

Cross sections and photographs of the failed end slabs are shown in Figure 3.3 through 3.11. The pressures registered at failure are listed in Table 1 along with data on the geometry of the vessel, index values for the circumferential and longitudinal prestresses, and the compressive strength of the concrete in the end slab. (The index value for the circumferential prestress is determined as the internal pressure required to balance the force, at time of test, in prestressing bands 1 and 2 located on and next to the end slab.)

Conditions of the end slab after testing indicated that final collapse occurred always through failure of the concrete in a complex state of stress but that the failures could be classified in two types depending on the location of final distress in the concrete.

One type of failure is illustrated in Fig. 3.3 and 3.6 which refer to solid slabs. As in the tests reported by Karlsson (2), a three-dimensional inclined crack carves out from the end slab the kernel shown in the lower photograph leaving behind a "cryptodome" to resist the internal pressure. Collapse occurs as a result of failure of the concrete in the cryptodome near the center of the slab. Viewed in two dimensions (in the vertical plane), this mode of failure has characteristics similar to the shear-compression failure observed in reinforced concrete beams.

The "shear-proper" or "punching" failure is illustrated best by the state of the failed end slab of vessel PV30 (Fig. 3.7) having a 12.5-in (305-mm) end slab with two-in. (50-mm) penetrations. After initiation of inclined cracking within the slab, concrete in the reduced area between the openings fails allowing the central portion of the slab to extrude along a nearly cylindrical failure surface.

The failure modes for each vessel are identified as SD (cryptodome) and SP (shear-proper) in Table 1. Not every failure could be classified as belonging clearly to one category or the other. The failed end slab of vessel PV29 Fig. 3.5), in addition to a well developed dome had a vertical failure plane through the outermost line of penetrations.

The detailed analysis of the shear strength of the end slabs is presented in Chapter 5. The maximum pressures developed by the test vessels are discussed here primarily for a qualitative understanding of the failure phenomena.

The raw results (maximum pressures attained) are illustrated in Fig. 3.12 for all ten tests to compare relative magnitudes of the strengths of end slabs with different properties.

For shear failure, it is not surprising that an increase in slab thickness results in an increase in strength and that, as observed for the 12.5-in. slabs, a reduction in concrete strength leads to lower strength.

From the relative magnitudes of the measured strengths for slab thicknesses of 10 and 12.5 in. (254 and 305 mm) SI units, it may be concluded that penetrations reduced the strength of the slab. However, the reduction was very small considering the amount of concrete removed by the penetrations. It may also be condluded that, on the basis of the recorded strength data, the effect of either type of penetration was approximately the same.

The increase in observed nominal shear strength at the net section with decrease of net section is reconcilable in terms of Coulomb's failure criterion.

Figure 3.13 provides a biased view of the data in Fig. 3.12.

The maximum nominal shear stress in the slab, v_m, corresponds to the value computed at the maximum pressure attained in the test. It was calculated at a radius of 12.5 for the solid slabs, 8 in. for the slabs with 5-in. penetrations, and at sections through the centerlines of the outermost arrays of penetrations for the slabs with 2-in. penetrations. Ordinates represent ratios of the nominal shear stress, v_m, to the square root of the compressive strength of the slab concrete (in psi).

The x-axis values (nominal prestress ratio) are the ratios of the gross to net cross-sectional area at the sections where the shear stress is calculated. In effect, they represent approximations to the ratio of the mean normal stress on the net section to the normal stress on the gross section, at the radius where the shear stress has been calculated.

In terms of the parameters used in Fig. 3.13, the increase in nominal shear strength (as a ratio of the square root of concrete strength) with decrease of net section may be shown to parallel the trend that would be indicated by the elementary friction concept.

Consider the idealized model in Fig. 3.14. A circular concrete section with perforations is subjected to six planar forces colinear with the axis of the "spokes" connecting the outer ring with the central section. The forces represent ideally the effect of the circumferential prestressing force. To simplify the model further, assume that the relationship between the circumferential stiffness of the outer ring and the radial stiffness of the spokes is such that a change in the width of the spokes causes relatively little change in the thrust acting on each spoke.

One bound to the resistance of the slab to a uniform load applied on the central solid section, perpendicular to the plane of the slab, may

be expressed simply in terms of friction. Accordingly, the shear force that can be transmitted through each spoke becomes a function of the normal force on the spoke modified by a constant coefficient. Shear strength would then be independent of the area of the net section; or the smaller the net section the higher would be the limiting nominal shear stress. This trend is seen in Fig. 3.13 and the model rationalizes, if only qualitatively, the relative insensitivity of the end-slab shear strength to the presence and size of the perforations.

3.3 Strains Measured on Walls of Penetrations

(a) Introductory Remarks

Strains were measured using electrical resistance gages at three levels on the walls of several penetrations of each test vessel with perforated end slabs. Because these measurements provide information on changes in the load-resisting mechanisms of the end slab, pressure-strain plots for four vessels (PV30 and PV34 with 2-in. [51 mm] and PV32 and PV35 with five-in. [1]7 mm] penetrations) are included in the report.

The locations and individual designations of the strain rosettes (45-deg. rosettes, gage length = 0.75 in. [19 mm], gage wideth = 0.14 in. [3.6 mm]) are shown in Fig. 3.15 and 3.16. The rosettes were mounted on the walls of the penetrations at three levels, at distances of 2-1/4, 6-1/4, and 10-1/4 in. [57, 159, and 280 mm] from the pressurized surface of the end slab.

Walls of five penetrations, as identified in Fig. 3.15, were instrumented in end slabs having 2-in. [51 mm] penetrations. Gages were mounted on opposite ends of a diameter perpendicular to a line joining the center of penetration to center of slab.

In end slabs having 5-in. penetrations, walls of two penetrations (locations shown in Fig. 3.16) were instrumented. Gages were mounted at four locations in plan, 90° apart, and designated by reference to the face of a clock viewed from above center of slab.

Strain data are shown in Figs. 3.17 through 3.115.

In reading and comparing these strain measurements it must be recognized that (1) horizontal (strain) scales are not all the same, (2) minus sign in the horizontal axis indicates tensile strain, (3) where the stress in the direction of the gage is low, the observed strain may be influenced appreciably by stress changes in orthogonal directions, and (4) gages at 45° to the horizontal read compressive or tensile strains depending on their orientations. In a few cases, the orientation, but not the location, of these diagonal gages were different in different vessels.

Each measured concrete strain increment was corrected by the corresponding mean increment indicated by a set of check gages, gages mounted on blocks of concrete located near the test specimen, in order to compensate for changes in the sensing system. The maximum total strain correction was less than 1×10^{-5}, or less than the overall accuracy of the strain measuring system.

Not all of the strain gages functioned throughout each test. Therefore, data for some of the strain gage locations are not plotted or are plotted only for part of the loading.

(b) Strains Measured in End-Slabs of Vessels PV30 and PV34

Test vessels PV30 and PV34 had end slabs with 2-in. [51 mm] penetrations. The main difference between the properties of the two test vessels was

the concrete compressive strength which was 6300 psi (43.4 MPa) for PV30 and 2440 psi (16.8 MPa) for PV34. The internal pressure at failure was 3210 psi (22.1 MPa) for PV30 and 1800 psi (12.4 MPa) for PV34.

For test vessel PV30, the initial indication of nonlinear strain response was provided by gages measuring horizontal strains in the central opening at level 1 or at the top level (Fig. 3.30). Both gages 29 and 20 deviated from linearity at slightly above 1000 psi (7 MPa) and indicated a sudden increase in strain which may be interpreted definitely as the development of radial cracking (due to tensile stresses in the circumferential direction) at an internal pressure of approximately 1500 psi (MPa).

The corresponding readings for vessel PV34 (Fig. 3.80) suggests only a small degree of nonlinearity at internal pressures below 1500 psi (10 MPa). This comparison is plausible in that tensile cracking at this location depends primarily on the external circumferential prestress and is relatively insensitive to changes in the tensile strength of the concrete.

For vessel PV30 with the higher concrete strength, the next critical event in internal stress distribution is signaled by the diagonal gages at level 2 in penetrations 1 and 3. Both compressive and tensile strain readings indicated (Fig. 3.19 and 3.20) definite nonlinear response at an internal pressure of approximately 1500 psi (10 MPa). The tensile strain readings were more significant in that, compared with the calculated compressive prestrain of 2×10^{-4} in the direction and at the location of the gages, a tensile strain increment of 5×10^{-4} would be a strong indication of cracking. The increase in strain rate of the gages reading compressive strain also suggests a rearrangement of the paths through which pressure is transmitted from the slab to the wall of the test vessel. The compressive strain increment at which nonlinear response was initiated

(approximately 5×10^{-4}) is too small to justify ascribing the observed phenomena to inherent inelastic action of the material (6300 psi [43.4 MPa] concrete). An increase in the ratio of compressive stress to internal pressure must have contributed to the increase in the observed strain rate.

For penetrations 1 and 3 of vessel PV34 (Fig. 3.70) with the lower concrete strength, a perceptible acceleration in the strain response is indicated to start at an internal pressure of approximately 750 psi (5 MPa). It would appear from the data for both vessels that internal inclined cracking was initiated in the end slabs within 3.5 in. (90 mm) of the inside face of the side wall at pressures approximately half the maximum pressure reached for each vessel.

For vessel PV34, the magnitude of the measured compressive strains at level two in penetrations 1 and 3 is also of interest. The final readings indicated a projected compressive strain increment of virtually 0.005 at failure (Fig. 3.73). The diagonal compressive strains recorded at level 3 of the same penetrations (Fig. 3.75) were of comparable magnitude though not as large. The values projected to the failure pressure of strains measured in penetrations four and five, which were located closer to the center of the slab span, were smaller (Fig. 3.86, 3.92).

Vertical strain readings, distorted as they are by background noise because of their typically low magnitudes, do confirm in both vessels PV30 and PV34 the changes in the load-carrying mechanism inferred from other strain measurements. Vertical strains at levels 1 and 2 of penetration 2 in PV30 stopped increasing at a pressure of 1800 psi (Fig. 3.29), while the vertical strain at level 3 continued to increase (Fig. 3.25). For PV34, vertical strains increased at a increasing rate at level 3 (Fig. 3.75) but not at level 1 (Fig. 3.67).

Strain measurements in PV30 and PV34 were in general agreement with the hypothesis of the development of a cryptodome within the thick end slab. Viewed in two dimensions, in the radial plane, this is tantamount to the development of an arch with its "crown" in the middle of the slab at the pressurized surface and with its "abutments" near the anchorages of the longitudinal prestressing rods. The flow of internal forces associated with this arch would tend to generate large compressive strains in the diagonal direction (in the radial plane) and very low strains in regions near the nonpressurized surface and within the inner radius of the slab.

(c) Strains Measured in End Slabs of Vessels PV32 and PV35

Because the penetrations in end slabs of vessels PV32 and PV35 were all at the same distance from the center of the slab, information provided by the strain measurements is not of as wide a scope as that from strain measurements in PV30 and PV34. The main difference in the properties of vessels PV32 and PV35 was the concrete strength which was 5720 psi for PV32 and 3150 for PV35. Failure pressures were 3075 psi for PV30 and 1900 psi for PV35.

It is noteworthy that the diagonal gages at the 6 and 12 o'clock positions at level 2 (mid-height) in both vessels indicated negligible strains, suggesting at least that these gages were functioning properly.

Readings of horizontal gages at level 1 signalled the reaching of the radial cracks to the 6 o'clock sides of the penetrations at approximately 1300 psi (9 MPa) for PV32 (Fig. 3.48) and 111 psi (7.6 MPa) for PV35 (Fig. 3.96). Data from both tests show that the gages at the 12 o'clock sides of the penetrations were relatively insensitive to the event (Fig. 3.48, 3.96).

In PV32, the change in the rate of increase of diagonal strains, at 3 and 9 o'clock locations at level 2, (Fig. 3.58 and 3.59) which occurred at approximately 2000 psi is attributable to the onset of inclined cracking. The increase in the compressive strain rate is attributable to rearrangement of internal stress distribution rather than to changes in the incremental stiffness of the material. It would appear from the strain measurements at level 2 that permanent internal damage occurred within the end slab at an internal pressure of approximately two-thirds of the ultimate pressure. Permanent damage refers to development of inclined cracks directly associated with shear failure.

For PV35, inclined cracking was indicated to have occurred at an internal pressure of approximately 1250 psi (Fig. 3.108 and 3.109) or at two-thirds of the ultimate pressure.

Reversal of the pressure-strain plots for 3 and 9 o'clock positions at level 3 (Fig. 3.49 and 3.97) is attributable to separation of the slab from the sidewall as a result of development of the crack at the reentrant corner.

(d) Concluding Remarks

Strains measured in the walls of the penetrations in vessels PV30 and PV32 indicated that the load-carrying mechanism of the end slab changed at a pressure of approximately two-thirds of the pressure corresponding to failure. Changes in the strain measurements were compatible with the anticipated effects of the development of inclined cracks in the radial plane.

Strain measurements also indicated that local nonlinear response was initiated at approximately one-third of the maximum pressure.

Strains measured in PV34 and PV35, vessels with lower concrete strengths, also indicated similar changes in internal stress redistribution resulting from inclined cracks. In comparison with the vessels having higher concrete strength, the pressure at which the redistribution took place was reduced, as a result of the change in concrete strength, by approximately one-sixth while the failure pressure was reduced by over a third. The strength of the end slab failing in shear was found to be more sensitive to the change in concrete strength than to the load at which inclined internal cracking develops.

4. THE ANALYTICAL MODEL

4.1 General Characteristics

The pressure vessel was idealized as an axisymmetric structure and modeled using axisymmetric quadrilateral isoparametric elements. Graphical interpretation of such an element in three dimensions is illustrated in Fig. 4.1a. Two displacement components were considered at each of the four nodes (I, J, K, L), resulting in a total of eight degrees of freedom. Nonlinearity resulting from changes in geometry was assumed to be negligible.

Force-displacement relationships for the model elements were patterned after behavior of concrete. Overall nonlinear response was obtained by recognizing local failures of the concrete in tension (cracking) and in combined compression and shear as described in this chapter.

Steel components were simulated by increases in the stiffness of the appropriate elements and by external forces which were varied during the loading process to account for changes in steel stress.

4.2 Concrete in Tension

A limiting-strain criterion was used to define the cracking of concrete in a given direction. On reaching that strain, stress in the concrete was abruptly reduced to one half the assumed tensile strength (rather than to zero) in order to approximate the gradual decay in strength of the concrete with further increase in strain. The nominal "after-strength" was reduced to an infinitesimally small value at a strain of ten times the cracking strain defined by f_t/E_c where f_t and E_c are the assumed values of tensile strength and Young's modulus for the concrete.

4.3 Concrete in Compression

Concrete in compression was assumed to have a limiting stress defined by Mohr's criterion of failure represented as follows:

$$I = \frac{\sigma_3}{f'_c + 4\sigma_1} \tag{4.1}$$

where I = index not to exceed unity

σ_3 = maximum principal compressive stress

σ_1 = minimum principal stress (zero if tensile)

The coefficient for σ_1 was based on the experimental work by Richart, Brown, and Brandtzaag (4). As long as the index I did not reach unity, the stiffness of the concrete was based on the initial modulus. After I = 1.0 was reached σ_3 was continually adjusted so that I = 1 was not exceeded and the shear stiffness was reduced abruptly to one half its original value to be maintained at that level up to a shear strain of ten times the cracking strain. For larger values of the shearing strain, the shear stiffness was reduced to an infinitesimally low value.

4.4 Modeling for the Effect of the Penetrations

The axisymmetric model is by definition not suited to accommodate the effects of penetrations in the end slab, if the centers for the penetrations are not coincident with the center of the end slab. However, their effects on internal strains and stresses may be approximated in an axisymmetric model by modifying the stiffnesses of appropriate elements in the end slabs.

For the specimens tested, the penetrations were contained in plan within a single circle (as in the case of 2-in. openings, Fig. 1.1) or between two concentric circles (as in the case of 5-in. openings, Fig. 1.1).

To represent the effect of the penetrations, the stiffness of the elements in these regions were reduced in proportion to the area of concrete removed. Accordingly, the equivalent moduli were expressed by Eq. 4.2.

$$\overline{E}_i = \overline{p}\, E_i \tag{4.2}$$

where $\overline{E}_i$ = the equivalent (reduced) stiffness modulus in direction i, $\overline{p}$ = ratio of net to gross area in the region of the penetrations, and E_i = the stiffness modulus for the material. The equivalent modulus need not be the same in all three directions.

The softening effect of the reduction factor is reflected in the form of higher displacements and strains in the region of the penetrations. Because of compatibility of strains in composite materials, these strains represent the strain field in the solid material left out by the penetrations. The stresses or stress increments obtained, however, represent the stress field existing in the equivalent homogeneous material with the reduced stiffnesses. An estimate of the stresses existing in the actual material can be obtained by multiplying these stresses by the inverse of the reduction factor:

$$\overline{\sigma}_i = \sigma_i/\overline{p} \tag{4.3}$$

The use of this modeling procedure for linear response of end slabs with penetrations was found to yield results comparable to those from three-dimensional finite-element analyses and from tests (2, 3).

4.5 Solution of Equations

Static equilibrium equations for the structural system are represented by Eq. 4.4.

$$[K(\{U\})]\{U\} = \{P\} \tag{4.4}$$

The system is nonlinear as a result of the variation of the stiffness matrix with changes in nodal displacements. The instantaneous stiffness matrix $[K(\{U\})]$ is assembled by adding the contributions of the individual elements according to their connectivities. By specifying appropriate kinematic constraints to simulate the displacement boundary conditions, the rigid body motions of the structure are eliminated. The instantaneous stiffness matrix becomes positive definite, hence a solution of the equations exists. The load vector $\{P\}$ is obtained by proper summation of all the forces applied on the structure.

In order to achieve a solution to the nonlinear equations, the system was assumed to be piecewise linear and the system solved incrementally. Gaussian elimination procedure was used to solve the linear equations. It required the least amount of operations of all the available techniques, provided that the nodes were numbered to minimize the bandwidth of the stiffness matrix.

In the purely incremental method, the loads are applied incrementally but no equilibrium iterations are performed (Fig. 4.2b). The stiffness matrix is updated at the beginning of each load step by incorporating the material properties at the end of the previous load increment. Variations of the method involve the addition of the residual forces to the next load increment so as to reduce the drift from the "correct"

curve (Fig. 4.2c). Accuracy is also improved by using the tangent stiffness corresponding to the midpoint of the load increment. This average or secant stiffness is estimated by using a numerical procedure such as Runge-Kutta.

The purely iterative method is a one-step Newton-Raphson process. The total loads are applied in a single step and iterations are performed until the procedure converges. The rate of convergence is also improved by updating the stiffness matrix during the iteration process. The major disadvantage of this one step method is that it provides only one point of the response history of the structure.

A combined incremental-iterative procedure is used in the solution process. The following is an outline of this generalized Newton-Raphson procedure used for solving the equilibrium equations.

1. A typical increment of external loads $\{\Delta P\}$ is applied to the structure.
2. The incremental displacements corresponding to the incremental loads are computed using the most recent stiffness matrix:

$$\{\Delta U\}_n = [K]^{-1}_{n-1} \{\Delta P\}_n \tag{4.5}$$

The increments of nodal displacements $\{\Delta u'\}$ for each element are extracted from the structural displacement increments:

$$\{\Delta u'\}_n = [L] \{\Delta U\}_n \tag{4.6}$$

where $[L]$ is a localizing matrix, and the total structural displacement vector is updated.

$$\{U\}_n = \{U\}_{n-1} + \{\Delta U\}_n \tag{4.7}$$

3. Incremental element strains are obtained from the strain displacement relations:

$$\{\Delta e\}_n = [B]\ \{\Delta u'\}_n \tag{4.8}$$

and added to the previous strains to give the total strains:

$$\{e\}_n = \{e\}_{n-1} + \{\Delta e\}_n \tag{4.9}$$

4. Approximate incremental stresses are obtained by using the stress-strain relations from the previous step or iteration:

$$\{\Delta\sigma\}_n = [D]_{n-1}\ \{\Delta e\}_n \tag{4.10}$$

Better estimates could be obtained by using the midpoint tangent moduli but that involves additional computations.

5. Adding the incremental stresses to the existing element stresses give the updated stresses:

$$\{\sigma\}_n = \{\sigma\}_{n-1} + \{\Delta\sigma\}_n \tag{4.11}$$

6. The total stresses and strains are evaluated according to the material criteria in use:

$$f(\{\sigma\}_n,\ \{e\}_n) = 0. \tag{4.12}$$

The outcome of this evaluation is generally an adjusted stress vector and the new tangent material matrix $[D]_n$ corresponding to the current stress and strain states.

7. Using the principle of minimum potential energy or virtual work, the element nodal forces corresponding to the adjusted stresses are computed.

$$\{r\} = \overline{p} \int_{vol.} [B]^T\ \{\sigma\}_n\ dv \tag{4.13}$$

Here $\bar{p}$ is the reduction factor for modeling the penetrations described in Section 4.4. If it is specified that the tangent stiffness matrix should be evaluated during the current step, then the element tangent stiffness is computed from

$$[K]_n = \bar{p} \int_{vol.} [B]^T [D]_n [B] \, dv \tag{4.14}$$

8. The static equilibrium of the structure is checked by comparing the total external nodal loads $\{P\}$ with the element nodal forces equivalent to the prevailing stresses in the structure. The equivalent forces vector for the whole structure is obtained by proper summation of the contributions of the individual elements. The difference is the residual force vector:

$$\{R\} = \{P\} - \{\sum^{m} \bar{p} \int_{vol.} [B]^T \{\sigma\} \, dv\} \tag{4.15}$$

9. The residual force vector $\{R\}$ is a measure of the convergence of the procedure. The vector is compared with the adopted convergence criterion. If the latter is satisfied, the next increment of external loads is applied and the whole procedure is repeated. If convergence is not achieved, existing residual forces are applied as external forces, and the solution proceeds again from the second step. The structural stiffness matrix may be reassembled and inverted at preselected iteration intervals.

It should be observed that any unbalanced forces neglected because of the convergence criterion are automatically incorporated in the subsequent load increment. This is a consequence of the manner of evaluating the residual forces outlined above.

4.6 Convergence Criteria

The convergence criterion used in nonlinear equilibrium analysis should reflect the balance between the internal stresses and the external forces. Evaluation of the norm of the residual-loads vector provides a reasonable choice. Physically it represents the magnitude of the resultant vector in the hypothetical multi-dimensional space. Hence, satisfactory convergence was assumed to have been attained when the inequality

$$|\{R\}| \; / \; |\{\Delta P\}| \leq c \tag{4.16}$$

was satisfied. Here $|\{R\}| = \sqrt{\{R\}^T \{R\}}$, the norm of the residuals, is compared with the norm of the increment of the applied loads $|\{\Delta P\}| = \sqrt{\{\Delta P\}^T \{\Delta P\}}$. Convergence tolerance c can be selected according to desired accuracy and available computing resources. In this investigation, a tolerance factor of 0.1% was used for most of the load steps. As the ultimate load is approached, the number of iterations necessary for a very fine tolerance increased rapidly, so values of c between 1% and 5% had to be tolerated. Additional insight into the performance of the numerical procedure was obtained by monitoring the norm of the displacement increments. They were found to follow the same pattern as the norms of the load vectors.

The question of the convergence of the incremental-iterative procedure is intimately related to the concept of simulating the failure of the structure being analyzed. In the physical world, the structure starts to fail when the applied loads produce internal stresses exceeding the carrying-capacity of the material at certain points of the continuum. The structure responds by redistributing the stresses to the less

stressed areas. Redistribution will result in a new stable equilibrium configuration as long as the ultimate capacity of the structure is not exceeded. Failure of the structure starts when the readjustment process starts a chain reaction whereby redistributed stresses generate larger stresses as stiffness of the structure drops and its deflections increase, leading to the collapse of the unstable structure. Failure is manifested in the formation of a "mechanism" in which part or all of the structure can undergo arbitrarily large rigid body motions.

The simulation of this sequence of events in a finite element environment is facilitated by the incremental-iterative procedure. As the external loads are incremented, some elements meet or exceed the transition criteria of the material model. The stiffnesses of these elements are adjusted and their excessive stresses are reapplied to the structure as residual loads in the subsequent iteration. These residual loads are resisted by the stiffer, less stressed elements. There will be a potential equilibrium configuration as long as an internal stress distribution that balances the applied loads can be established without violating the constraints of the material properties. Distress is initiated when the elements fail to accommodate the residual loads. Because this is accompanied by a steady drop in the stiffness, the displacements keep on increasing and more elements shed off part or all of the load they have been carrying. This, in turn, inflates the residual loads. This process continues until the numerical procedure becomes unstable. The simulated instability and failure of the structure is related to the condition of the stiffness matrix of the structure.

The deterioration of the stiffness matrix reflects the decay in the stiffness of the actual structure. When the stiffness matrix ceases to be positive definite, rigid body displacements of one or more of the degrees of freedom become possible and the numerical procedure becomes unstable. The literal application of the procedure does not distinguish between an insignificant localized failure and the global failure of the structure. However, localized failures can be circumvented easily by avoiding zero values in the main diagonal of the element material matrix. In this way the stiffness matrix of the structure will not become positive semidefinite, while relatively large displacements can still be obtained. This mathematical model approach has the advantage of providing an insight into the conditions at the point of failure of the structure. The mechanism of failure of the structure may then be deduced from the sequence and configuration of the elements that have met the failure requirements.

5. COMPARISON OF ANALYTICAL AND EXPERIMENTAL RESULTS

5.1 Introductory Remarks

The analytical model assembled to simulate the experimental models has two special features in addition to the use of a simple material model for the concrete:

(1) The object of the modeling effort has been the successful simulation of the changes in internal-force trajectories rather than tracing the changes in crack geometry. The main benefit provided by this choice was freeing the model from having to satisfy a very difficult and unnecessary test. Internal-crack trajectories tend to be very sensitive to properties of the material model and to the numerical accuracy achievable in the strain computations. But simulation of crack development is not essential because overall behavior is defined by the main force trajectories and not directly by inferred crack locations.

(2) Three-dimensional phenomena, introduced by the presence of penetrations in the end slab, have been represented in a two-dimensional model by modifying the stiffness of certain elements.

The critical experimental test for the model is whether it reproduces overall behavior, represented by the relationship between internal pressure and slab deflection. However, the plausibility of the two features indicated above requires comparisons at a "lower" level of response. Consequently, this chapter contains a detailed discussion, for a particular vessel, of calculated changes in deformations principal-stress trajectories, and internal strains. This is followed by comparisons of pressure-deflection relationships for all test vessels. A discussion

of the calculated effect of concrete strength on end-slab strength concludes the chapter.

5.2 Calculated Response for a Test Vessel

(a) Assumed Properties for PV30

The axisymmetric analytical model is compared with the vertical section of the experimental model in Fig. 5.1. The vessel was represented by 124 nodes defining 100 rectangular isoparametric elements. The four node quadrilateral isoparametric element is known to be excessively stiff in shear. In order to circumvent this, nonconforming modes are added to the normal definition of the element. Of the total, only 12 of the elements were used for the skirt wall because the contribution of nonlinear response in the wall to the overall response was anticipated to be small and because the main function of the elements representing the wall in the analytical model was simply to provide a satisfactory boundary to the end slab. It is only necessary to provide enough elements so as to not unduly constrain the rotation of the vertical wall.

The effective prestressing forces were applied as equivalent nodal loads. The magnitudes shown in Fig. 5.1 in kips (1000 lb. or 4.4 kN) correspond to a segment of the vessel subtending an angle of one radian at the axis of symmetry. The coordinates of the nodal points involved were selected to coincide with the centroids of the prestressing rods and the bands of wrapped wire. Because no elements were used to model the circumferential prestressing wires, their stiffnesses were incorporated into the concrete wall in the form of an equivalent additional thickness of 1.25 in. (38 mm), smeared over the entire height of the wall. The increase in the prestressing forces with the deformation of the vessel

was estimated from the calculated and measured deflections at the load points. These force increments were assumed to vary linearly with the internal pressure, and were added to the initial forces.

In order to make use of the nonconforming modes effectively, the 88 elements in the end slab included four additional non-nodal degrees of freedom. This enabled the elements to respond to the sharp stress gradients in the slab. The nonconforming modes were, however, shut off in the 12 slender elements representing the wall. In this way, parasitic shear stresses were prevented from cropping up in the head while the stiffness of the wall was adequately represented.

The nodes along the axis of symmetry were not allowed to displace radially because of axial symmetry. Those along the bottom of the wall were completely restrained since the closing steel plate does not allow any appreciable displacements.

The region in the slab containing the penetrations was represented by 64 elements (arranged 8 rows by 8 columns, starting at axis of symmetry). A stiffness reduction factor of 0.6 was determined from the ratio of the gross plan area to the actual plan area of the penetrations. Because the triangular pattern of the penetrations softened the end slab equally in all directions, isotropic material properties with reduced moduli were used. Interaction between the radial and hoop directions was suppressed by setting the appropriate values of Poisson's ratio to zero.

(b) Numerical Solution Procedure

Behavior was defined by eight solutions obtained for internal pressures increasing from zero by finite selected increments. The solution for zero internal pressure represented the condition of the

vessel under the initial prestressing forces. It was needed as a benchmark for calculated response in subsequent steps because the laboratory measurements started after prestressing. Sequence of loading, number of iterations in every load step and instances of reassembling and solving the system of equations are summarized in Table 3. Convergence was achieved with no residual loads in each of the first six loading steps. In the seventh load step, iteration was stopped when the norm of the residual loads was less than 5% of that of the applied loads. In the eighth load step, residual loads started by decreasing slightly. Then they increased steadily until their magnitude exceeded that of the applied load increment. The iterations were continued until it was evident that no convergence could be achieved. Although the solution obtained does not represent equilibrium conditions, it represents the unstable conditions before failure. The complete solution required less than 90 seconds of central-processor time on the CDC Cyber 175 system of the Digital Computer Laboratory at the University of Illinois.

(c) Calculated Changes in Deformation

Profiles of one-half of the end slab indicated by the eight solutions are shown in Fig. 5.2a through 5.2h. The plotted deflected shape is exaggerated in that the nodal displacements were plotted to a scale 150 times that of the dimensions of the vessel.

The deflected shapes provide little insight into the response of the end slab other than indicating the primary source of the increase in deflection rate at internal stresses over 2000 psi (13.8 MPa). The distortion is indicated to be concentrated at the slab-wall interface.

(d) Calculated Principal Stresses

Changes in the behavior of the end-slab are defined by the plots of principal stress magnitudes and directions in Fig. 5.3a through 5.3h.

The principal-stress plot for 1000 psi internal pressure suggests the tendency of the end slab toward dome-action even at relatively low stresses. Radial tensile stresses near the re-entrant corner and the center of the slab near the exterior surface are indicated to be small relative to the "diagonal" compressive stresses. This tendency is emphasized in solutions corresponding to higher internal-pressure levels. The trajectories of the compressive stresses suggest that the pressure on the inside surface of the slab is transmitted to the external reactions (provided by the forces representing the prestressing reinforcement) primarily through dome action. The boundary of the softened region (representing penetrations) is also identified by the stress patterns.

The failure mechanism may be inferred from Fig. 5.4 which shows the relative values of the failure indices (Eq. 4.1) for the elements. The intensity of the shading, as identified in the upper left-hand corner of the figure, indicates the relative magnitude of the failure index. The distribution of the magnitudes of the failure indices shows that failure is likely to occur at a section near the edge of the perforated region.

(e) Comparison of Calculated and Measured Strains

The measured pressure-strain data for PV30 are reproduced in Fig. 5.5 through 5.33 in order to compare them with calculated pressure-strain curves shown on the same figures by broken lines. Locations and orientations for the strain gages are indicated in Fig. 3.15.

It is seen from Figs. 5.5 through 5.33 that the comparison was, in general, quite favorable especially with respect to the shape of the pressure-strain curves. Consider, as a measure of success of the theoretical model, comparison of the measured and calculated strains for the gages oriented diagonally (Figs. 5.7, 5.8, 5.11, 5.12, 5.15, 5.16, 5.19, 5.24, 5.25, and 5.31). In all cases but one, the shape of the curve was simulated quite well by the analytical model. The one negative result was obtained for tensile strain at level 3 of penetrations 1 and 3 (Fig. 5.16). The tendency of the one measured curve was to increase at an increasing rate with pressure, while calculations indicated hardly any increase in strain above 1500 psi. On the other hand excellent correlation was observed at levels 1 and 3 of penetrations 4 and 5 (Fig. 5.24 and 5.25).

The generally good correlation of calculated and measured strains, especially the correct simulation of changes in strain rates, indicates that the analytical model may be used reliably in studying the local as well as overall behavior of the end slab and in determining the characteristics of the collapse mechanism. The results are made more noteworthy by the fact that it is virtually impossible to tune a credible model to match observed strains in as many locations as they were measured.

5.3 Comparisons of Pressure-Deflection Curves

Complete sets of solutions were obtained for the specific material properties of one vessel of each type. The measured and calculated relationships between internal pressure and vertical deflection at center of end slab are presented for the vessels with solid end

slabs in Fig. 5.33, for the vessels with 5-in. penetrations in Fig. 5.34, and for the vessels with 2-in. penetrations in Fig. 5.35.

Vessels PV26 and PV28 with solid end slabs were directly representable by the analytical axisymmetric model. Modeling of the effect of penetrations in vessels PV27 and PV30 with 2-in. penetrations was described in a preceding section of this chapter. The effect of the 5-in. penetrations in vessels PV27 and PV32 was approximated in the model by modifying the moduli (in all three directions) of the elements within two circles containing the penetrations by 0.53, ratio of the net to the gross area in that region. The modulus in the hoop direction was further modified by a factor of 0.1 to reflect the softening in that direction. Coupling between the hoop and the other two directions was eliminated.

The limiting pressure for the calculated results corresponds to the pressure at which the solution became unstable and therefore its magnitude is influenced by the choice of the load increment. Instability might have been obtained at a slightly lower pressure. The mean ratio of the measured to calculated maximum pressure deviated less than 1% for all cases considered except for PV28 for which the measured value exceeded the calculated by 8%.

As would be expected from the comparisons for strains, the analytical model provided a good estimate of the load at which appreciable nonlinear response was initiated. (It should be noted that curves for PV26 and PV28 refer to "retests.") In general, the analytical model indicated larger displacements than observed in the range of nonlinear response.

5.4 Calculated Effect of Concrete Strength

Three sets of solutions were obtained, each set at a different concrete strength, for the geometrical properties of PV31 which had an end slab with 2-in. penetrations. Initial parameters for the reinforcement were also set equal to those of PV31.

The calculated pressure-deflection (at end-slab center) relationships are plotted in Fig. 5.36 for concrete strengths of 6000, 4000, and 2000 psi. These curves indicate that, for the properties assumed, the pressure level at which nonlinear response begins is relatively insensitive to changes in concrete strength. This indication is compatible with the fact that a substantial portion of the effective tensile strength is provided by the prestress which was kept constant for the three cases.

The calculated strengths are plotted against concrete strength in Fig. 5.37. On the basis of these results, the strength of the end slabs for PV31 would be expected to be reduced at an increasing rate with decreasing concrete strength. Also, use of concrete with a strength in excess of 6000 psi would be expected not to improve the slab strength appreciably.

Results from tests of PV30, PV31, and PV34 are also plotted in Fig. 5.37. Even though the comparison of results from PV30 and PV34 with the calculated results is not strictly valid because of small differences in prestress levels, it may be concluded that the trend as well as the magnitudes of the test results were in agreement with results based on the analytical model.

6. SUMMARY

The object of this investigation was the development of a method to permit reliable calculation of the strength of end slabs of prestressed concrete nuclear reactor vessels.

The experimental study included the tests to failure under internal pressure of ten small-scale cylindrical vessels with flat end slabs. The vessels were prestressed circumferentially and longitudinally. The end slab had no additional reinforcement.

The experimental variables were the end-slab thickness, size and arrangement of penetrations in the end slab, and the concrete strength. The penetrations, which were not reinforced by sleeves or liners, were closed by steel plates at the pressurized surface of the slabs (Fig. 1.1).

Each vessel was pressurized to failure over a period of approximately three hours. The range of attained maximum pressures was from 1800 psi (12.4 MPa) to 3765 psi (26.0 MPa). End slabs of all test vessels failed in shear. Failures were violent despite the use of fluid to develop the internal pressure.

The failure pressures indicated decisively the effects of changes in slab thickness and concrete strength. However, end-slab strength was relatively insensitive to changes in the amount of cross section removed by the penetrations.

An axisymmetric nonlinear finite-element model was developed to simulate the behavior of the physical models. The model was successful in indicating the observed changes in (a) internal stress paths (Fig. 5.3), (b) internal strains (Figs. 5.5 through 5.32), and (c) slab deflections (Figs. 5.33 through 5.35) as well as the observed strength of the test vessels.

A significant feature of the analytical model is that it uses a very simple failure criterion for the concrete (Mohr in compression and limiting strain in tension). Close agreement between experimental and analytical results confirms that overall nonlinear response phenomena in thick end slabs of prestressed concrete vessels may be estimated satisfactorily without the necessity of detailed information on the response of concrete subjected to a three-dimensional stress field.

Shear strengths of the test vessels were calculated successfully without any "calibration" constants derived from the test results of the vessels. Required input data were limited to information on the geometry of the vessel, effective prestress forces, the compressive strength of the concrete, and the type of loading.

7. REFERENCES

1. S. L. Paul, et al, "Strength and Behavior of Prestressed Concrete Vessels for Nuclear Reactors," Civil Engineering Studies, Structural Research Series No. 346, University of Illinois, Urbana, July 1969.

2. B. I. Karlsson and M. A. Sozen, "Shear Strength of End Slabs with and without Penetrations in Prestressed Concrete Reactor Vessels," Civil Engineering Studies, Structural Research Series No. 380, University of Illinois, Urbana, July 1971.

3. J. D. Reins, et al., "Shear Strength of End Slabs of Prestressed Concrete Nuclear Reactor Vessels," Civil Engineering Studies, Structural Research Series No. 429, University of Illinois, Urbana, July 1976. (ORNL/SUB/4161-1, Dist. Cat. UC-77)

4. F. E. Richart, A. Brandtzaeg, and R. L. Brown, "A Study of the Failure of Concrete Under Combined Compressive Stresses," Bulletin No. 185, University of Illinois, Engineering Experiment Station, November 1928.

TABLE 1 - Maximum Internal Pressure at Failure

Mark	Nominal Slab Thickness in. (mm)	Concrete Comp Strength psi (MPa)	Penetrations No.	Penetrations Dia. in. (mm)	Prestress Index Long.[a] psi (MPa)	Prestress Index Circum.[b] psi (MPa)	Failure Pressure psi (MPa)	Failure Mode[c]
PV26	10 (254)	6710 (46.3)	-	-	5010 (34.5)	1560 (10.8)	2610 (18.0)	SD
PV27	10 (254)	6845 (47.2)	6	5 (127)	5340 (36.8)	1560 (10.8)	2400 (16.6)	SD
PV29	10 (254)	5480 (37.8)	37	2 (50.8)	5330 (36.8)	1710 (11.8)	2400 (16.6)	SD
PV28	12.5 (317.5)	6420 (44.3)	-	-	5760 (39.7)	1700 (11.7)	3765 (26.0)	SD
PV30	12.5 (317.5)	8300 (43.4)	37	2 (50.8)	5340 (36.8)	1690 (11.7)	3210 (22.1)	SP
PV31	12.5 (317.5)	4970 (34.3)	37	2 (50.8)	5500 (37.9)	1680 (11.6)	2800 (193.)	SP
PV32	12.5 (317.5)	5720 (39.4)	6	5 (127)	5540 (38.2)	1780 (12.3)	3075 (21.2)	SP
PV33	12.5 (317.5)	4875 (33.6)	6	5 (127)	5400 (37.2)	1780 (12.3)	3100 (21.4)	SP
PV34	12.5 (317.5)	2440 (16.8)	37	2 (50.8)	5180 (35.7)	1850 (12.7)	1800 (12.4)	SP
PV35	12.5 (317.5)	3150 (21.7)	6	5 (127)	5240 (36.1)	1780 (12.3)	1900 (13.1)	SP

[a]Total effective prestress force divided by horizontal cross-sectional area of cavity.

[b]Mean effective prestress force in prestressing bands 1 and 2 divided by vertical tributary area of cavity.

[c]SD = Shear failure after complete cormation of cryptodome. SP = Shear failure by punching.

TABLE 2 - Nominal Shear Stresses in End Slab

Mark	Meas. Slab Thickness in.	Penetrations No. x Size in.	Maximum Pressure psi	Shear Stress at Slab Edge[a]		Maximum Shear Stress[b]	
				v psi	$v/\sqrt{f'_c}$	v_m psi	$v_m/\sqrt{f'_c}$
PV26	9.81	-	2610	1660	20.3	-	-
PV27	10.06	6 x 5	2400	1490	18.0	2370	28.8
PV29	9.94	37 x 2	2400	1510	20.4	2820	38.1
PV28	12.38	-	3765	1900	23.7	-	-
PV30	12.22	37 x 2	3210	1640	20.7	3070	38.7
PV31	12.02	37 x 2	2800	1460	20.7	2720	38.6
PV32	12.30	6 x 5	3075	1560	20.7	2490	33.0
PV33	12.45	6 x 5	3100	1560	22.3	2480	35.6
PV34	12.20	37 x 2	1800	920	18.6	1720	34.8
PV35	12.40	6 x 5	1900	960	17.1	1530	27.6

[a]Nominal shear stress at the slab-wall interface

[b]Nominal shear stress at the net section through the penetrations.

TABLE 3 - Incremental Loads and Sequences of Iterations for PV30

Load Step	Internal Pressure psi	Number of Iterations	Number of Reformations of Stiffness Matrix
1	0	2	1
2	1000	4	1
3	1500	4	1
4	2000	14	2
5	2500	24	4
6	2700	32	6
7	3000	56	11
8	3250	71	14
	Total	207	40

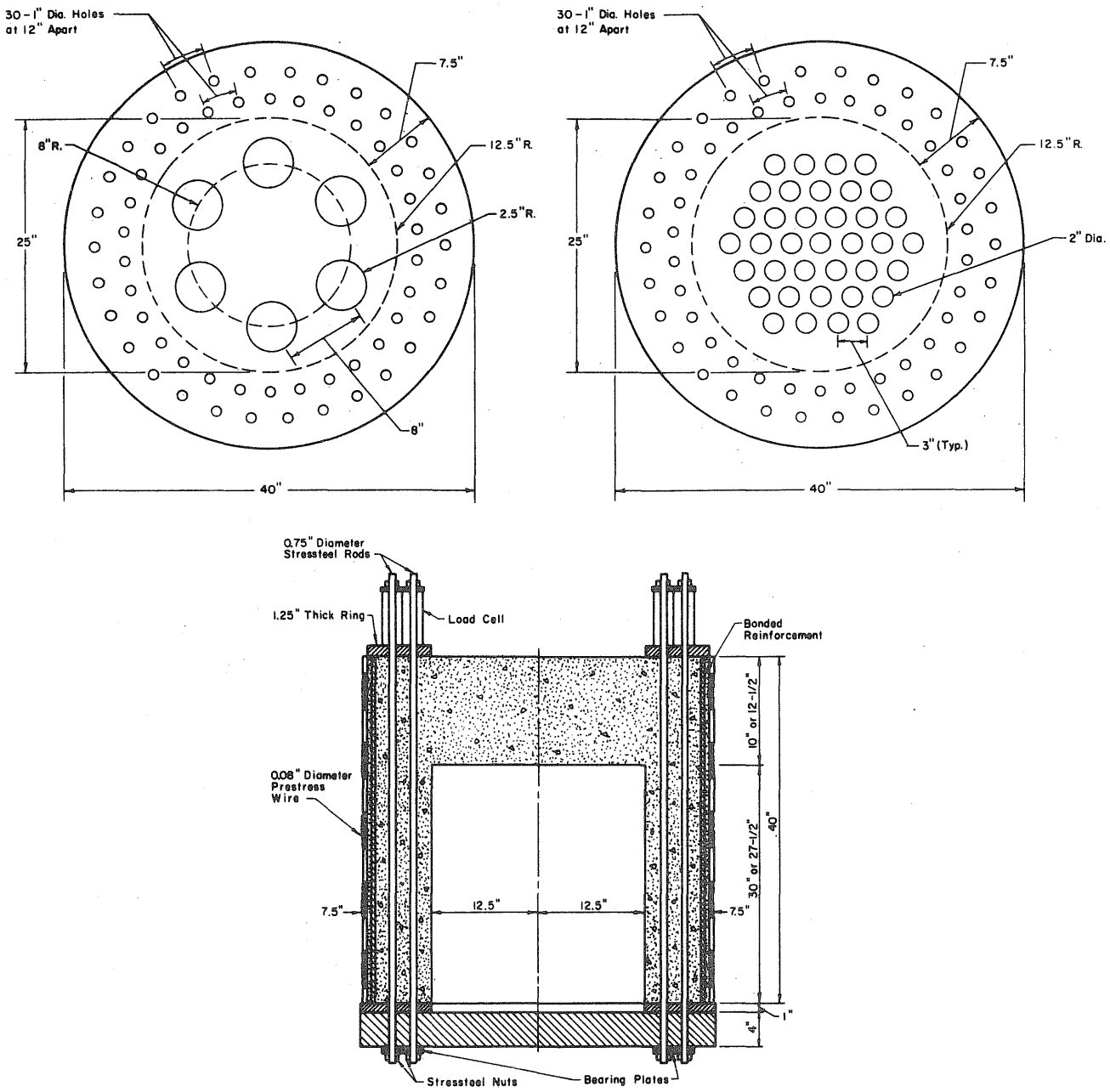

Fig. 1.1 Penetration Patterns and Cross-section of Vessel

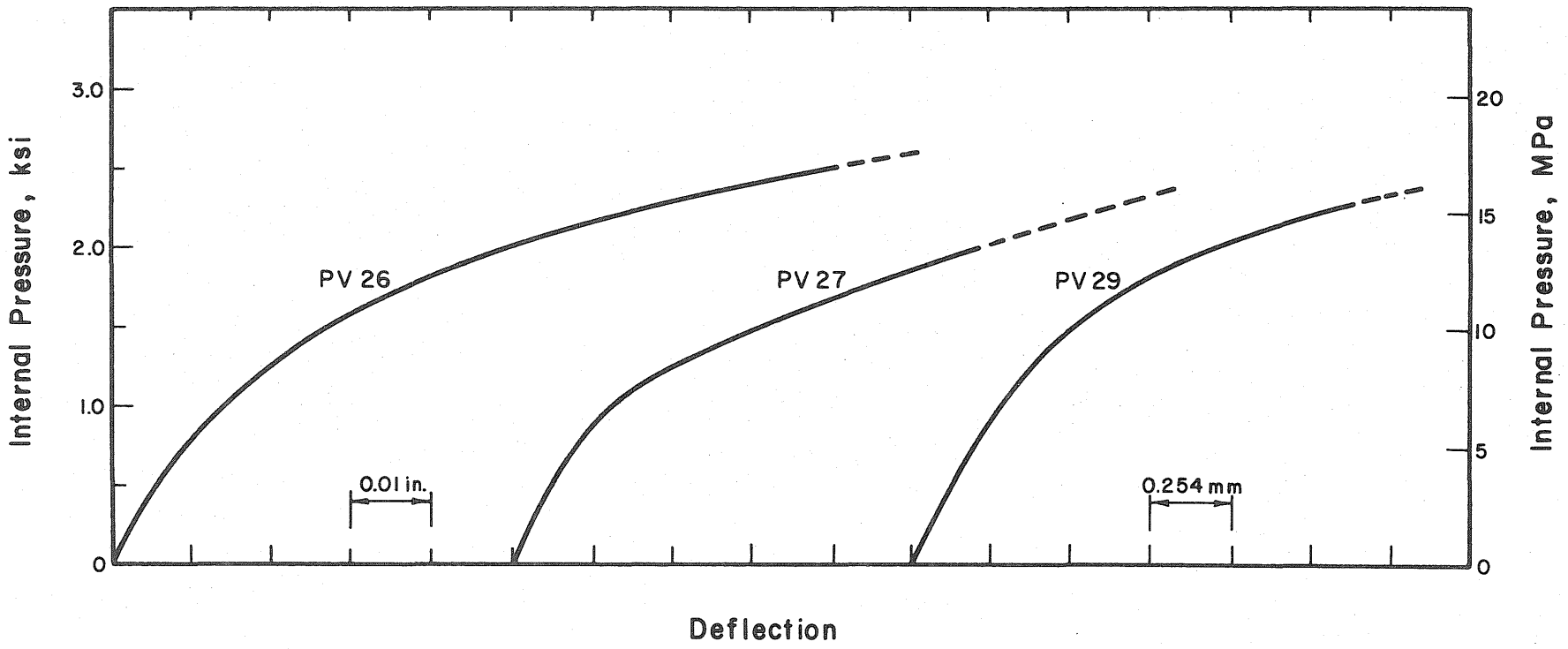

Fig. 3.1 Measured Relationships Between Internal Pressure and Total Deflection at Midspan of End Slab for Test Vessels with 10-in. End Slabs

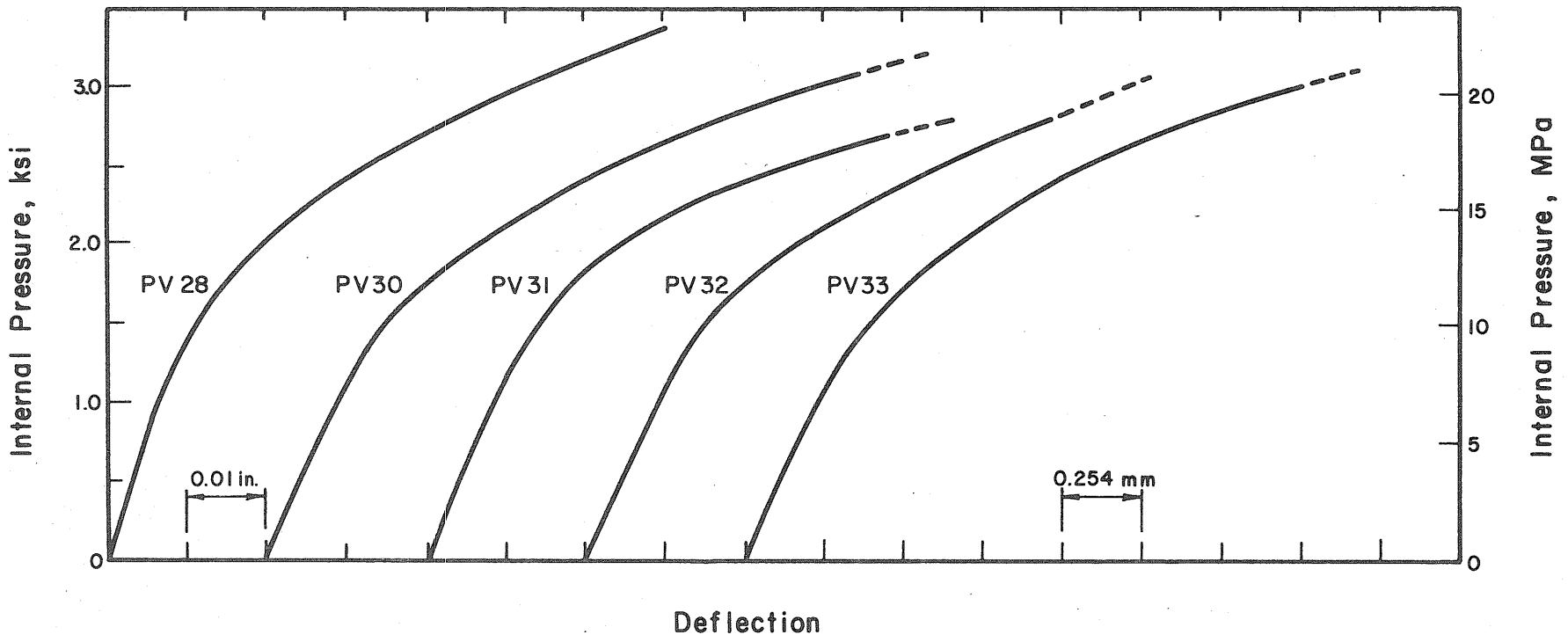

Fig. 3.2 Measured Relationships Between Internal Pressure and Total Deflection at Midspan of End Slab for Test Vessels with 12.5 in. End Slabs

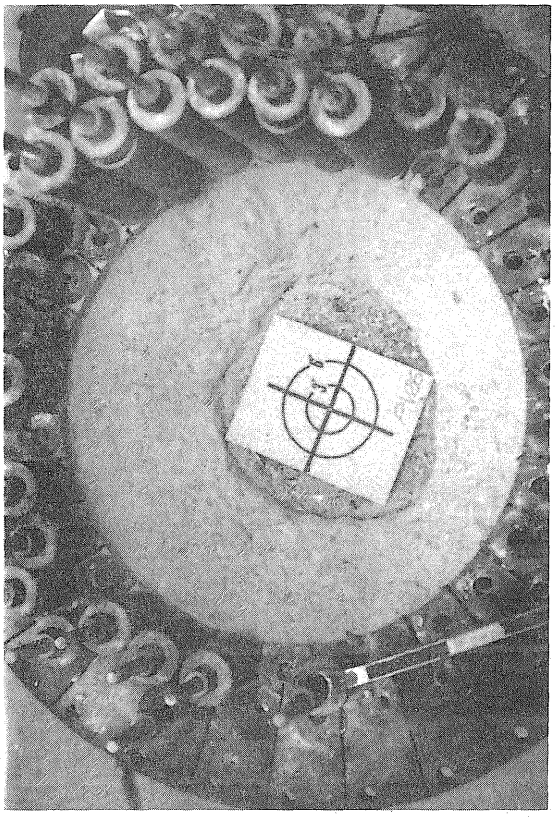

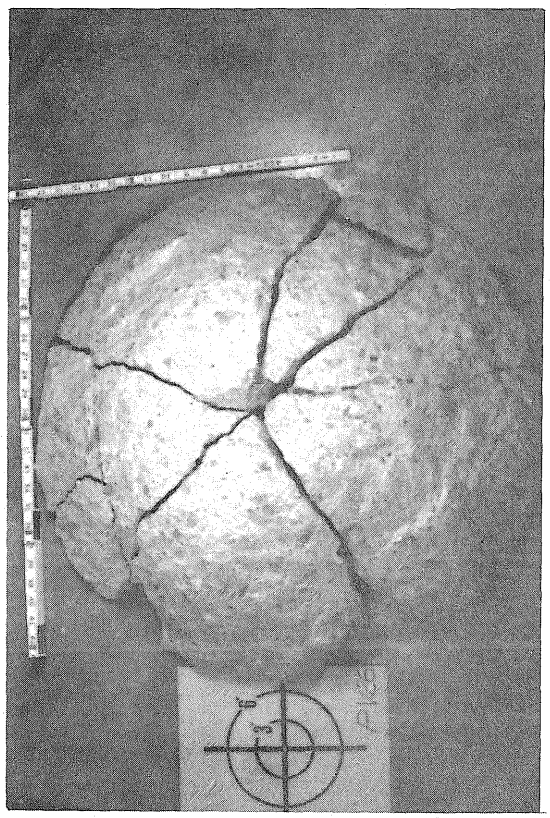

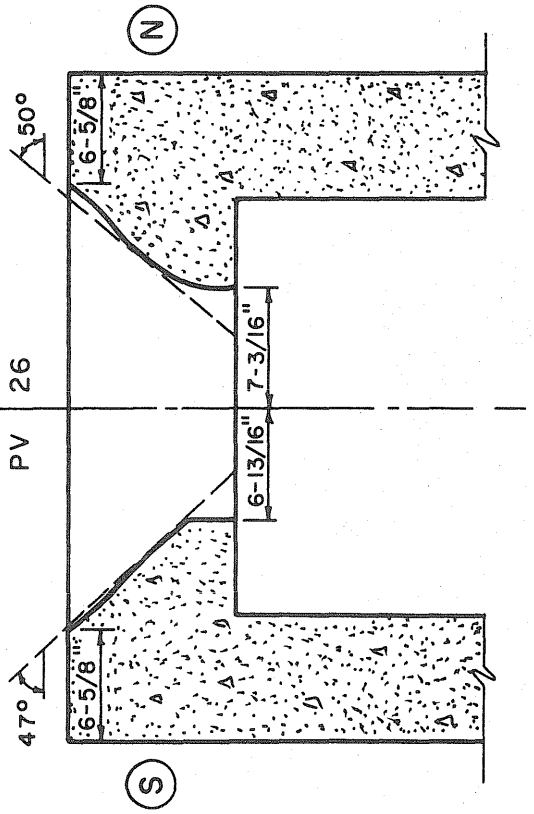

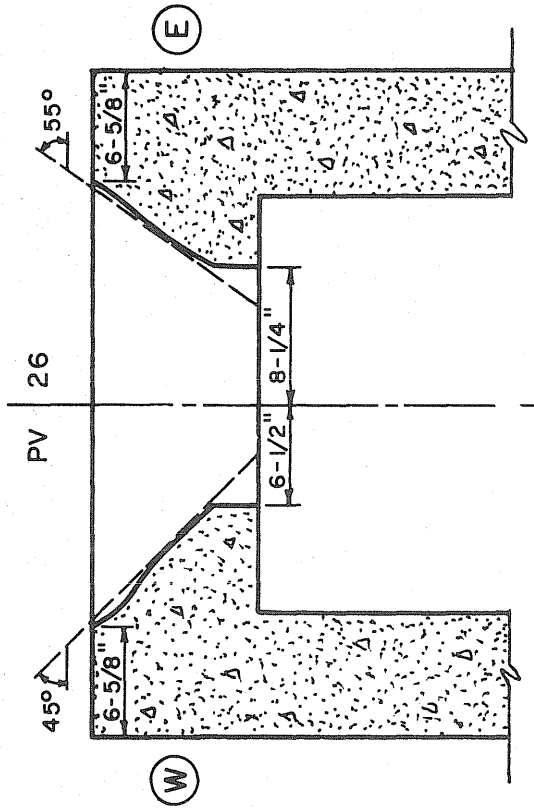

Fig. 3.3 End Slab after Test, PV26

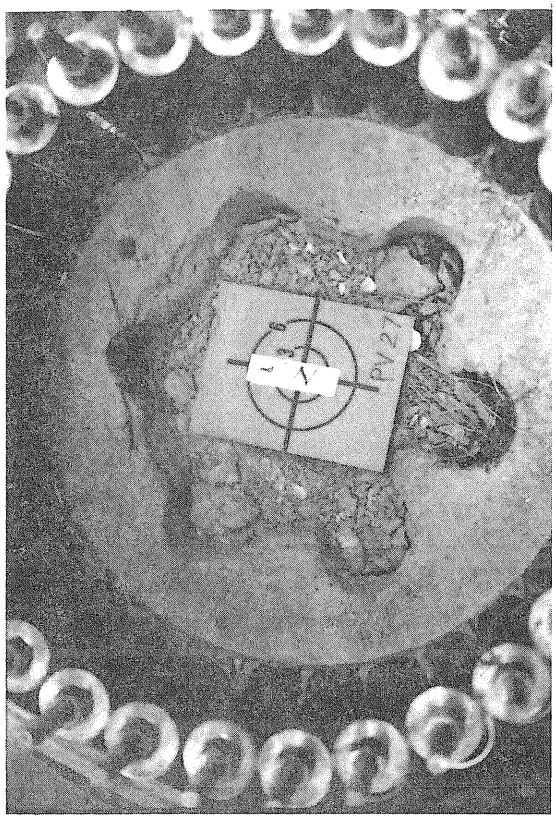

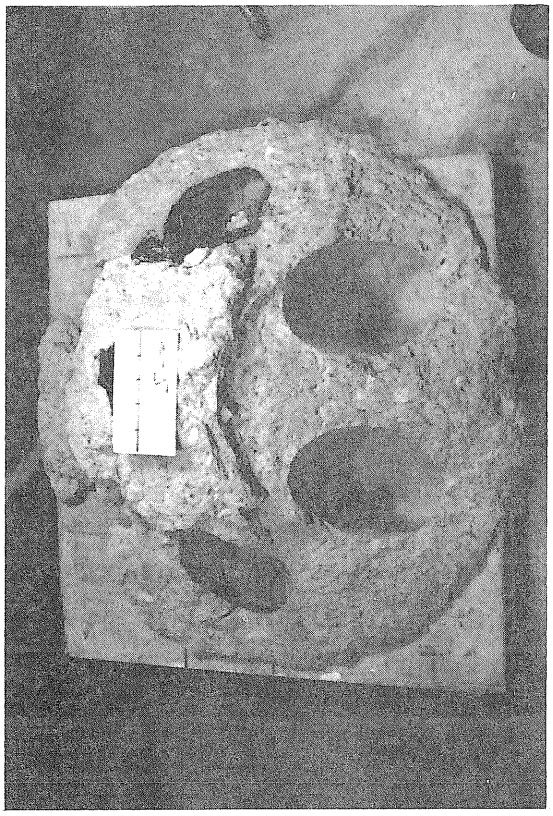

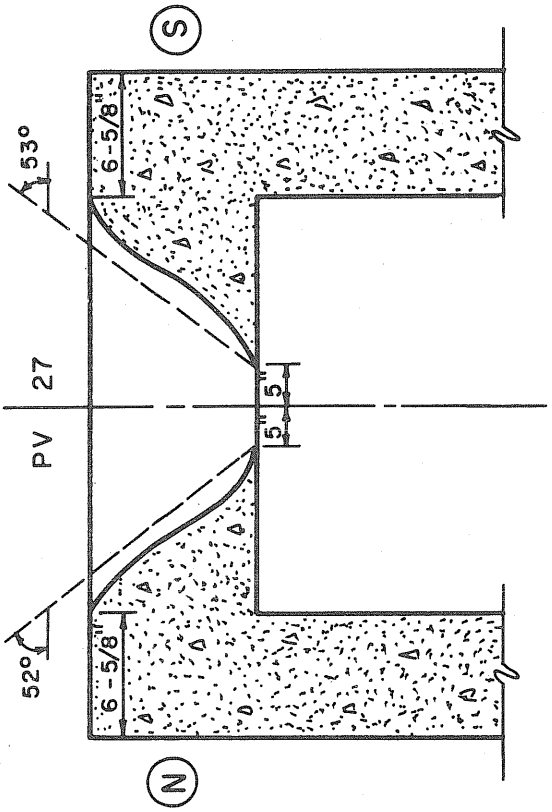

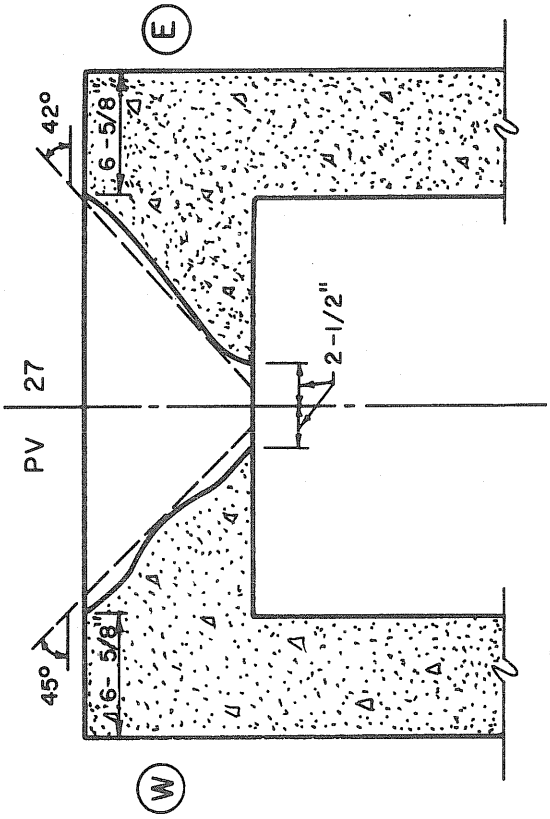

Fig. 3.4 End Slab after Test, PV27

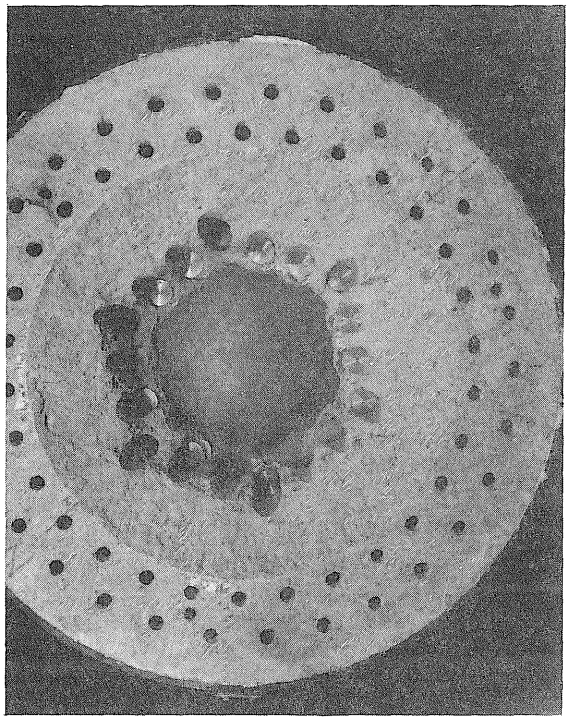

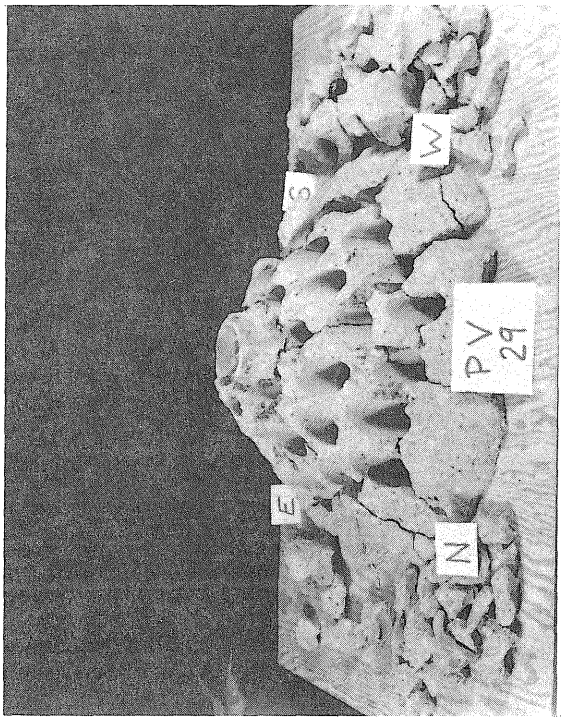

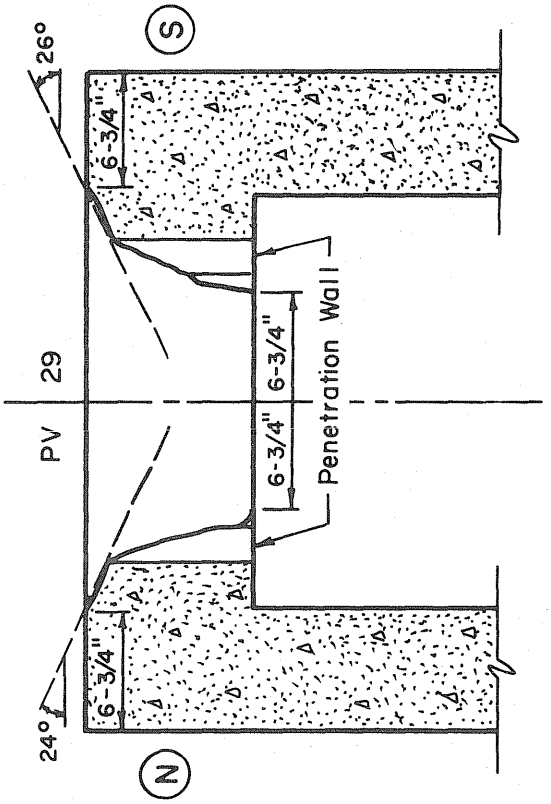

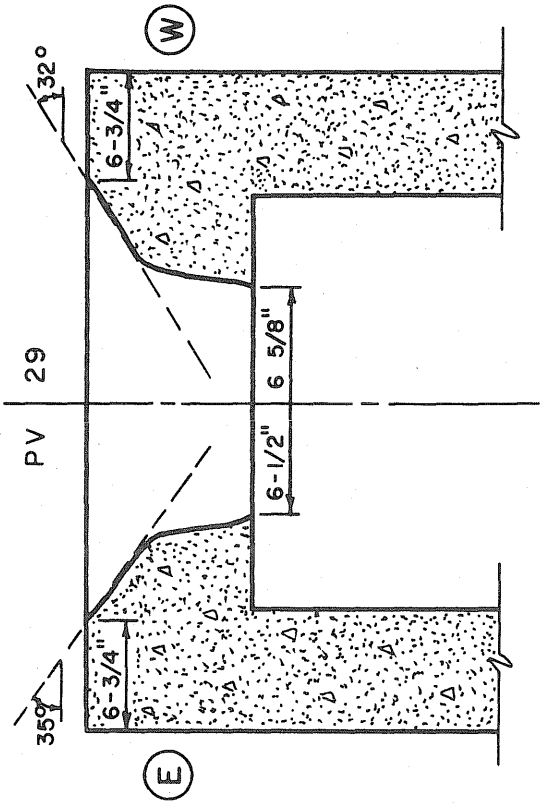

Fig. 3.5 End Slab after Test PV29

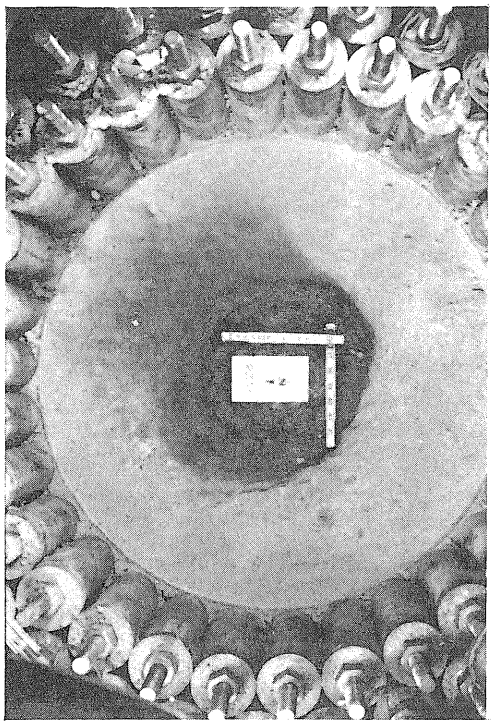

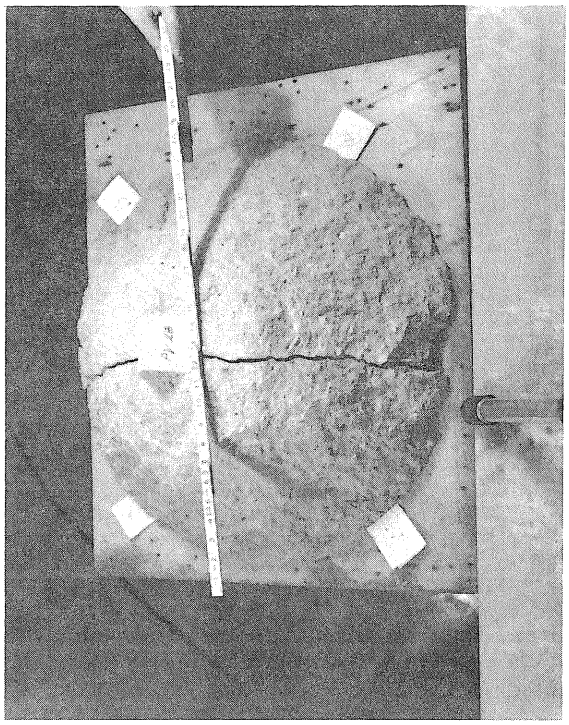

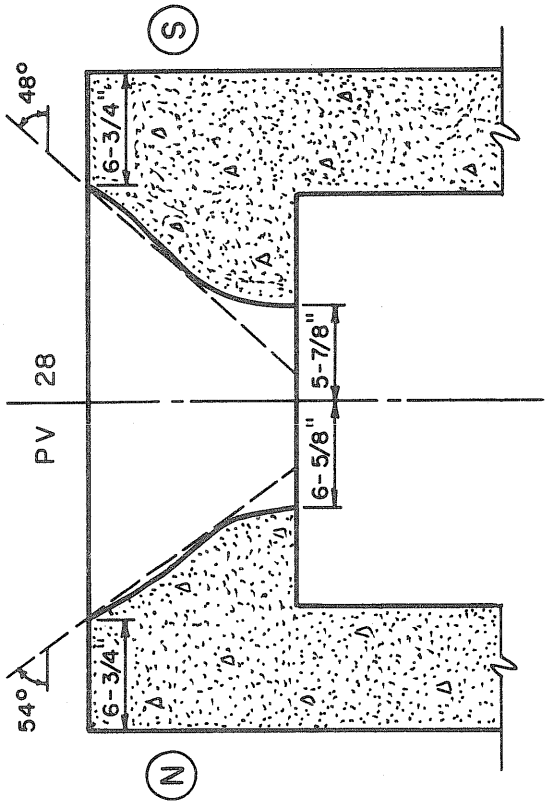

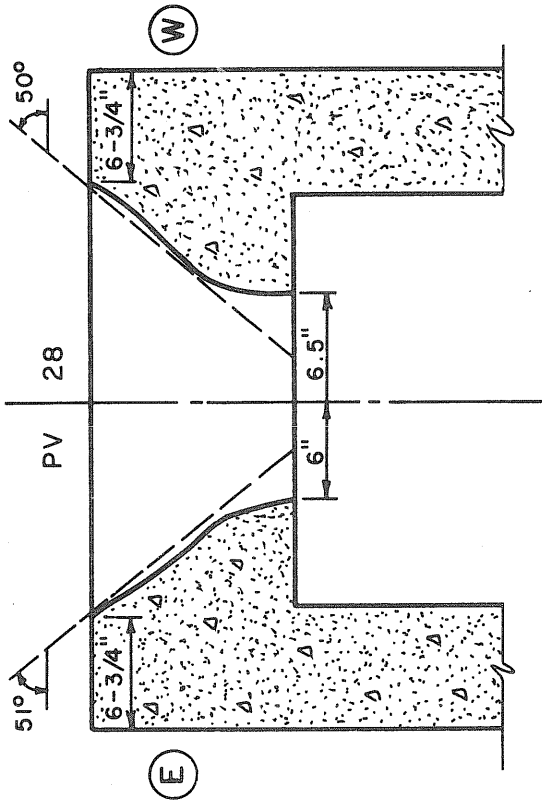

Fig. 3.6 End Slab after Test PV28

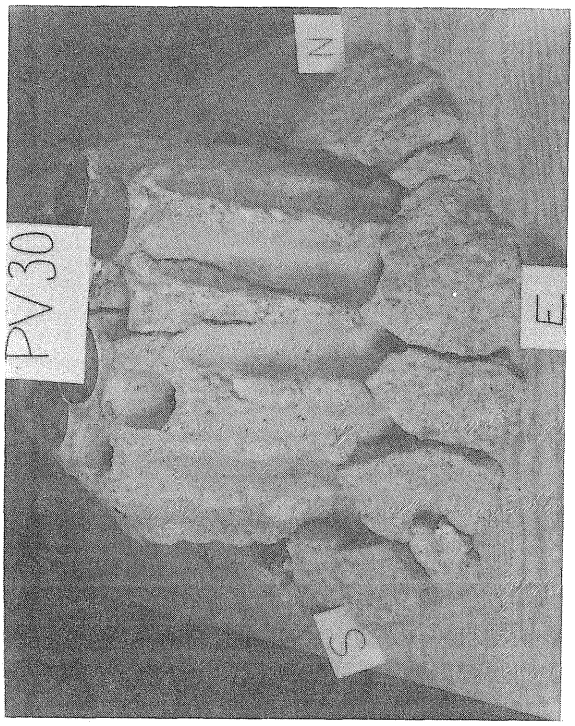

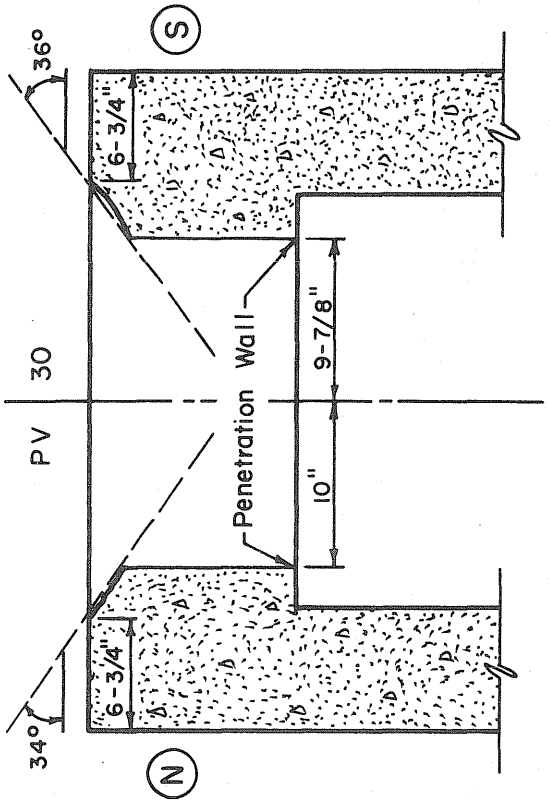

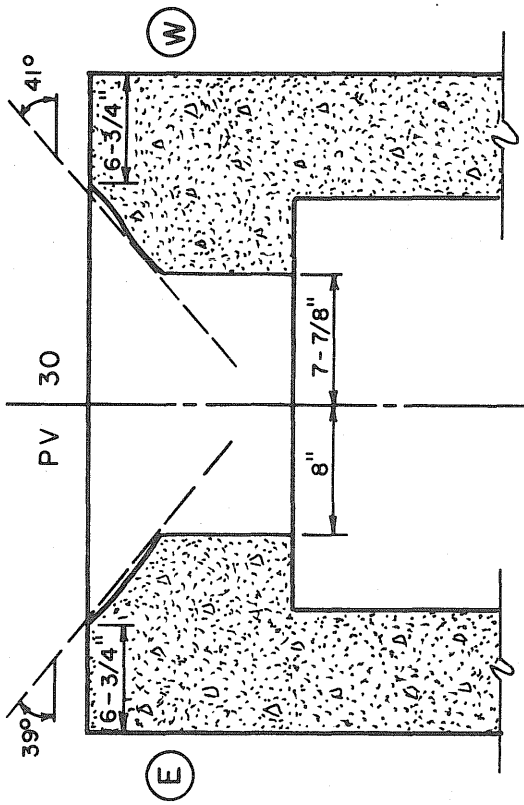

Fig. 3.7 End Slab after Test PV30

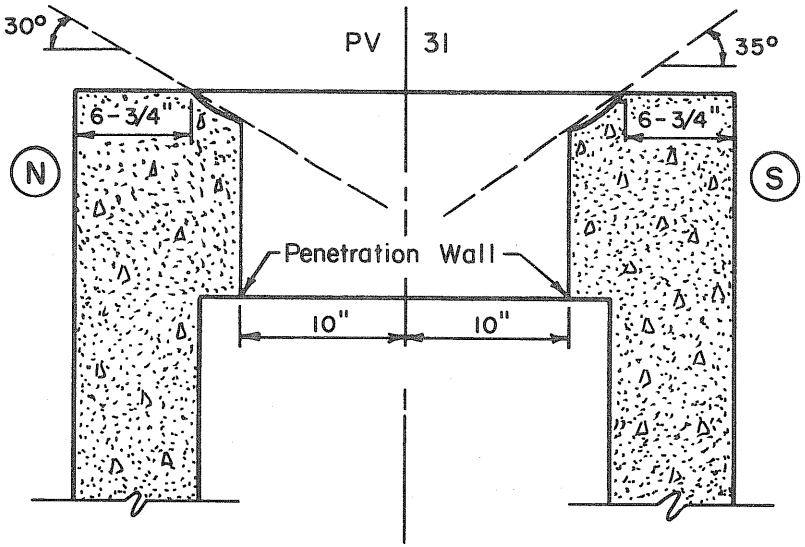

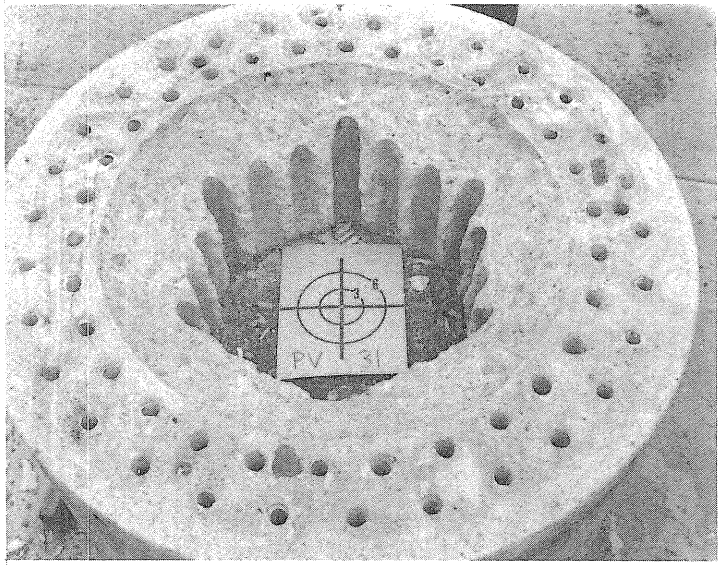

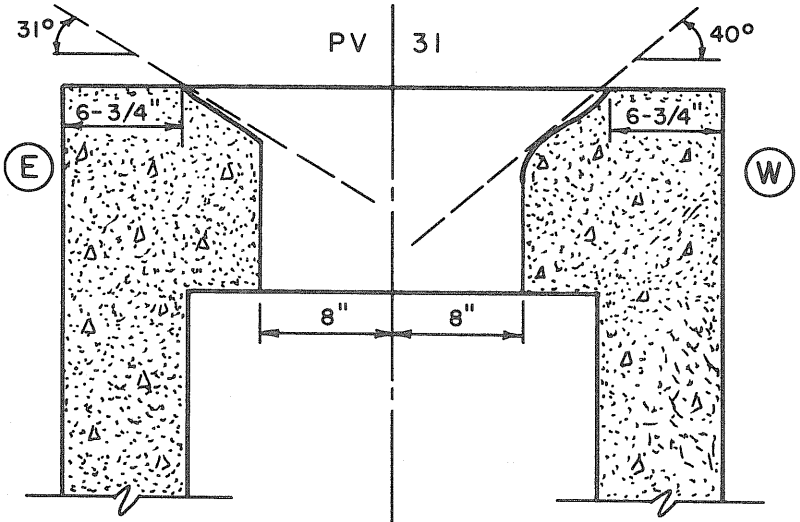

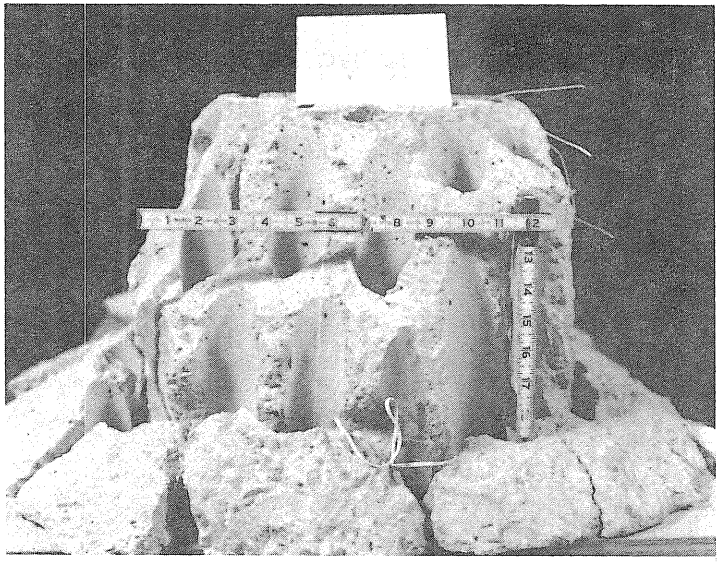

Fig. 3.8a End Slab after Test PV31

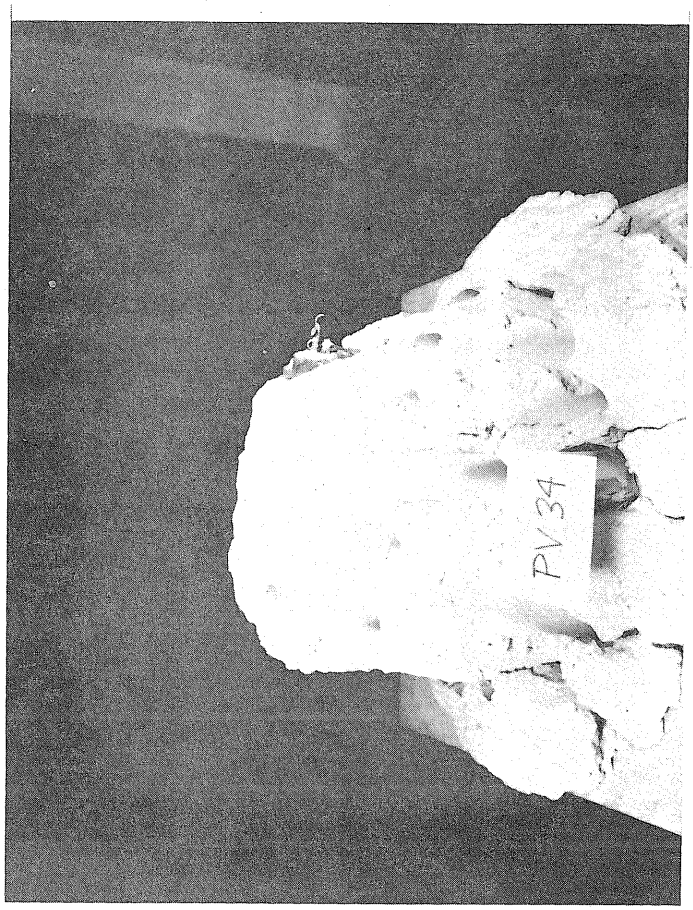

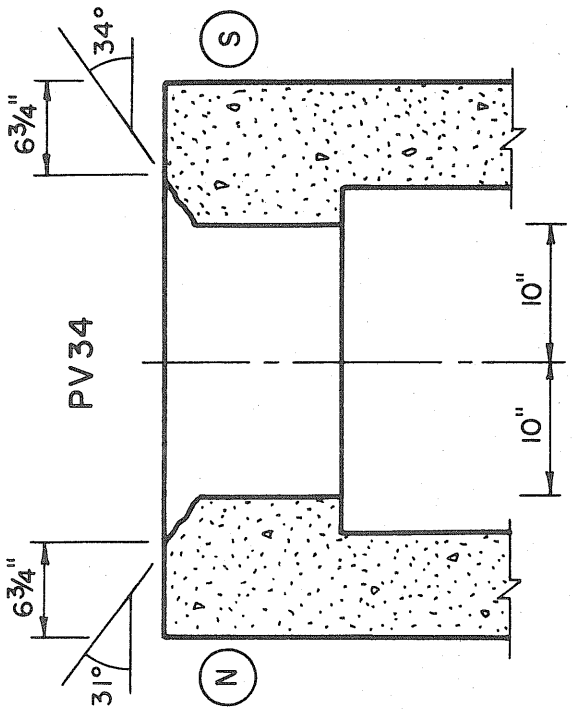

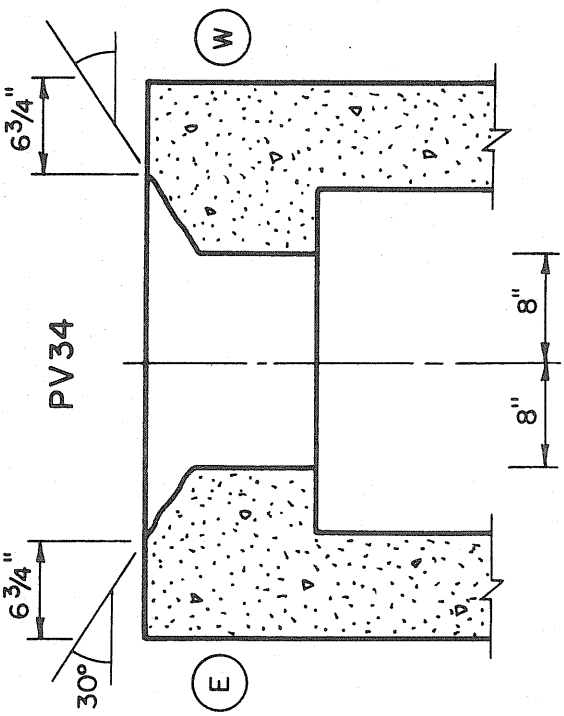

Fig. 3.8b End Slab After Test PV34

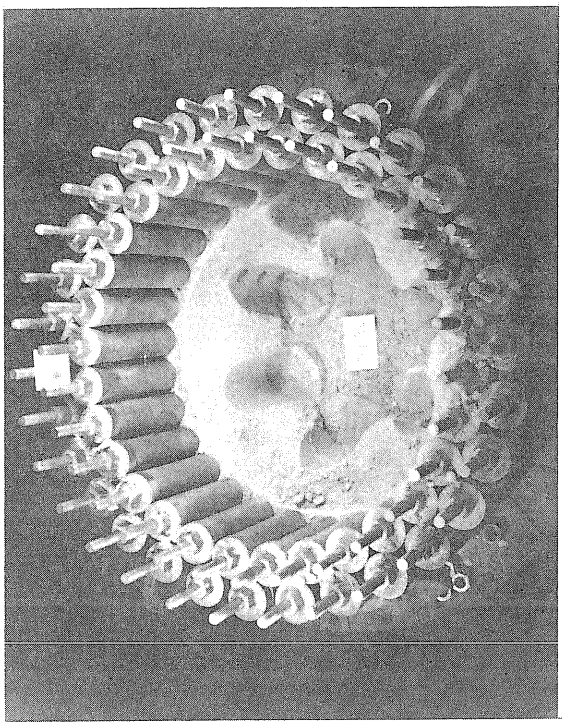

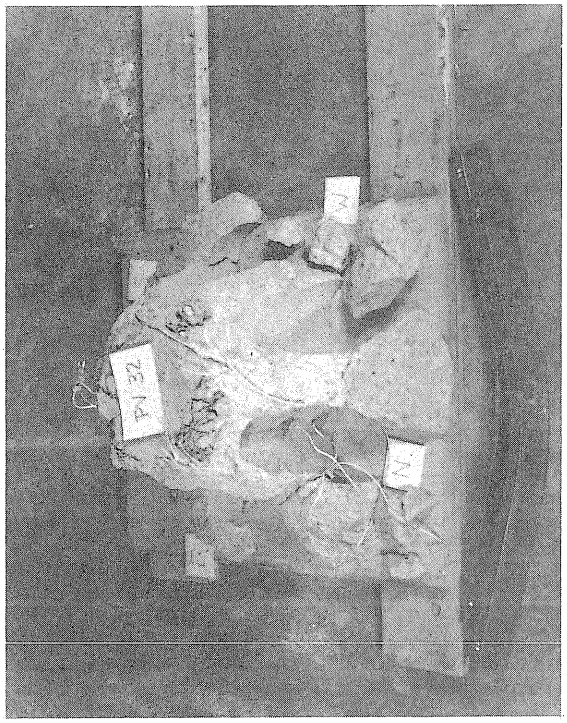

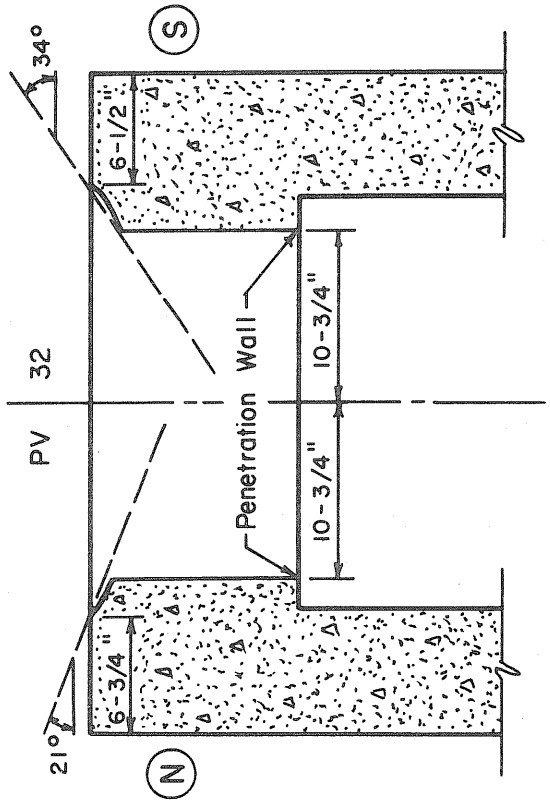

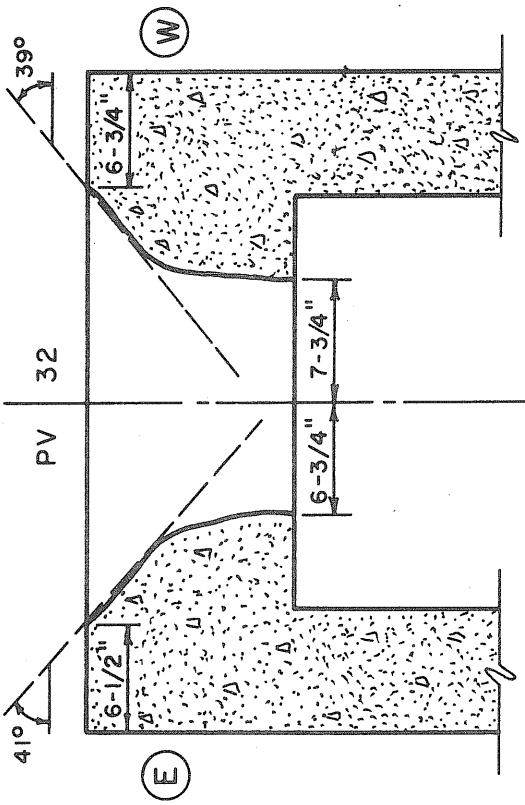

Fig. 3.9 End Slab after Test PV32

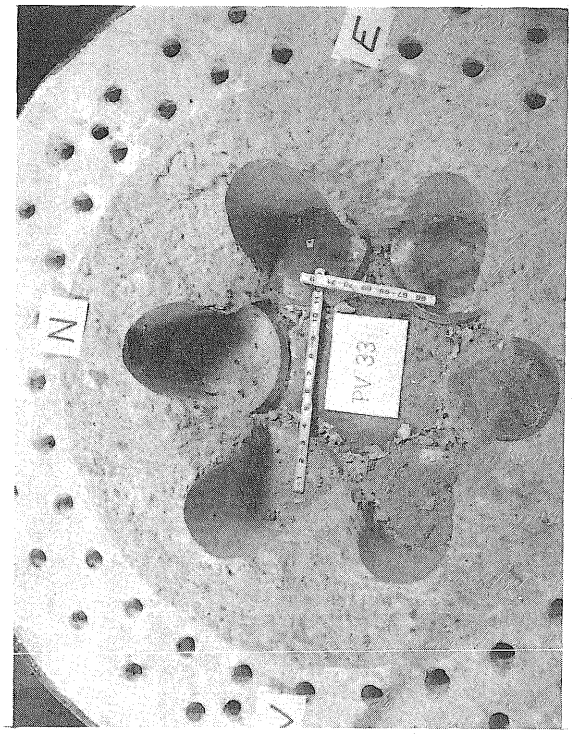

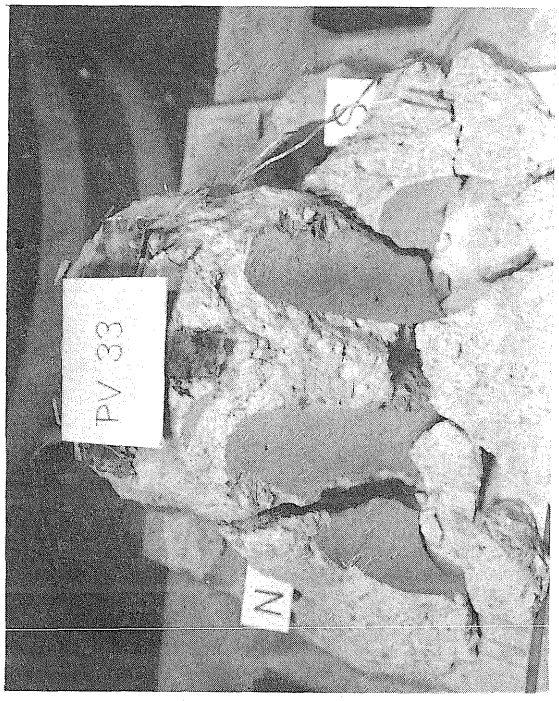

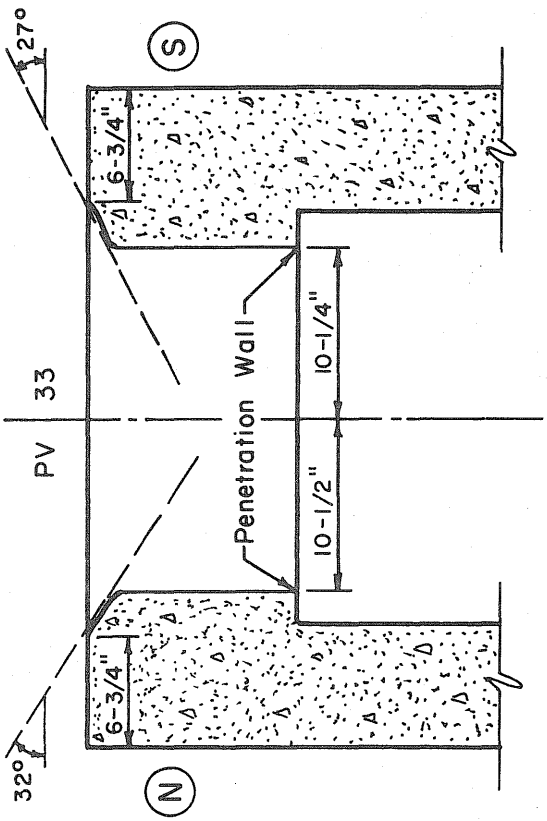

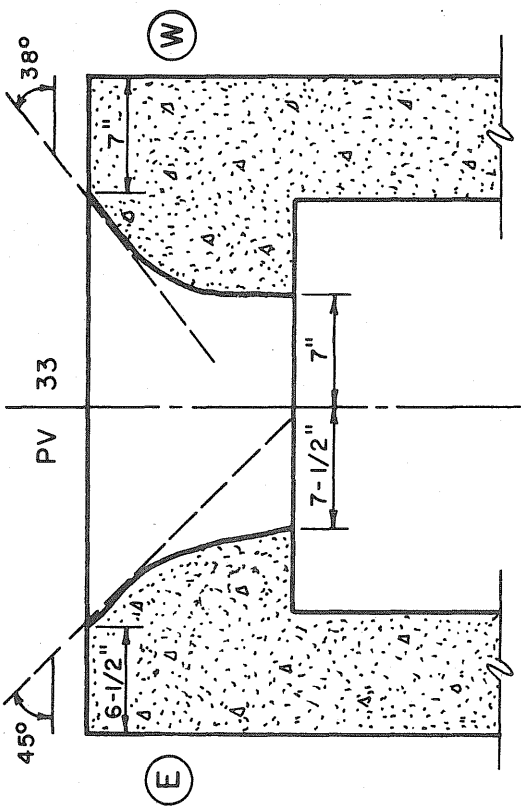

Fig. 3.10 End Slab after Test PV33

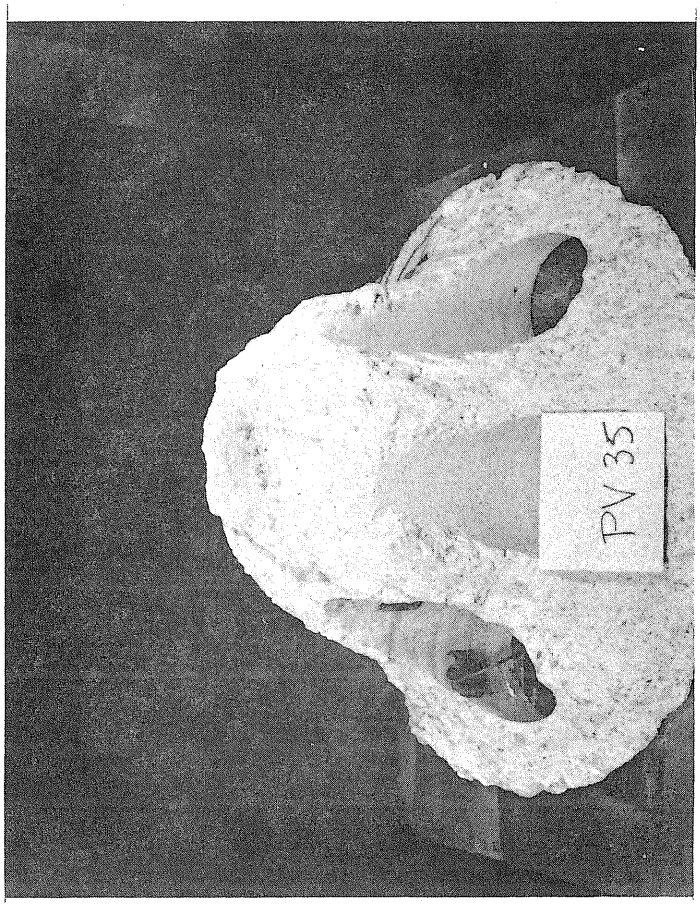

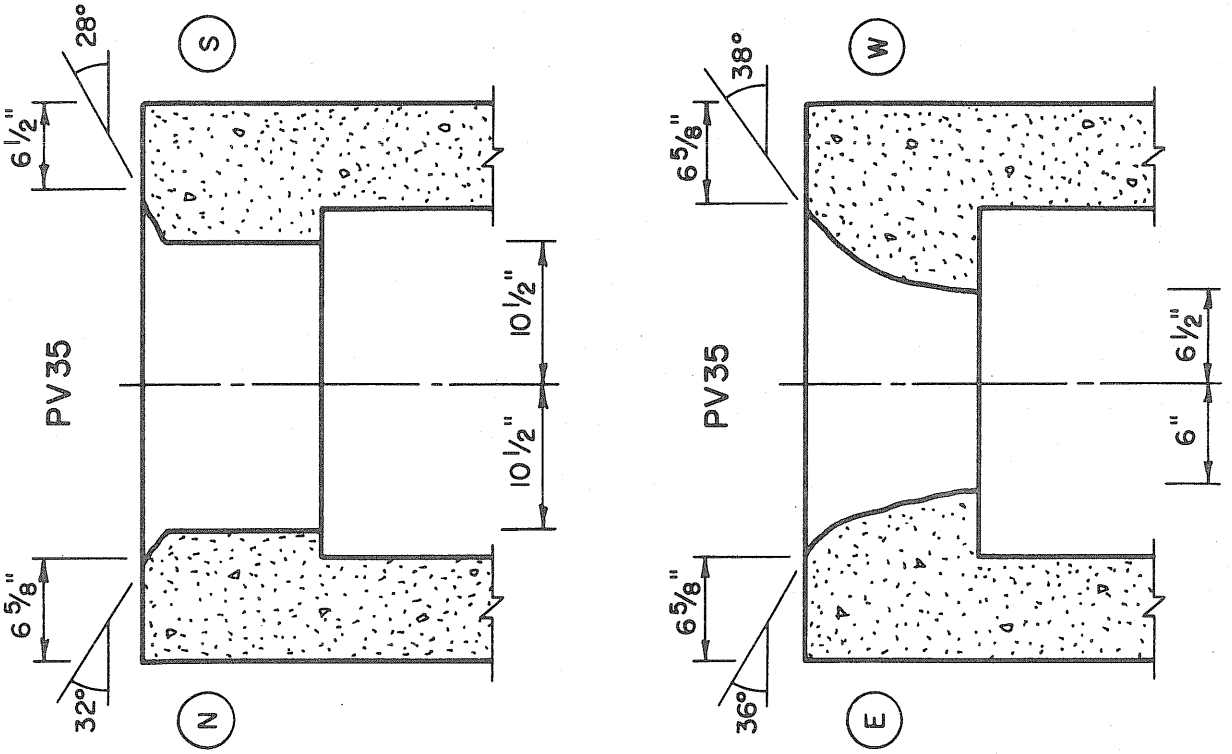

Fig. 3.11 End Slab After Test PV35

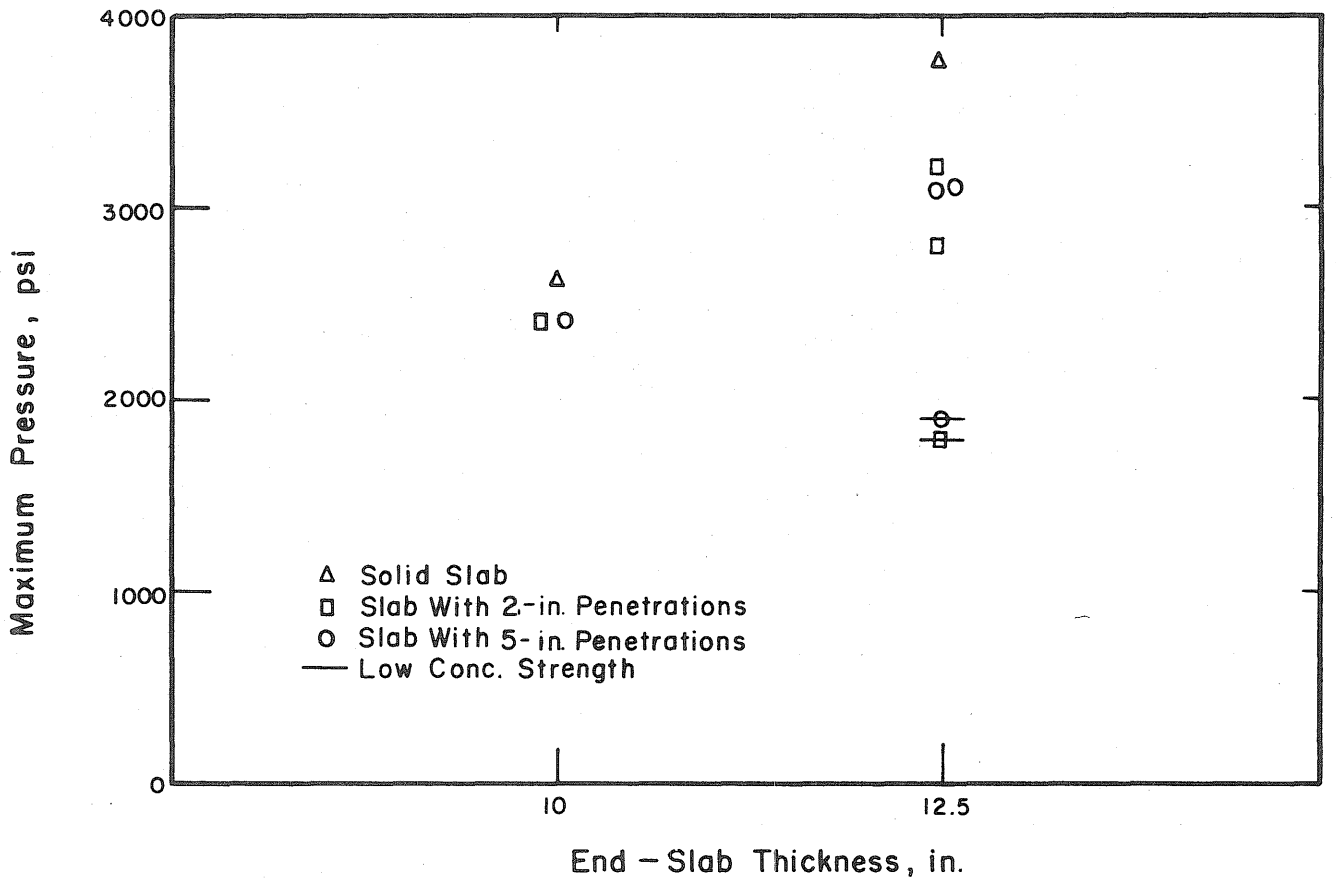

Fig. 3.12 Measured Maximum Internal Pressures

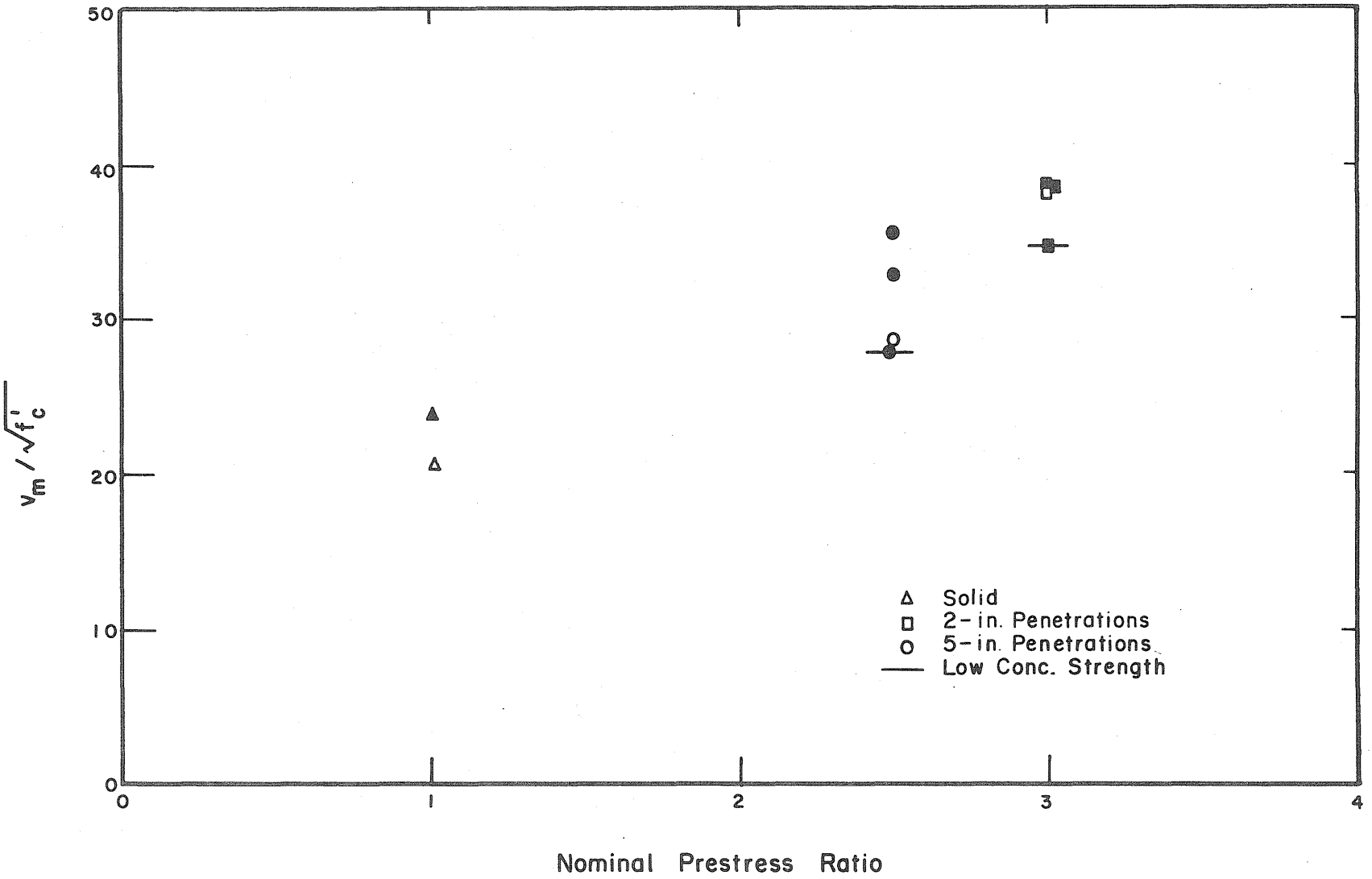

Fig. 3.13 Variation of Unit Nominal Shear Stress (Normalized) with a parameter Reflecting the Effect of Circumferential Prestress

NOTE: Filled-in symbols represent data from vessels with 12.5-in. thick slabs.

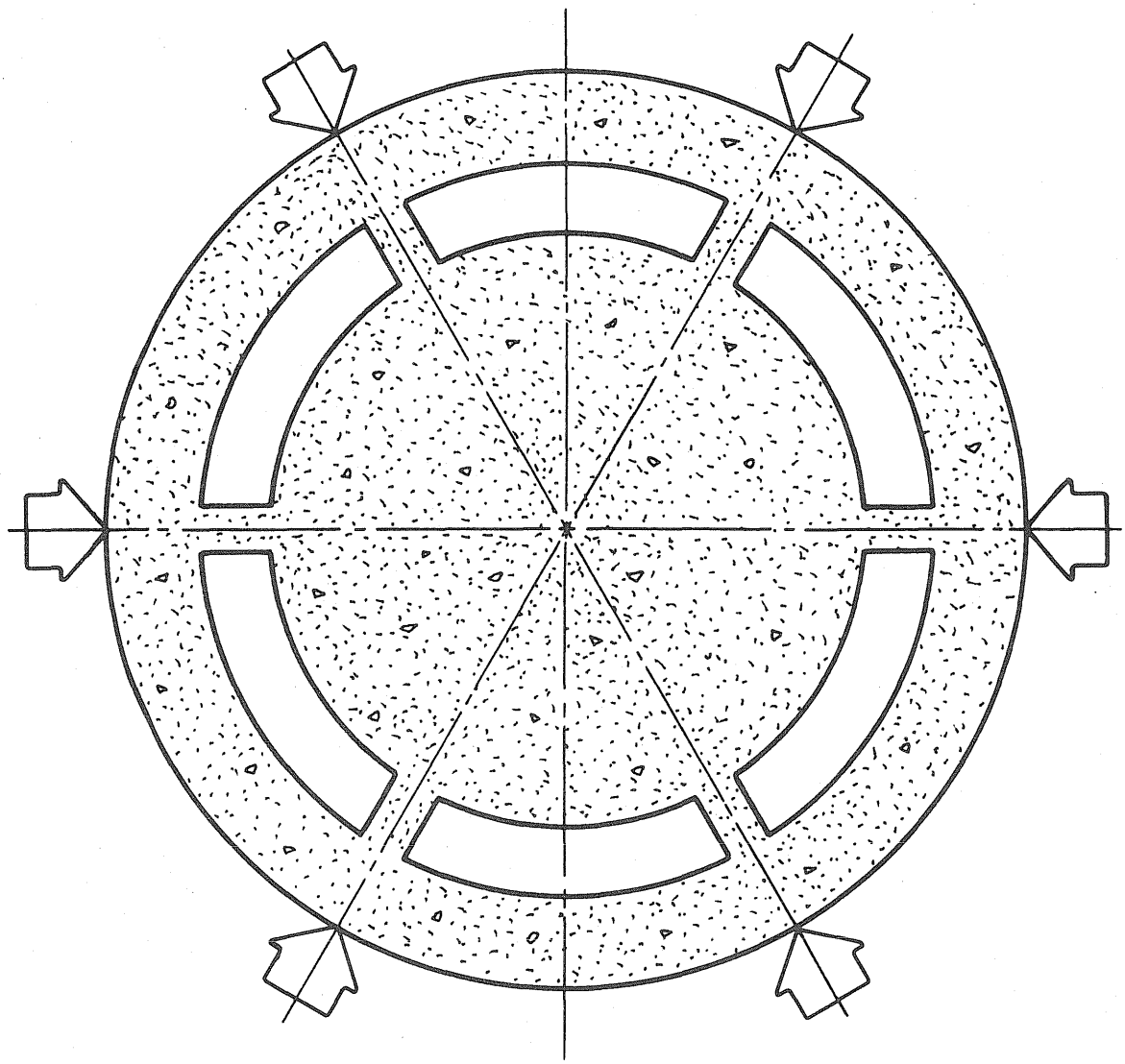

Fig. 3.14 Idealized Model for Perforated End Slabs

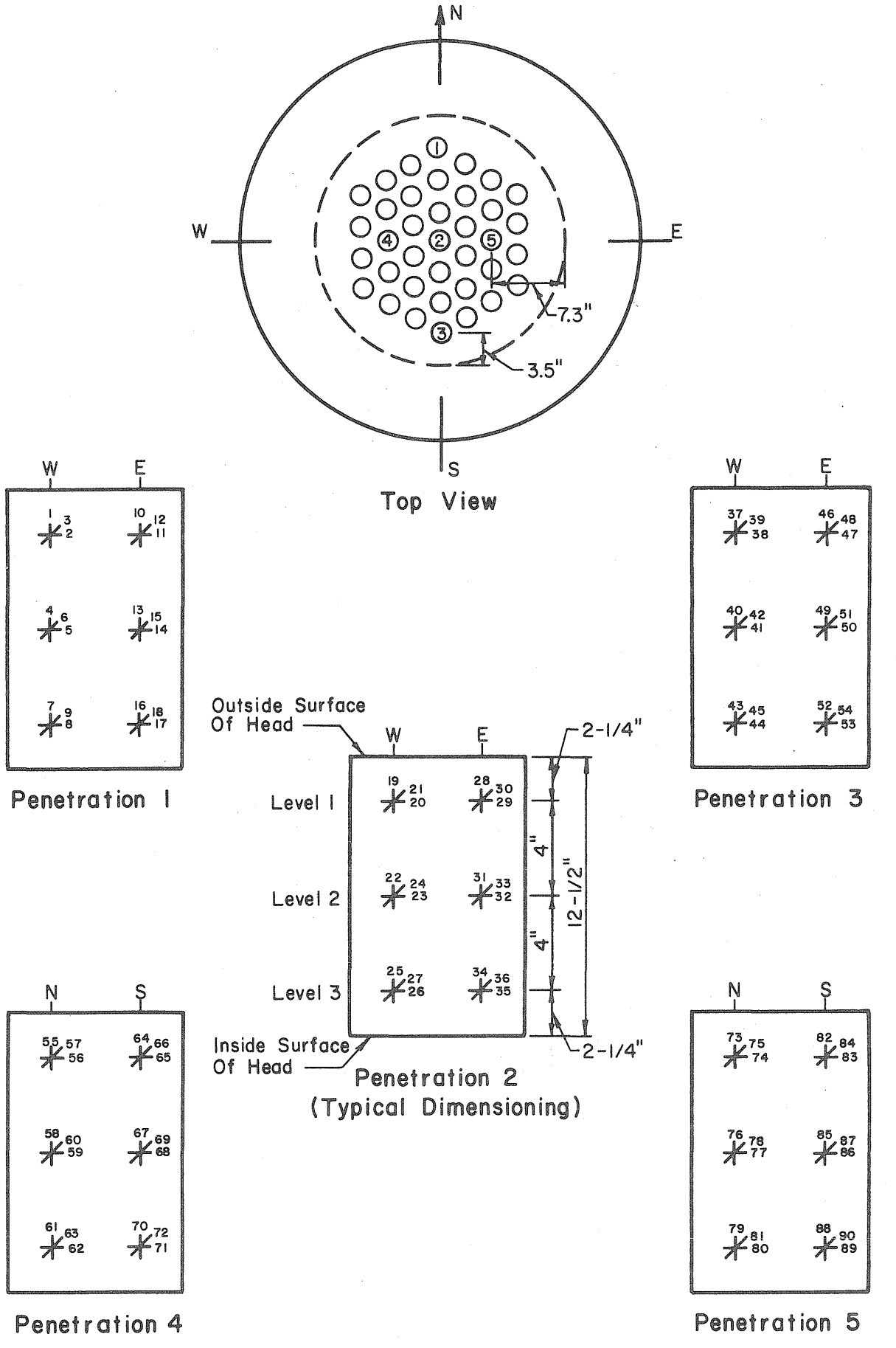

Fig. 3.15a Location of Strain Gages in End Slab with 2-in. Penetrations

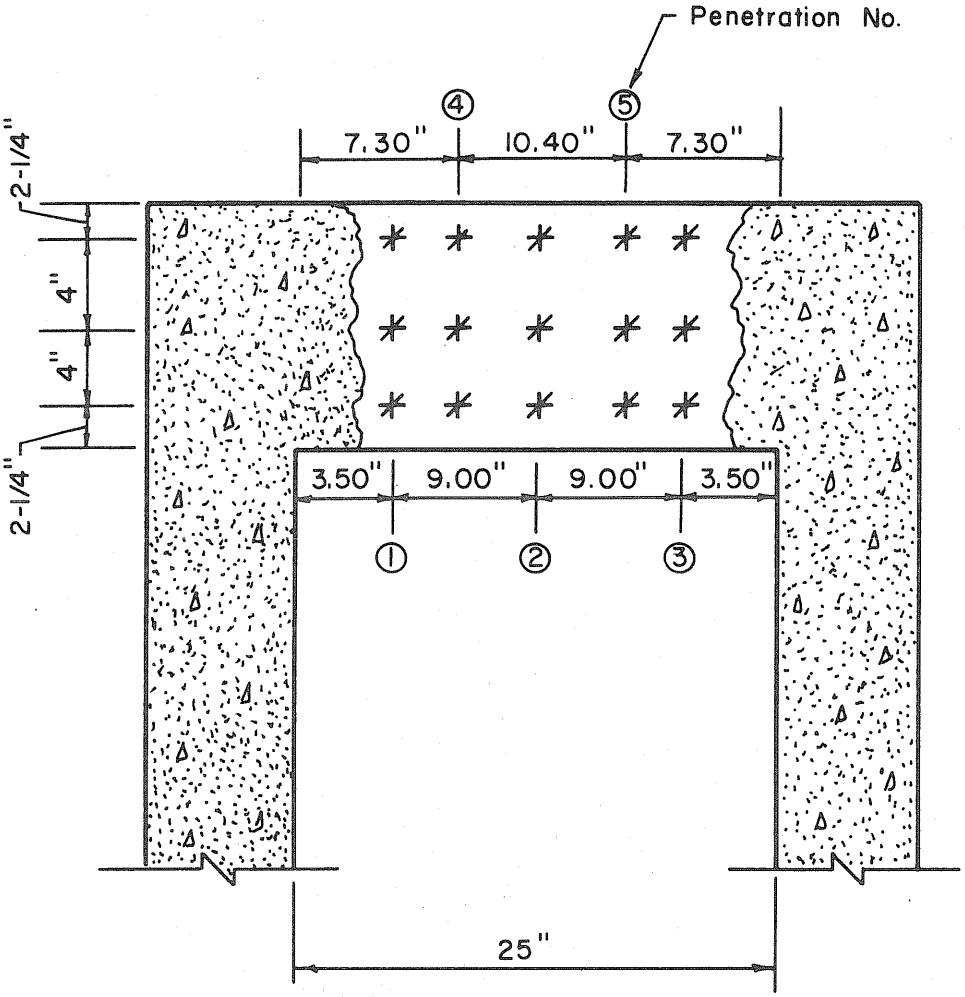

Fig. 3.15b Location of Strain Rosettes in the Vertical Plane
(See Fig. 3.15a for location of penetrations in plan).

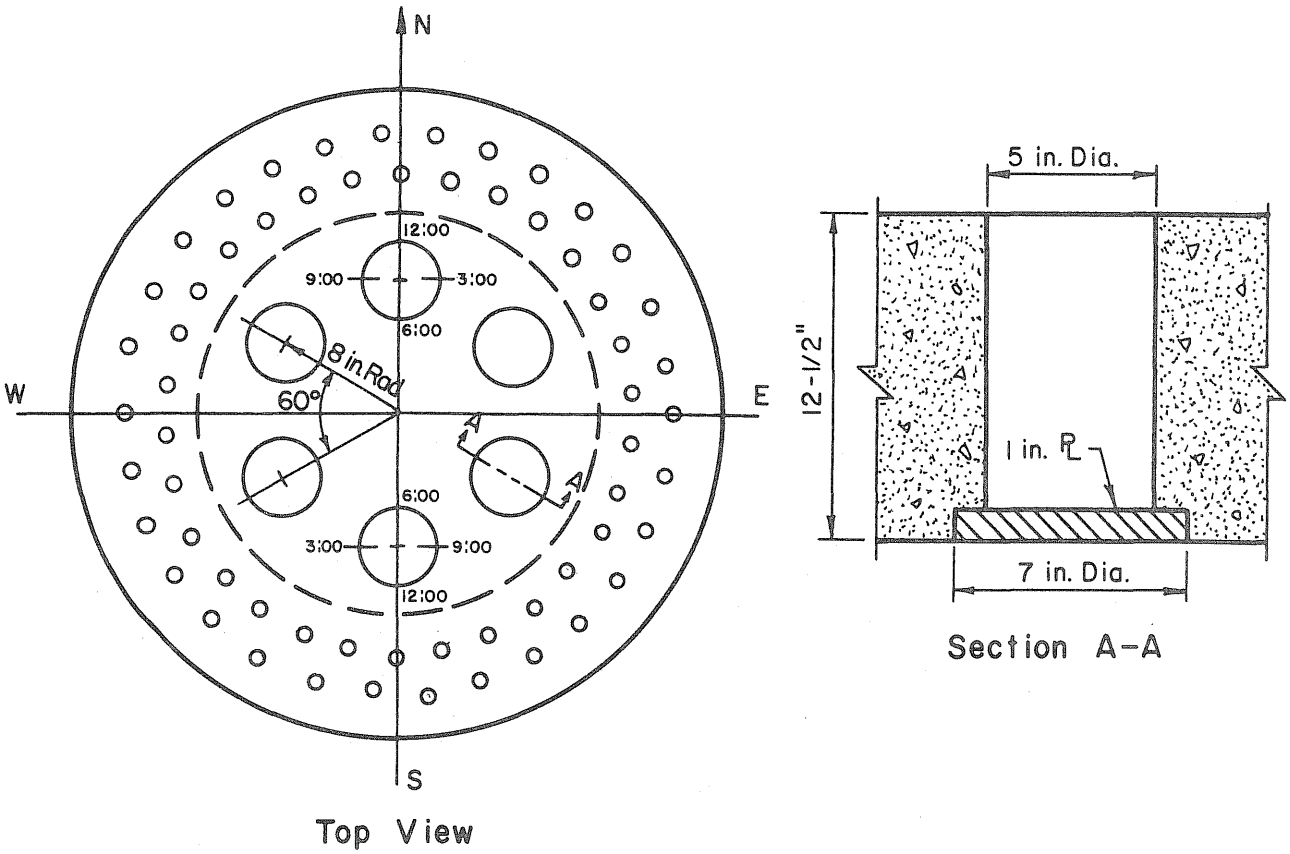

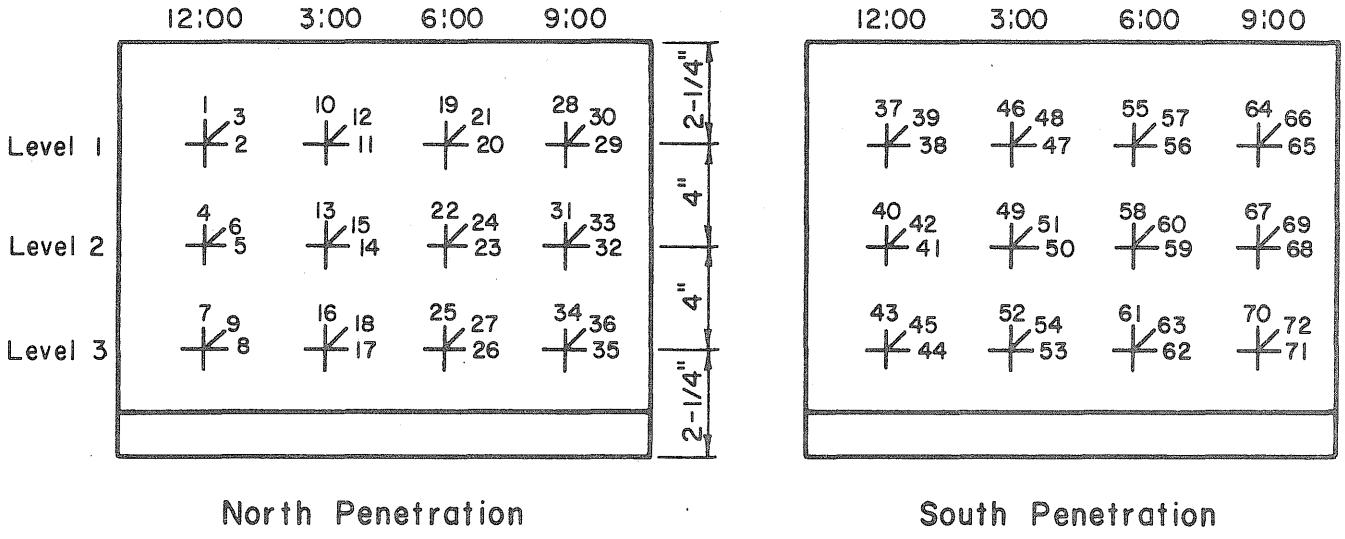

Fig. 3.16a Location of Strain Gages in End Slab with 5-in. Penetrations

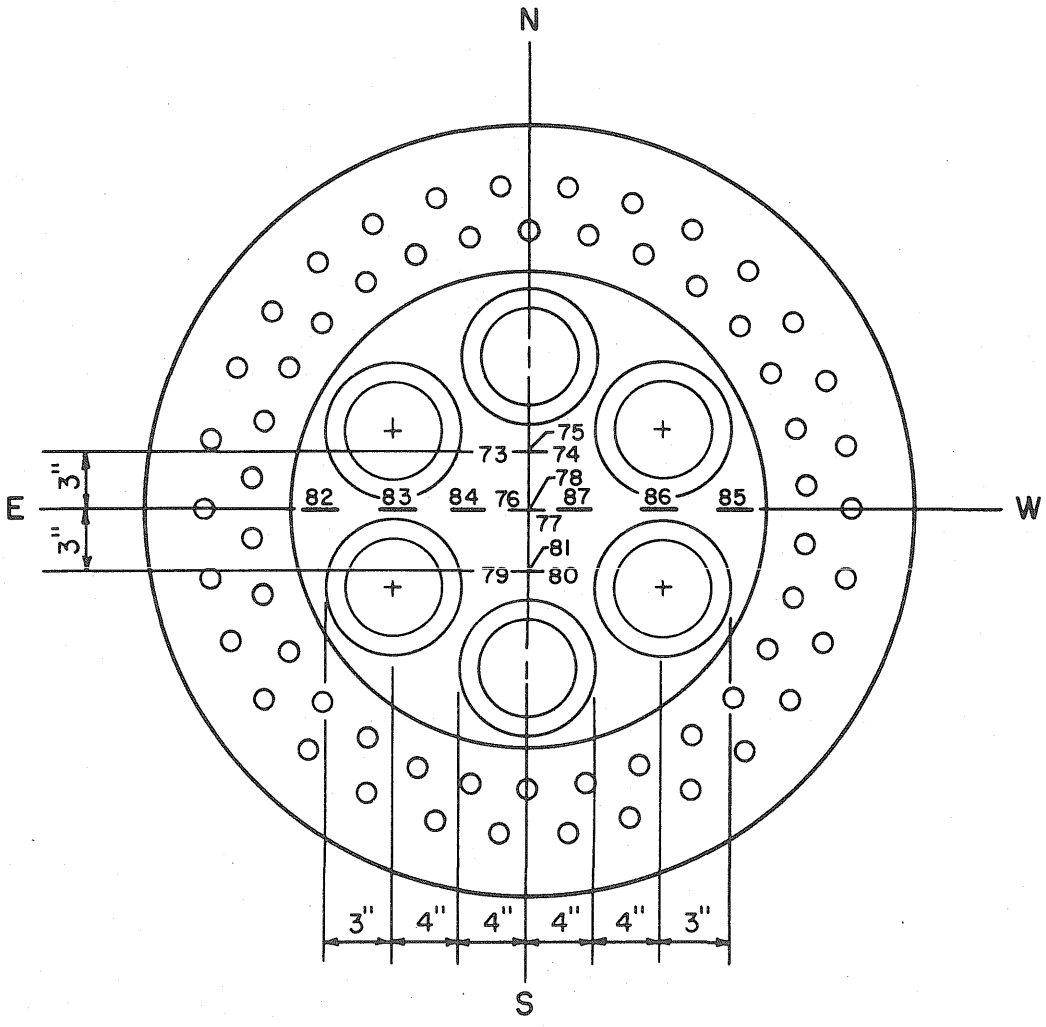

Fig. 3.16b Location of Strain Gages on Inside Face of End Slab with 5-in. Penetrations

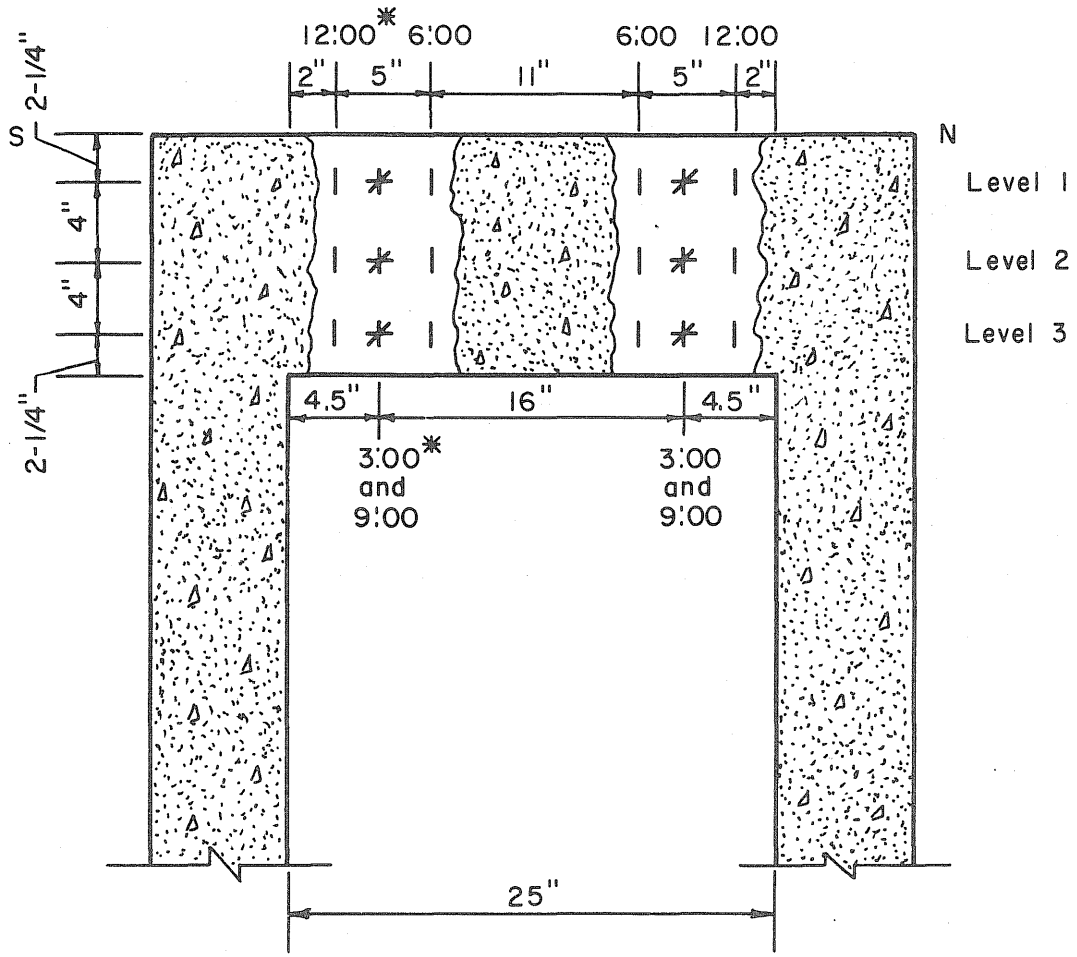

Fig. 3.16c Location of Strain Rosettes in the Vertical Plane (*Numerals designating location in plan. See Fig. 5.31a)

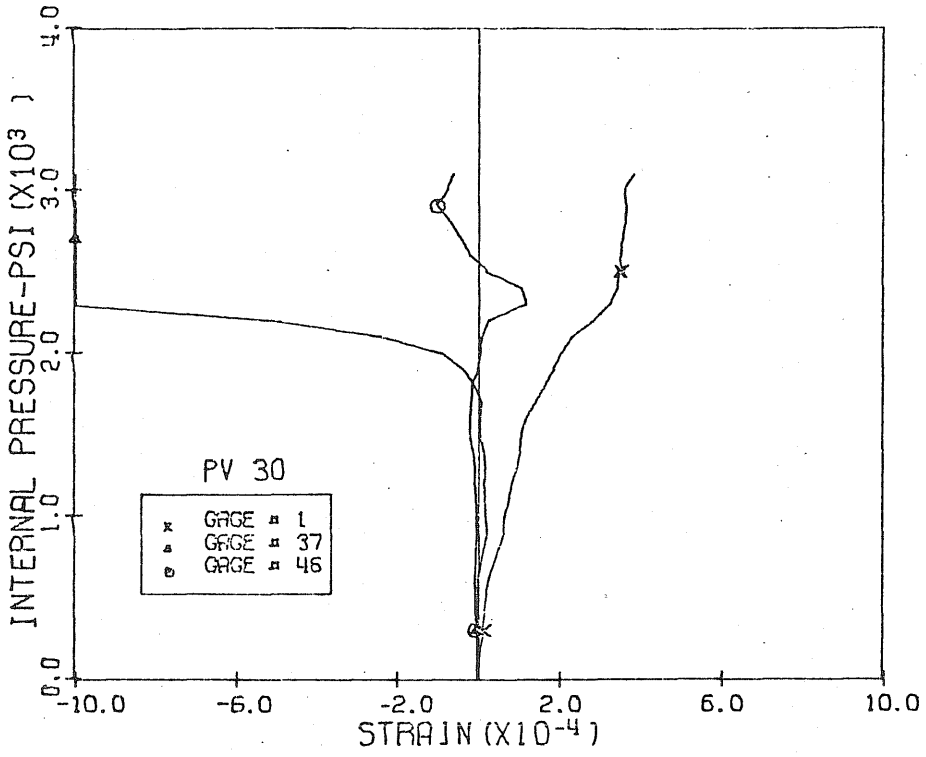

Fig. 3.17 Measured Vertical Strains, Level 1, Pen. 1 & 3, PV30

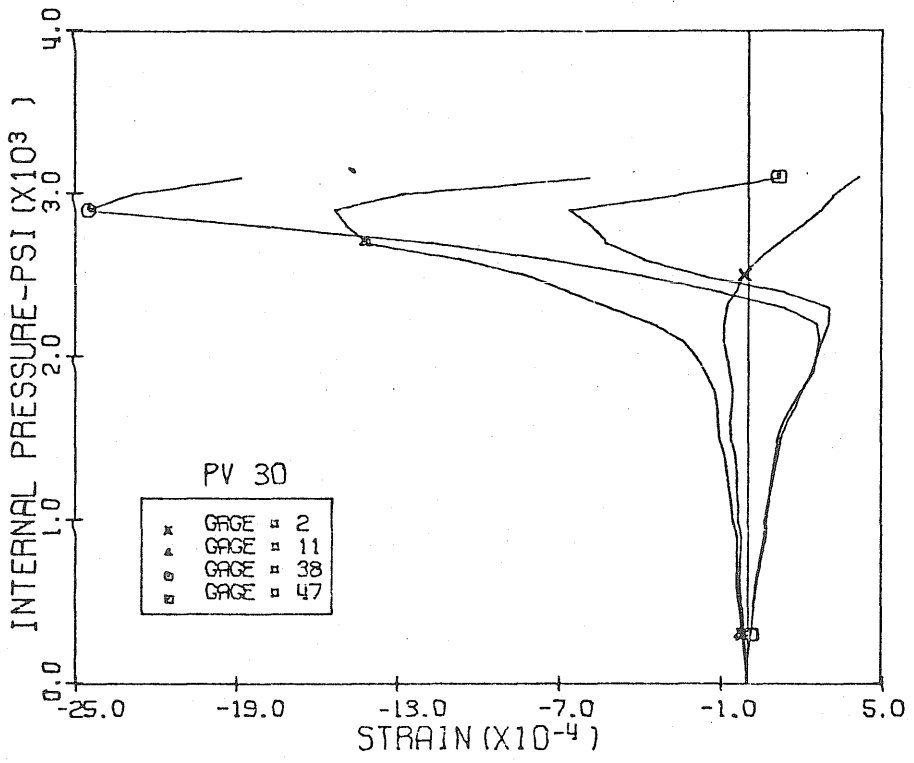

Fig. 3.18 Measured Horizontal Strains, Level 1, Pen. 1 & 3, PV30

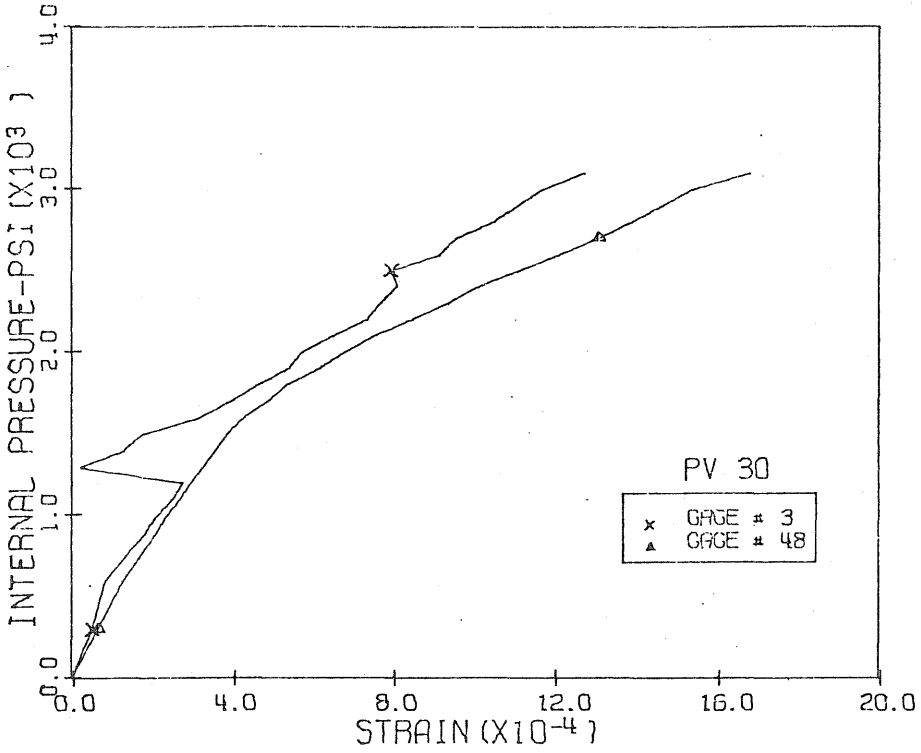

Fig. 3.19 Measured Comp. Diag. Strains, Level 1, Pen. 1 & 3, PV30

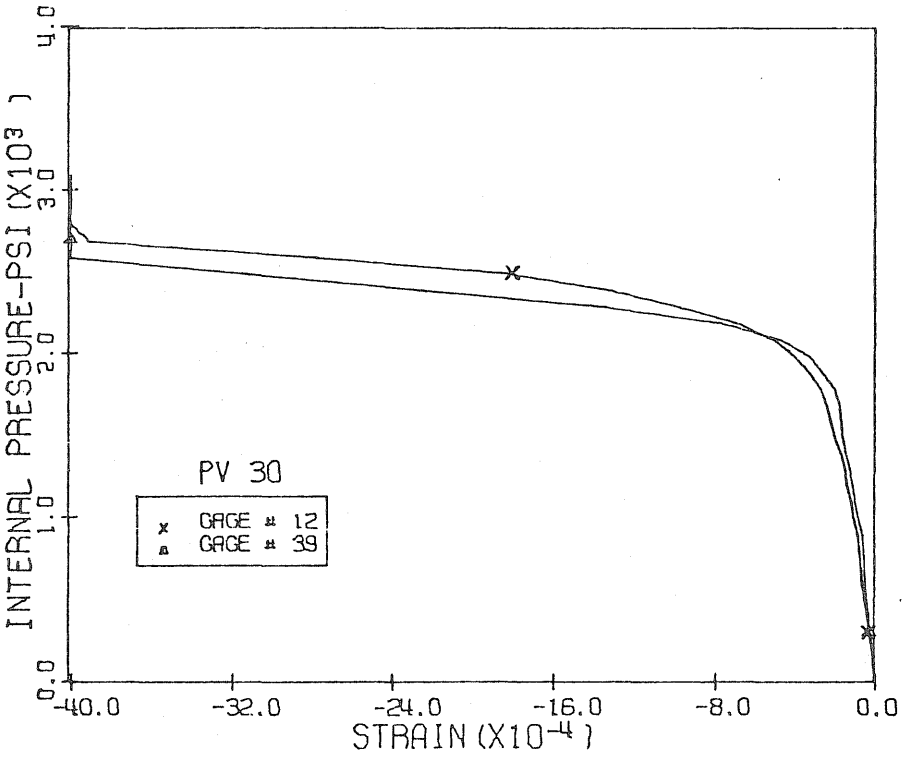

Fig. 3.20 Measured Tens. Diag. Strains, Level 1, Pen. 1 & 3, PV30

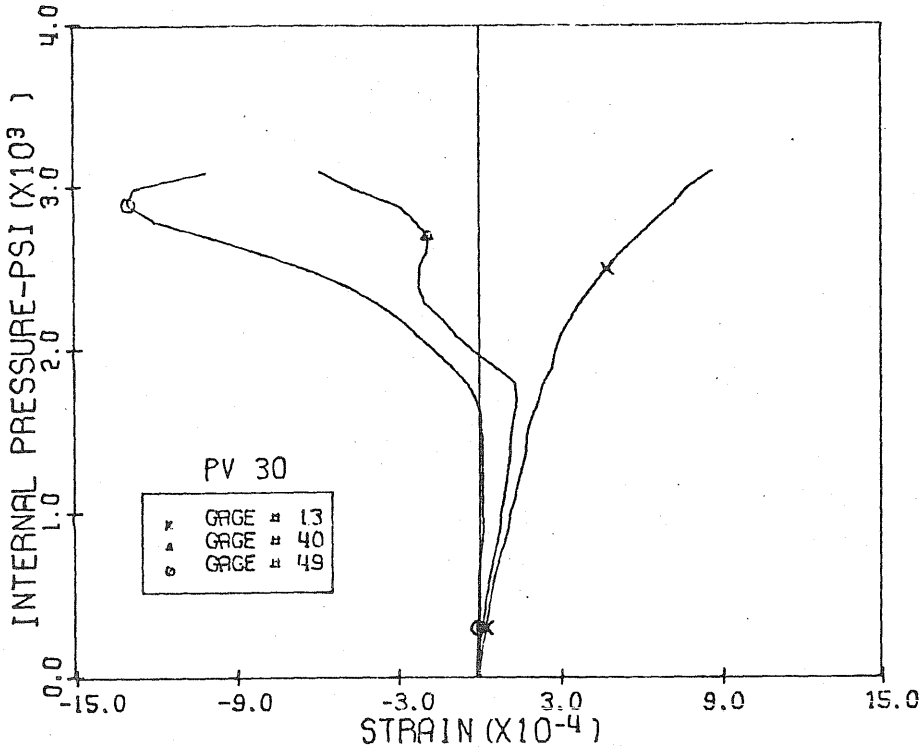

Fig. 3.21 Measured Vertical Strains, Level 2, Pen. 1 & 3, PV30

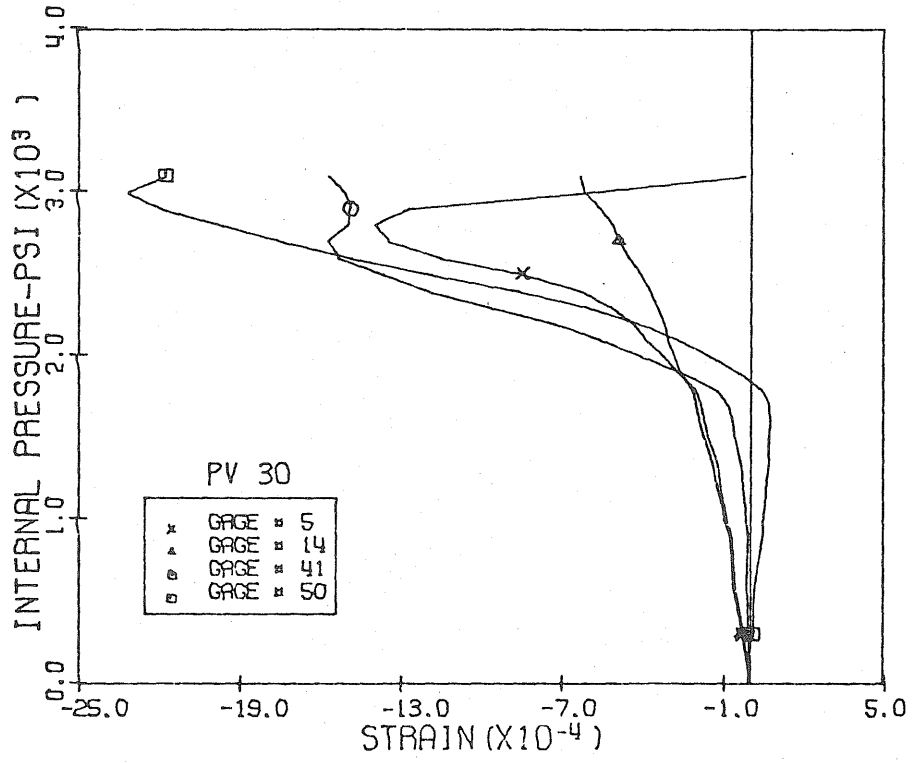

Fig. 3.22 Measured Horizontal Strains, Level 2, Pen. 1 & 3, PV30

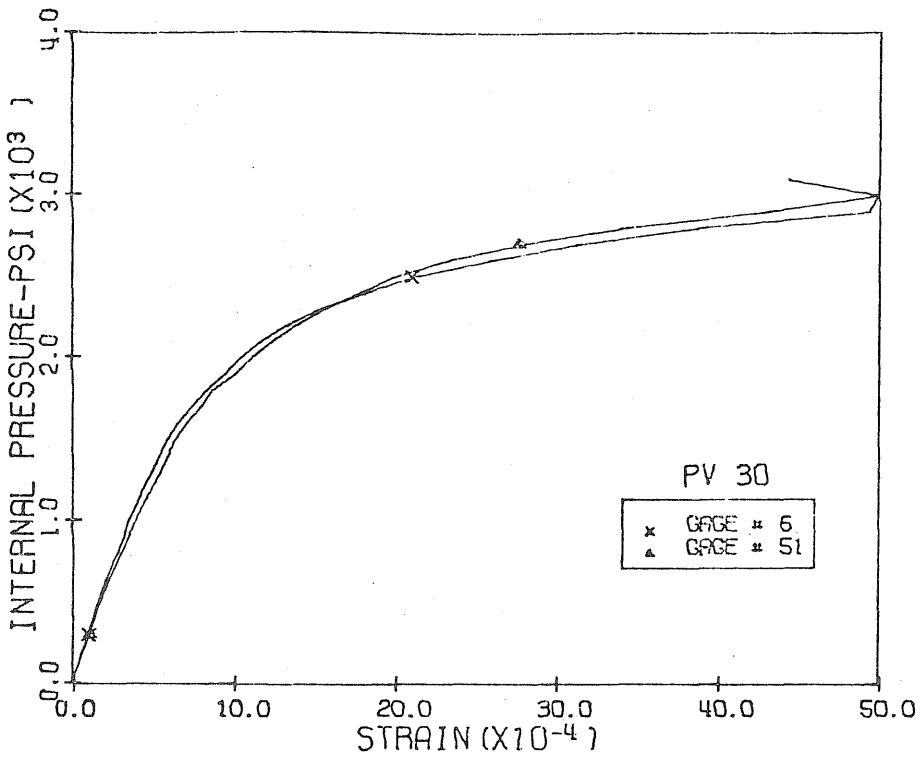

Fig. 3.23 Measured Comp. Diag. Strains, Level 2, Pen. 1 & 3, PV30

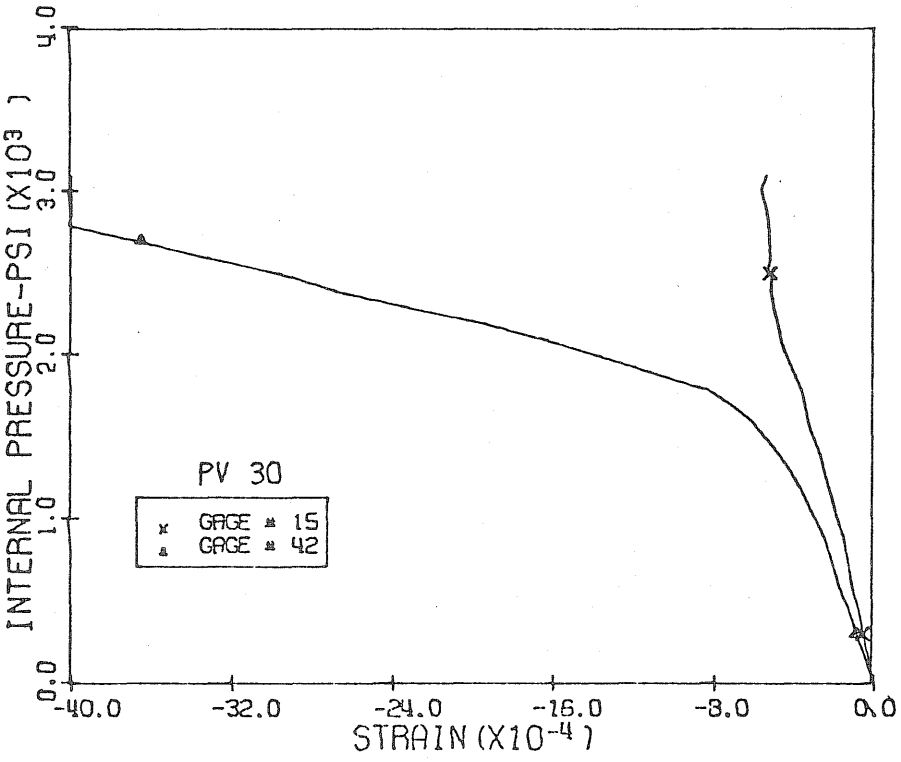

Fig. 3.24 Measured Tens. Diag. Strains, Level 2, Pen. 1 & 3, PV30

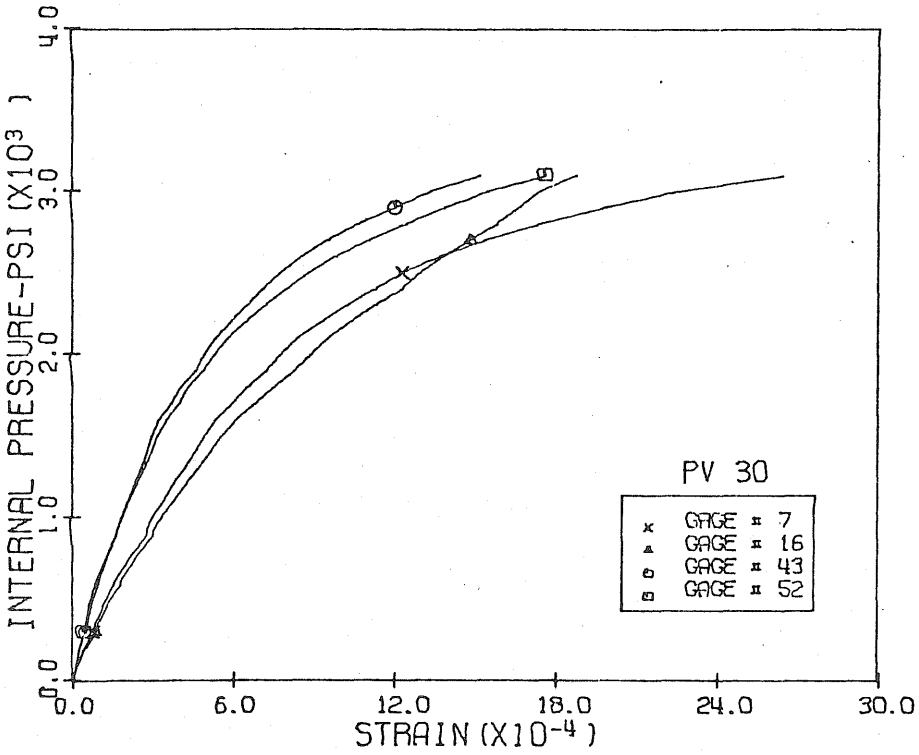

Fig. 3.25 Measured Vertical Strains, Level 3, Pen. 1 & 3, PV30

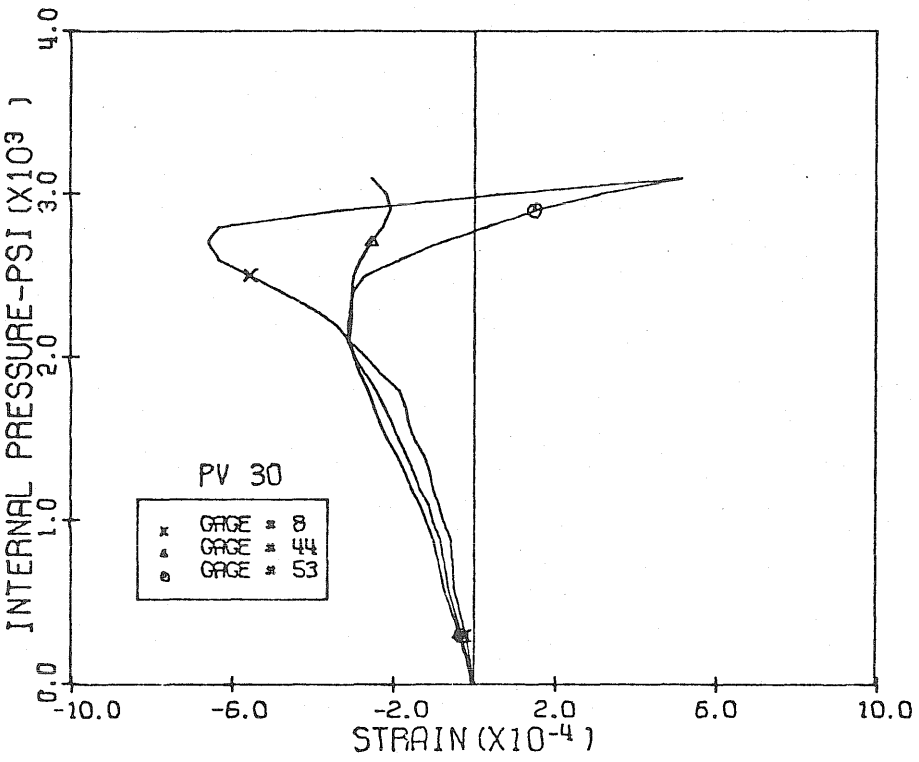

Fig. 3.26 Measured Horizontal Strains, Level 3, Pen. 1 & 3, PV30

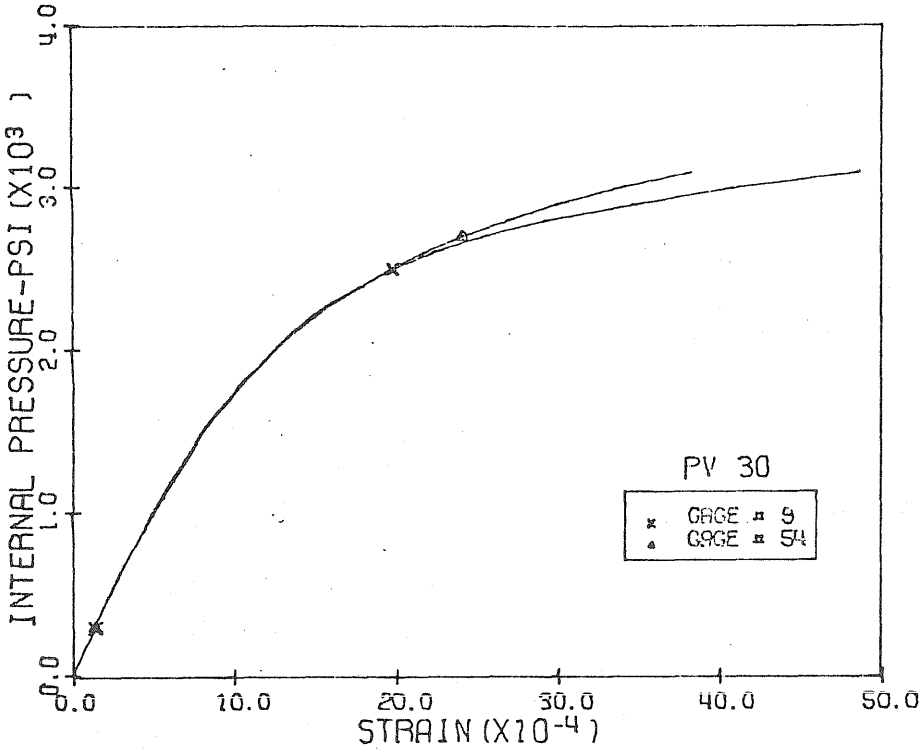

Fig. 3.27 Measured Comp. Diag. Strains, Level 3, Pen. 1 & 3, PV30

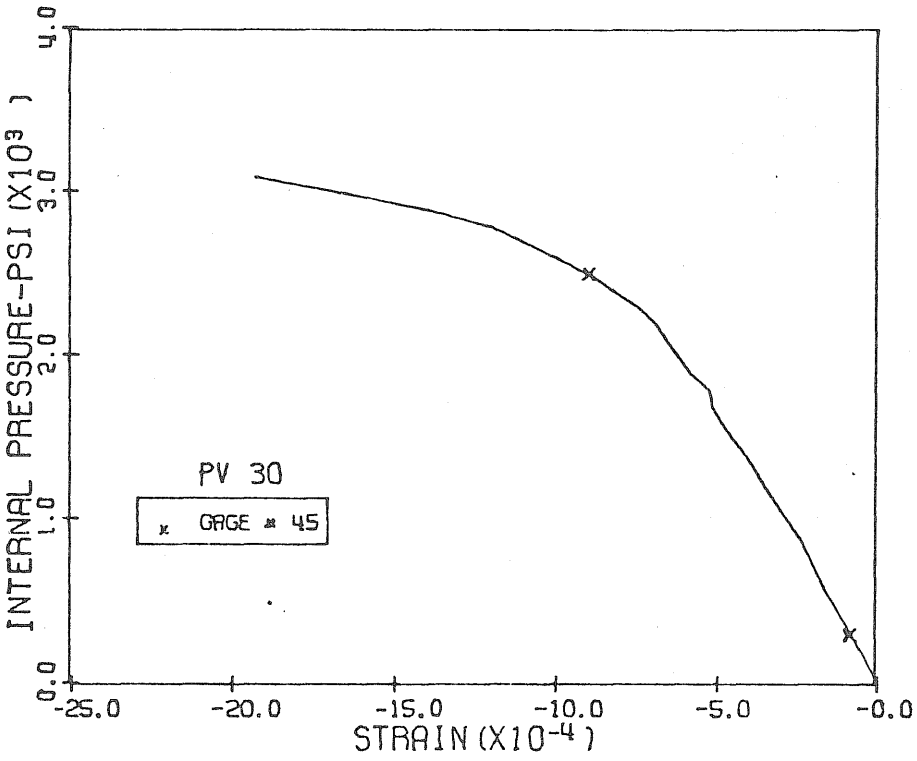

Fig. 3.28 Measured Tens. Diag. Strains, Level 3, Pen. 1 & 3, PV30

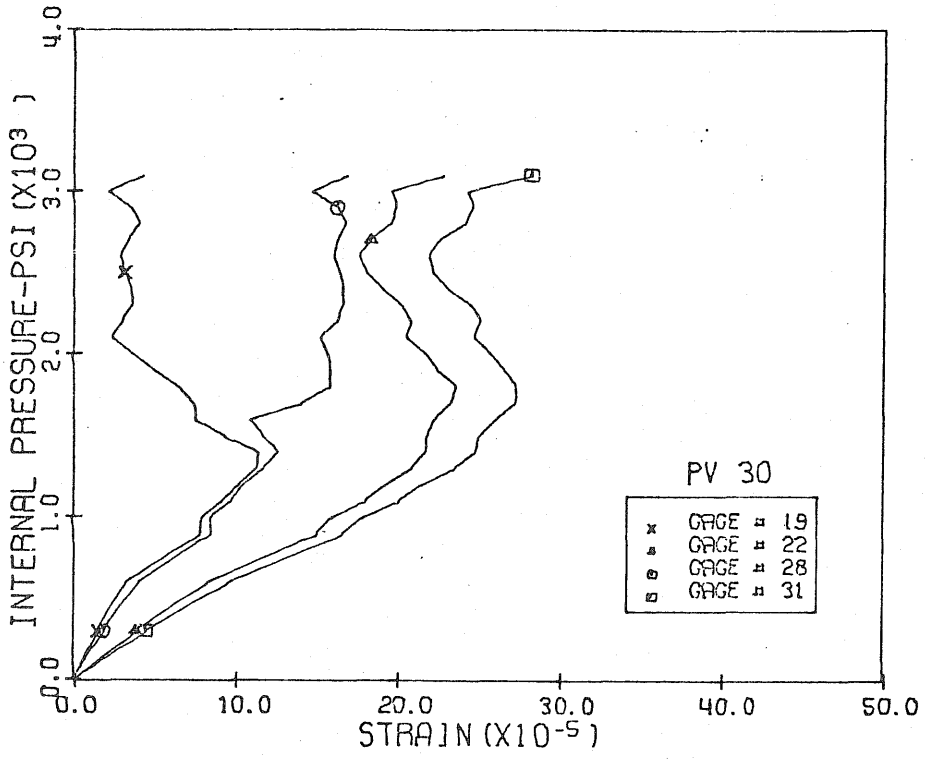

Fig. 3.29 Measured Vertical Strains, Level 1 & 2, Penetration 2, PV30

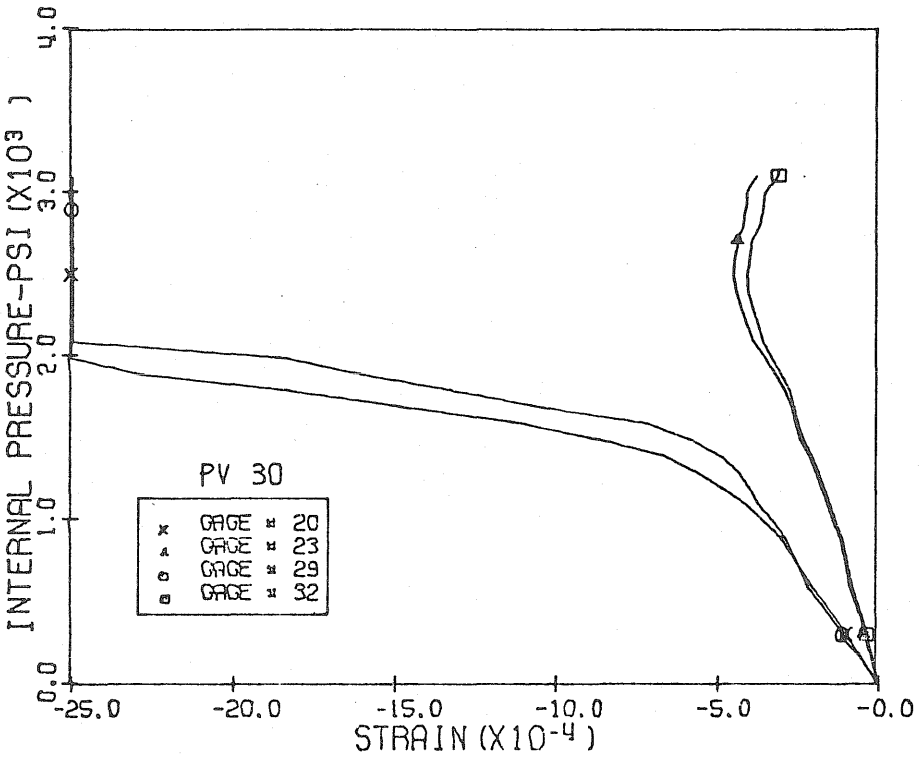

Fig. 3.30 Measured Horizontal Strains, Level 1 & 2, Penetration 2, PV30

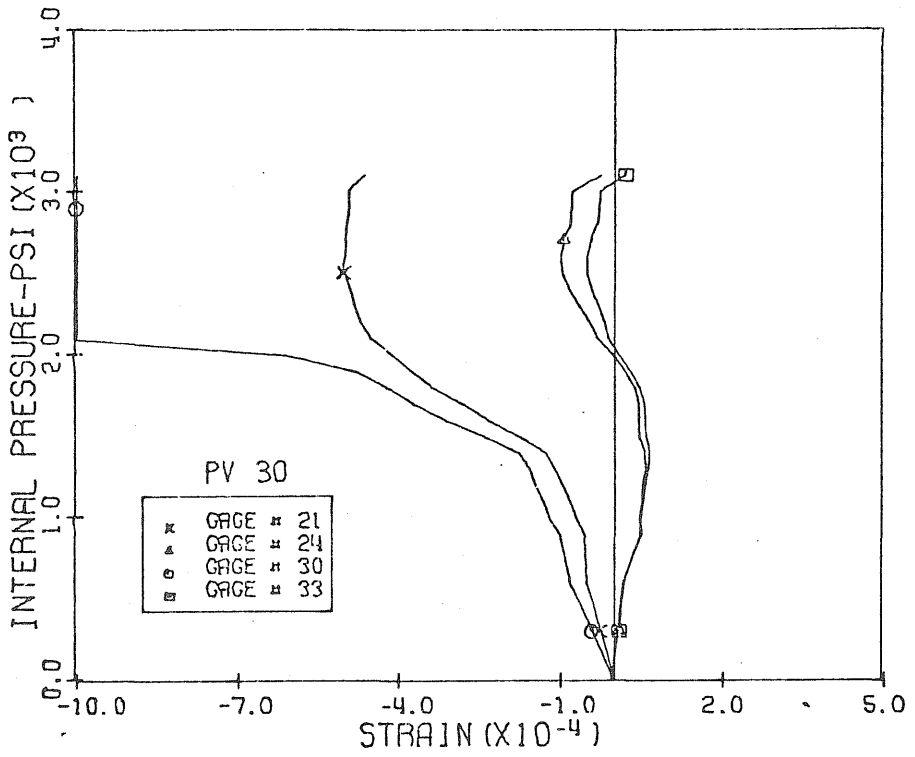

Fig. 3.31 Measured Diagonal Strains, Level 1 & 2, Penetration 2, PV30

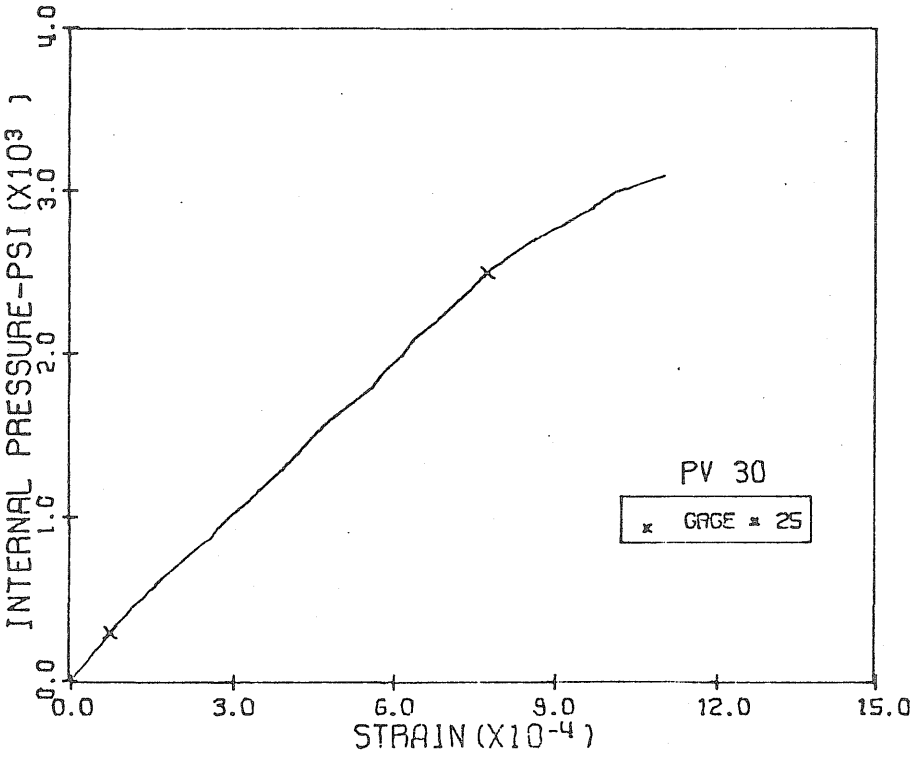

Fig. 3.32 Measured Vertical Strains, Level 3, Penetration 2, PV30

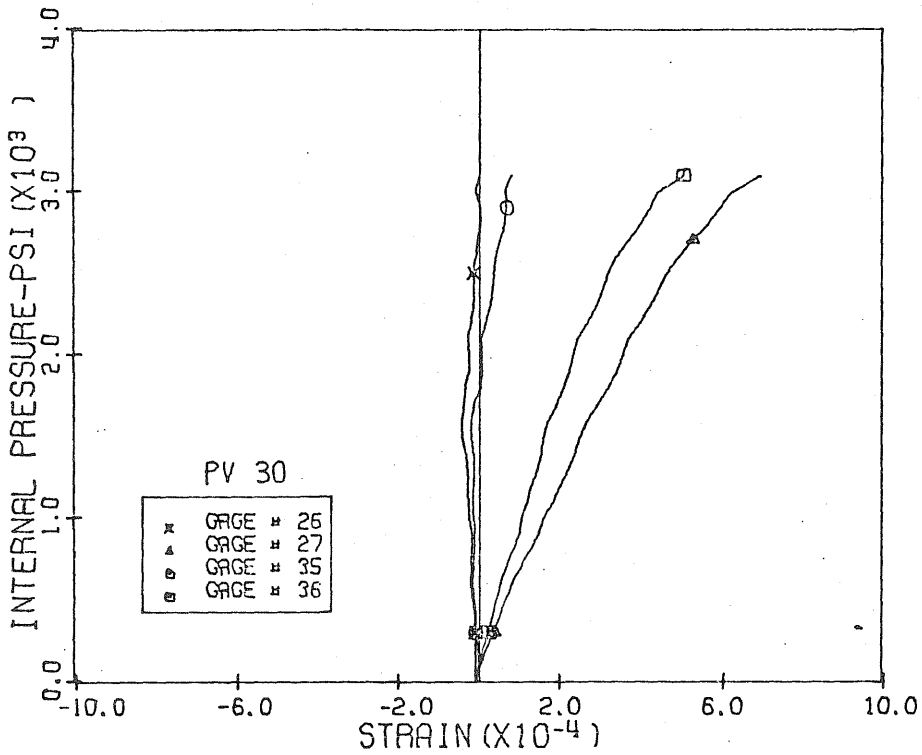

Fig. 3.33 Measured B6 Level 3, Penetration 2, PV30

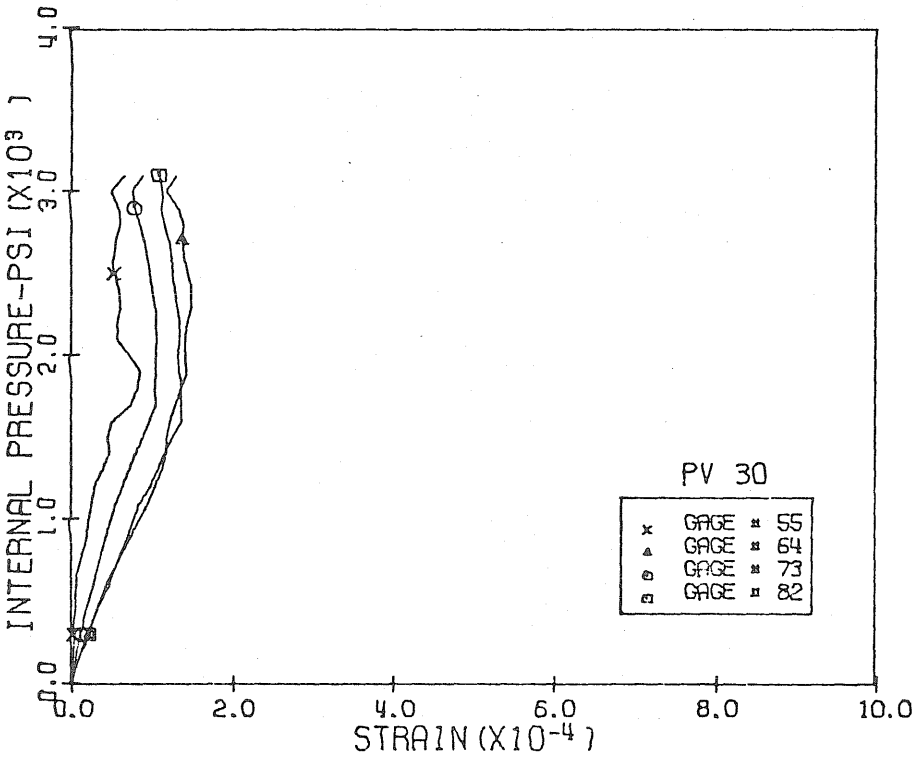

Fig. 3.34 Measured Vertical Strains, Level 1, Pen. 4 & 5, PV30

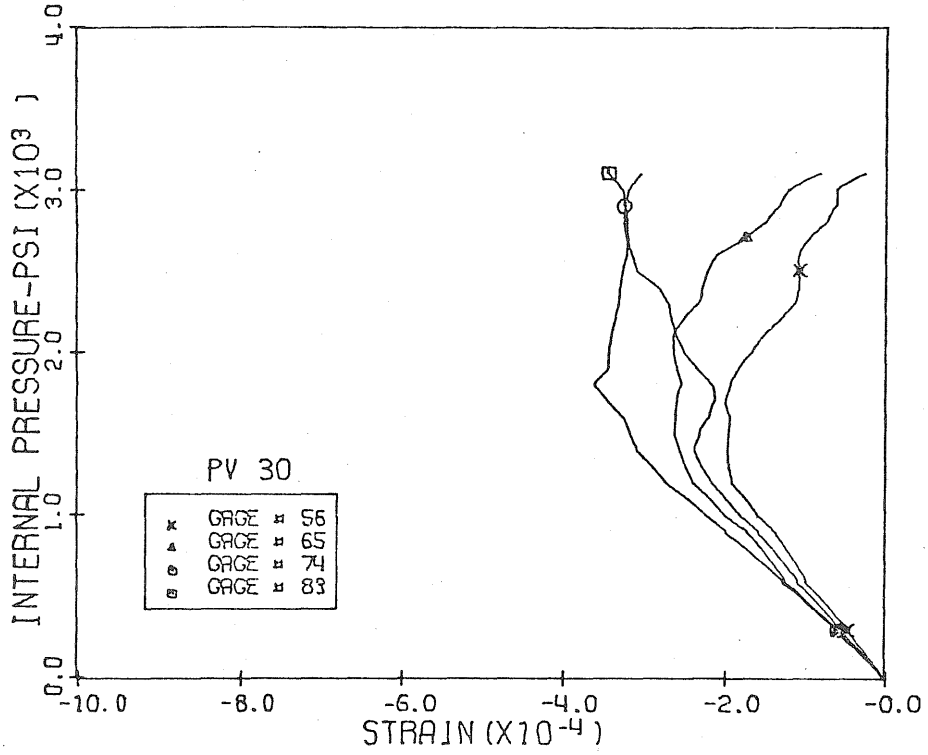

Fig. 3.35 Measured Horizontal Strains, Level 1, Pen. 4 & 5, PV30

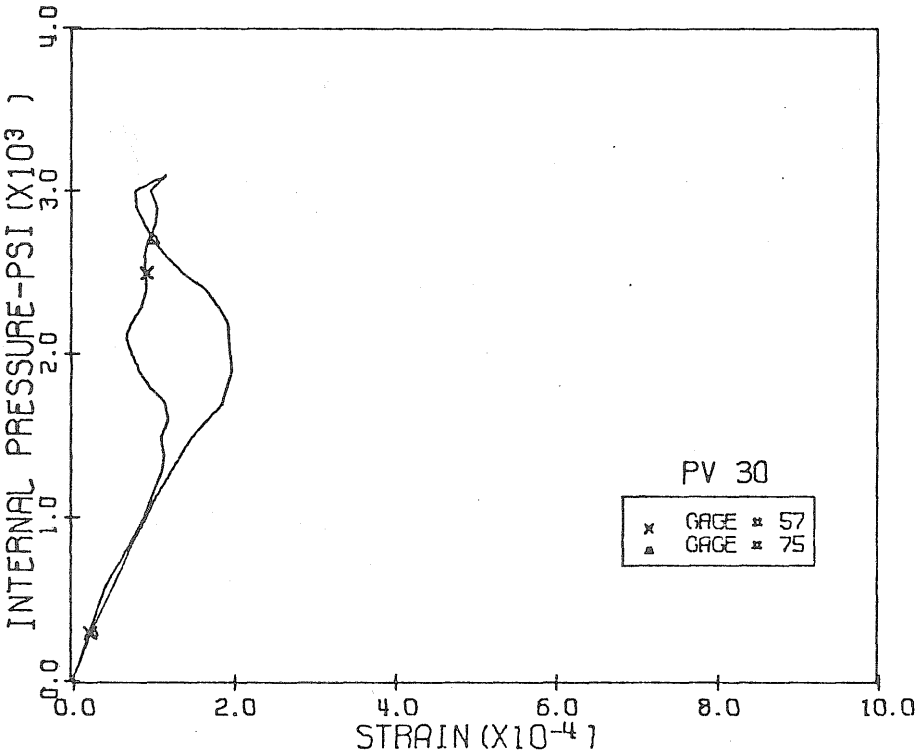

Fig. 3.36 Measured Comp. Diag. Strains, Level 1, Pen. 4 & 5, PV30

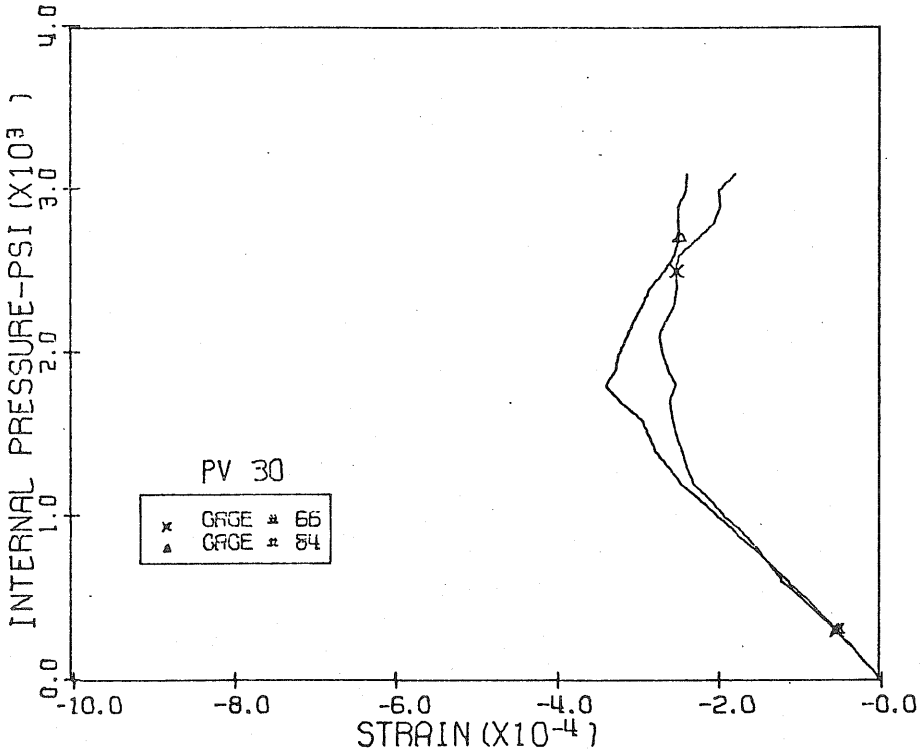

Fig. 3.37 Measured Tens. Diag. Strains, Level 1, Pen. 4 & 5, PV30

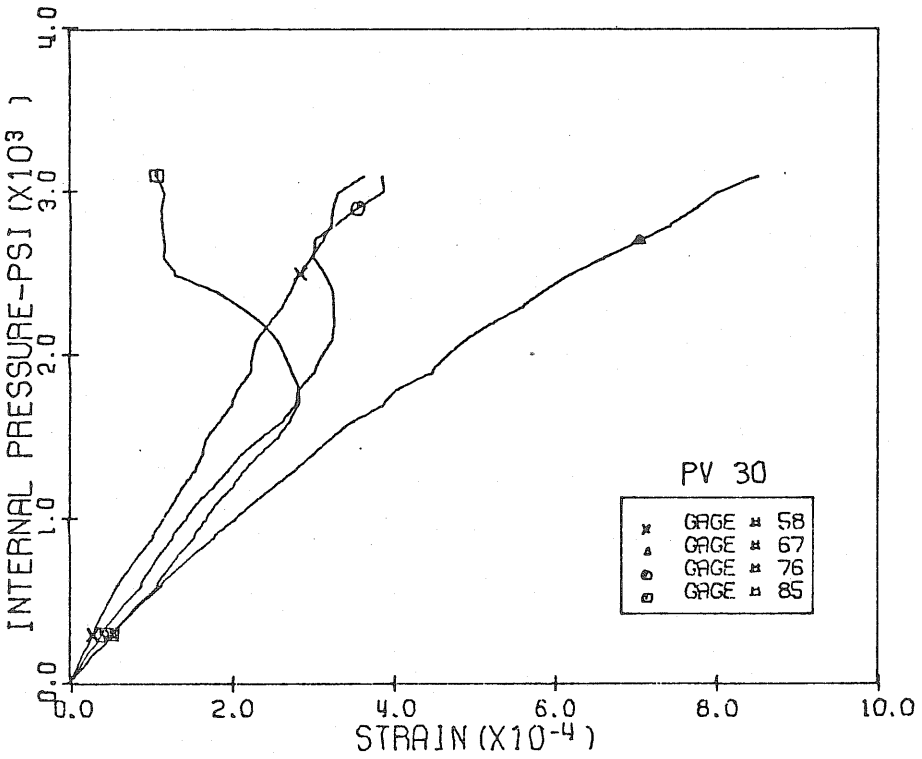

Fig. 3.38 Measured Vertical Strains, Level 2, Pen. 4 & 5, PV30

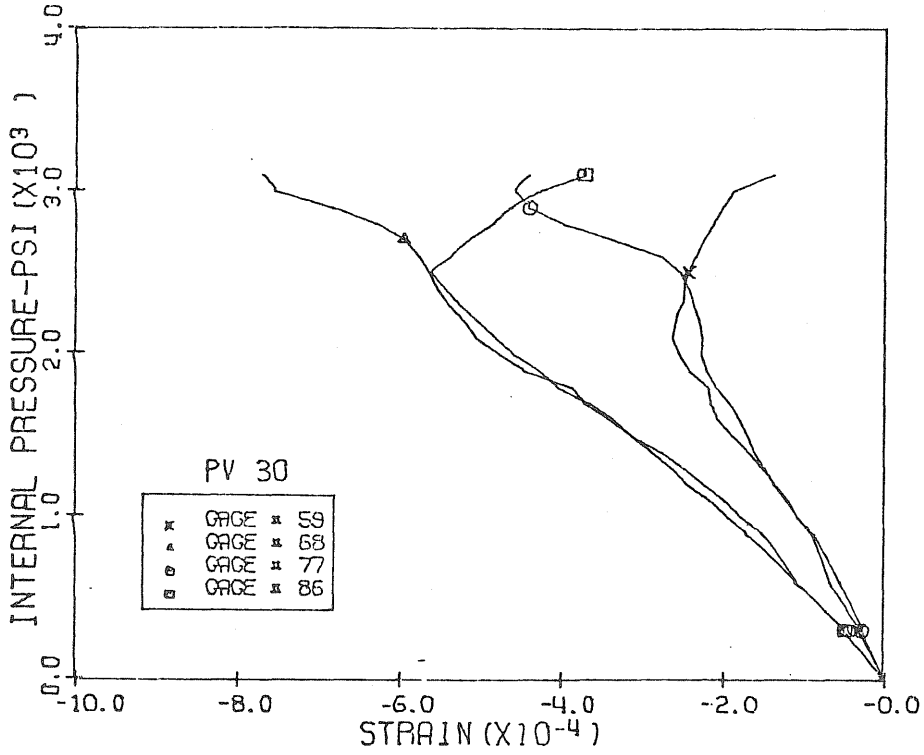

Fig. 3.39 Measured Horizontal Strains, Level 2, Pen. 4 & 5, PV30

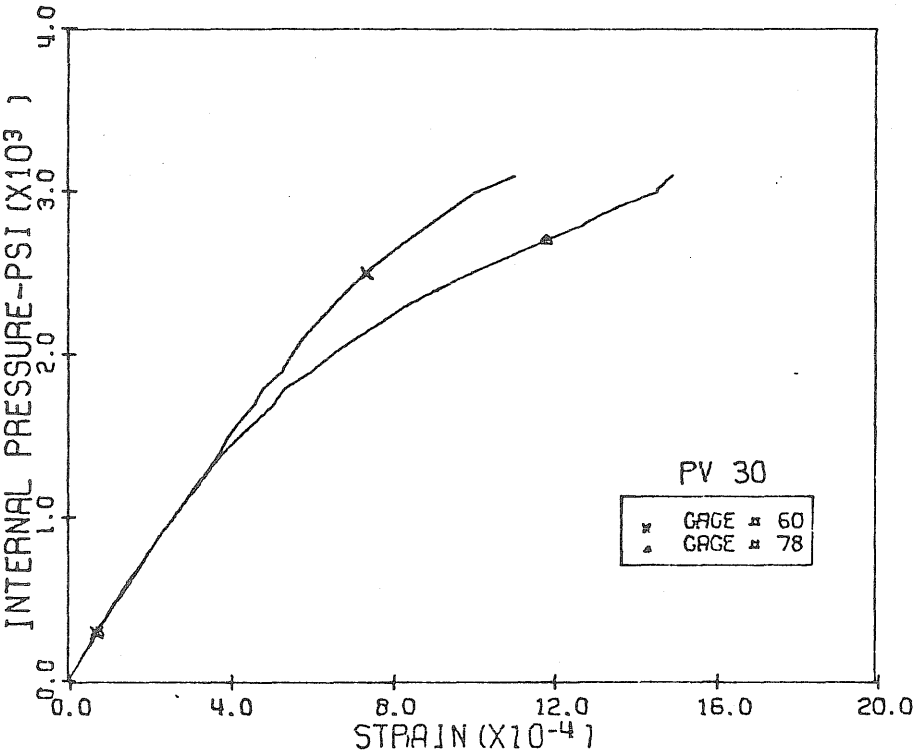

Fig. 3.40 Measured Comp. Diag. Strains, Level 2, Pen. 4 & 5, PV30

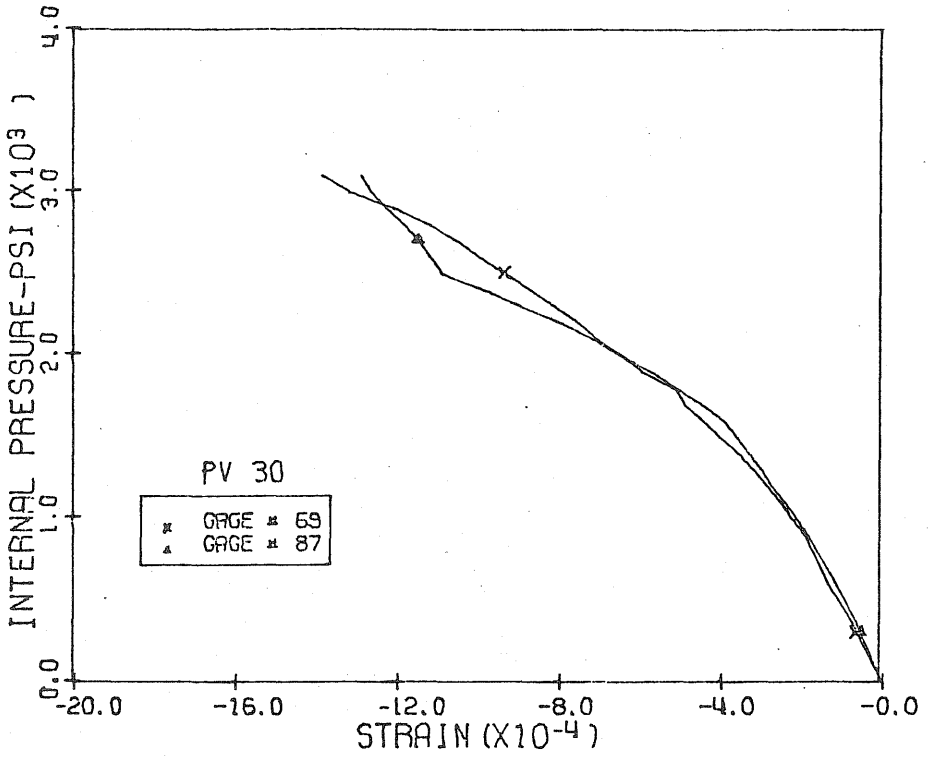

Fig. 3.41 Measured Tens. Diag. Strains, Level 2, Pen. 4 & 5, PV30

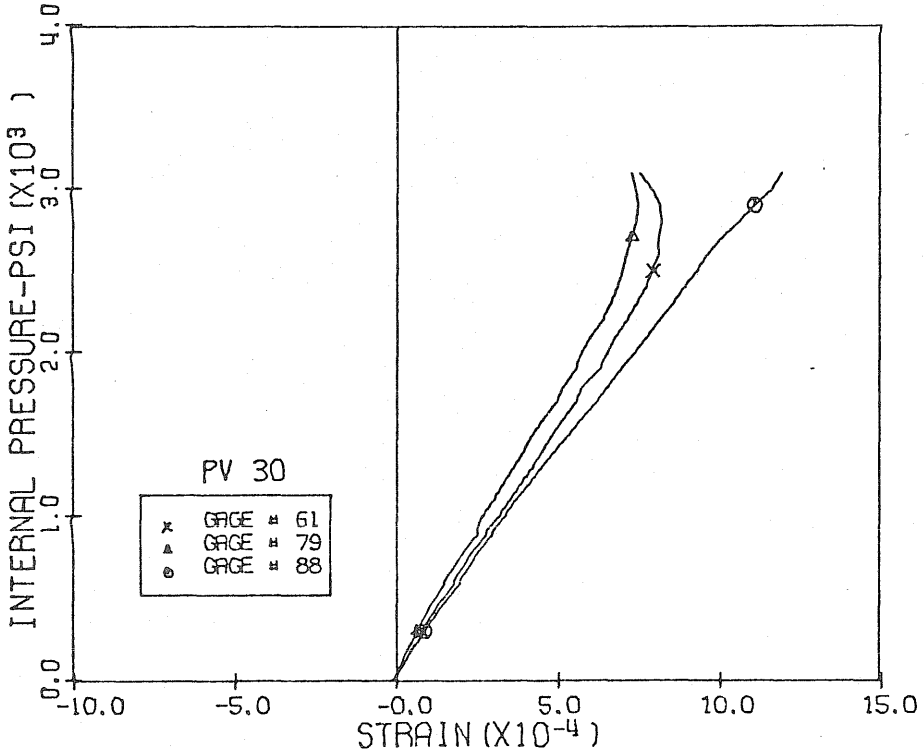

Fig. 3.42 Measured Vertical Strains, Level 3, Pen. 4 & 5, PV30

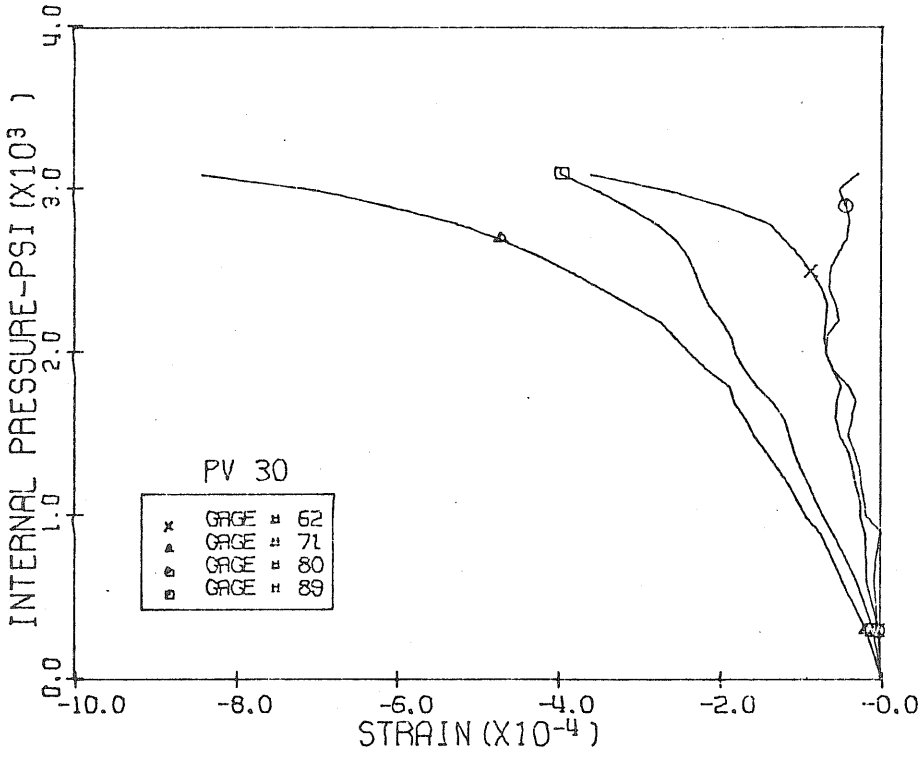

Fig. 3.43 Measured Horizontal Strains, Level 3, Pen. 4 & 5, PV30

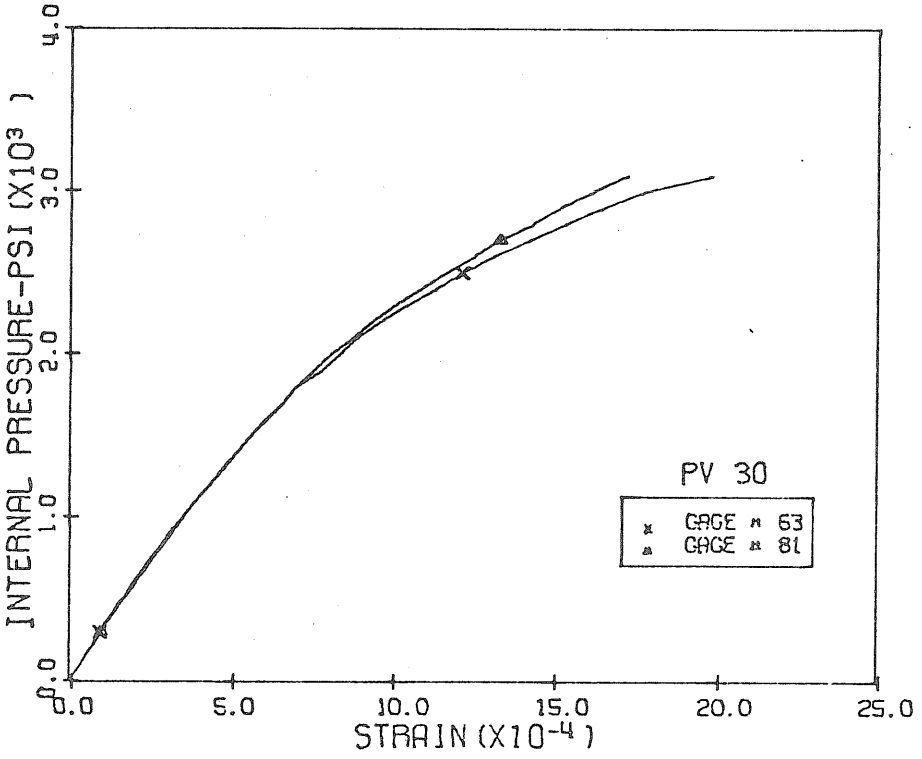

Fig. 3.44 Measured Comp. Diag. Strains, Level 3, Pen. 4 & 5, PV30

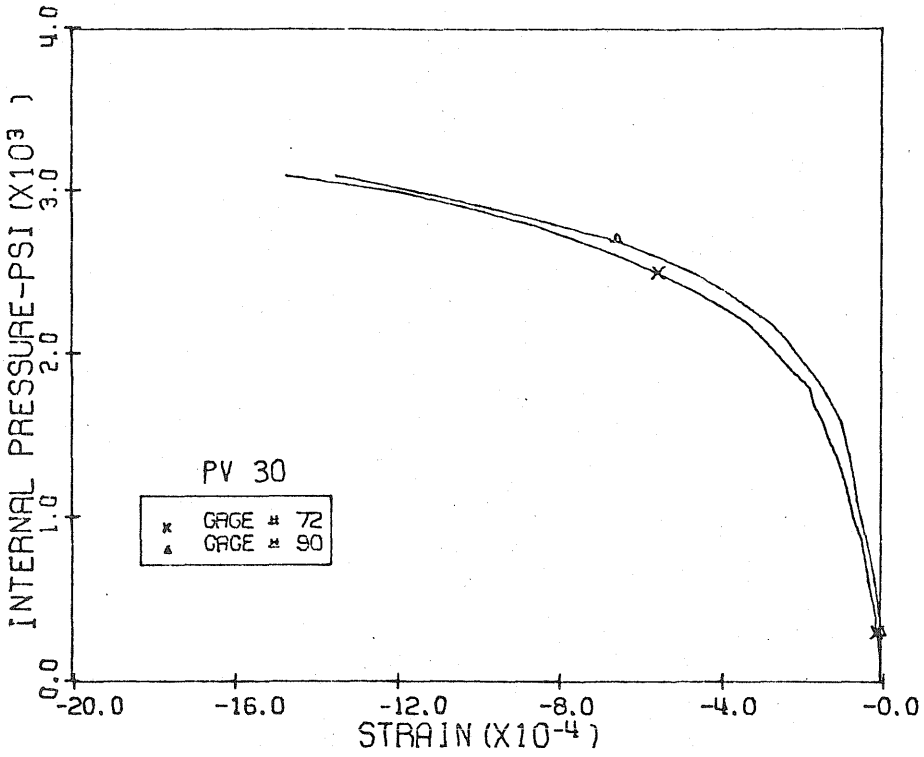

Fig. 3.45 Measured Tens. Diag. Strains, Level 3, Pen. 4 & 5, PV30

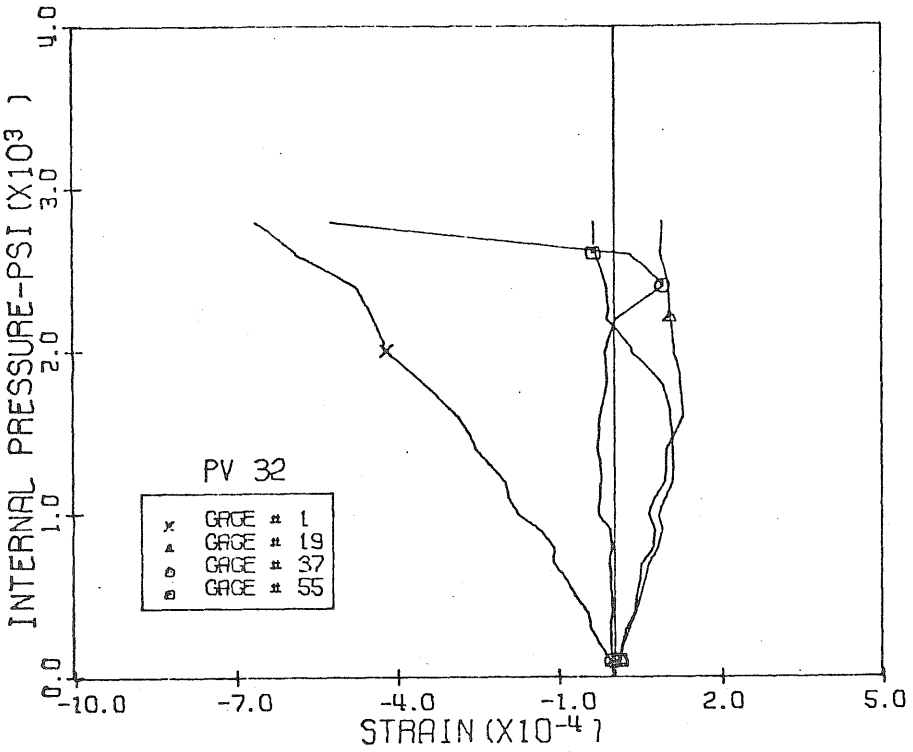

Fig. 3.46 Measured Vertical Strains, Level 1, 12:00 & 6:00 Pos., PV32

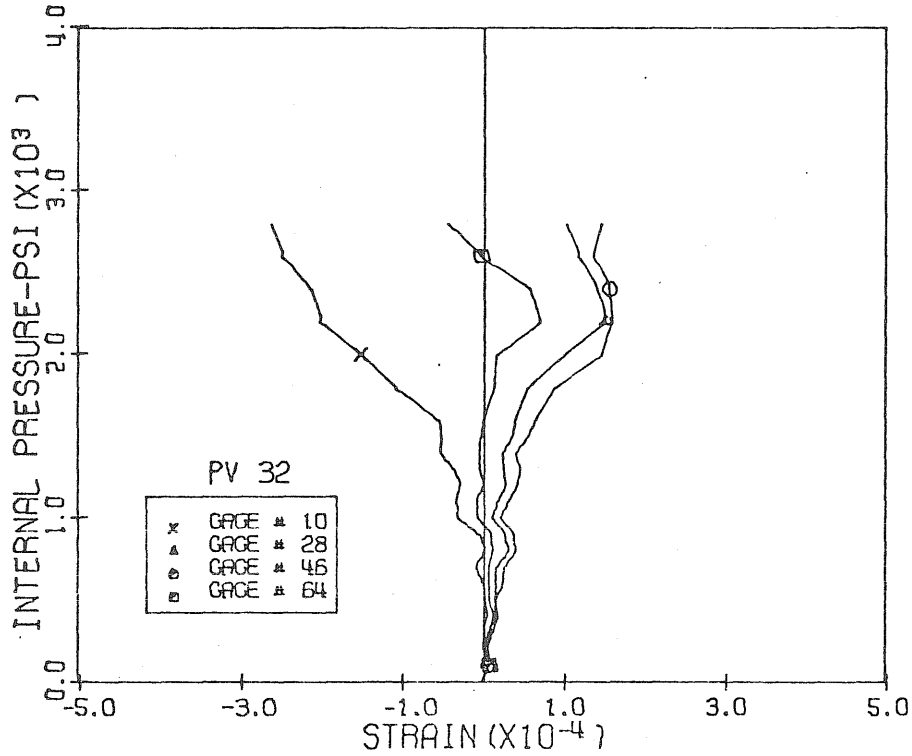

Fig. 3.47 Measured Vertical Strains, Level 1, 3:00 & 9:00 Pos., PV32

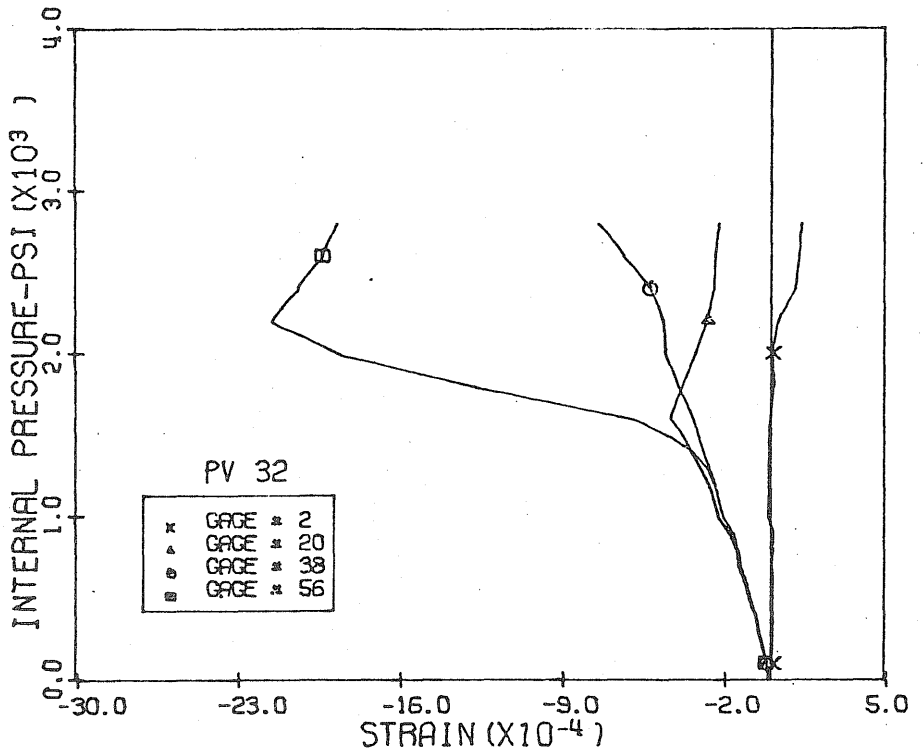

Fig. 3.48 Measured Horizontal Strains, Level 1, 12:00 & 6:00 Pos., PV32

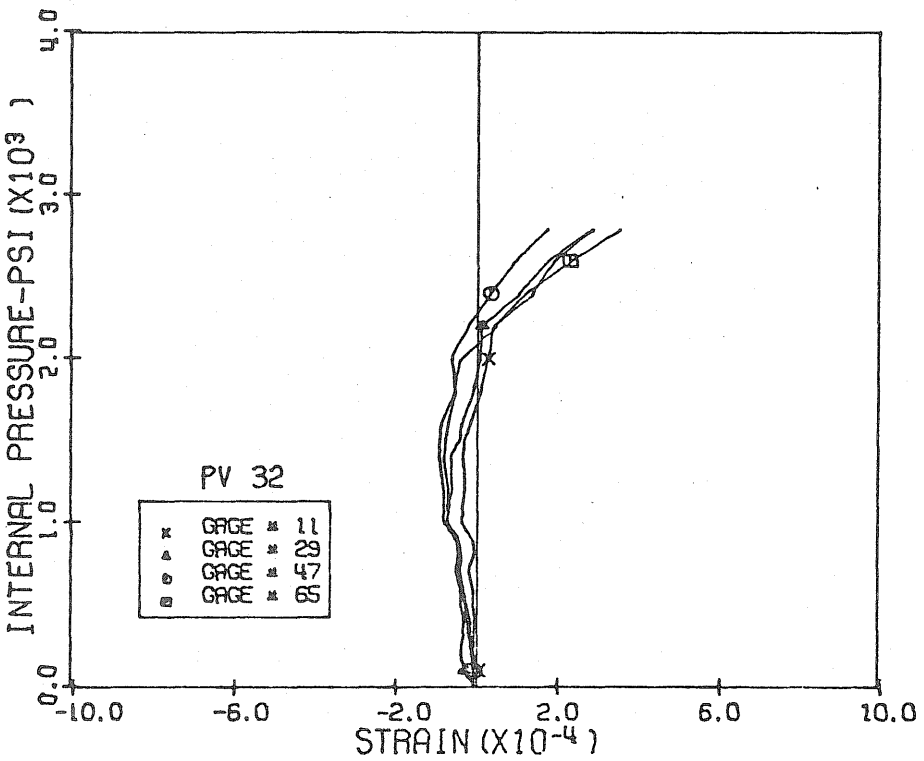

Fig. 3.49 Measured Horizontal Strains, Level 1, 3:00 & 9:00 Pos., PV32

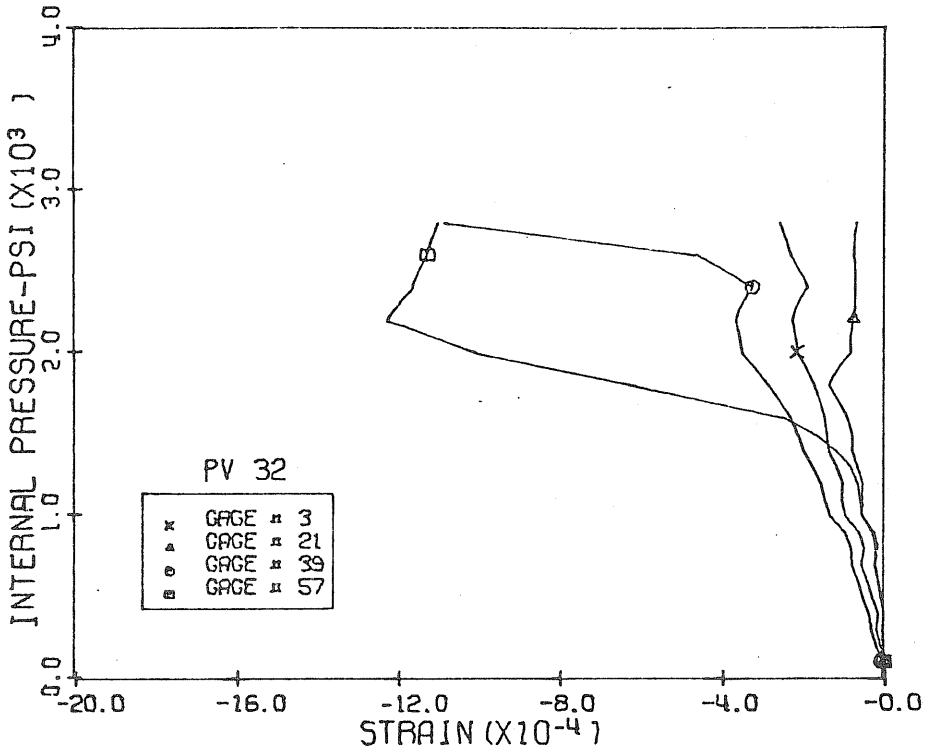

Fig. 3.50 Measured Diagonal Strains, Level 1, 12:00 & 6:00 Pos., PV32

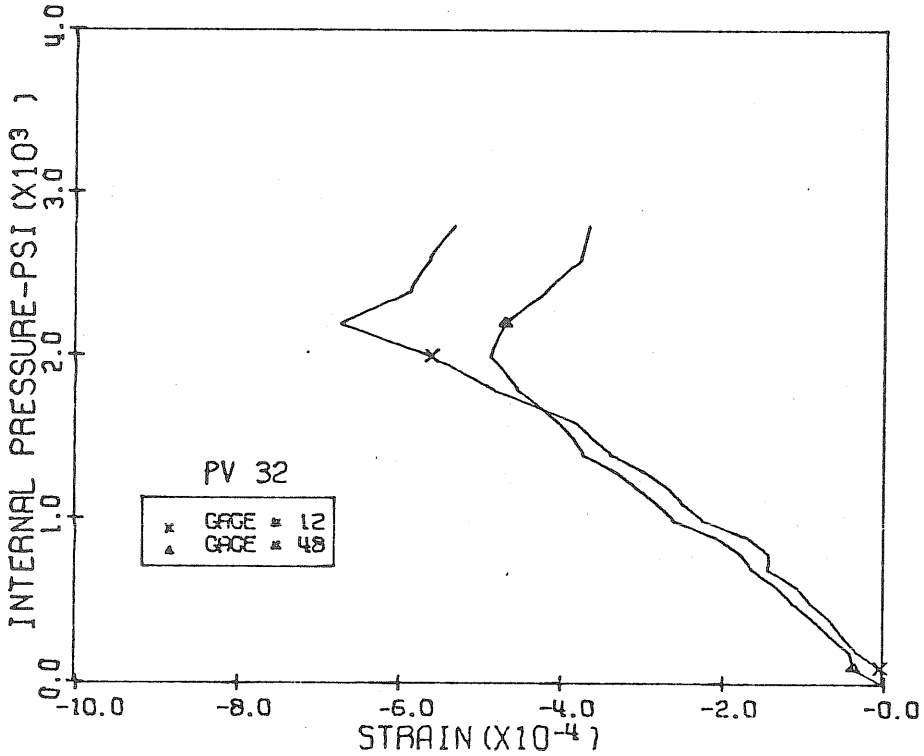

Fig. 3.51 Measured Tens. Diag. Strains, Level 1, 3:00 Pos., PV32

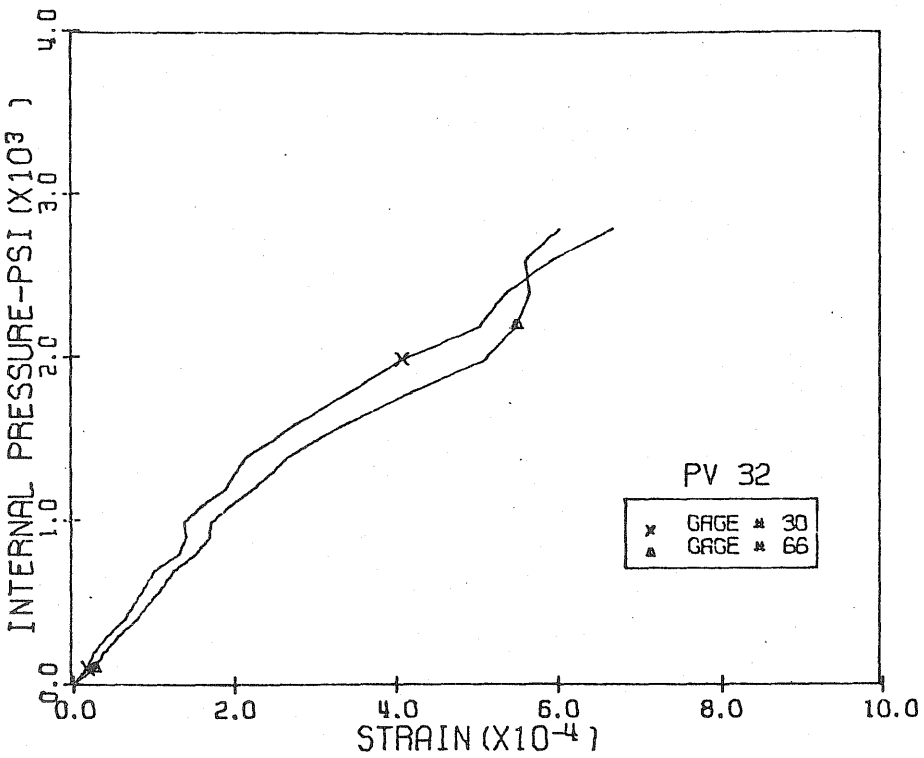

Fig. 3.52 Measured Comp. Diag. Strains, Level 1, 9:00 Pos., PV32

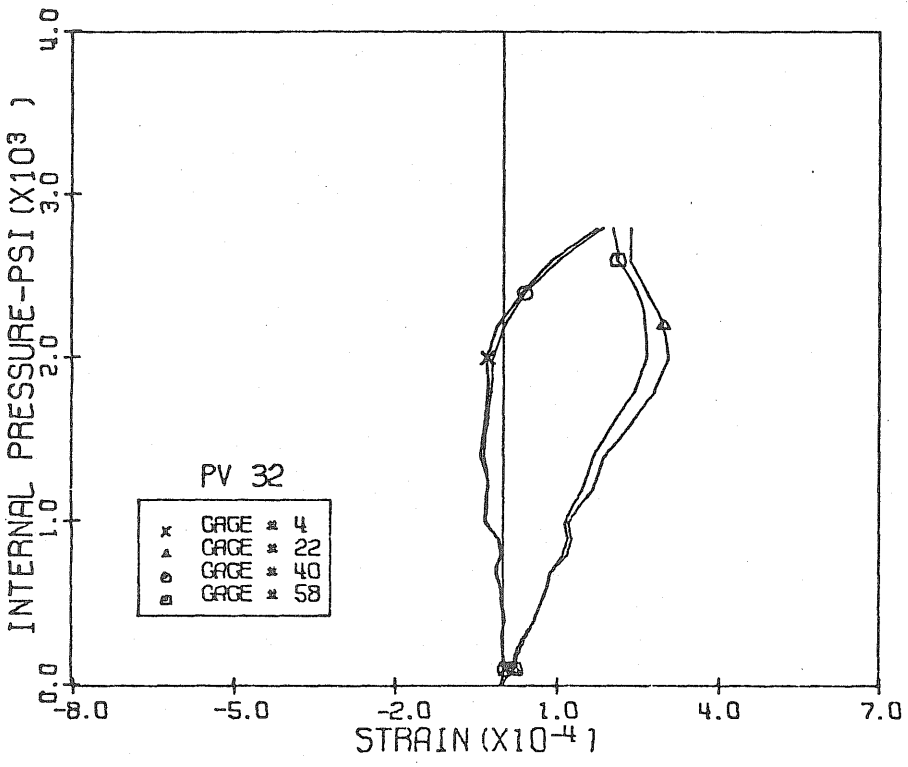

Fig. 3.53 Measured Vertical Strains, Level 2, 12:00 & 6:00 Pos., PV32

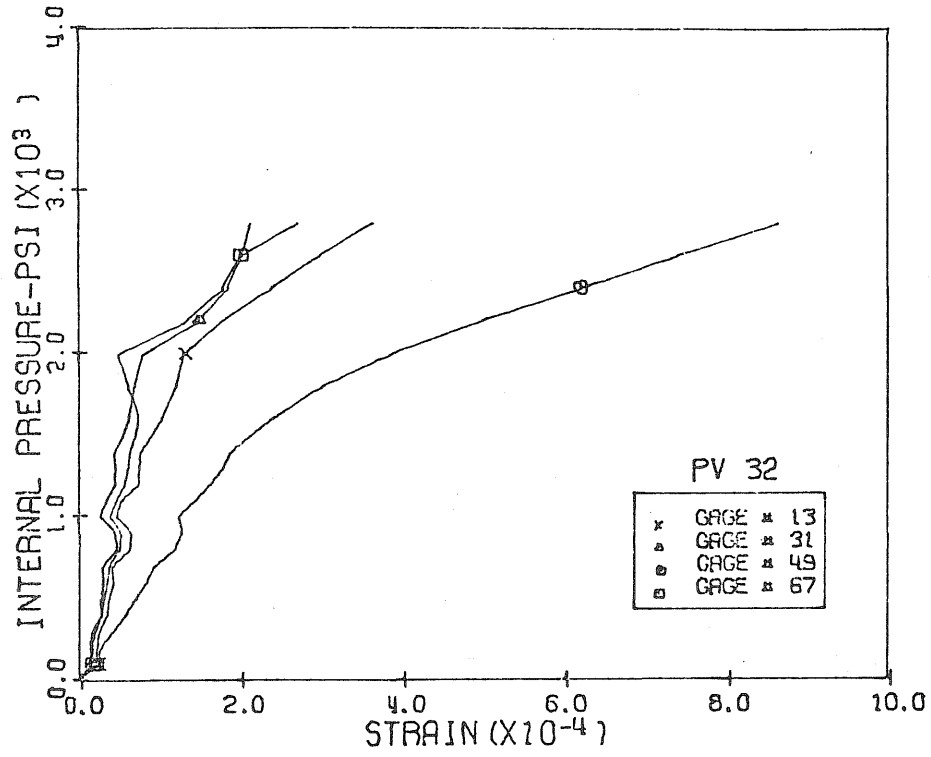

Fig. 3.54 Measured Vertical Strains, Level 2, 3:00 & 9:00 Pos., PV32

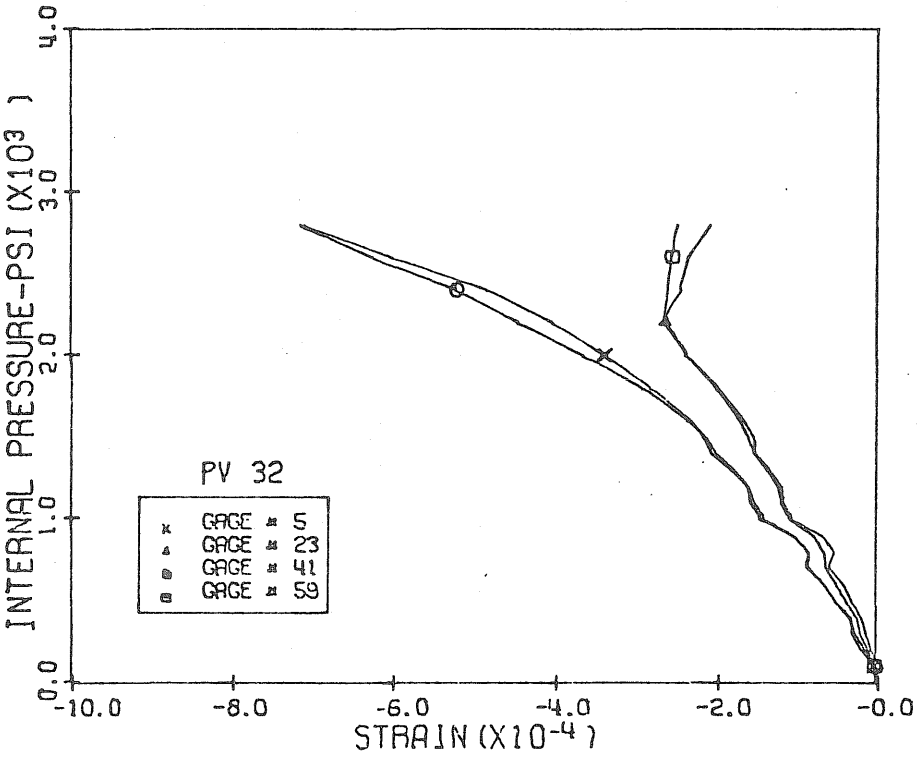

Fig. 3.55 Measured Horizontal Strains, Level 2, 12:00 & 6:00 Pos., PV32

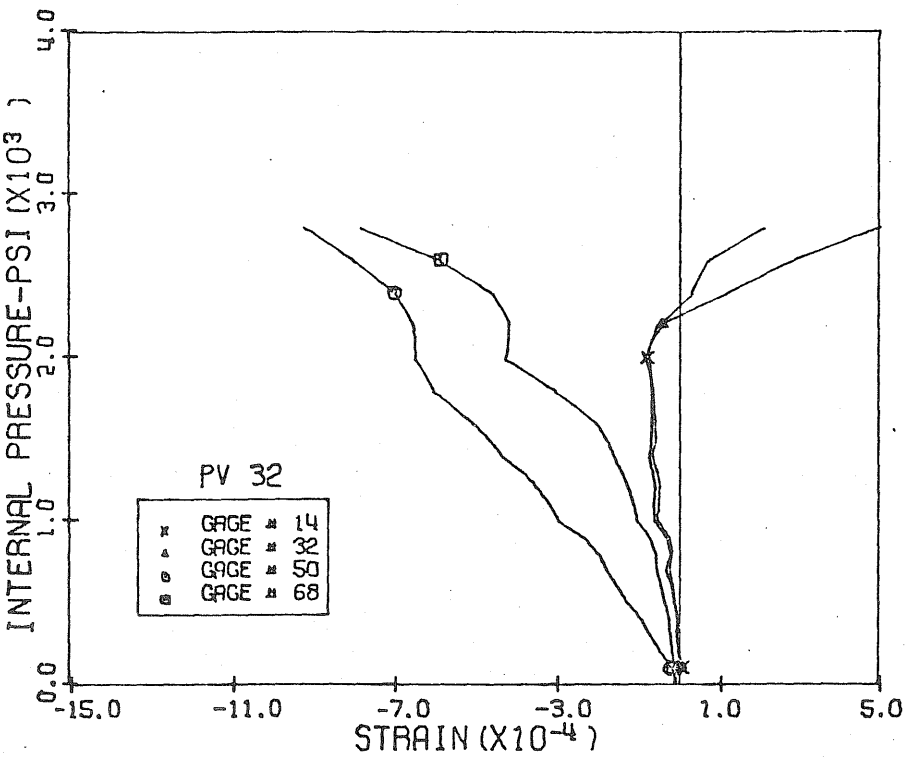

Fig. 3.56 Measured Horizontal Strains, Level 2, 3:00 & 9:00 Pos., PV32

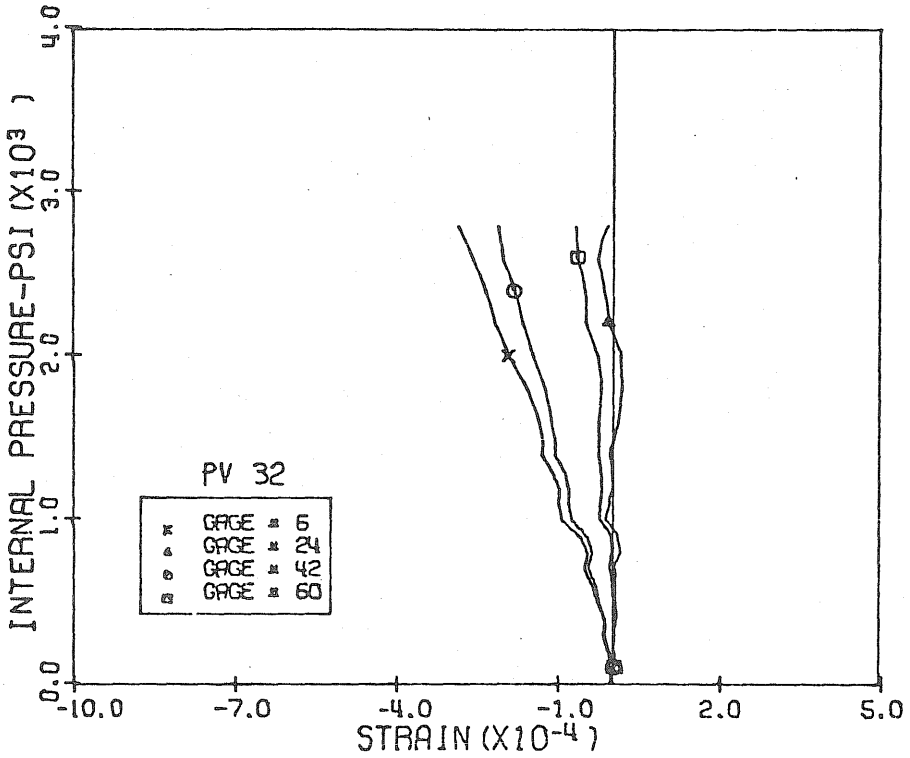

Fig. 3.57 Measured Diagonal Strains, Level 2, 12:00 & 6:00 Pos., PV32

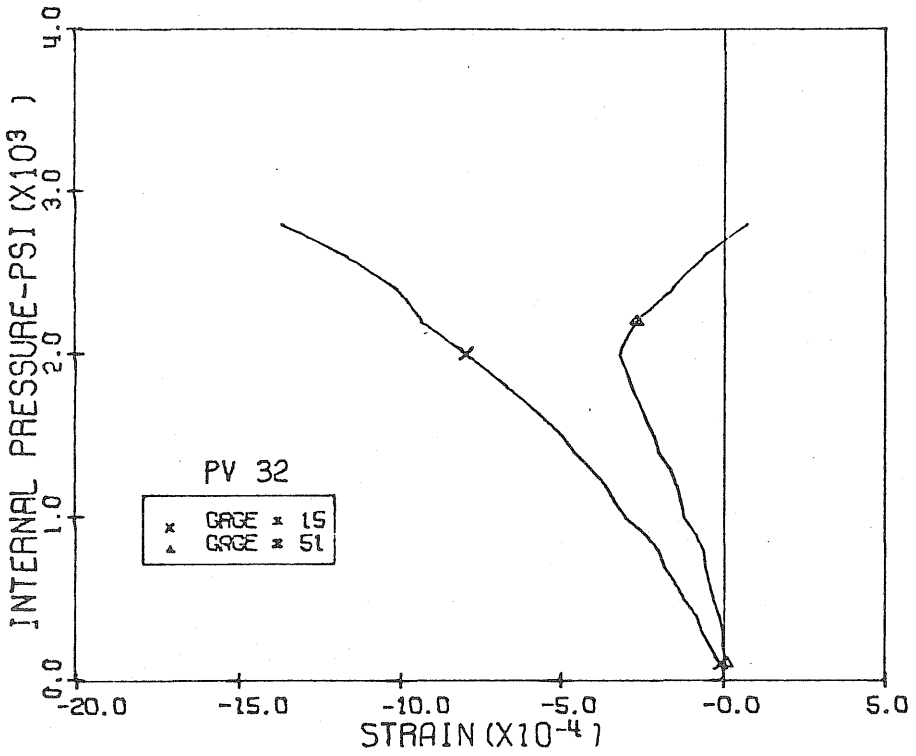

Fig. 3.58 Measured Tens. Diag. Strains, Level 2, 3:00 Pos., PV32

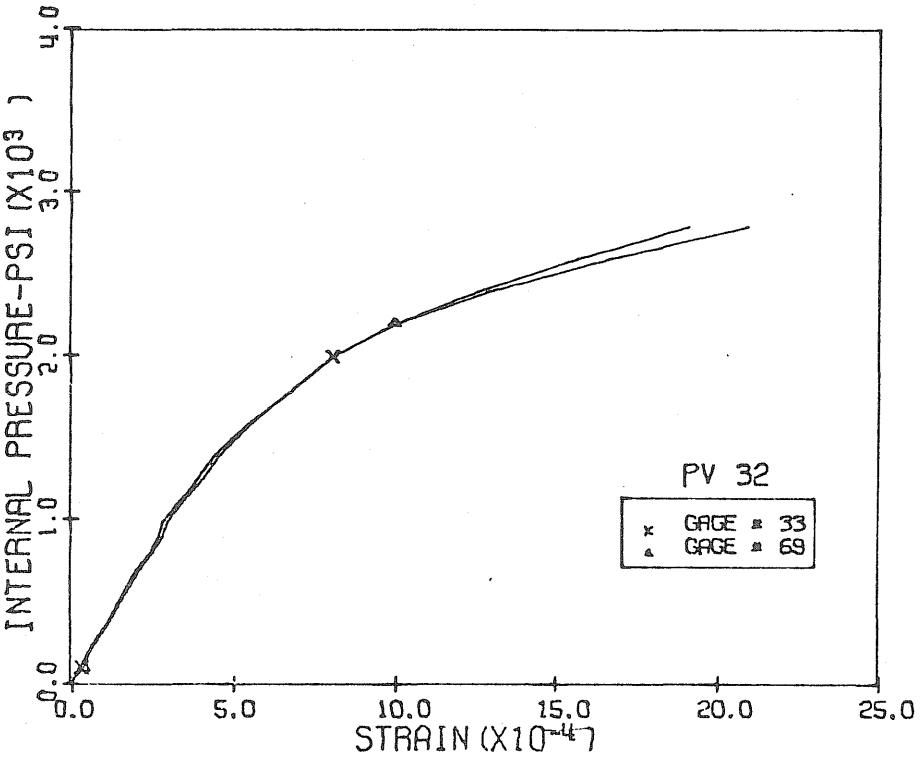

Fig. 3.59 Measured Comp. Diag. Strains, Level 2, 9:00 Pos., PV32

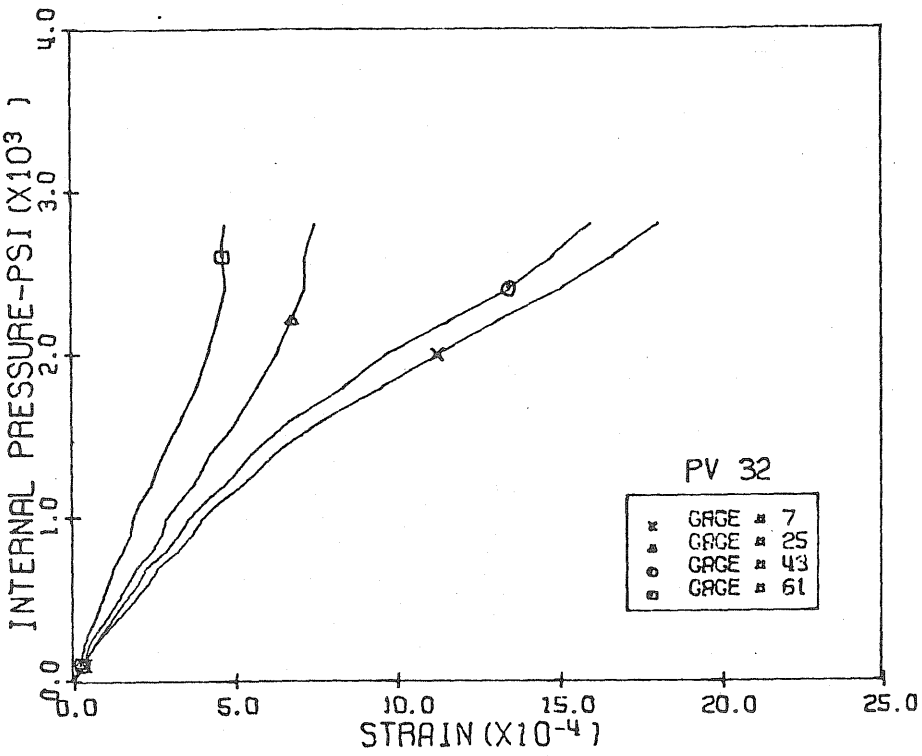

Fig. 3.60 Measured Vertical Strains, Level 3, 12:00 & 6:00 Pos., PV32

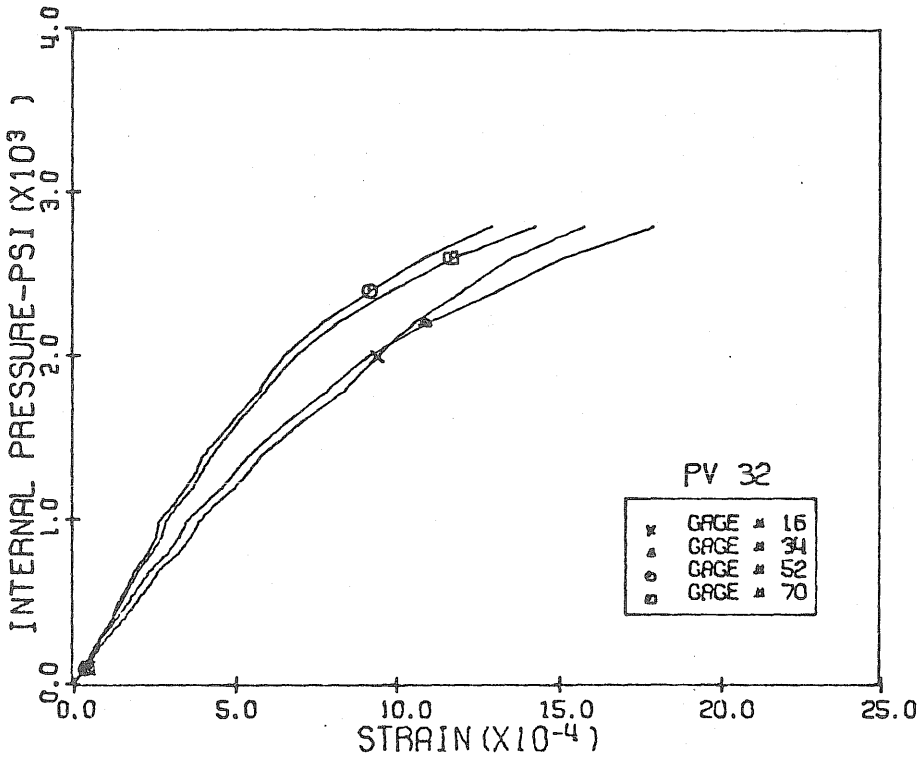

Fig. 3.61 Measured Vertical Strains, Level 3, 3:00 & 9:00 Pos., PV32

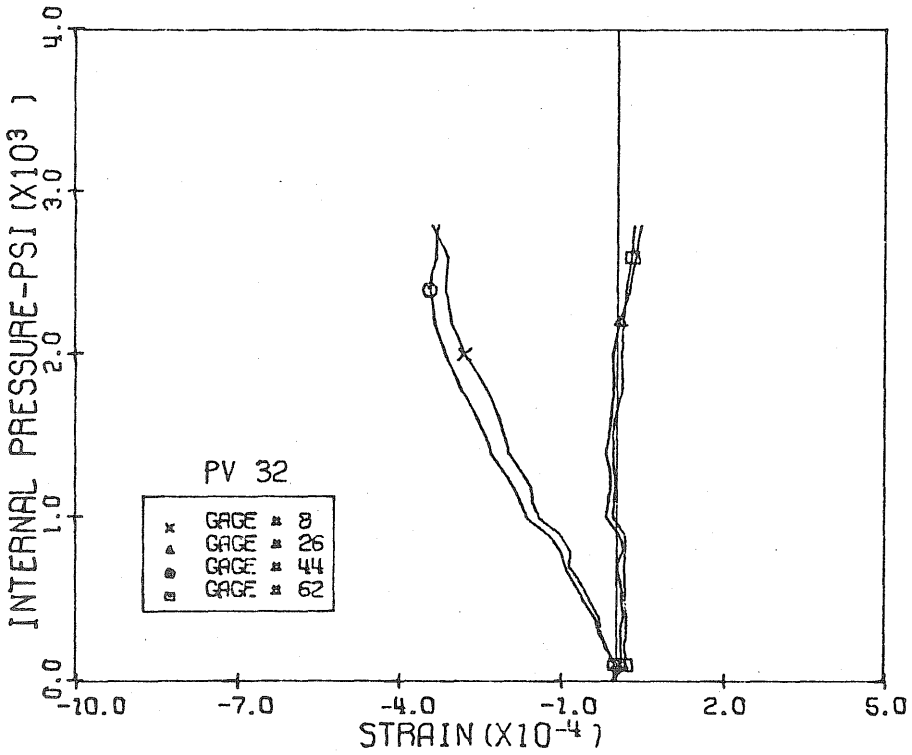

Fig. 3.62 Measured Horizontal Strains, Level 3, 12:00 & 6:00 Pos., PV32

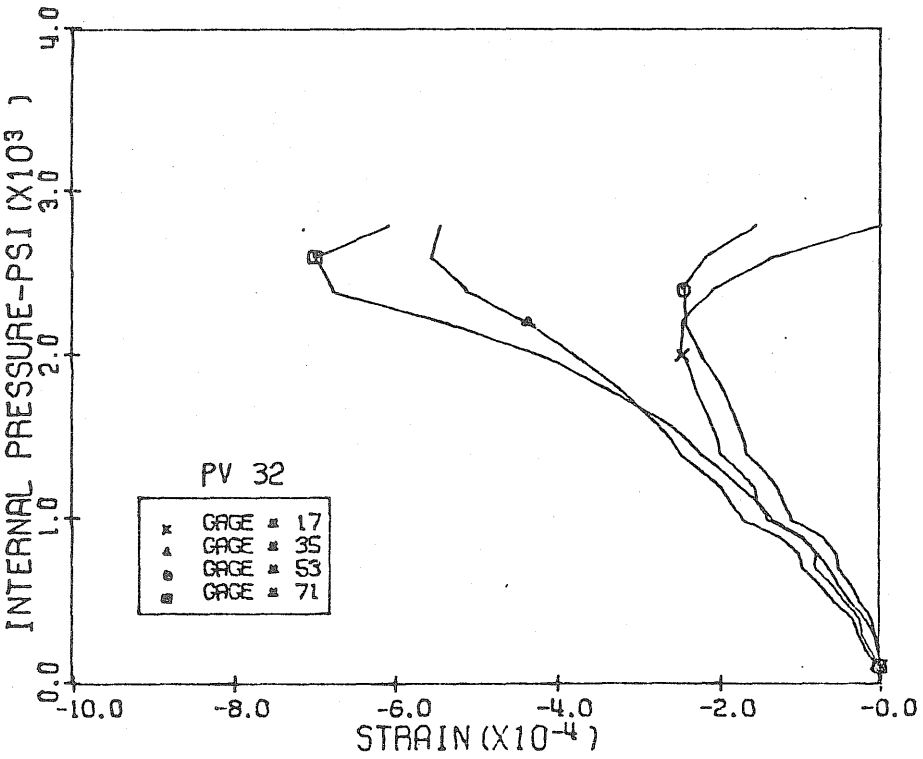

Fig. 3.63 Measured Horizontal Strains, Level 3, 3:00 & 9:00 Pos., PV32

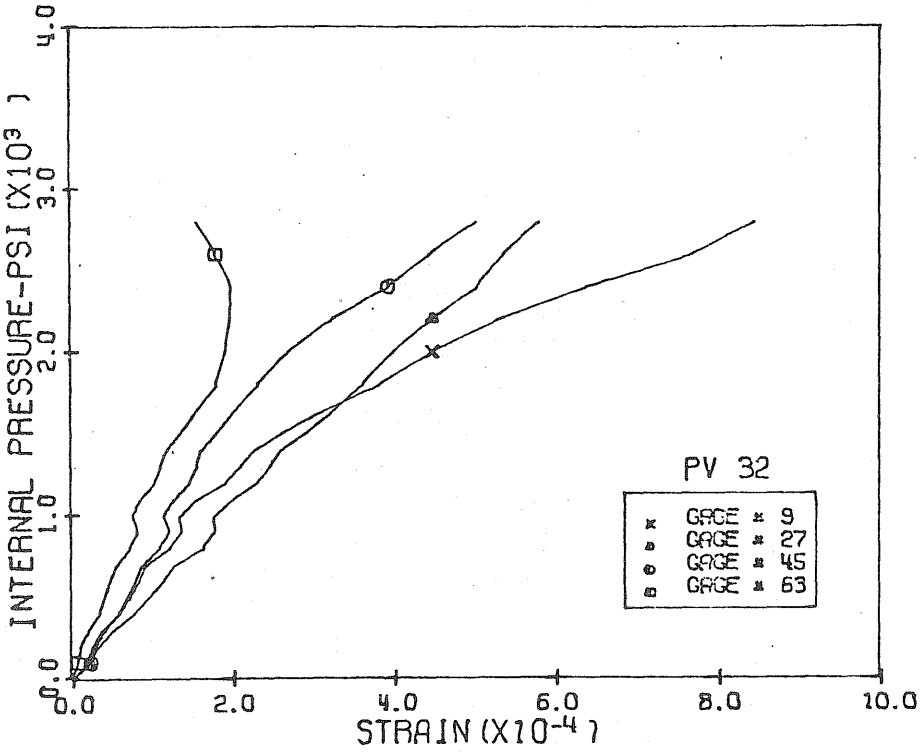

Fig. 3.64 Measured Diagonal Strains, Level 3, 12:00 & 6:00 Pos., PV32

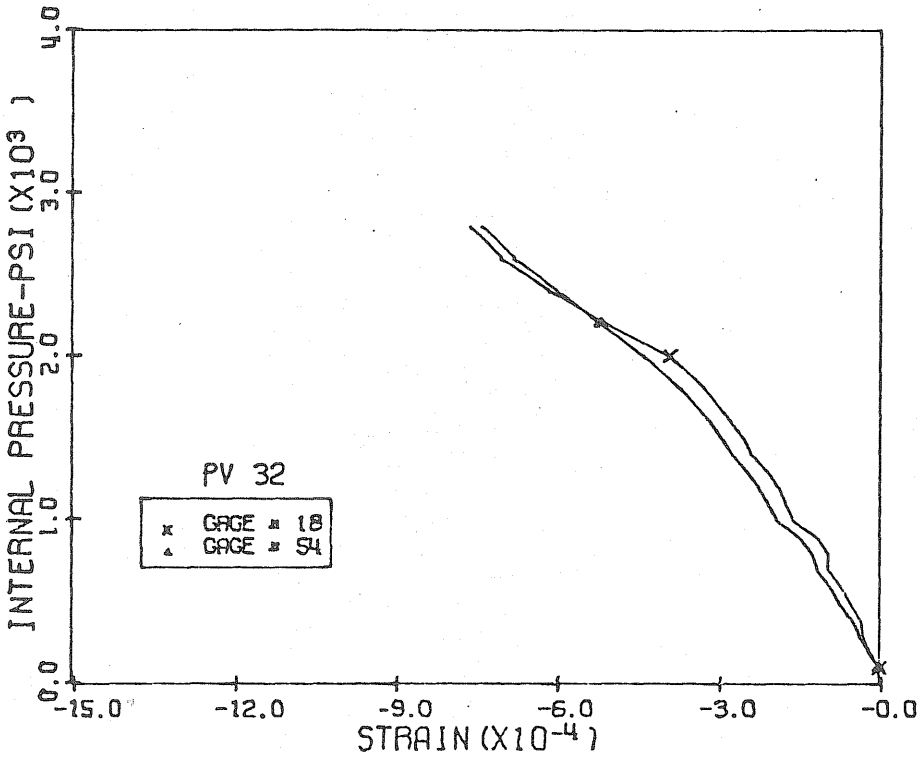

Fig. 3.65 Measured Tens. Diag. Strains, Level 3, 3:00 Pos., PV32

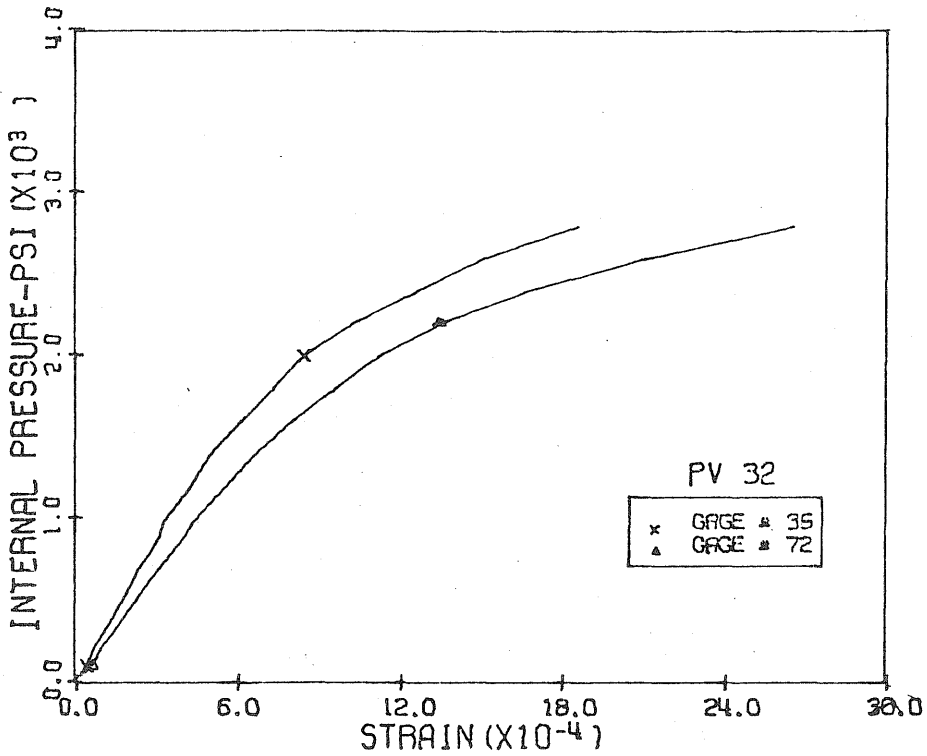

Fig. 3.66 Measured Comp. Diag. Strains, Level 3, 9:00 Pos., PV32

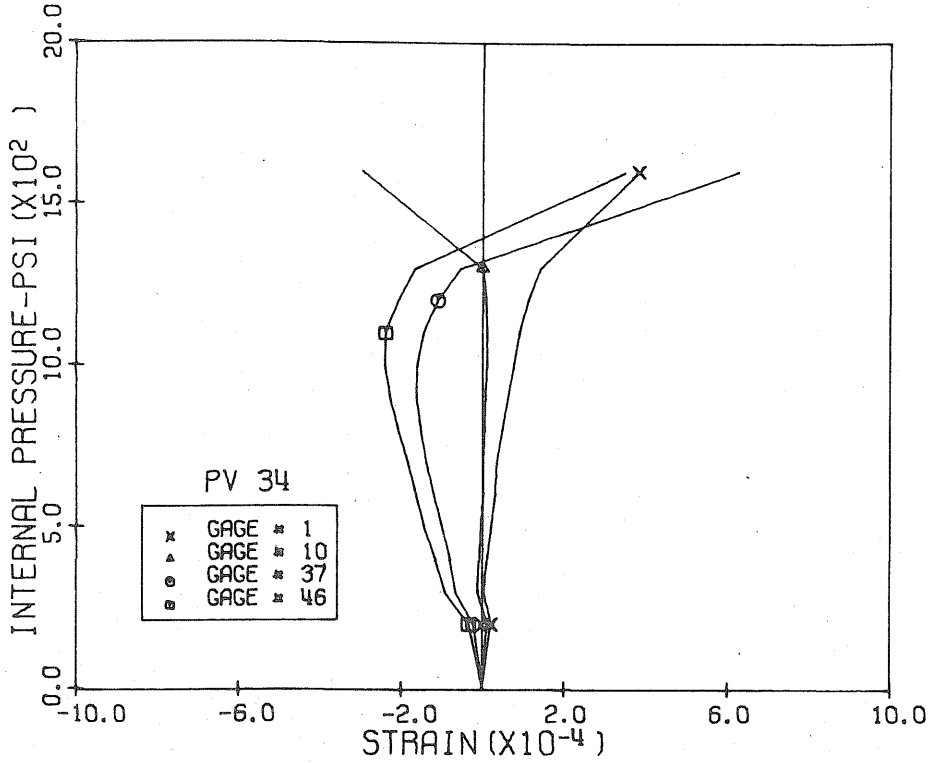

Fig. 3.67 Measured Vertical Strains, Level 1, Pen. 1 & 3, PV34

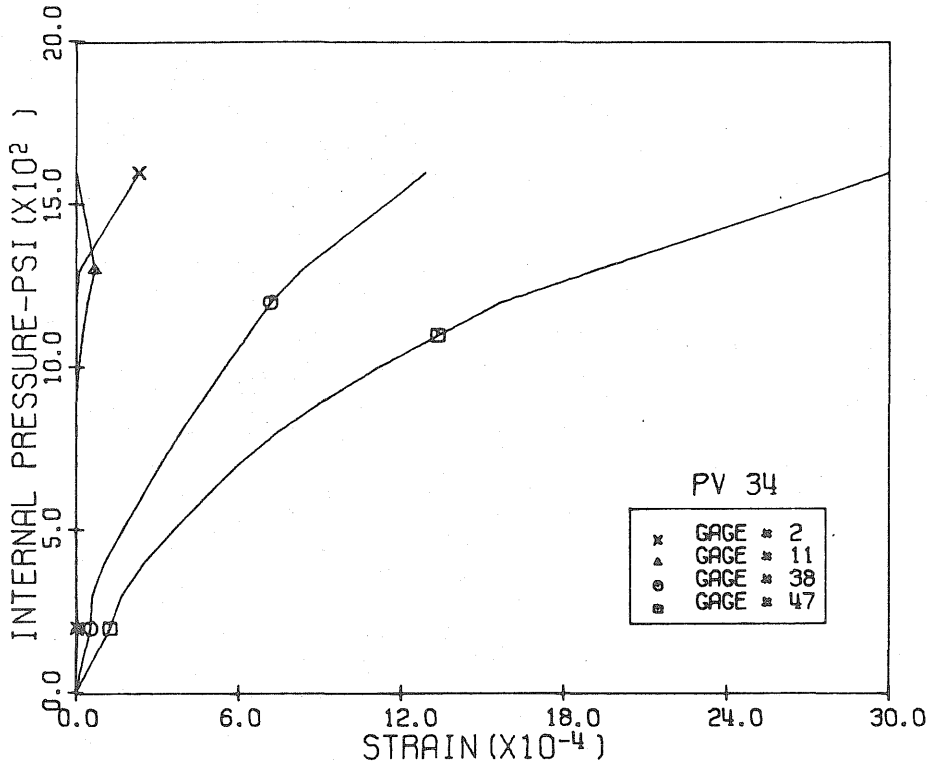

Fig. 3.68 Measured Horizontal Strains, Level 1, Pen. 1 & 3, PV34

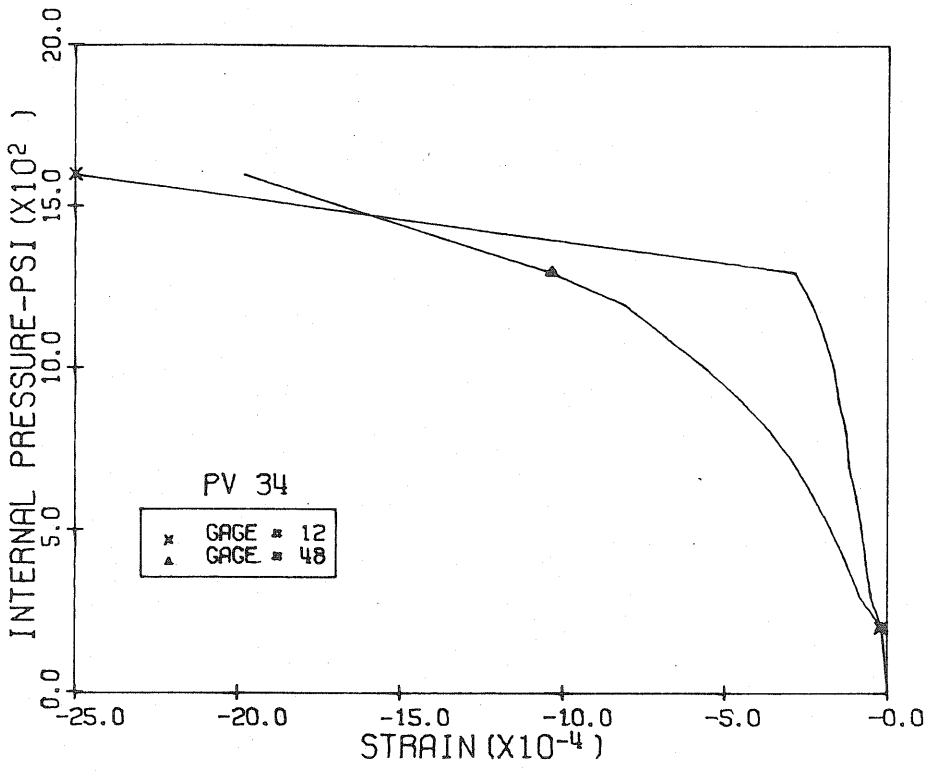

Fig. 3.69 Measured Comp. Diag. Strains, Level 1, Pen. 1 & 3, PV34

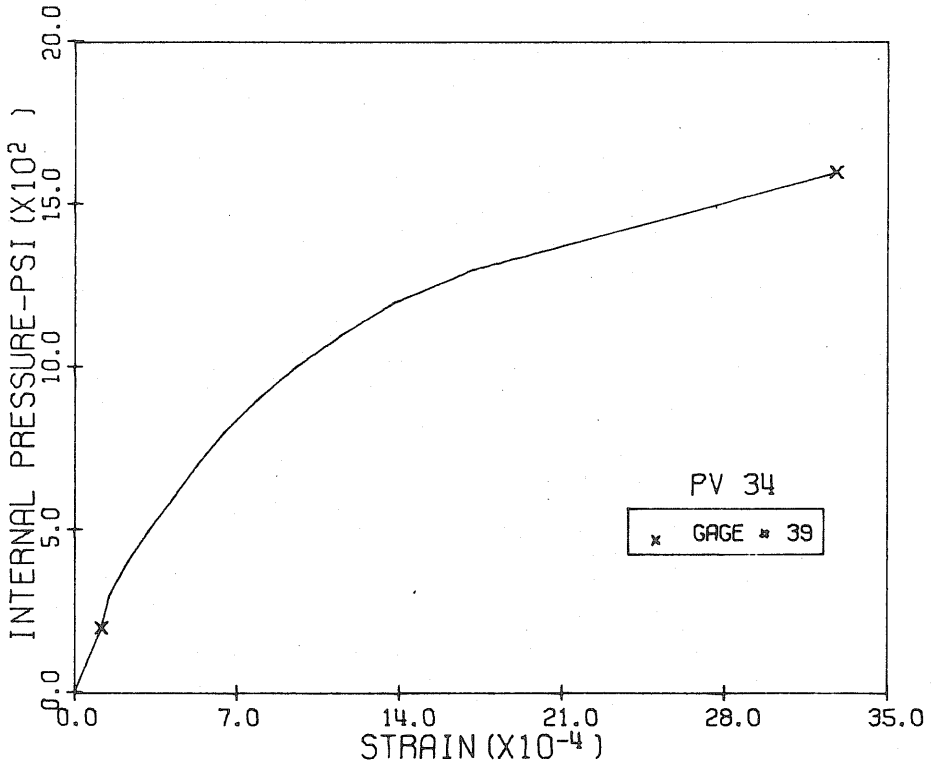

Fig. 3.70 Measured Tens. Diag. Strains, Level 1, Pen. 1 & 3, PV34

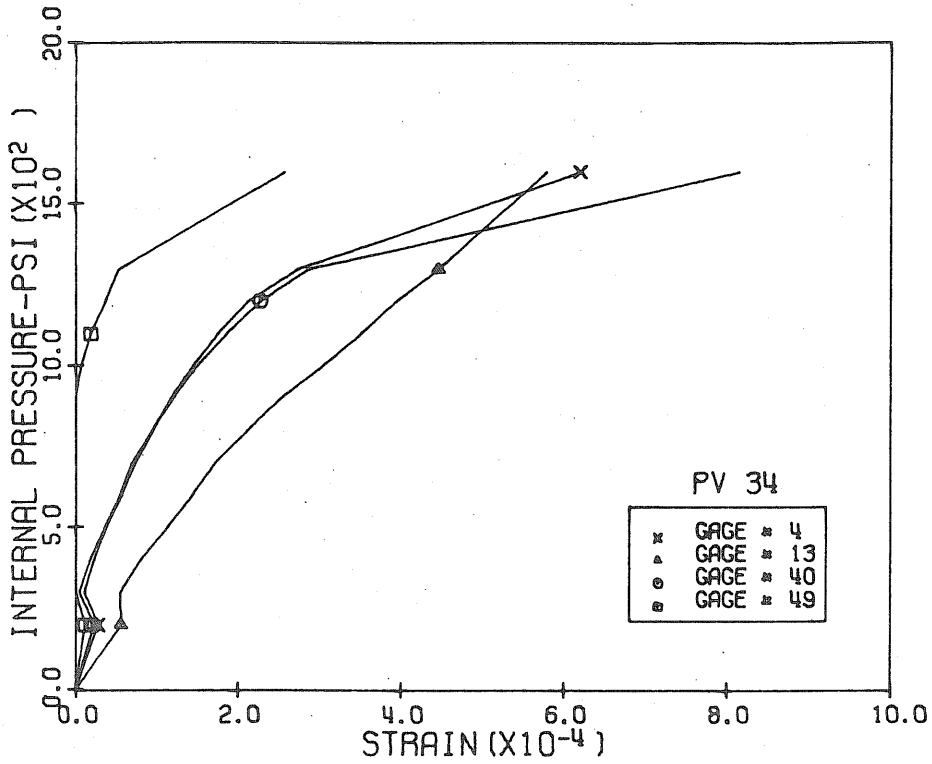

Fig. 3.71 Measured Vertical Strains, Level 2, Pen. 1 & 3, PV34

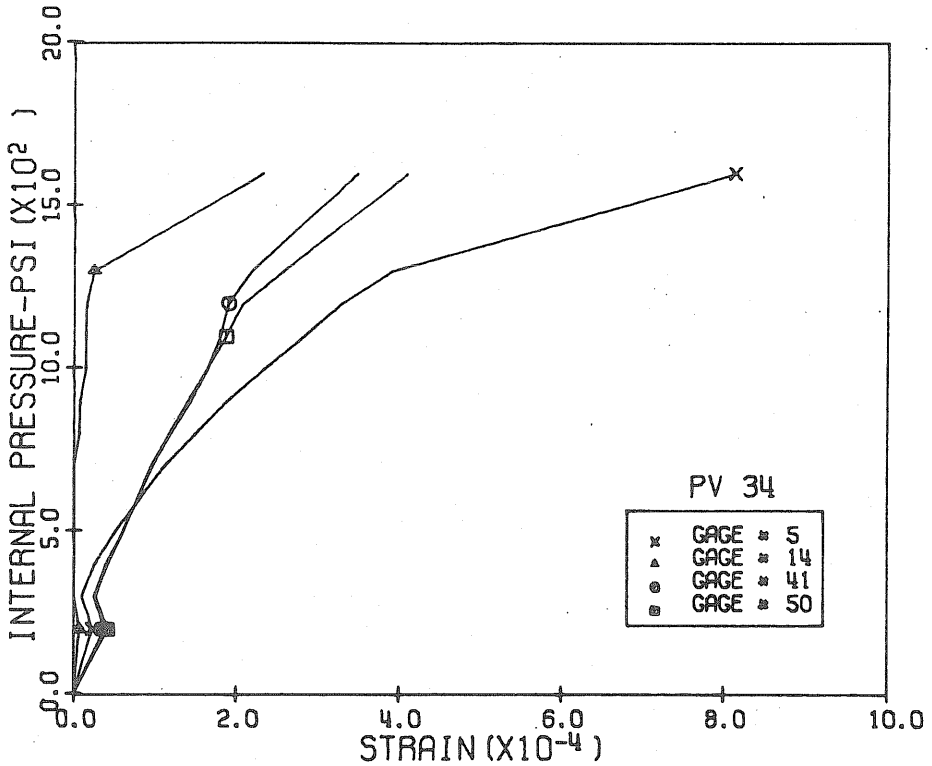

Fig. 3.72 Measured Horizontal Strains, Level 2, Pen. 1 & 3, PV34

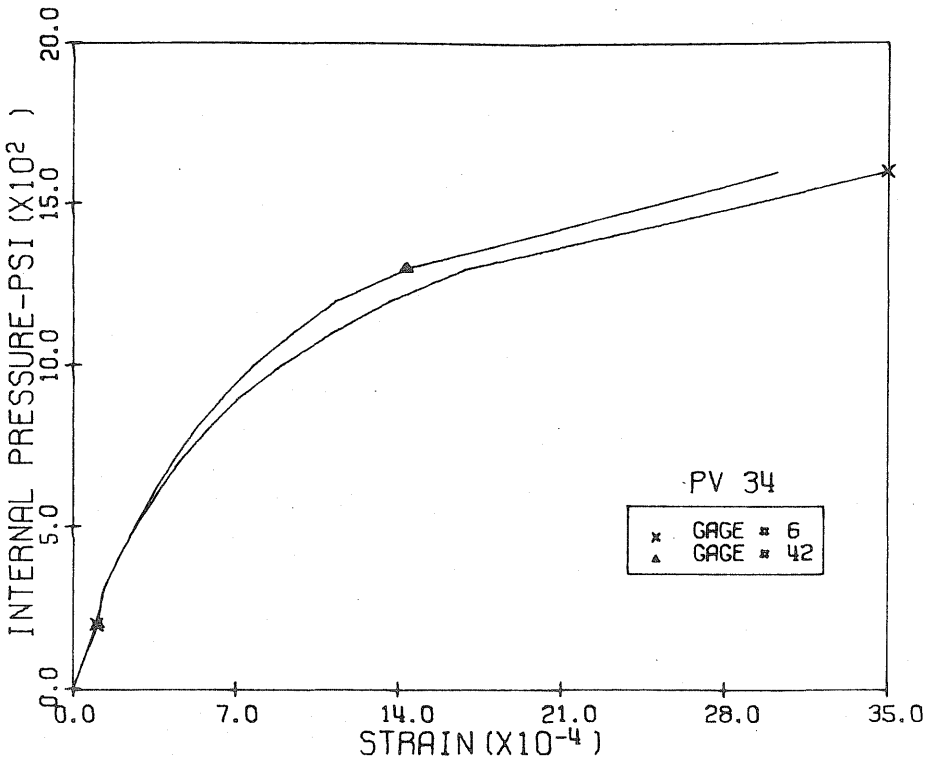

Fig. 3.73 Measured Comp. Diag. Strains, Level 2, Pen. 1 & 3 PV34

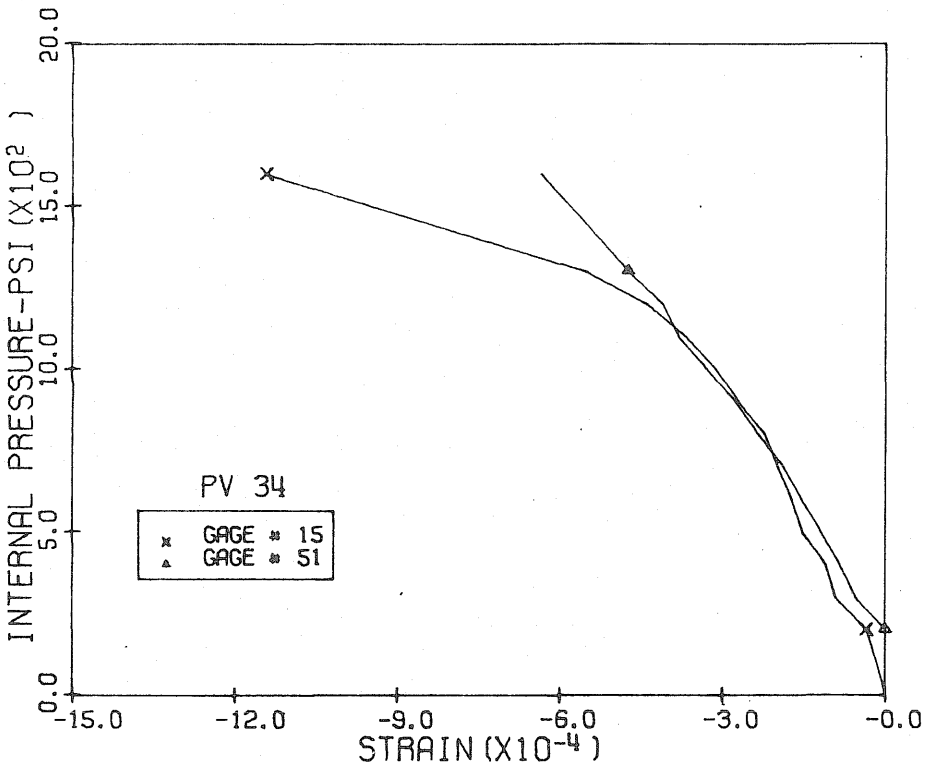

Fig. 3.74 Measured Tens. Diag. Strains, Level 2, Pen. 1 & 3, PV34

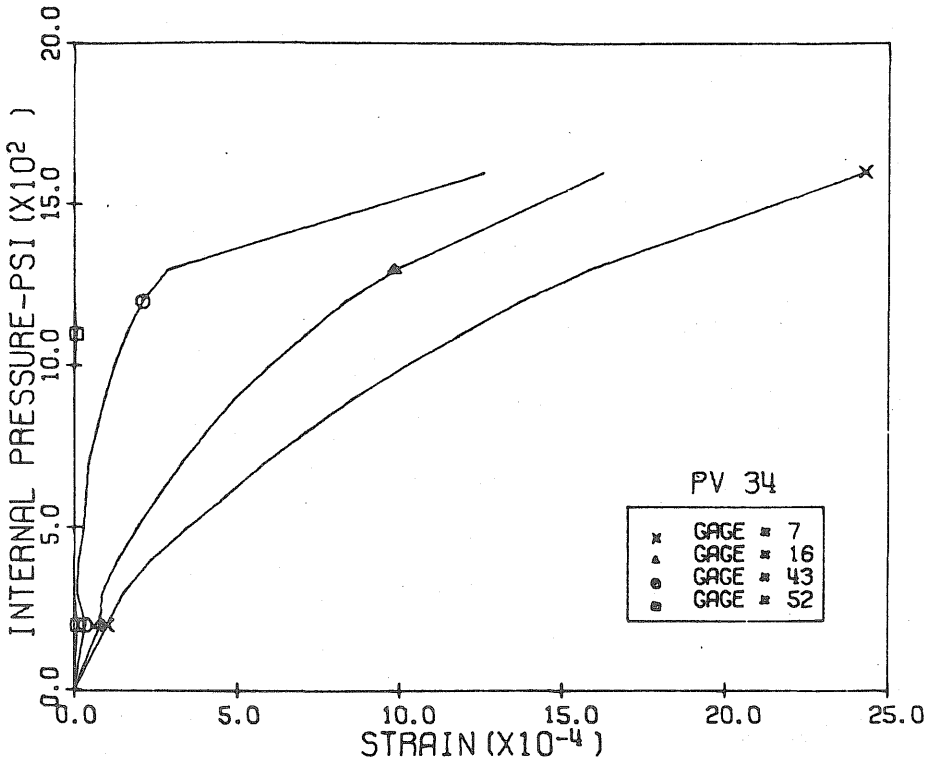

Fig. 3.75 Measured Vertical Strains, Level 3, Pen. 1 & 3, PV34

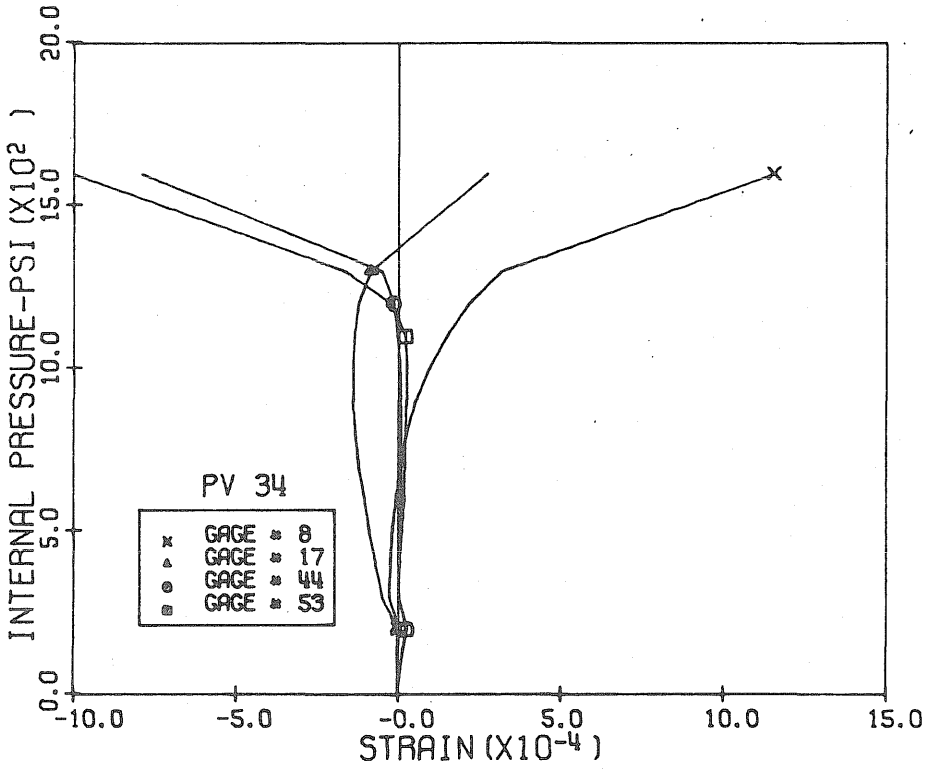

Fig. 3.76 Measured Horizontal Strains, Level 3, Pen. 1 & 3, PV34

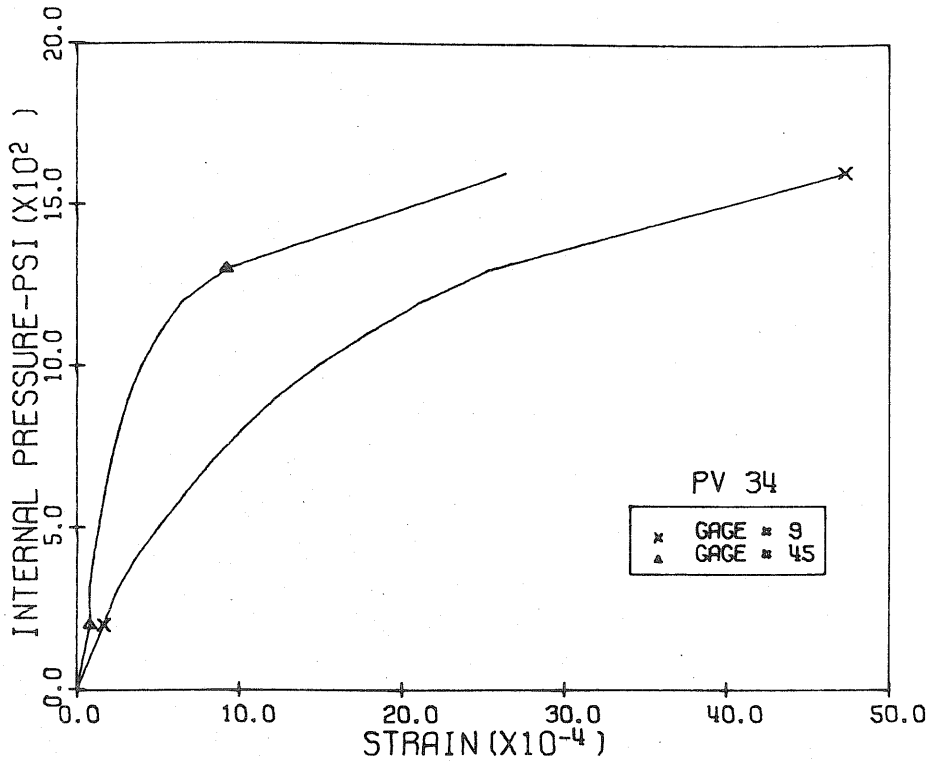

Fig. 3.77 Measured Comp. Diag. Strains, Level 3, Pen. 1 & 3, PV34

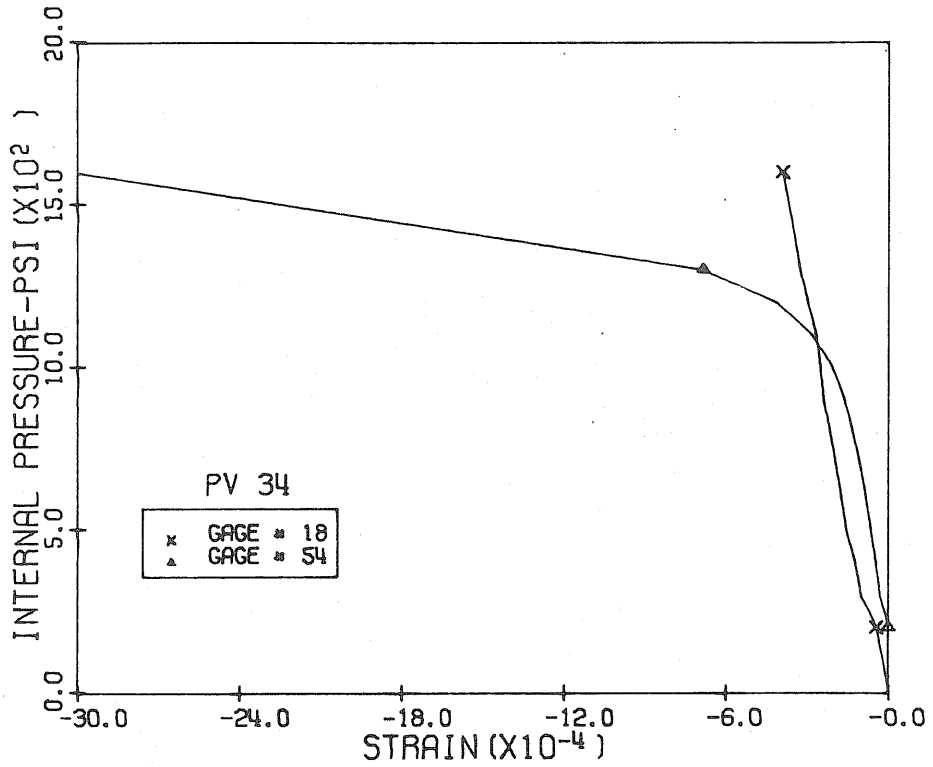

Fig. 3.78 Measured Tens. Diag. Strains, Level 3, Pen. 1 & 3, PV34

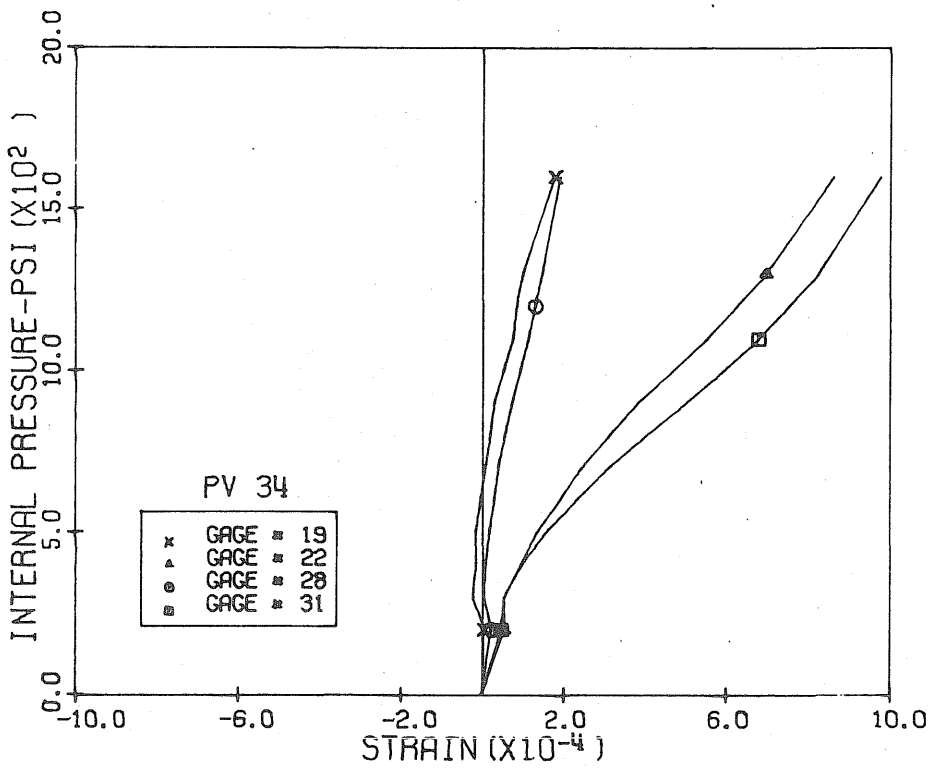

Fig. 3.79 Measured Vertical Strains, Level 1 & 2, Penetration 2, PV34

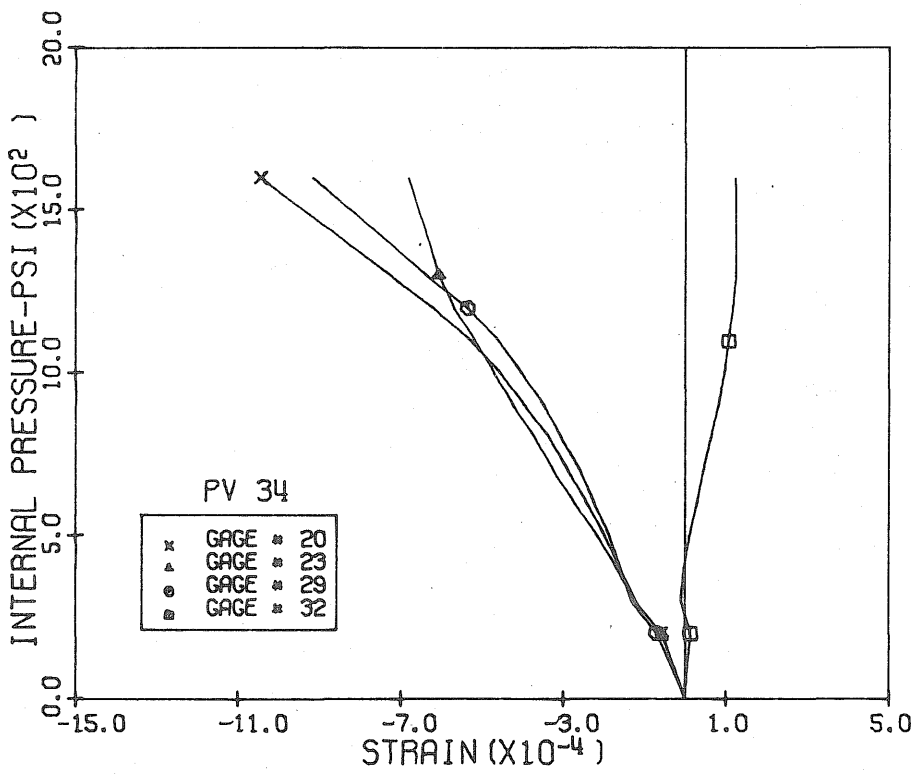

Fig. 3.80 Measured Horizontal Strains, Level 1 & 2, Penetration 2, PV34

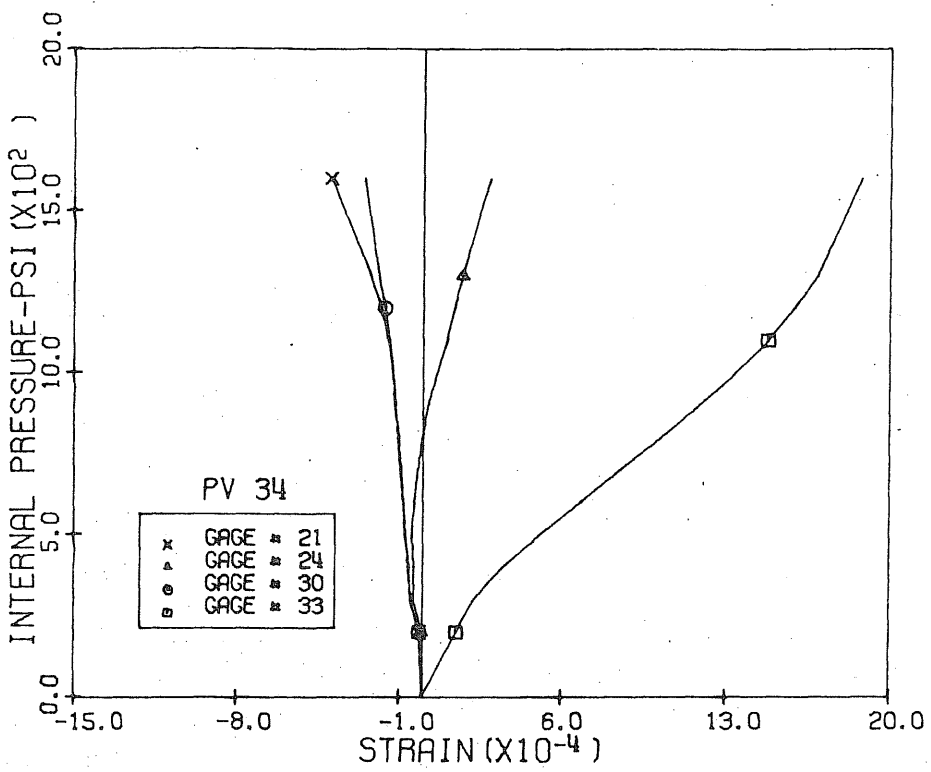

Fig. 3.81 Measured Diagonal Strains, Level 1 & 2, Penetration 2, PV34

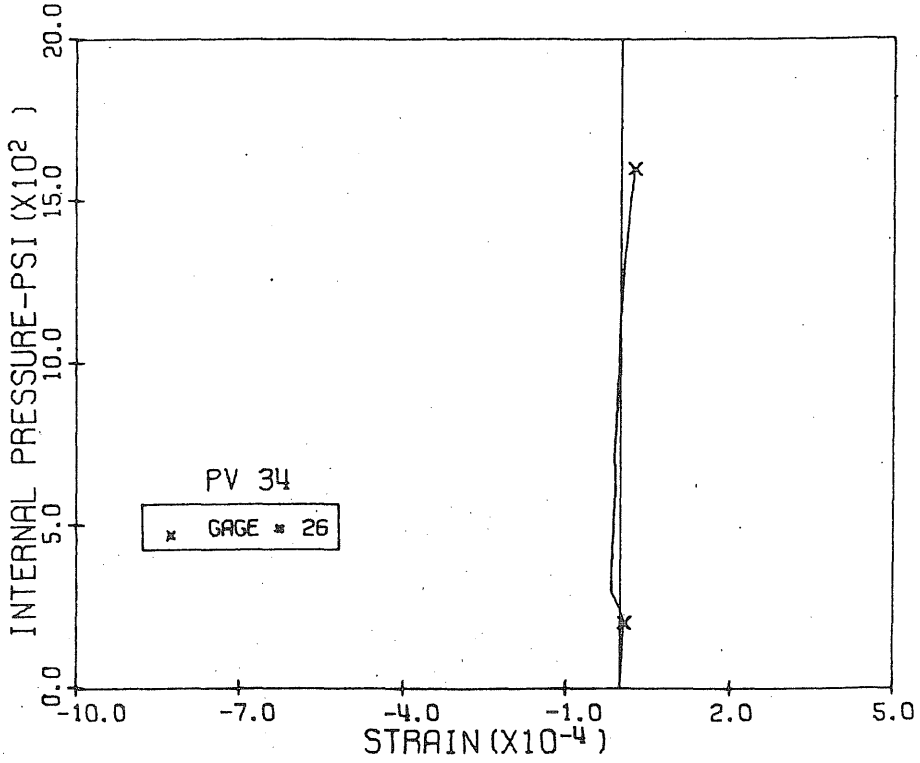

Fig. 3.82 Measured Horizontal Strains, Level 3, Penetration 2, PV34

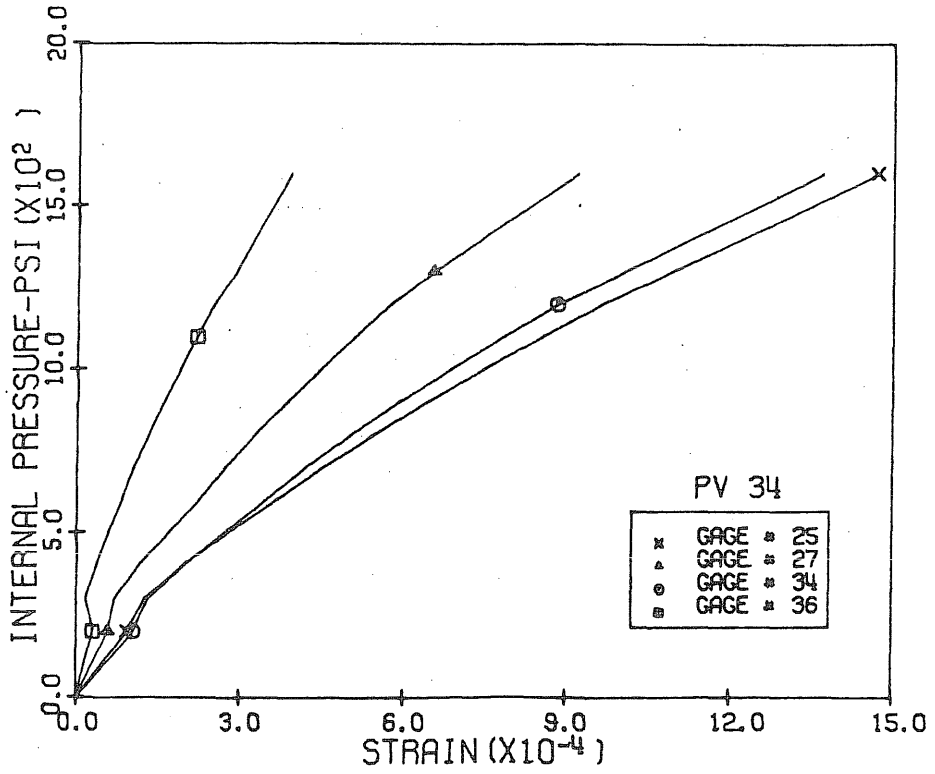

Fig. 3.83 Measured Vertical Strains, Level 3, Penetration 2, PV34

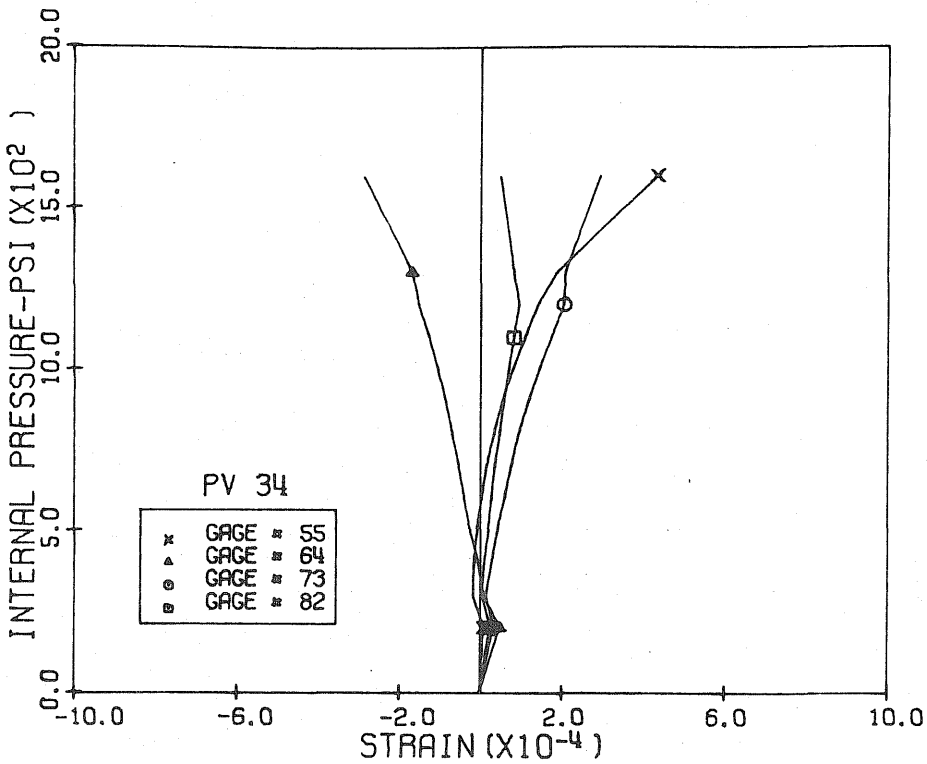

Fig. 3.84 Measured Vertical Strains, Level 1, Pen. 4 & 5, PV34

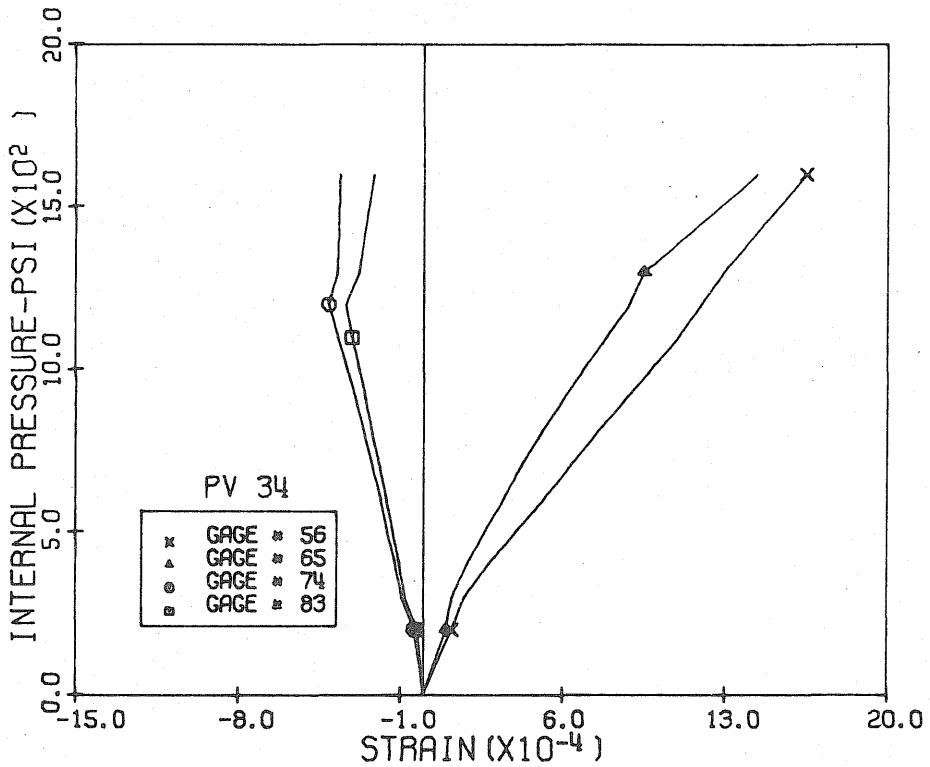

Fig. 3.85 Measured Horizontal Strains, Level 1, Pen. 4 & 5, PV34

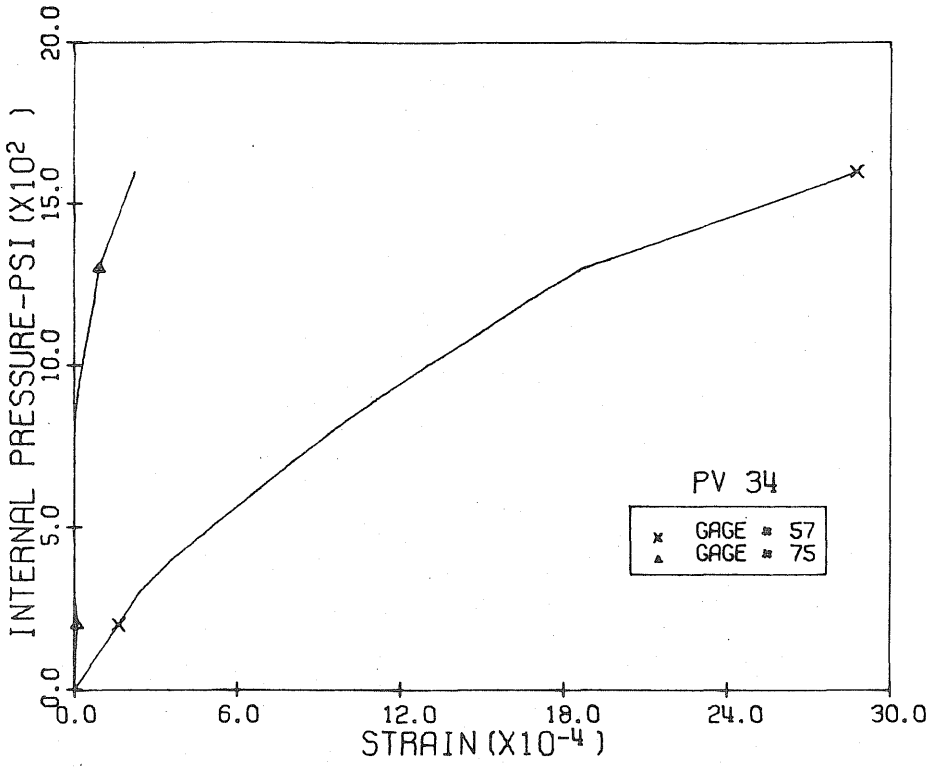

Fig. 3.86 Measured Comp. Diag. Strains, Level 1, Pen. 4 & 5, PV34

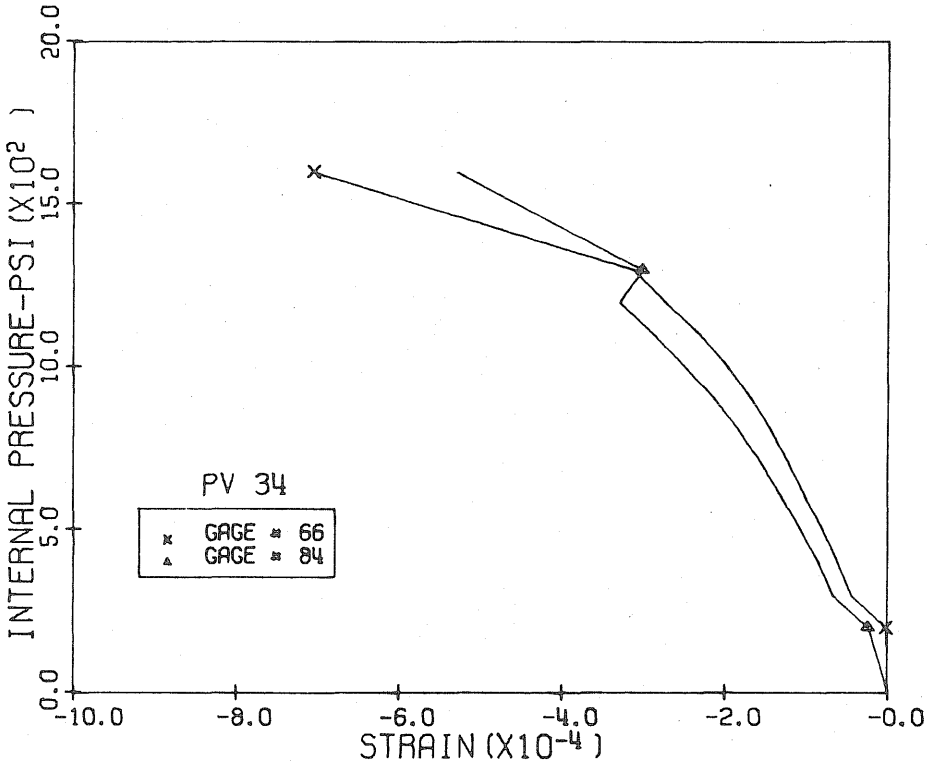

Fig. 3.87 Measured Tens. Diag. Strains, Level 1, Pen. 4 & 5, PV34

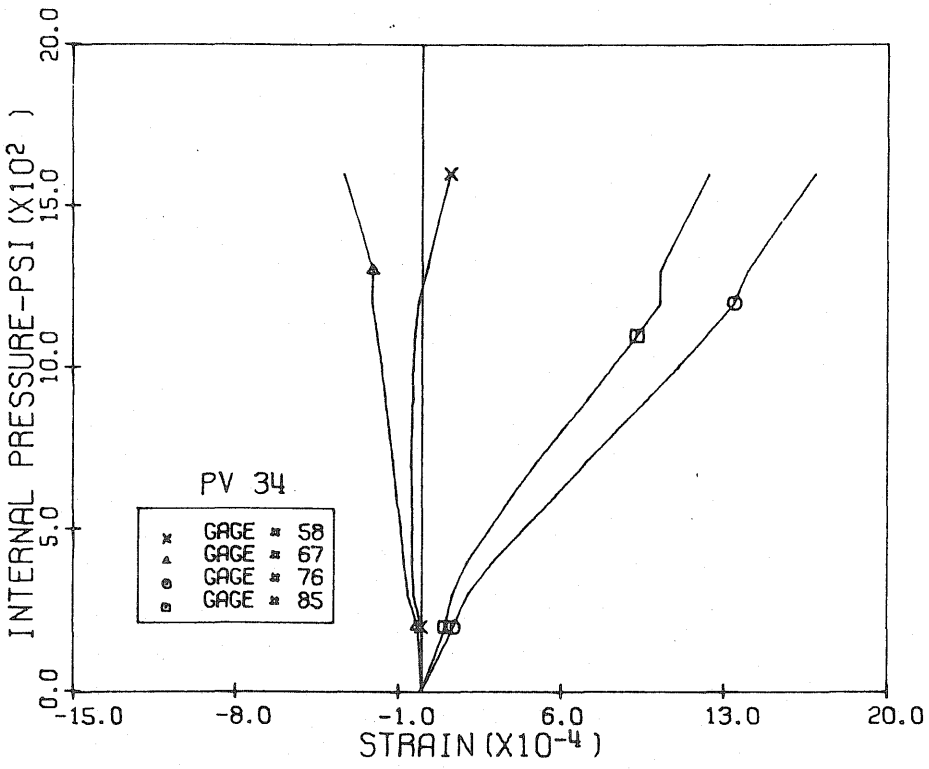

Fig. 3.88 Measured Vertical Strains, Level 2, Pen. 4 & 5, PV34

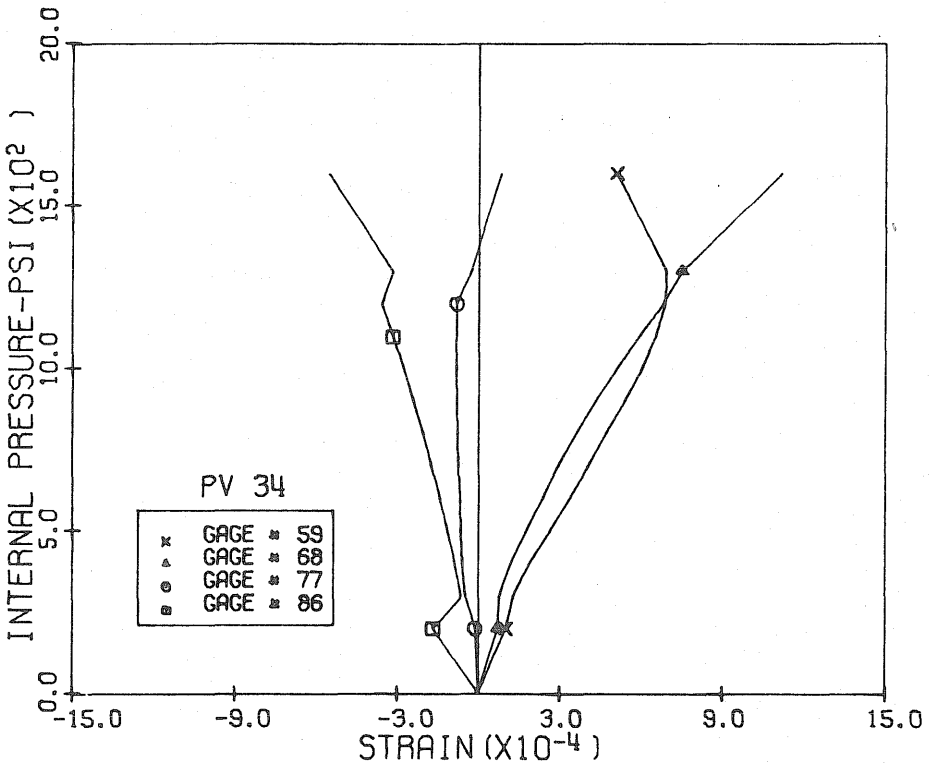

Fig. 3.89 Measured Horizontal Strains, Level 2, Pen. 4 & 5, PV34

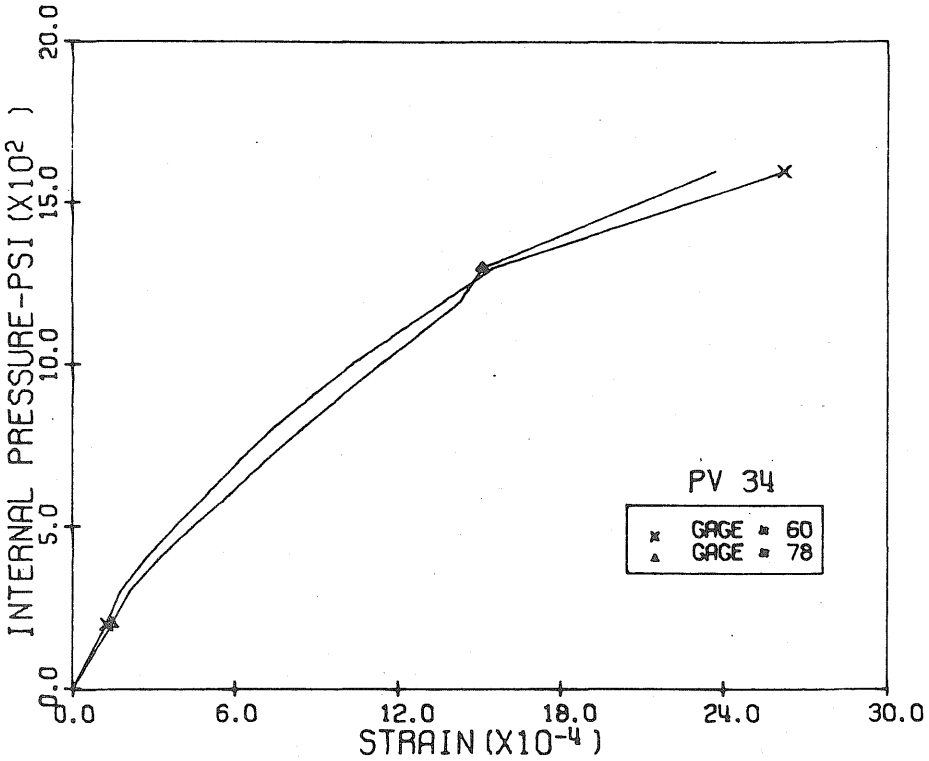

Fig. 3.90 Measured Comp. Diag. Strains, Level 2, Pen. 4 & 5, PV34

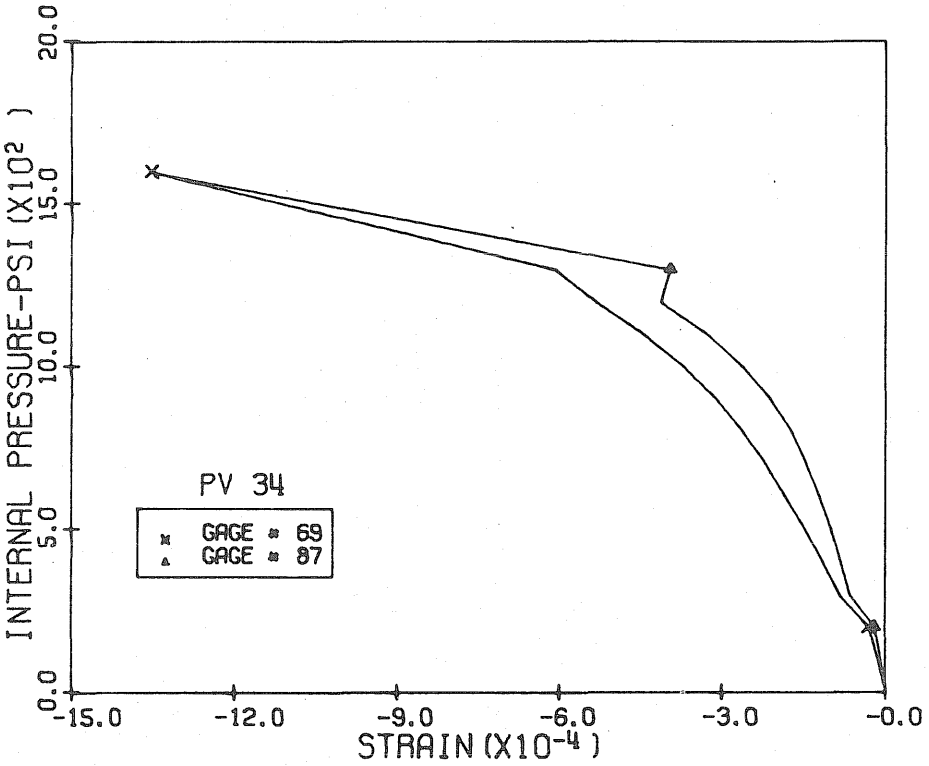

Fig. 3.91 Measured Tens. Diag. Strains, Level 2, Pen. 4 & 5, PV34

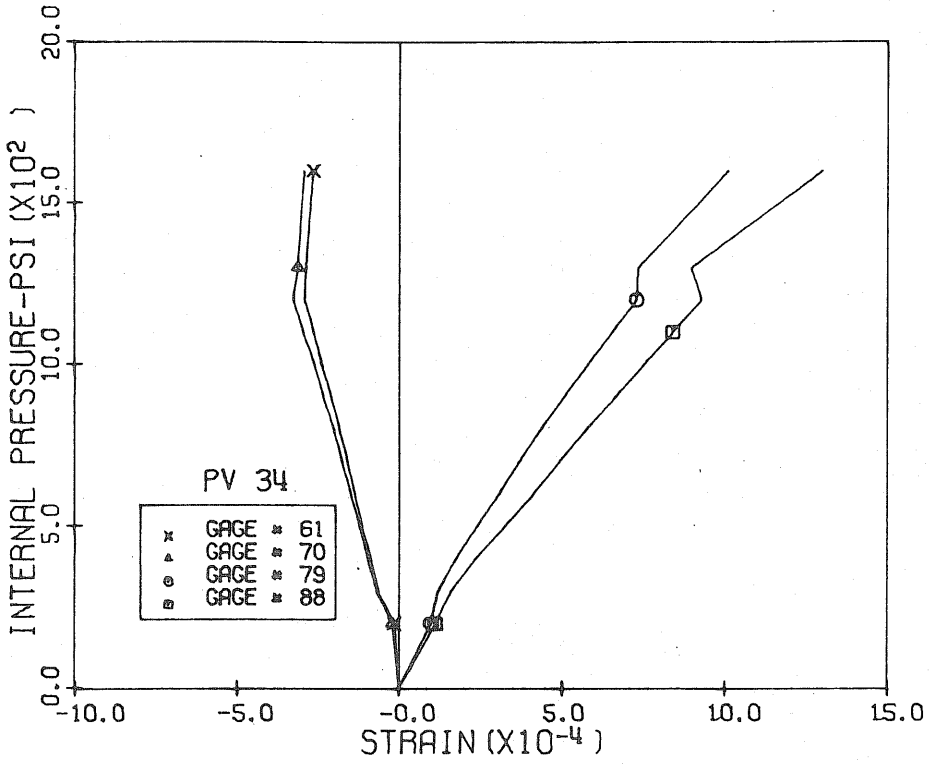

Fig. 3.92 Measured Vertical Strains, Level 3, Pen. 4 & 5, PV34

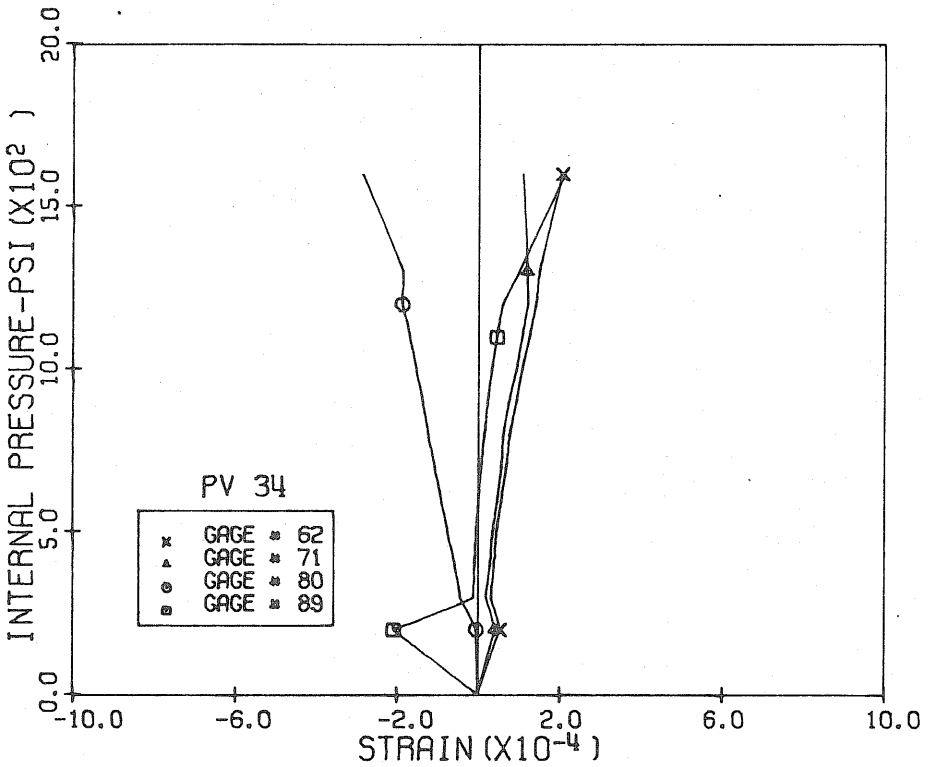

Fig. 3.93 Measured Horizontal Strains, Level 3, Pen. 4 & 5, PV34

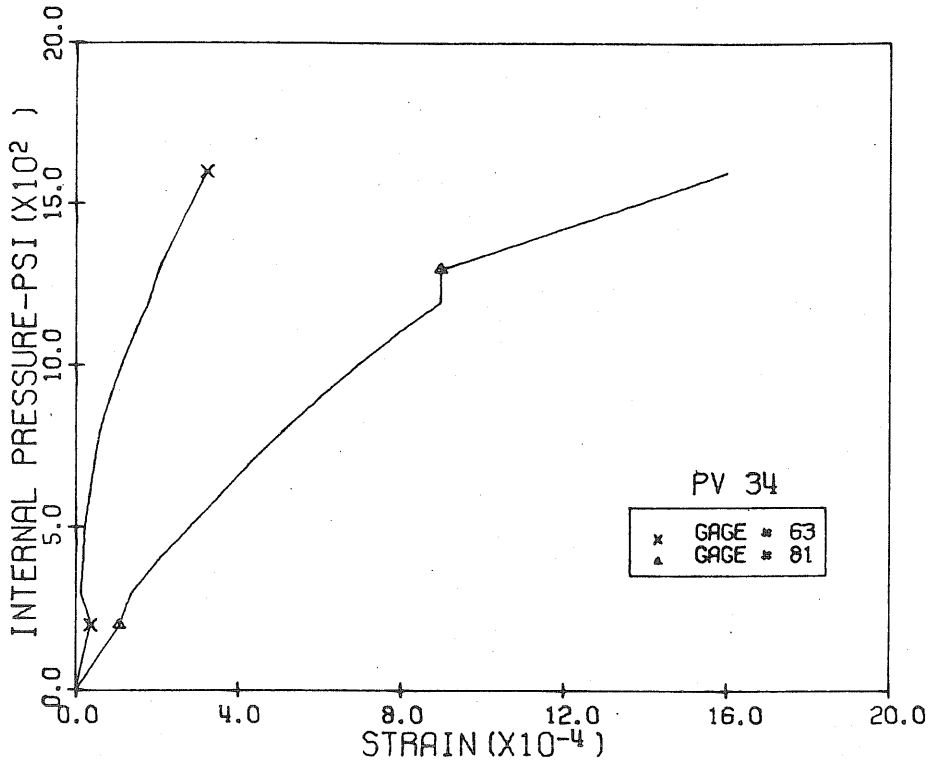

Fig. 3.94 Measured Comp. Diag. Strains, Level 3, Pen. 4 & 5, PV34

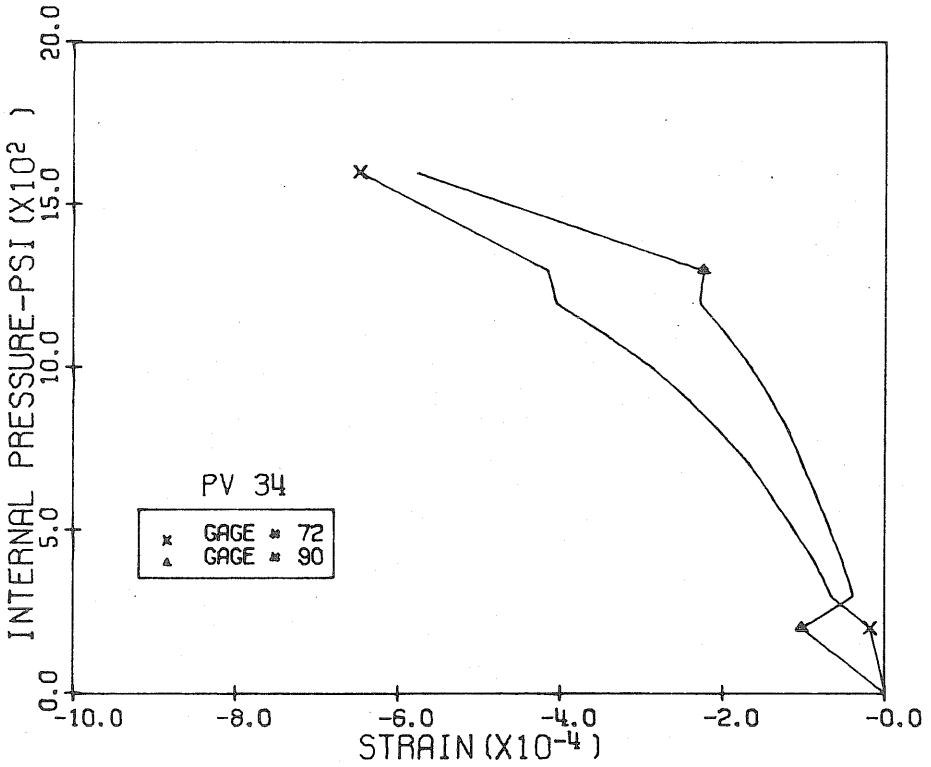

Fig. 3.95 Measured Tens. Diag. Strains, Level 3, Pen. 4 & 5, PV34

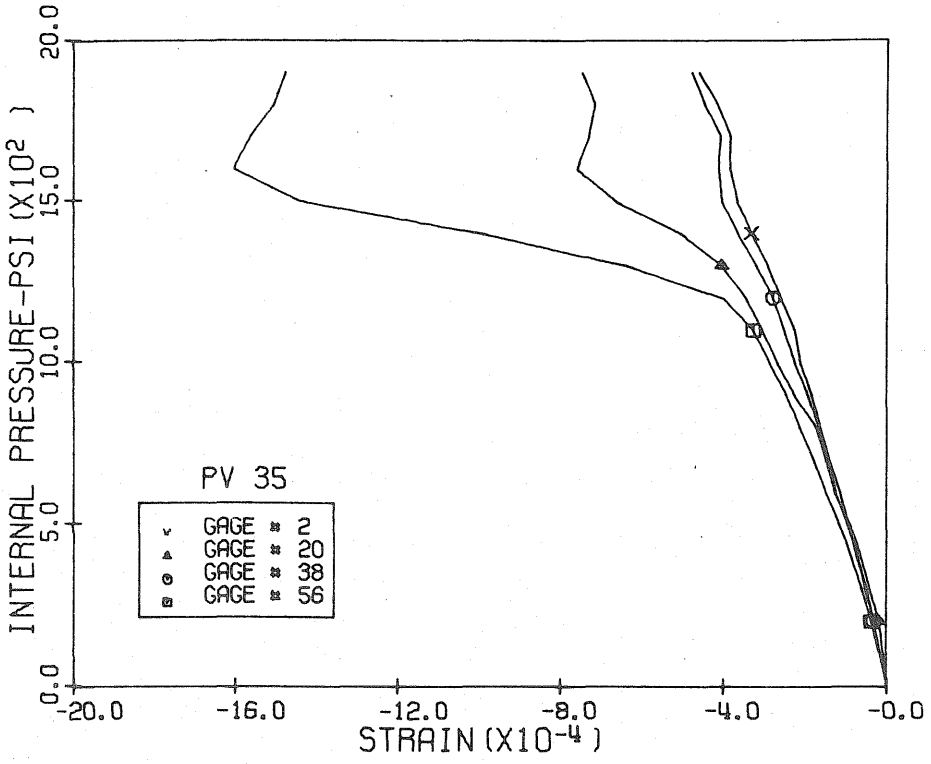

Fig. 3.96 Measured Horizontal Strains, Level 1, 12:00 & 6:00 Pos., PV35

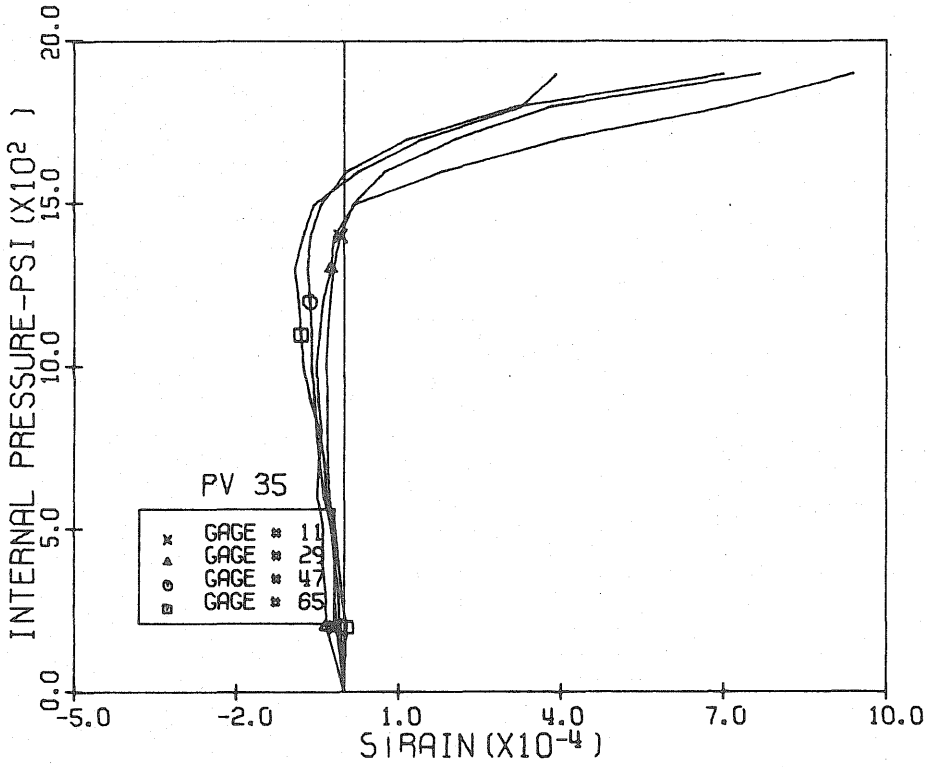

Fig. 3.97 Measured Horizontal Strains, Level 1, 3:00 & 9:00 Pos., PV35

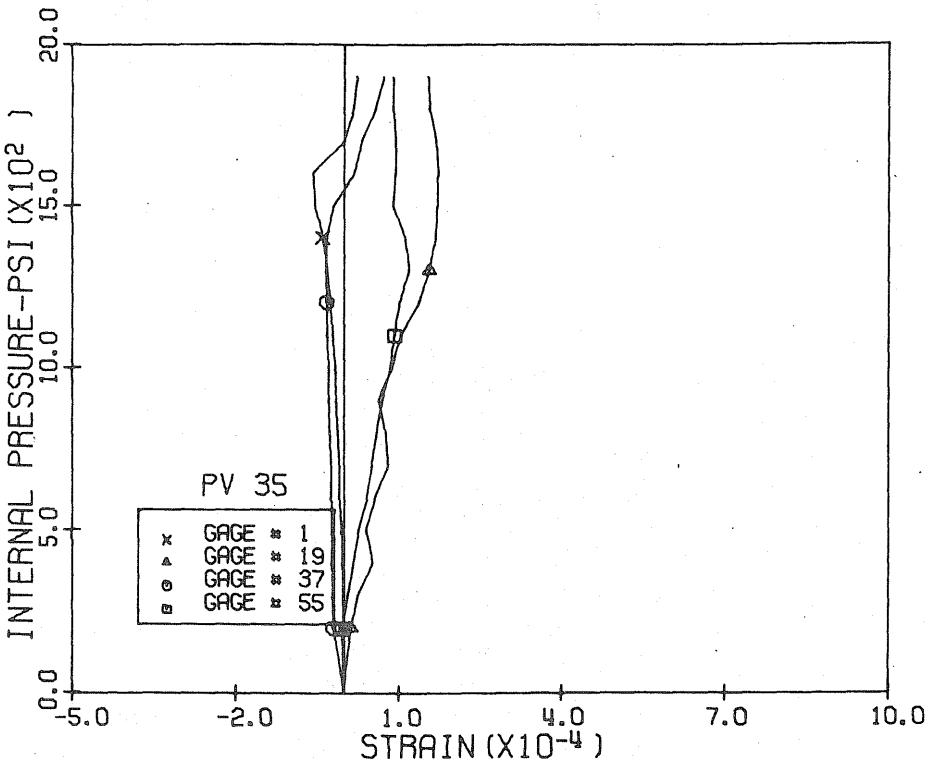

Fig. 3.98 Measured Vertical Strains, Level 1, 12:00 & 6:00 Pos., PV35

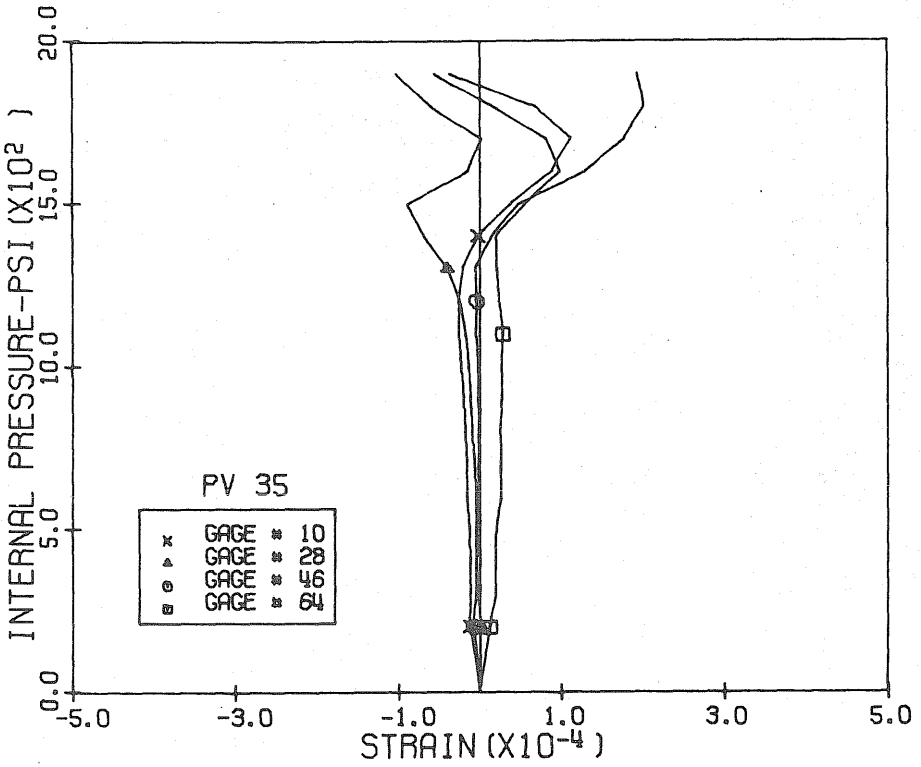

Fig. 3.99 Measured Vertical Strains, Level 1, 3:00 & 9:00 Pos., PV35

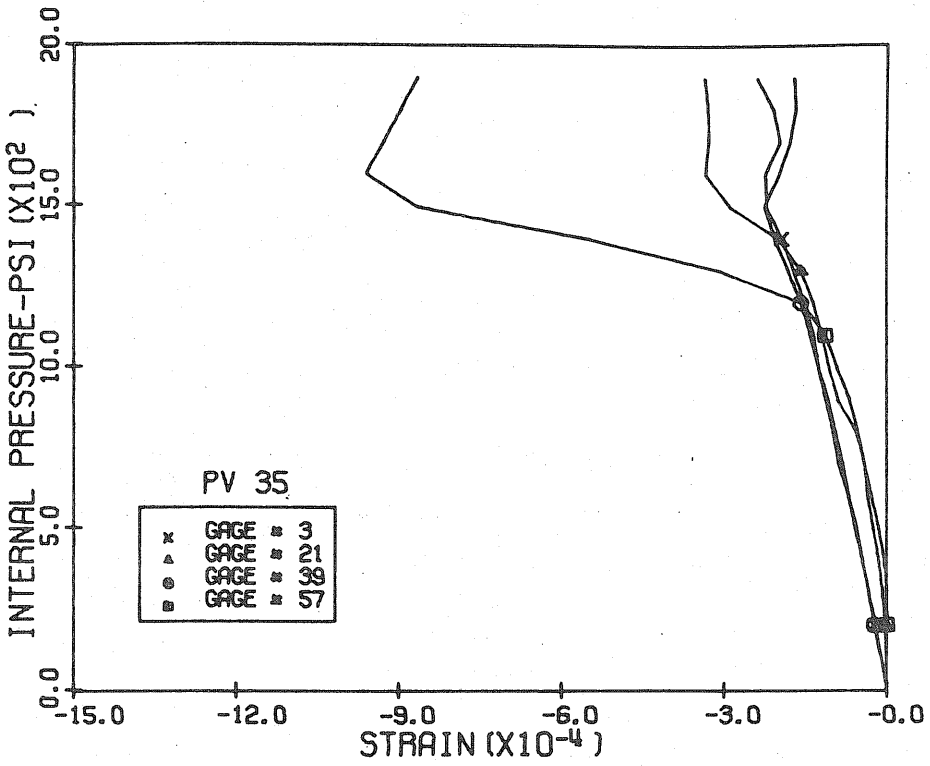

Fig. 3.100 Measured Tens. Diag. Strains, Level 1, 12:00 & 6:00 Pos., PV35

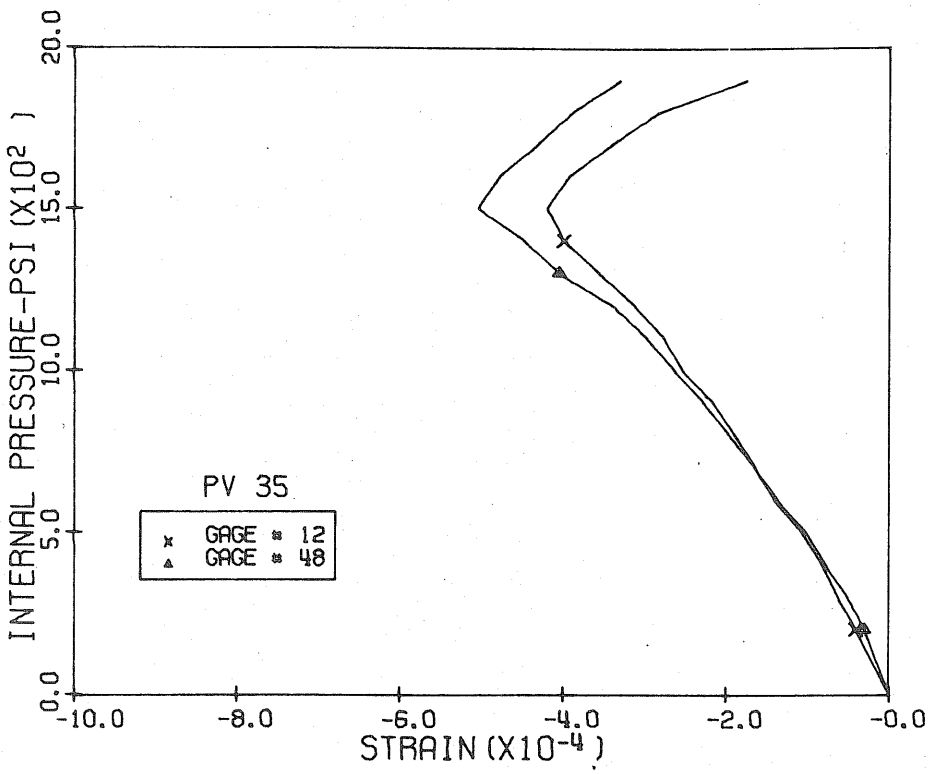

Fig. 3.101 Measured Diagonal Strains, Level 1, 3:00 Pos., PV35

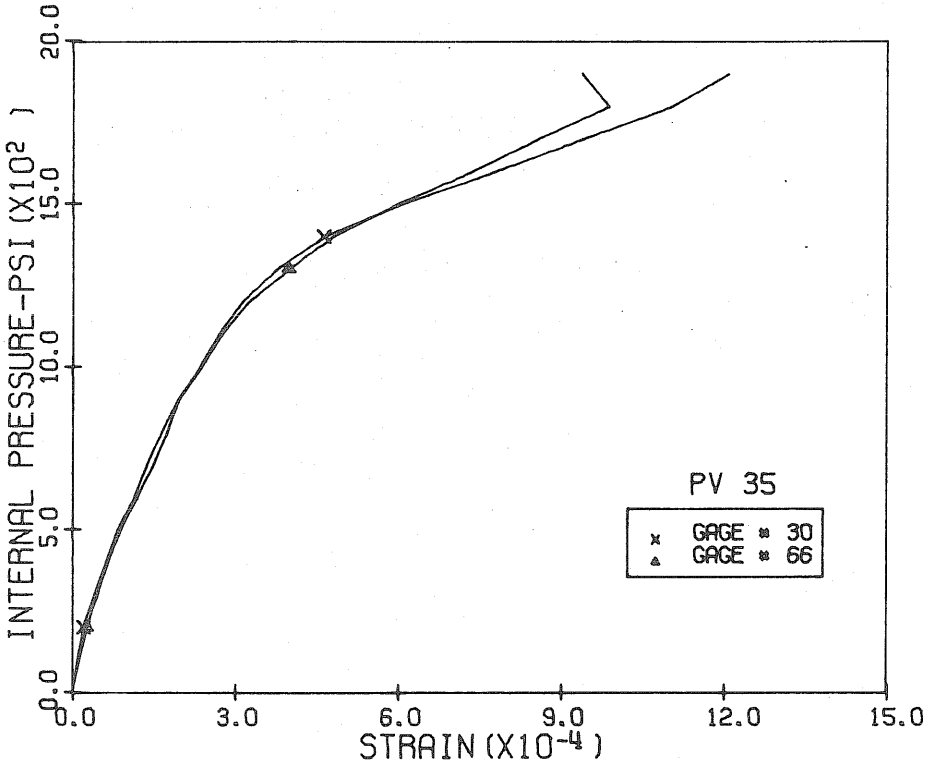

Fig. 3.102 Measured Tens. Diag. Strains, Level 1, 9:00 Pos., PV35

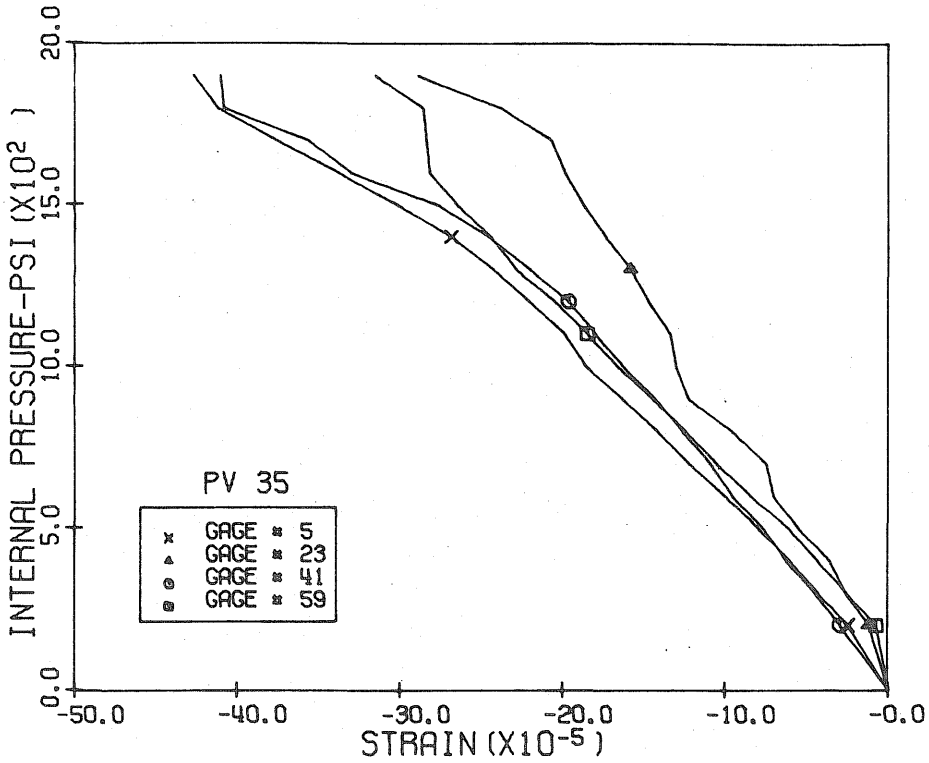

Fig. 3.103 Measured Horizontal Strains, Level 2, 12:00 & 6:00 Pos., PV35

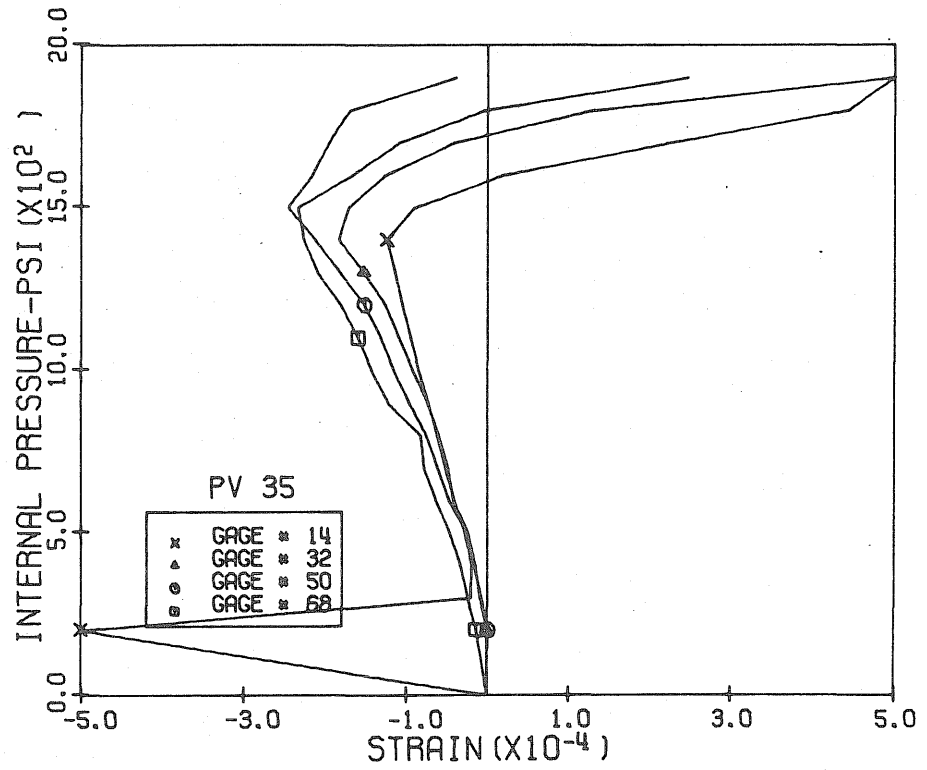

Fig. 3.104 Measured Horizontal Strains, Level 2, 3:00 & 9:00 Pos., PV35

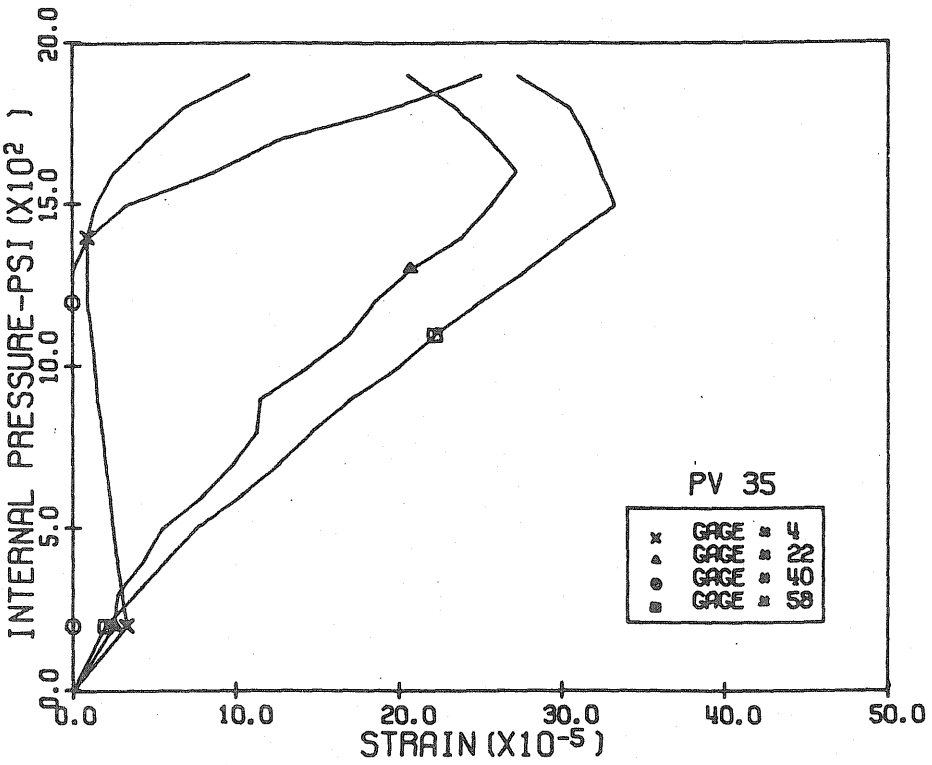

Fig. 3.105 Measured Vertical Strains, Level 2, 12:00 & 6:00 Pos., PV35

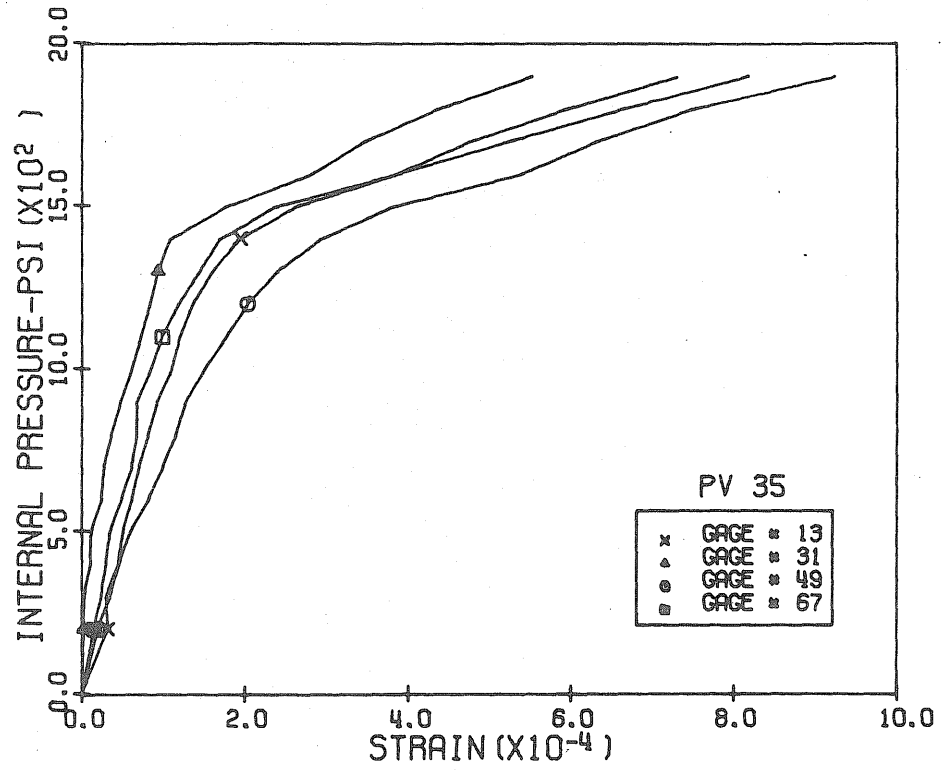

Fig. 3.106 Measured Vertical Strains, Level 2, 3:00 & 9:00 Pos., PV35

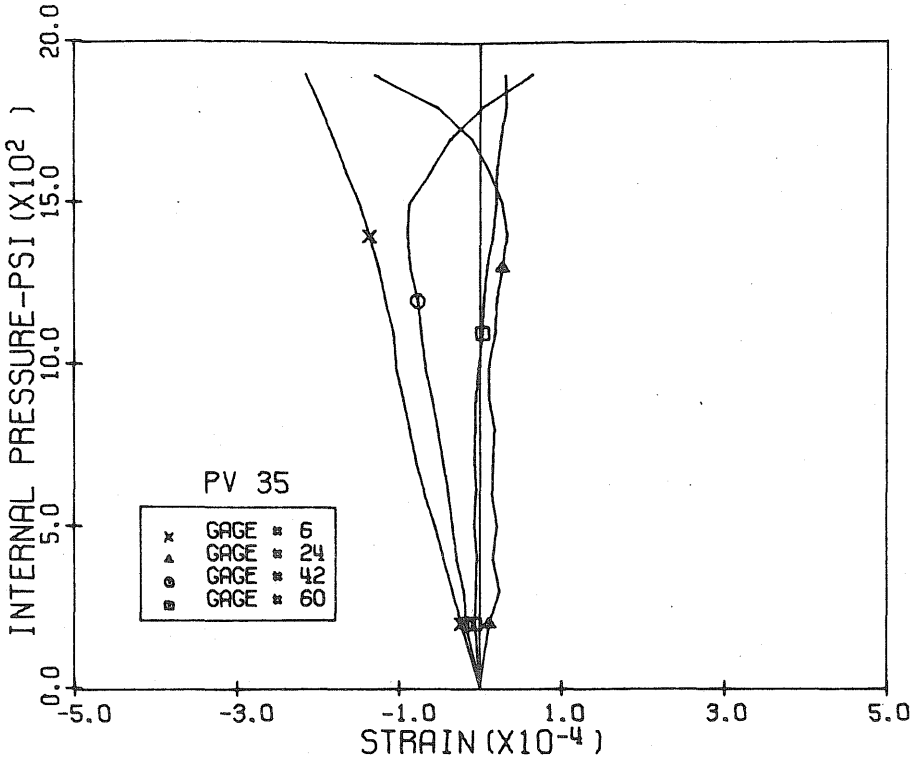

Fig. 3.107 Measured Diagonal Strains, Level 2, 12:00 & 6:00 Pos., PV35

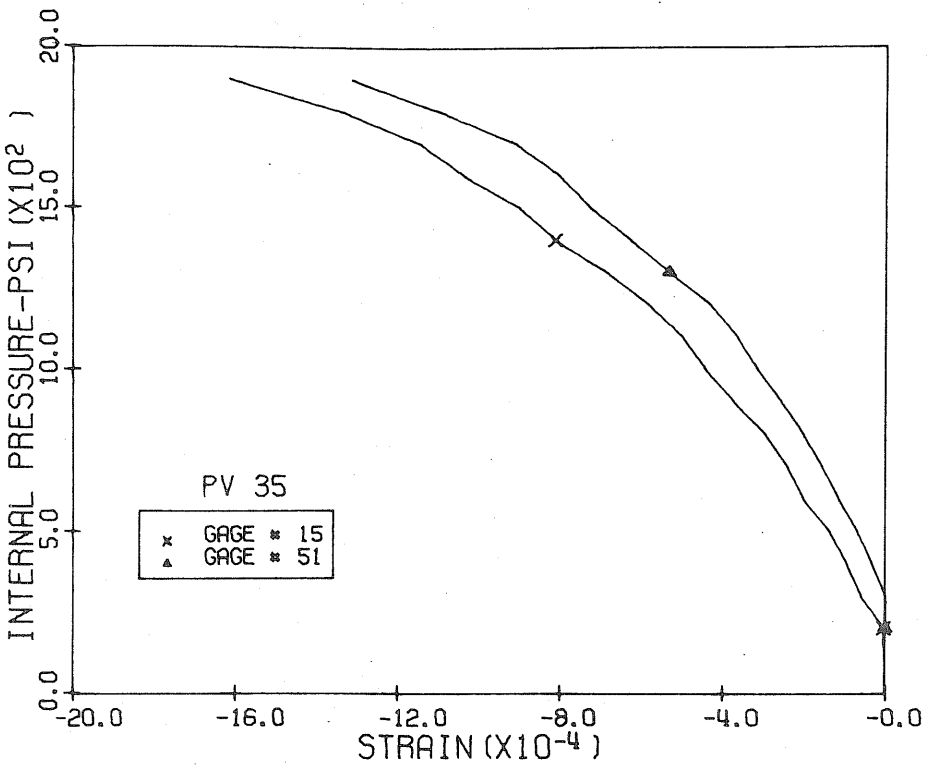

Fig. 3.108 Measured Tens. Diag. Strains, Level 2, 3:00 Pos., PV35

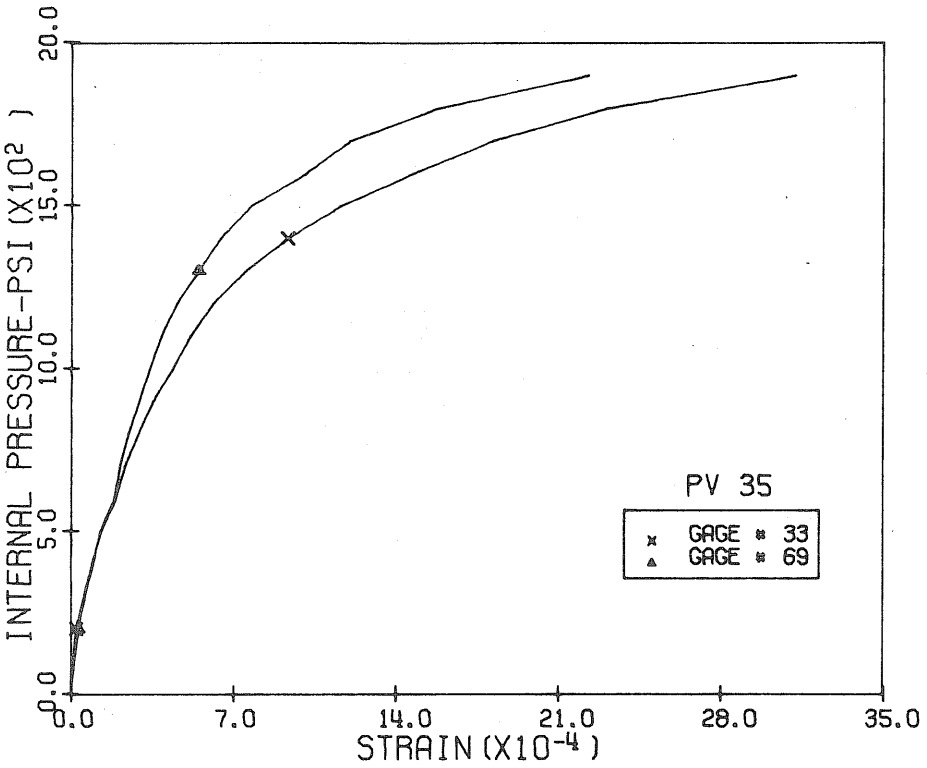

Fig. 3.109 Measured Comp. Diag. Strains, Level 2, 9:00 Pos., PV35

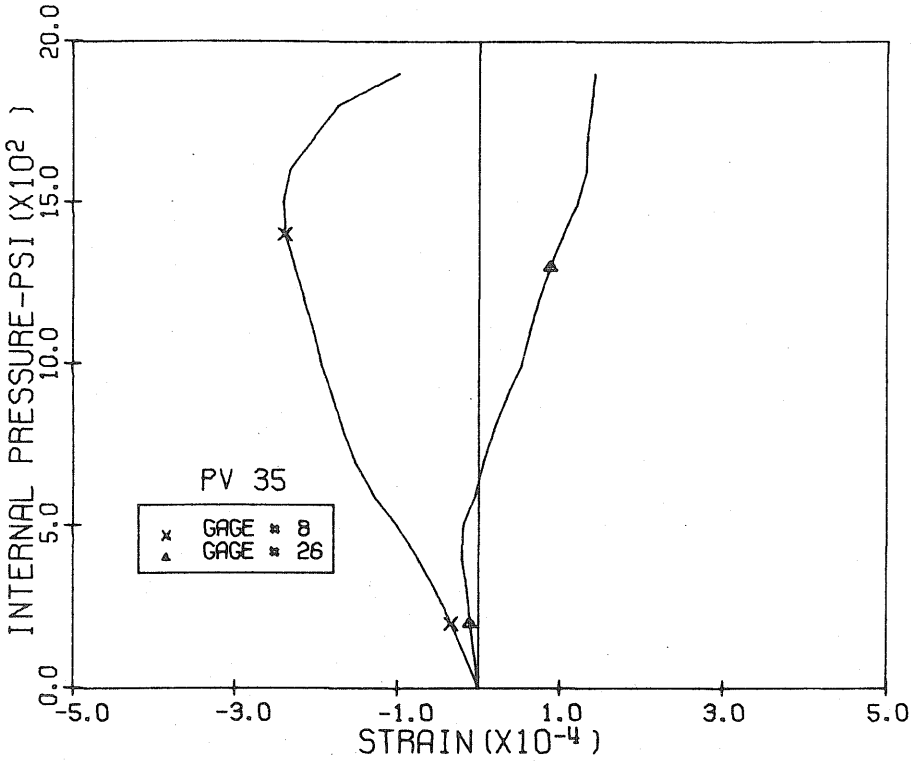

Fig. 3.110 Measured Horizontal Strains, Level 3, 12:00 & 6:00 Pos., PV35

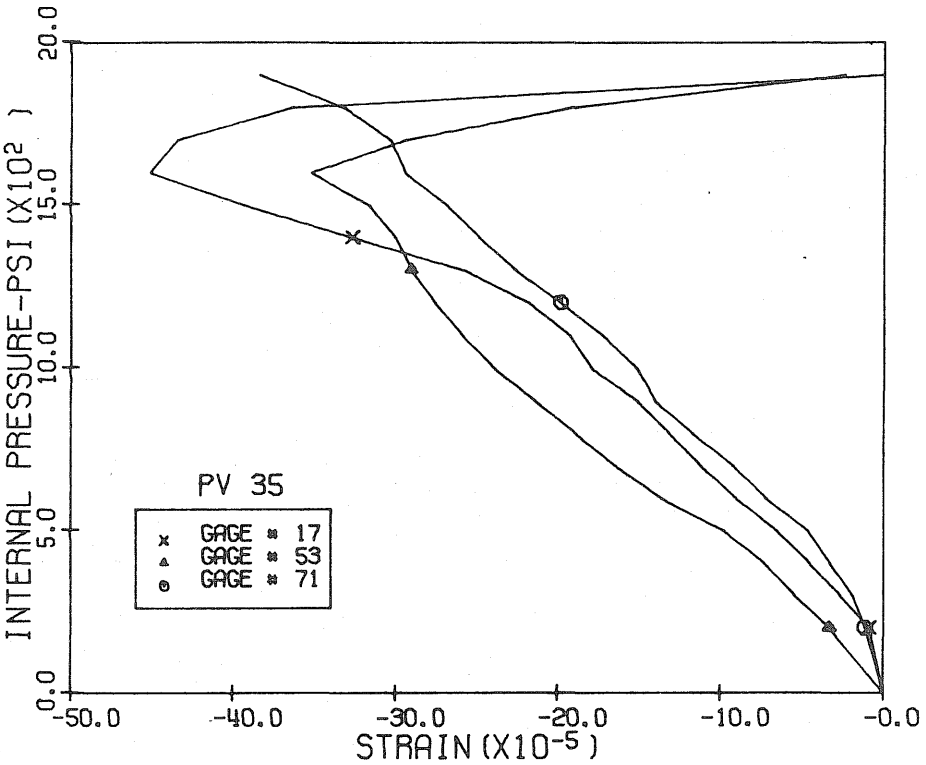

Fig. 3.111 Measured Horizontal Strains, Level 3, 3:00 & 9:00 Pos., PV35

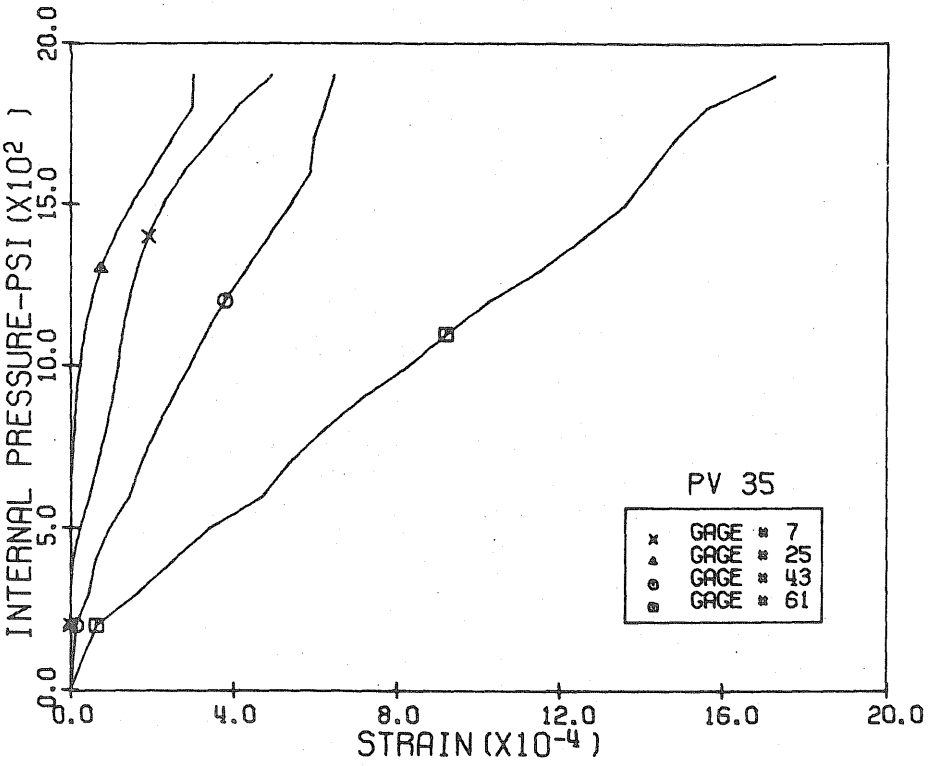

Fig. 3.112 Measured Vertical Strains, Level 3, 12:00 & 6:00 Pos., PV35

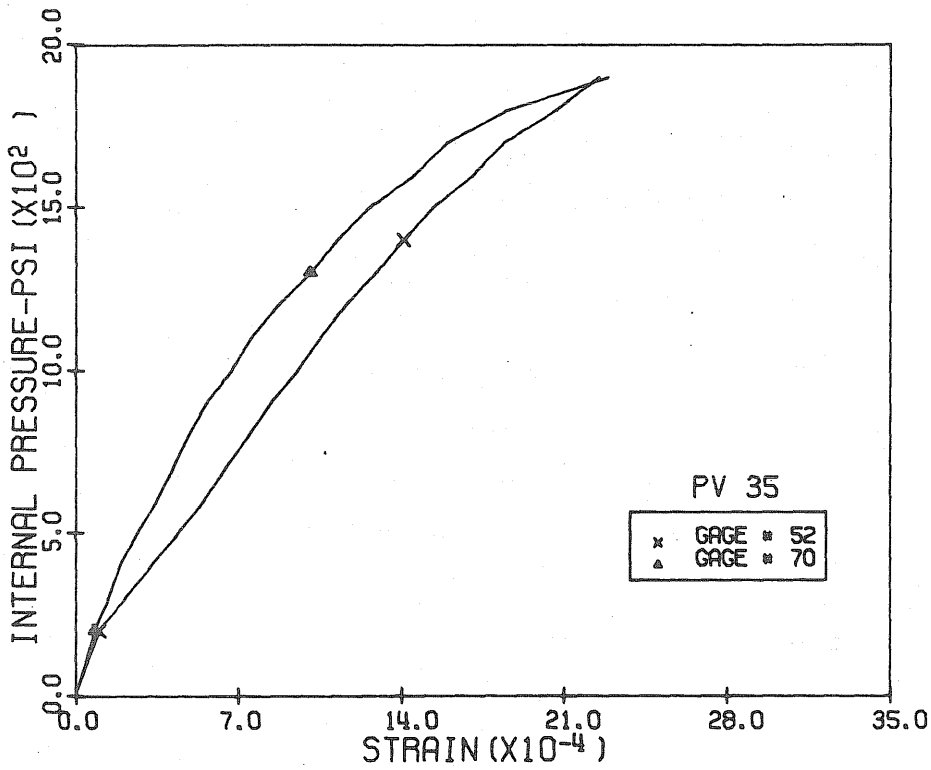

Fig. 3.113 Measured Vertical Strains, Level 3, 3:00 & 9:00 Pos., PV35

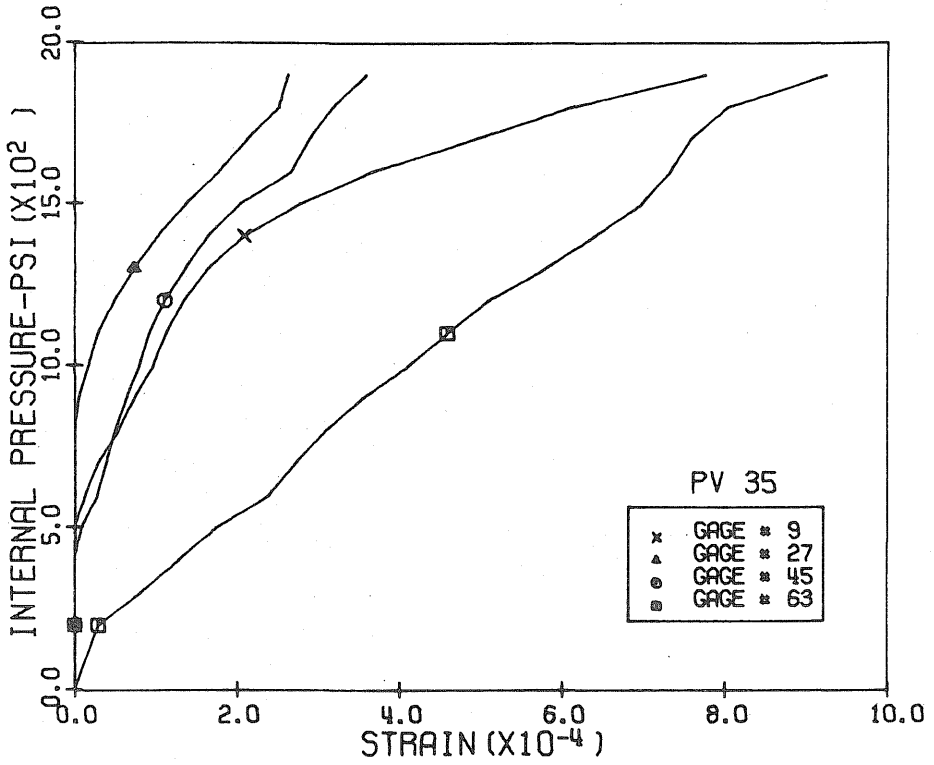

Fig. 3.114 Measured Diagonal Strains, Level 3, 12:00 & 6:00 Pos., PV35

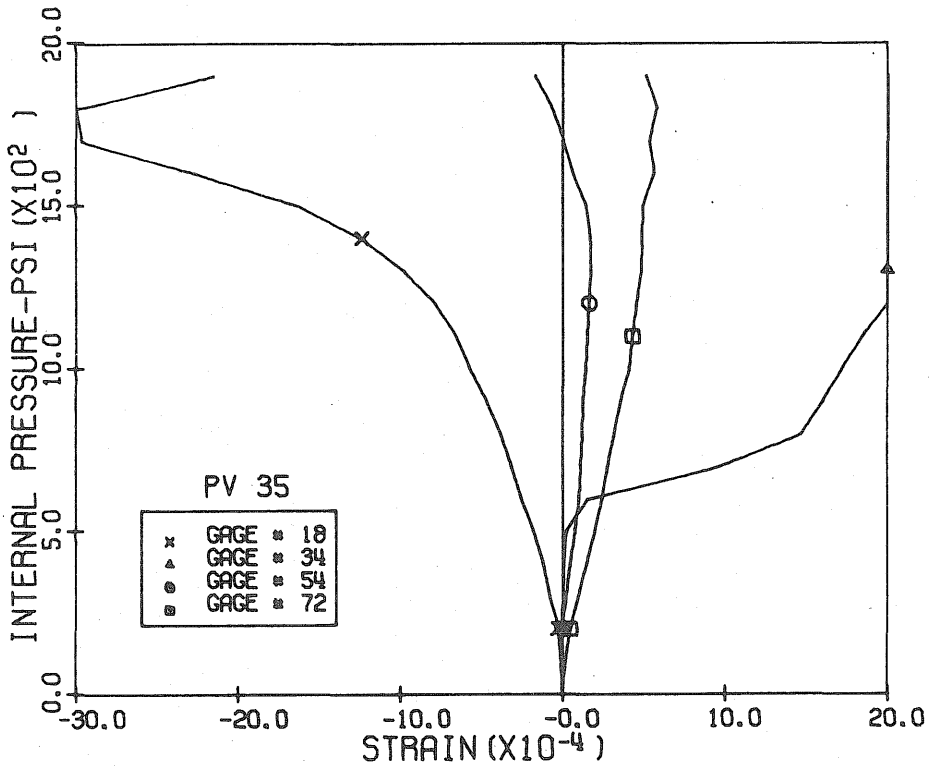

Fig. 3.115 Measured Diagonal Strains, Level 3, 3:00 & 9:00 Pos., PV35

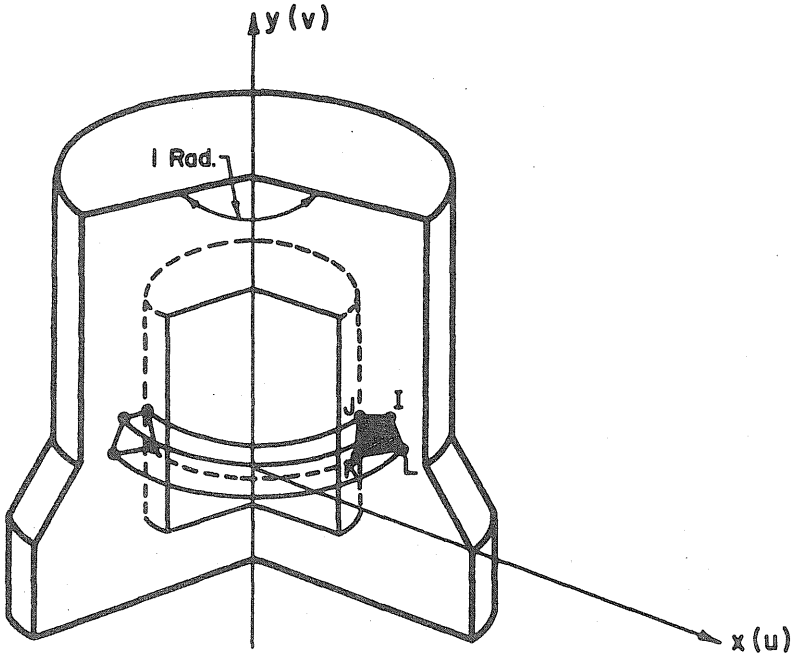

(a) Element of an Axisymmetric Solid

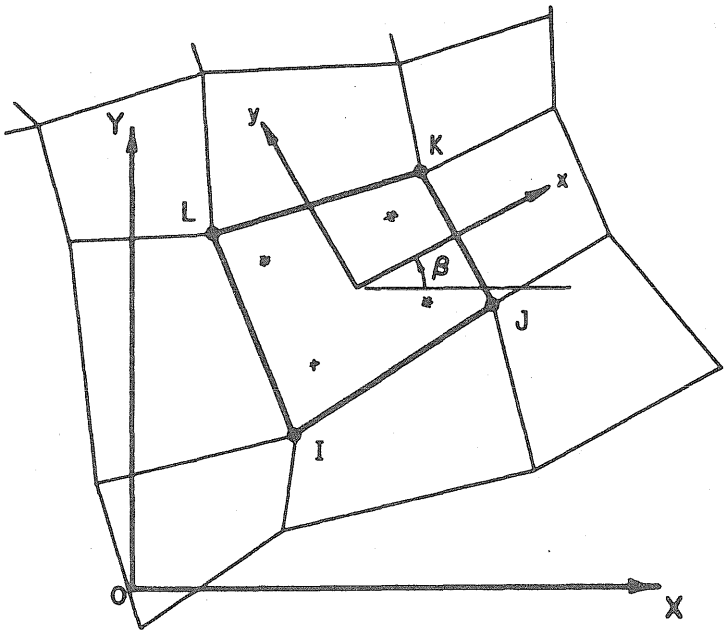

(b) Local and Global Coordinate Systems

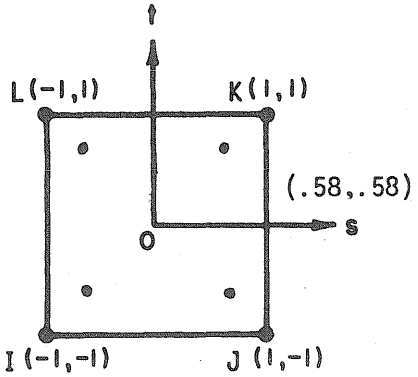

(c) Natural Coordinates of an Element and the Location of the Integration Points

Fig. 4.1 Graphical Representation of Axisymmetric Element

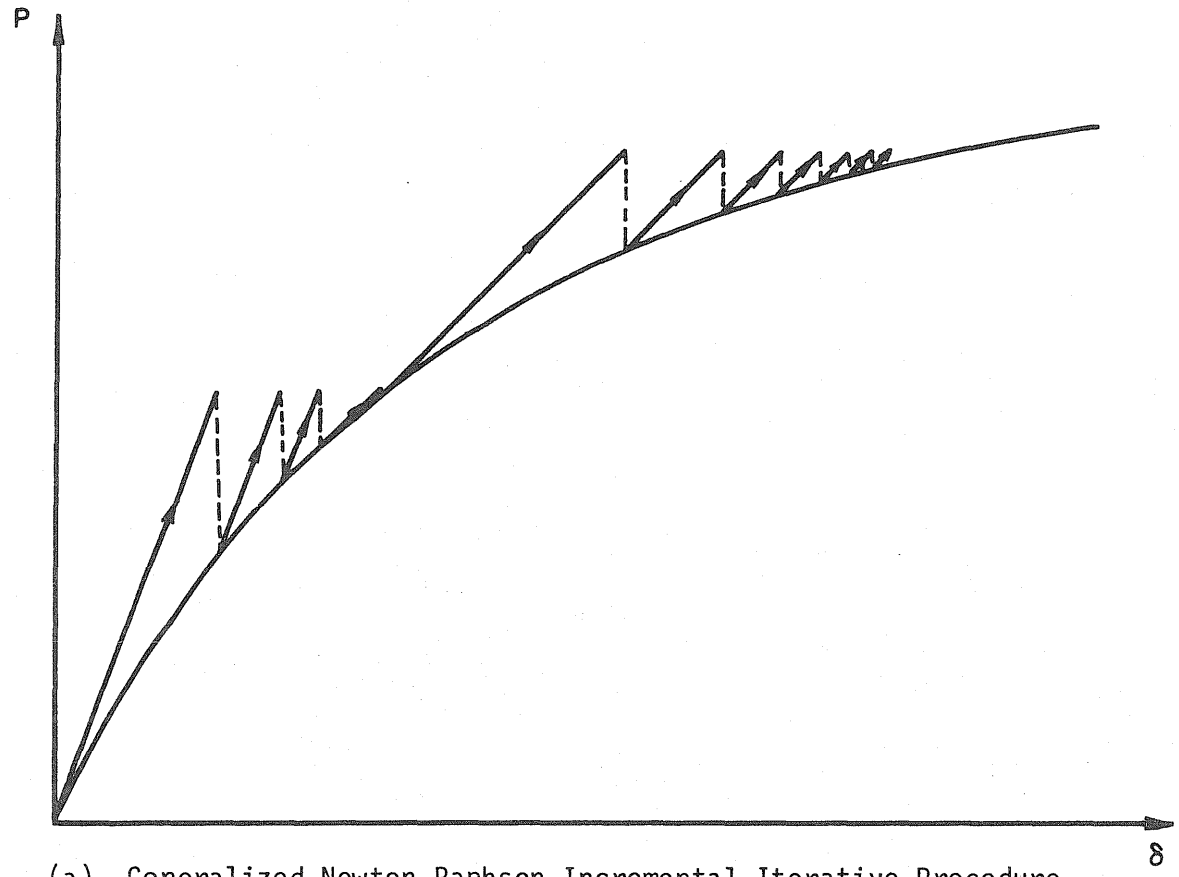

(a) Generalized Newton-Raphson Incremental-Iterative Procedure

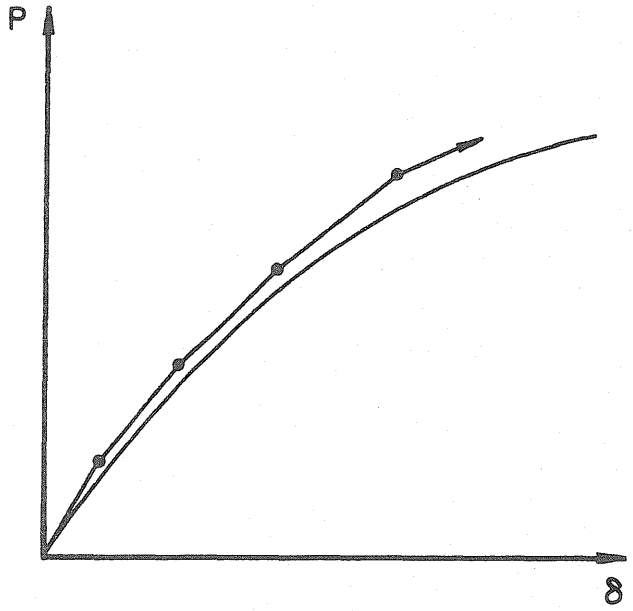

(b) Incremental Solution Procedure

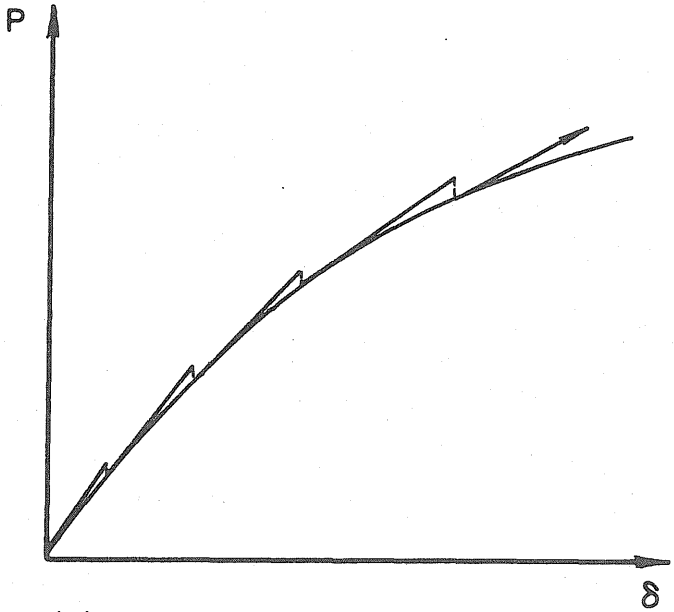

(c) Incremental Solution Procedure with Residual Load Corrections

Fig. 4.2 Incremental Solution Schemes

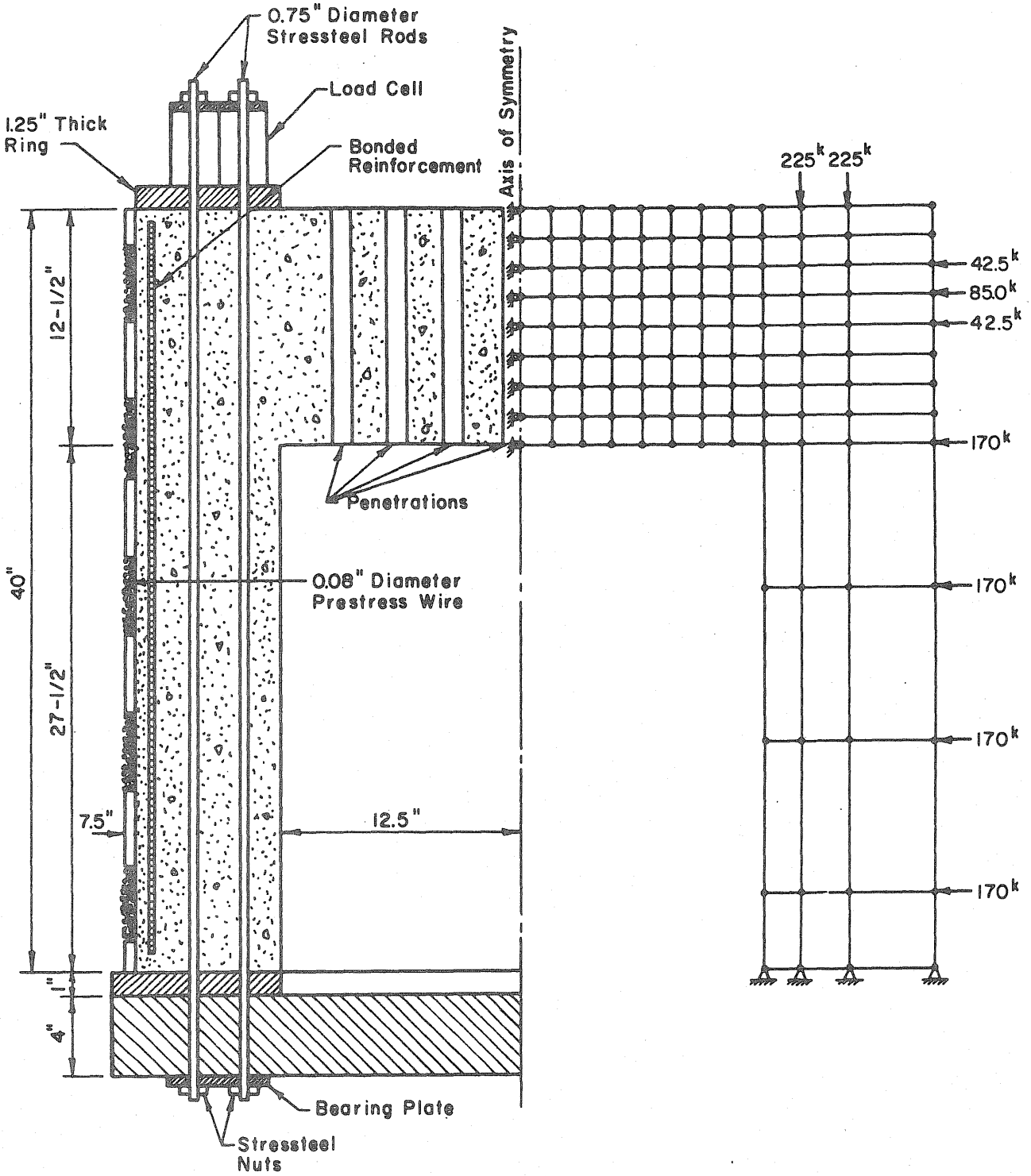

Fig. 5.1 Cross-section of PV30 and the Axisymmetric Finite Element Mesh Used in the Analysis

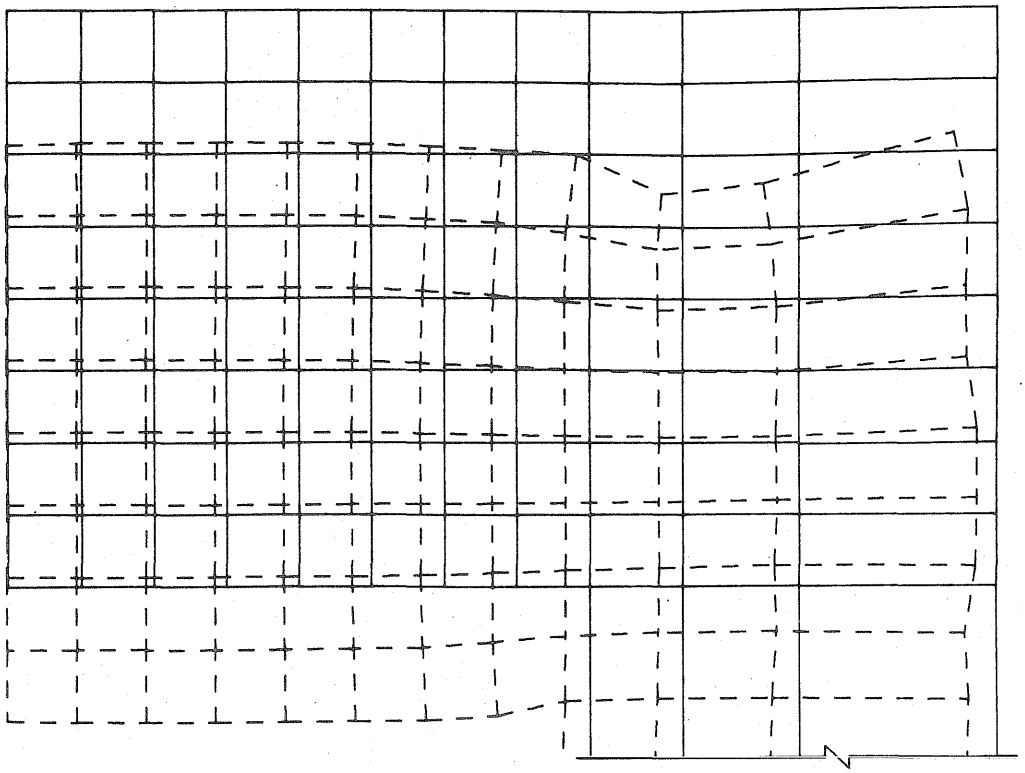

Fig. 5.2a Deflected Shape of End Slab
Under Prestressing Forces Only

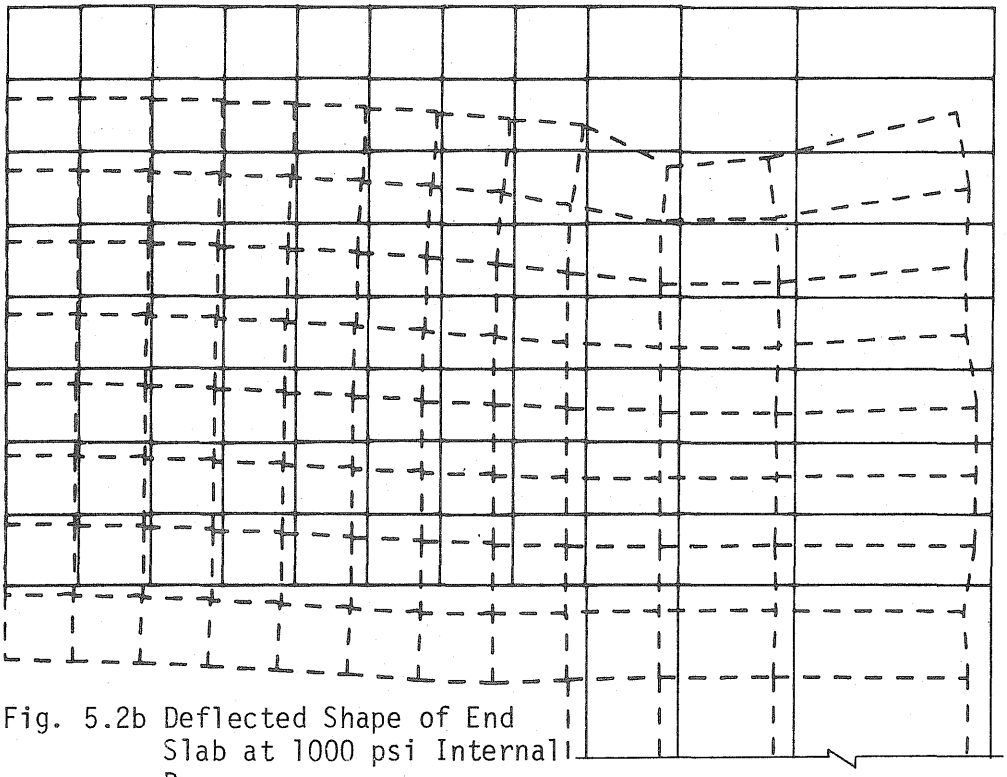

Fig. 5.2b Deflected Shape of End
Slab at 1000 psi Internal
Pressure

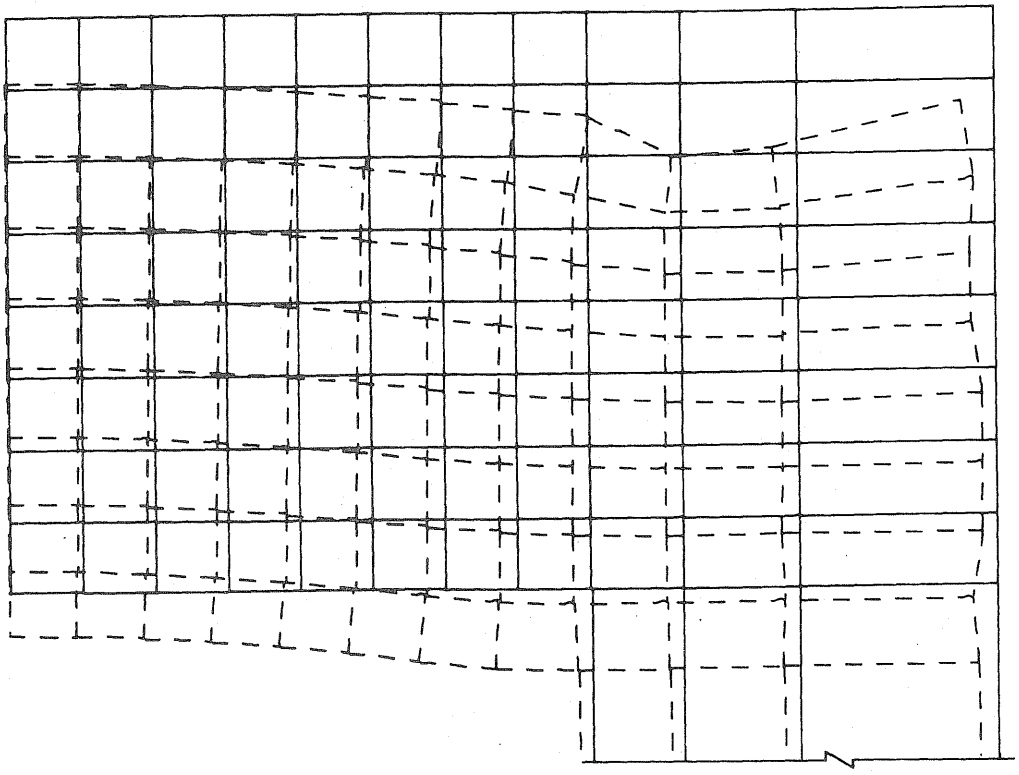

Fig. 5.2c Deflected Shape of End Slab at 1500 psi Internal Pressure

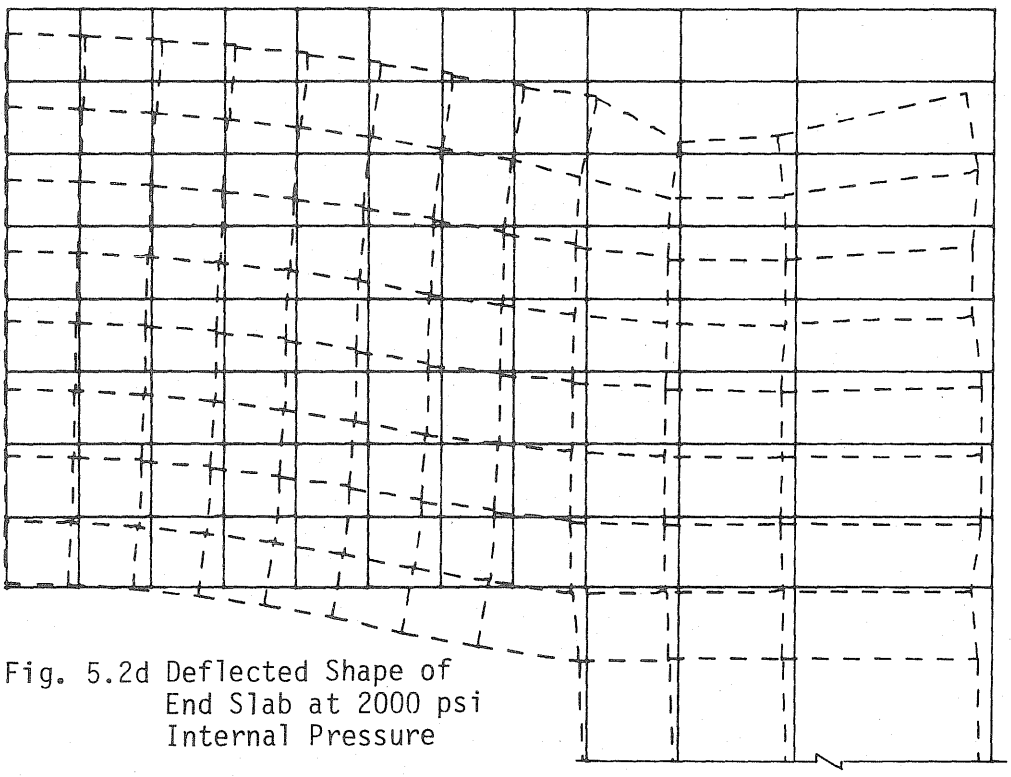

Fig. 5.2d Deflected Shape of End Slab at 2000 psi Internal Pressure

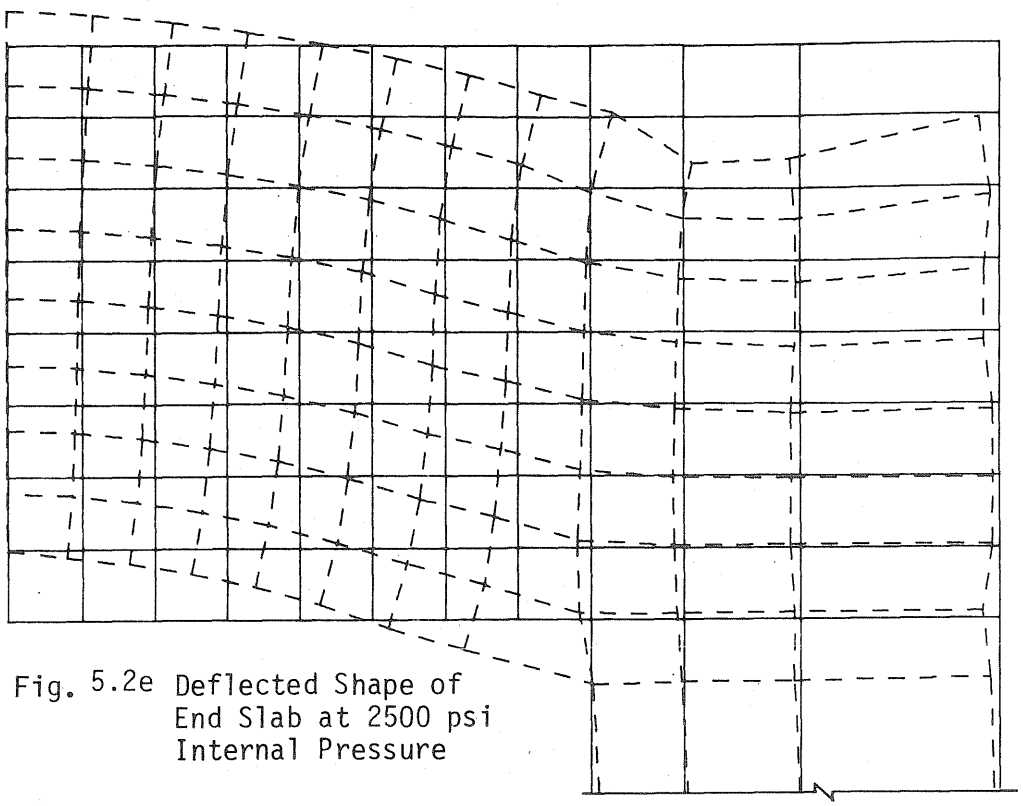

Fig. 5.2e Deflected Shape of End Slab at 2500 psi Internal Pressure

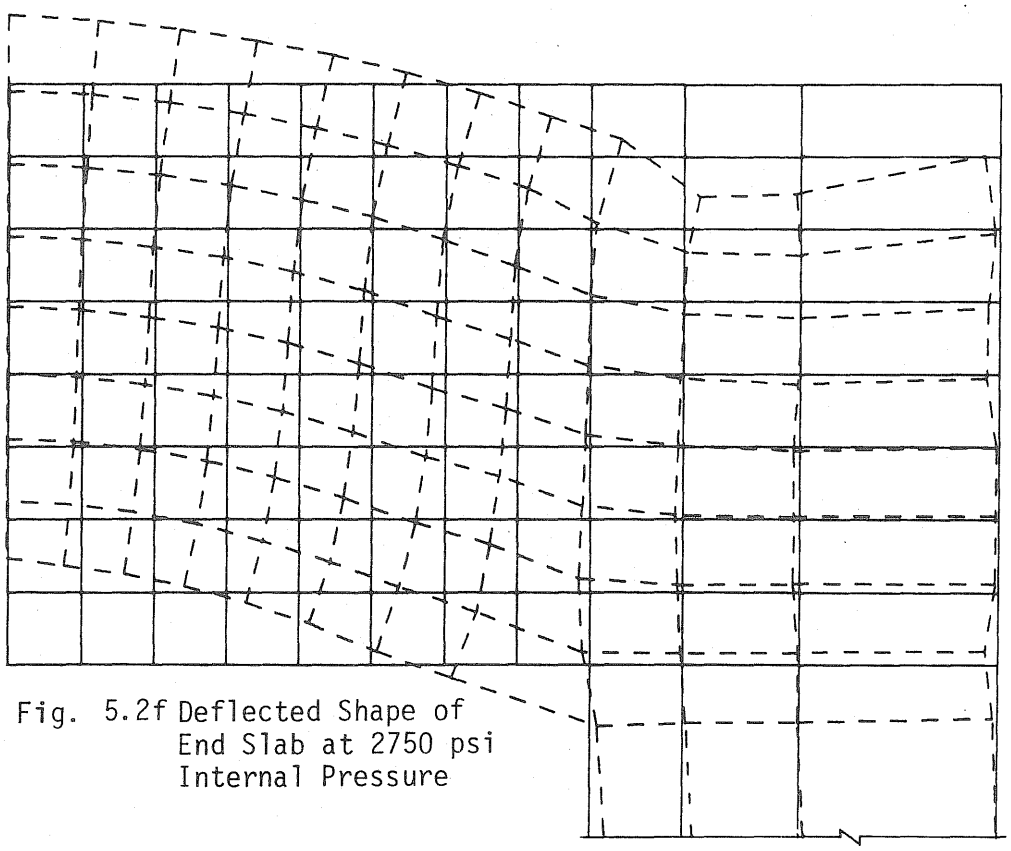

Fig. 5.2f Deflected Shape of End Slab at 2750 psi Internal Pressure

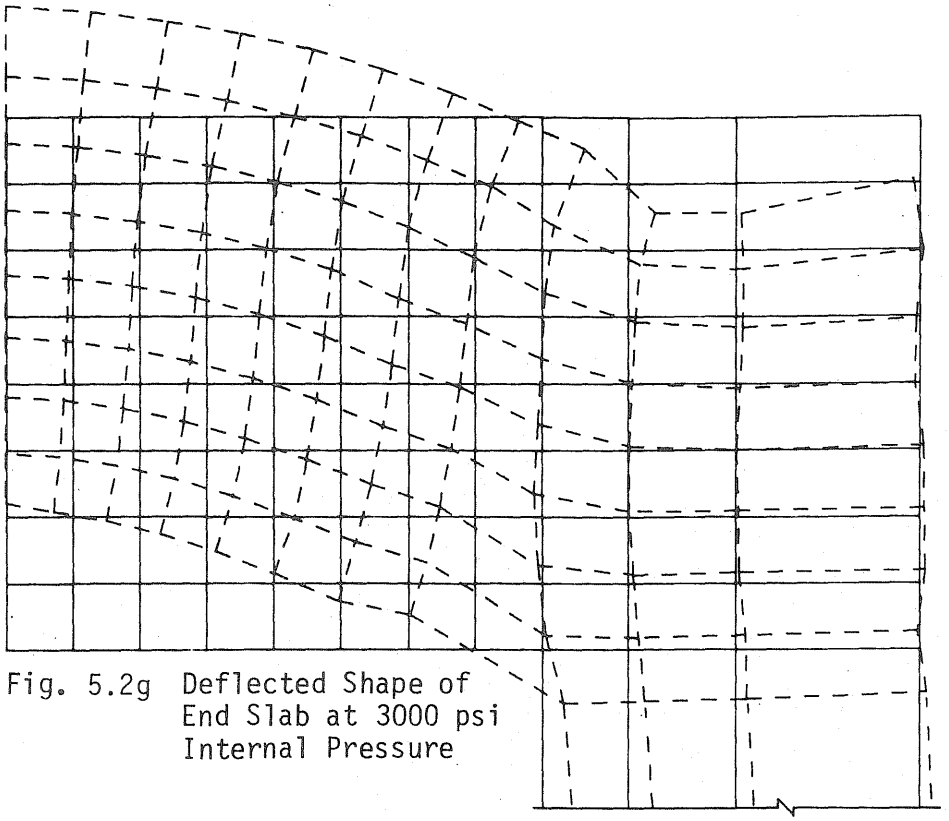

Fig. 5.2g Deflected Shape of End Slab at 3000 psi Internal Pressure

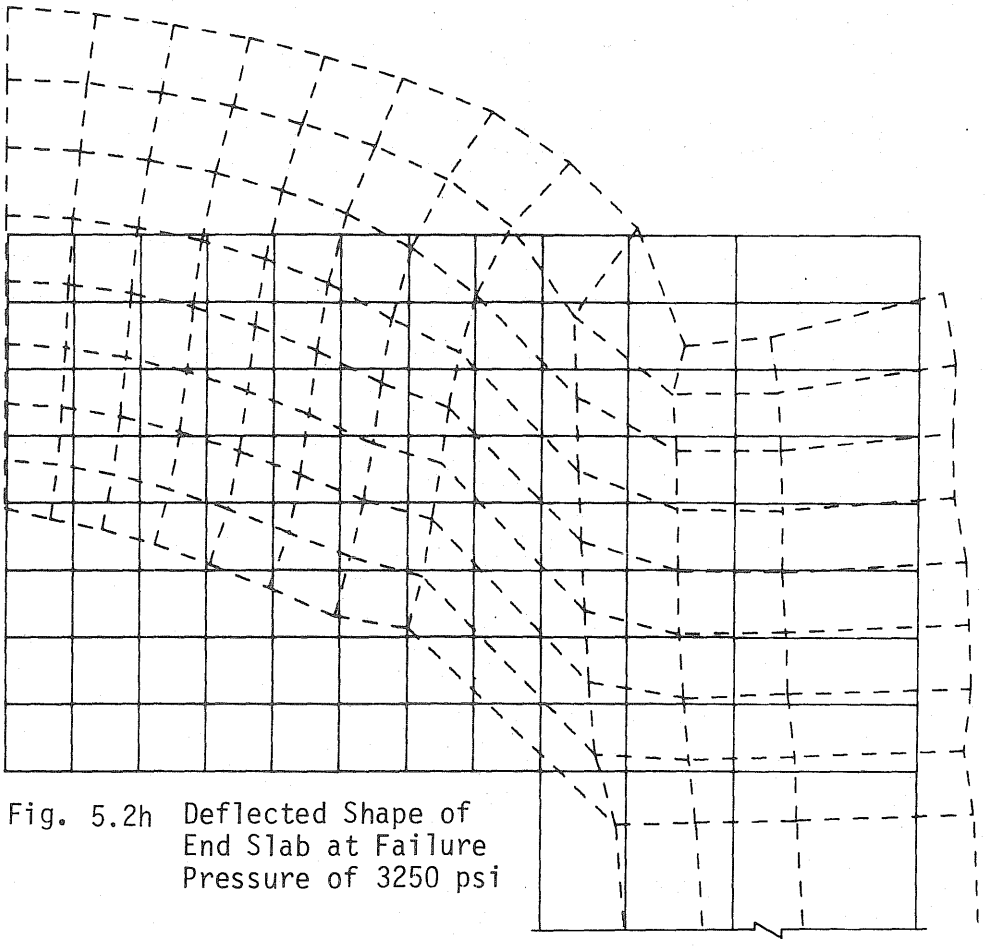

Fig. 5.2h Deflected Shape of End Slab at Failure Pressure of 3250 psi

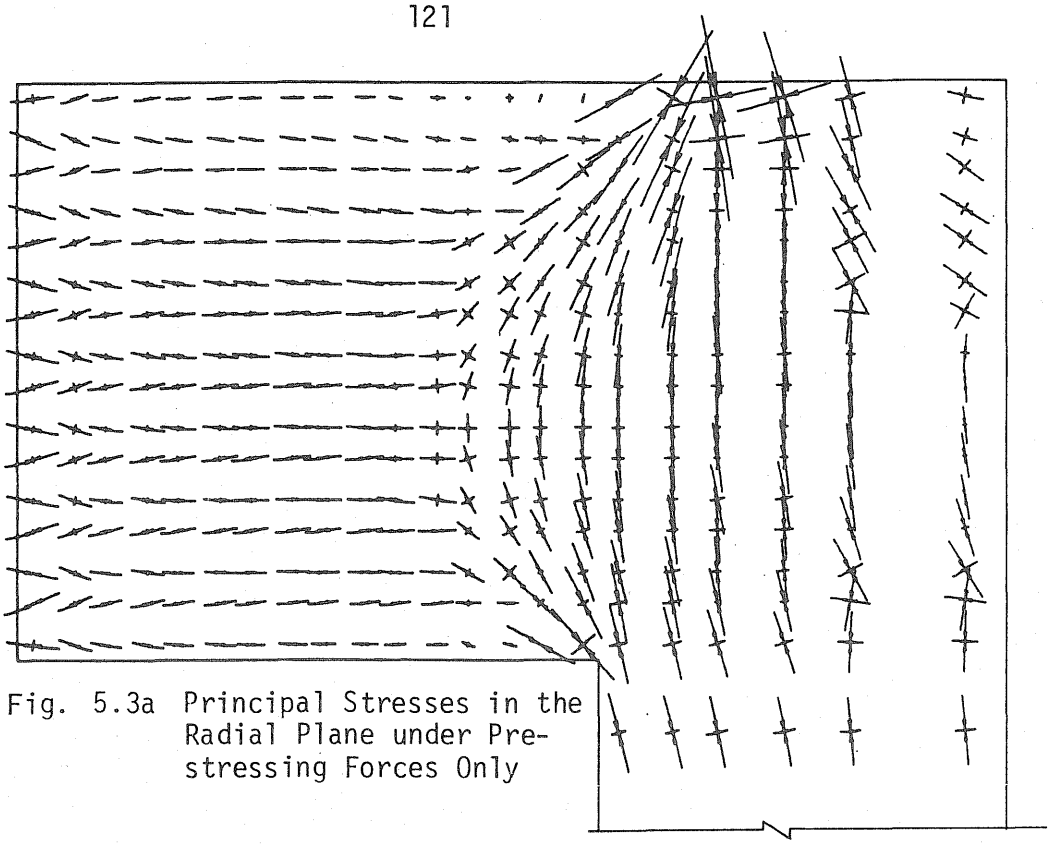

Fig. 5.3a Principal Stresses in the Radial Plane under Prestressing Forces Only

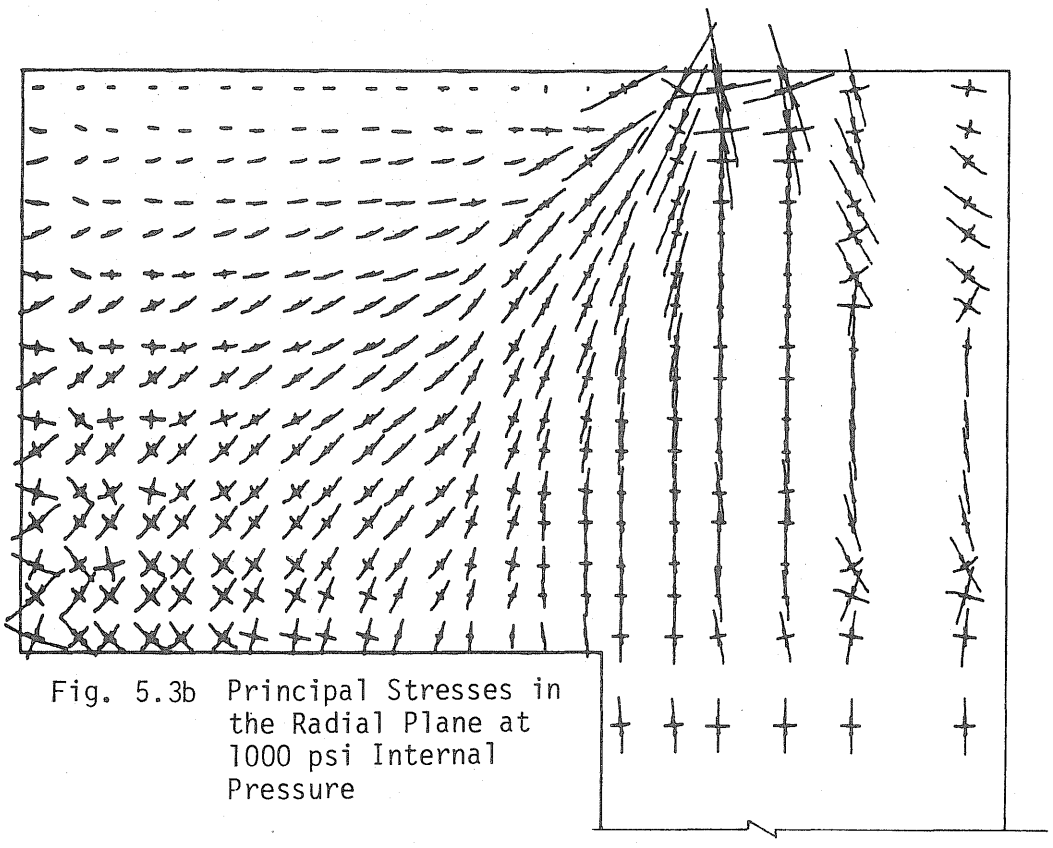

Fig. 5.3b Principal Stresses in the Radial Plane at 1000 psi Internal Pressure

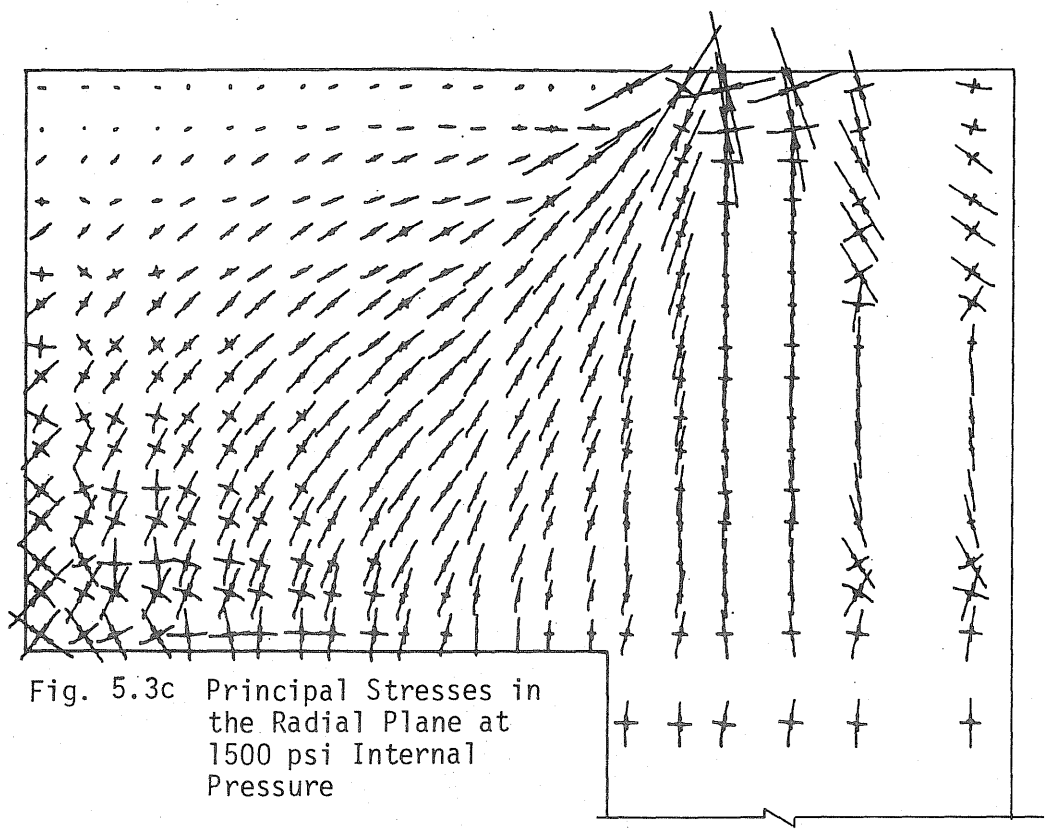

Fig. 5.3c Principal Stresses in the Radial Plane at 1500 psi Internal Pressure

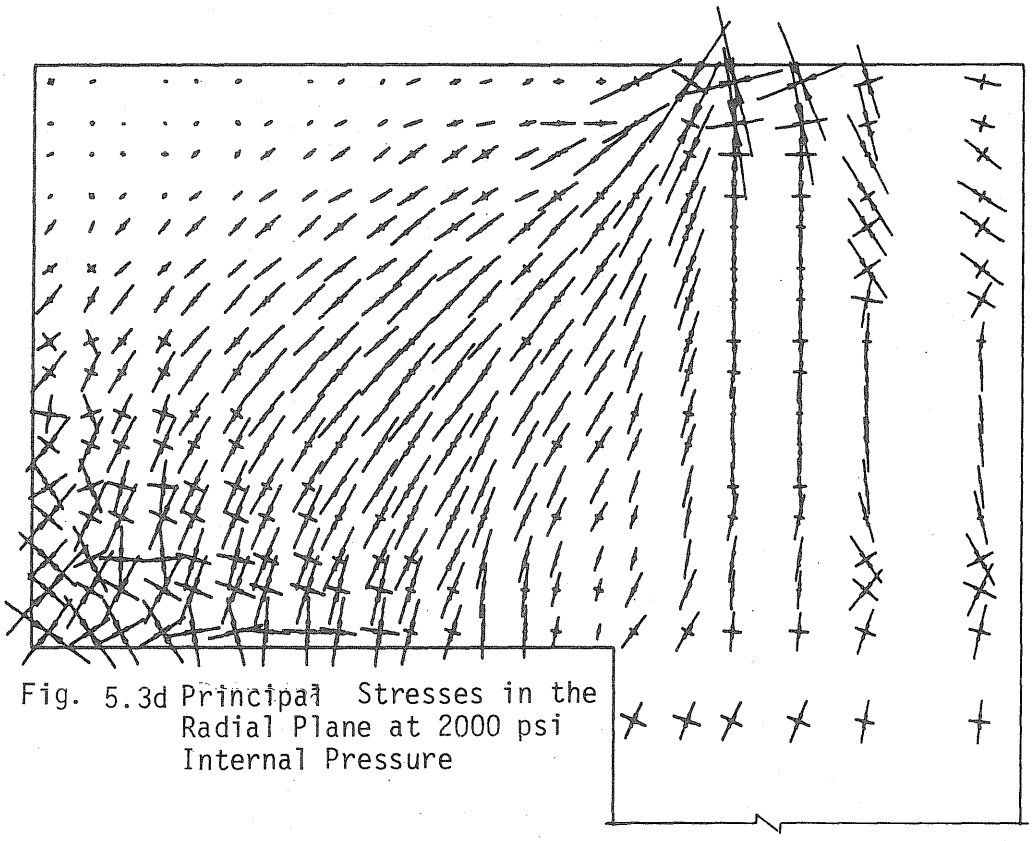

Fig. 5.3d Principal Stresses in the Radial Plane at 2000 psi Internal Pressure

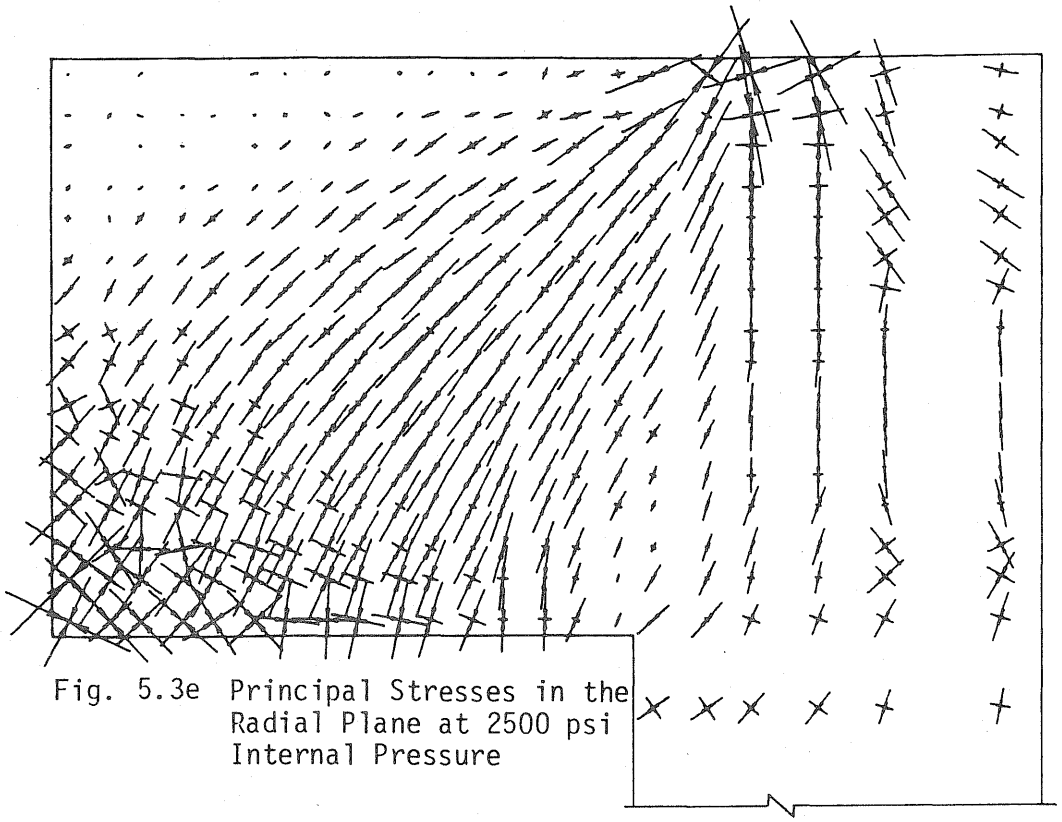

Fig. 5.3e Principal Stresses in the Radial Plane at 2500 psi Internal Pressure

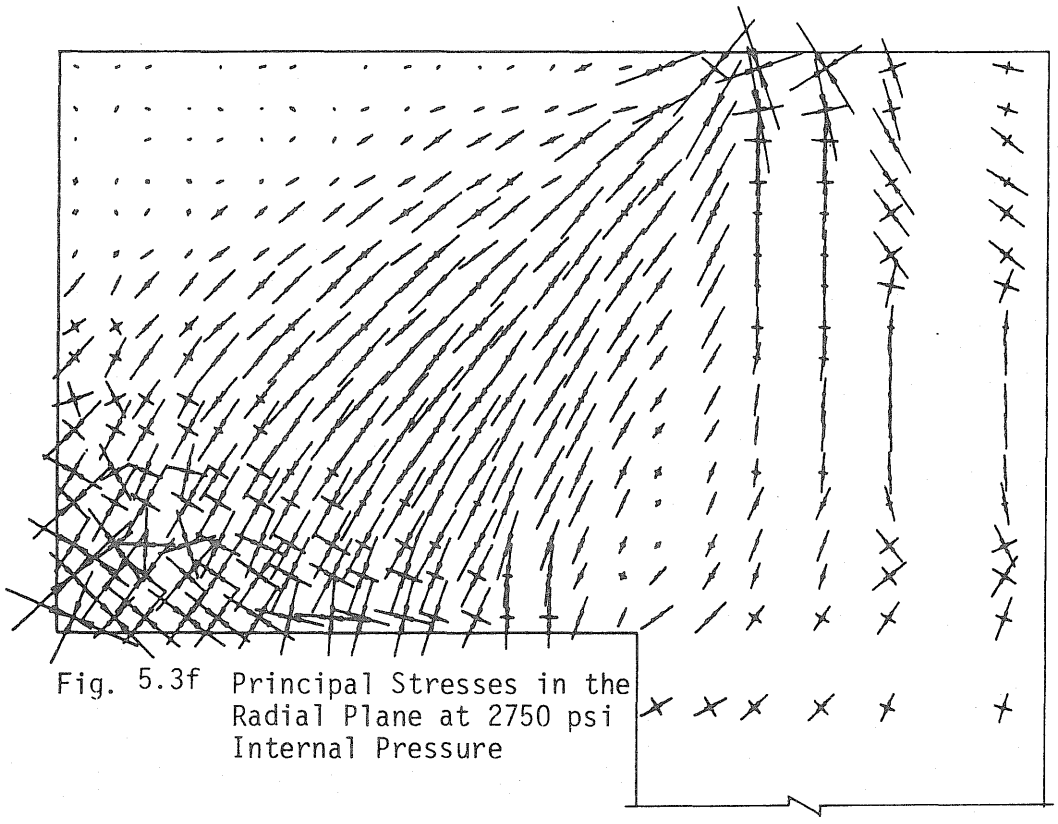

Fig. 5.3f Principal Stresses in the Radial Plane at 2750 psi Internal Pressure

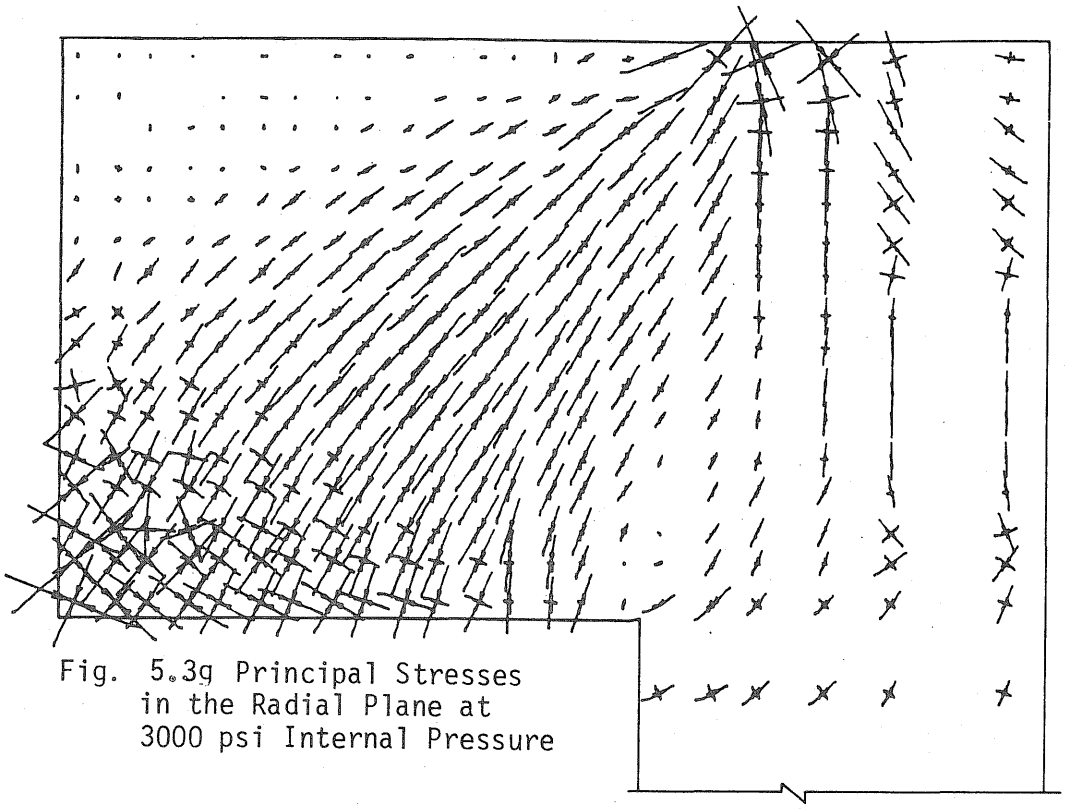

Fig. 5.3g Principal Stresses in the Radial Plane at 3000 psi Internal Pressure

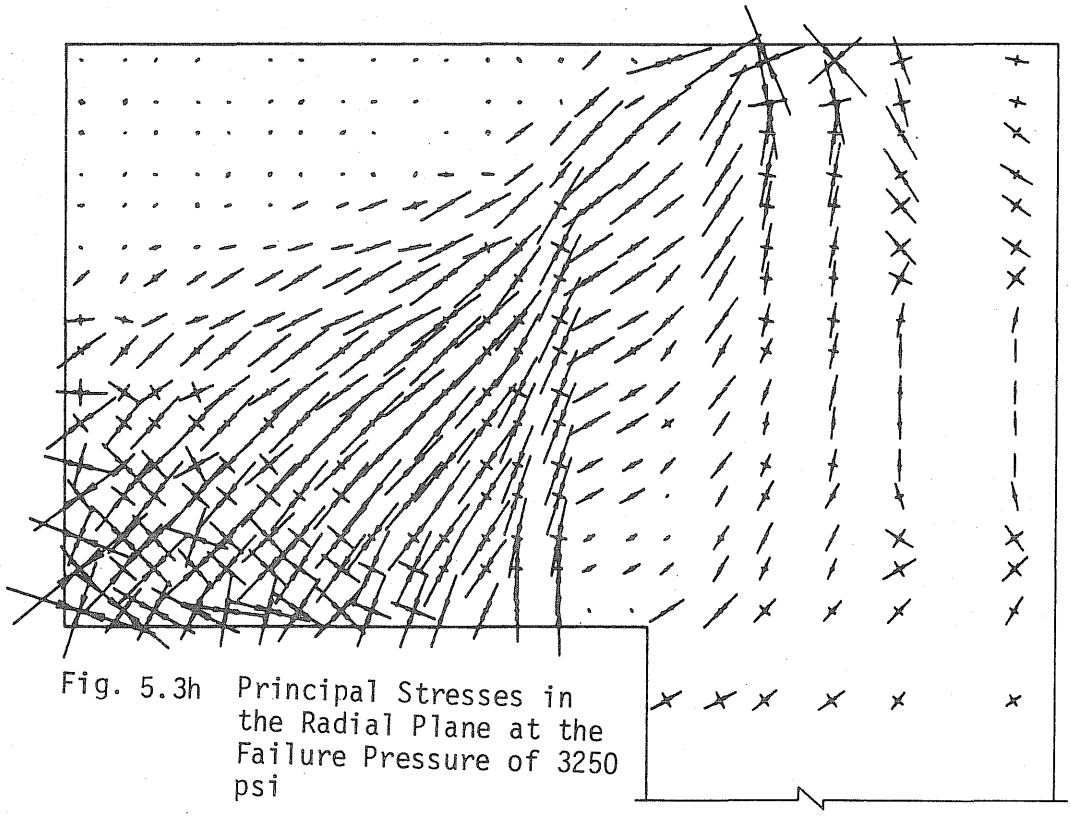

Fig. 5.3h Principal Stresses in the Radial Plane at the Failure Pressure of 3250 psi

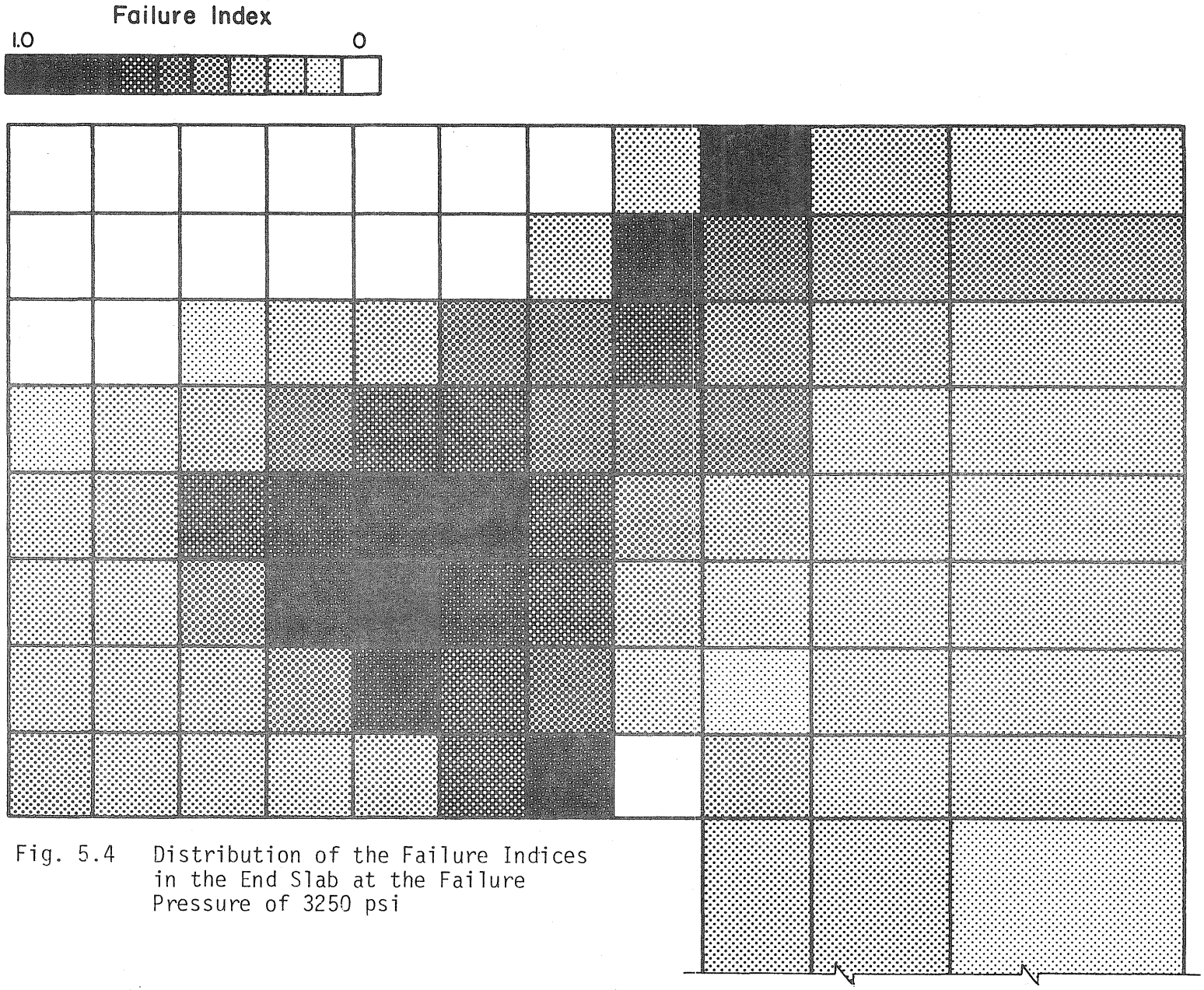

Fig. 5.4 Distribution of the Failure Indices in the End Slab at the Failure Pressure of 3250 psi

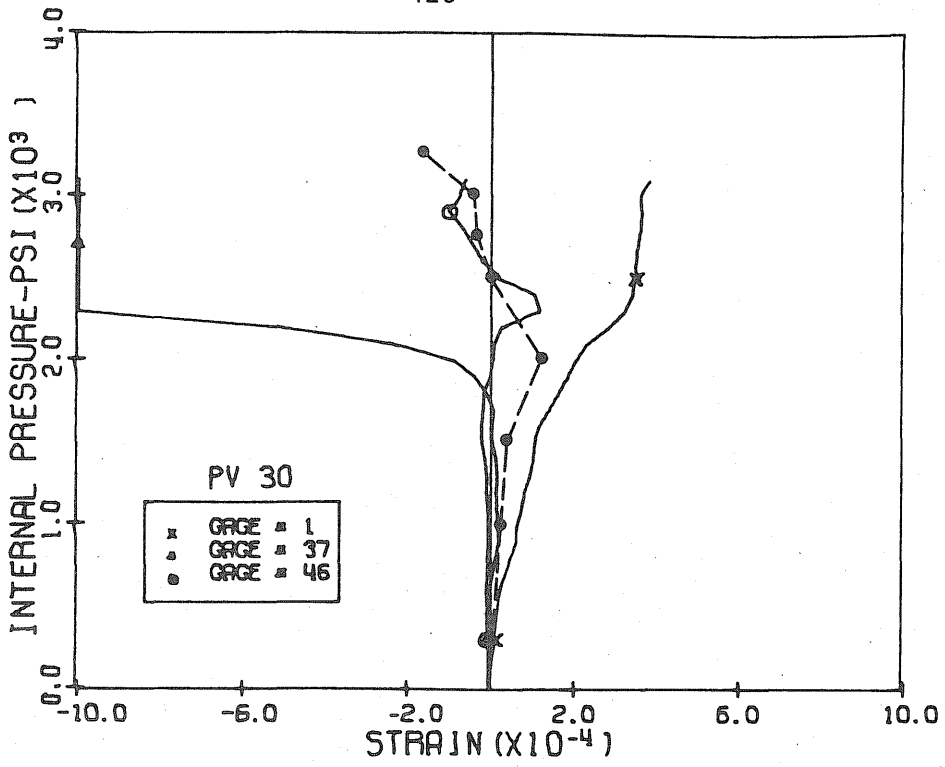

Fig. 5.5 Measured and Calculated Vertical Strains, Level 1 Penetrations 1 and 3, PV30

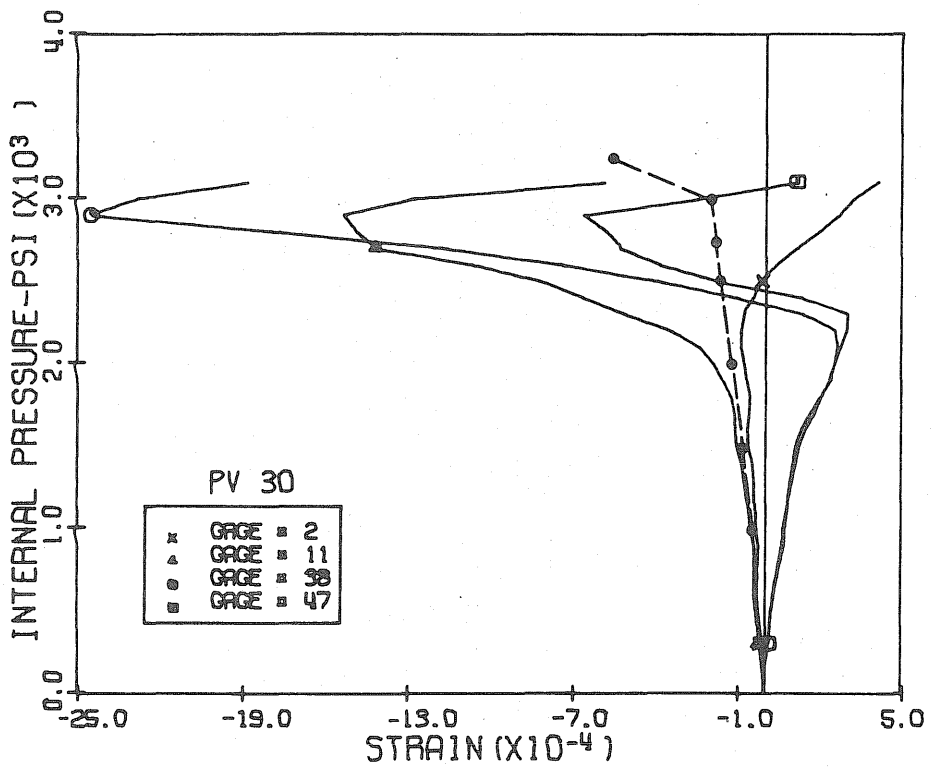

Fig. 5.6 Measured and Calculated Horizontal Strains, Level 1 Penetrations 1 and 3, PV30

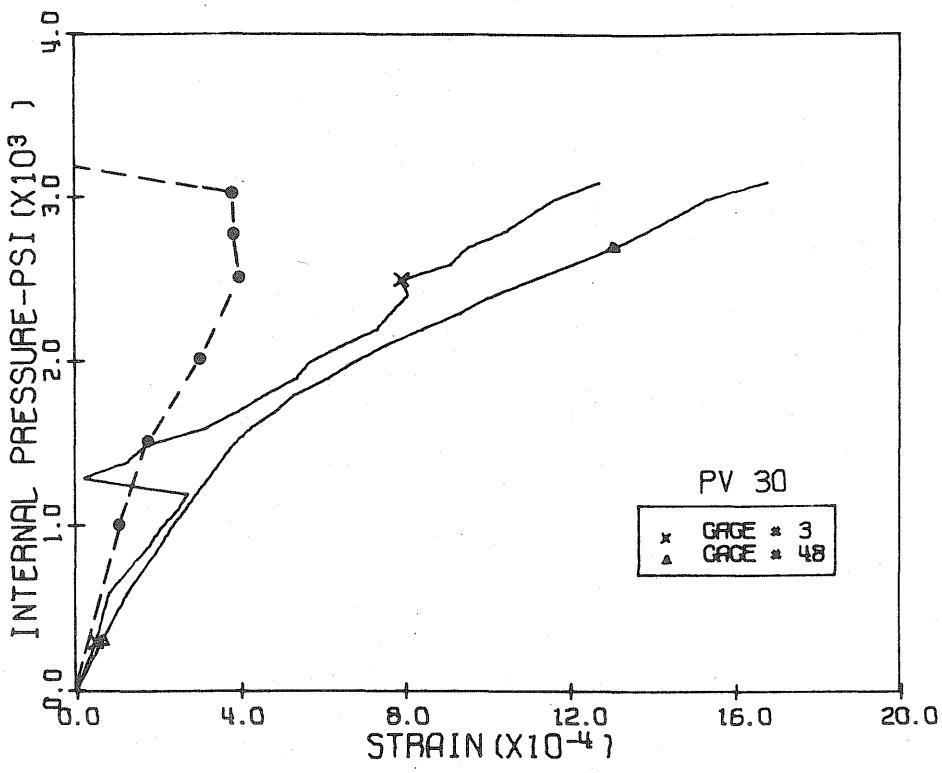

Fig. 5.7 Measured and Calculated Compression Diagonal Strains, Level 1 Penetrations 1 and 3, PV30

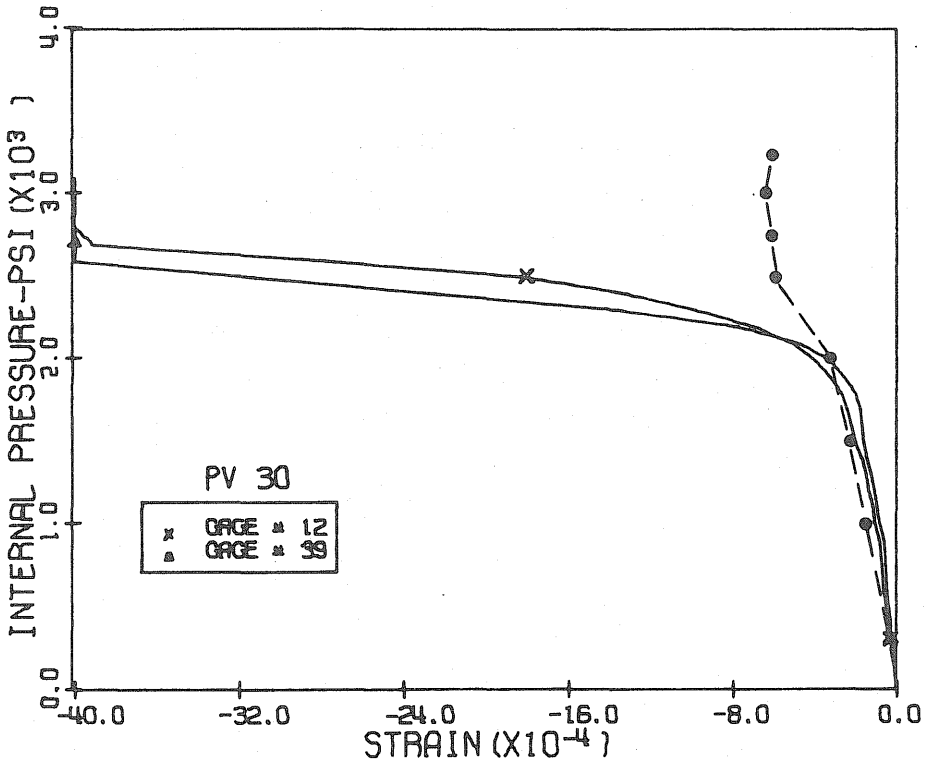

Fig. 5.8 Measured and Calculated Tension Diagonal Strains, Level 1 Penetrations 1 and 3, PV30

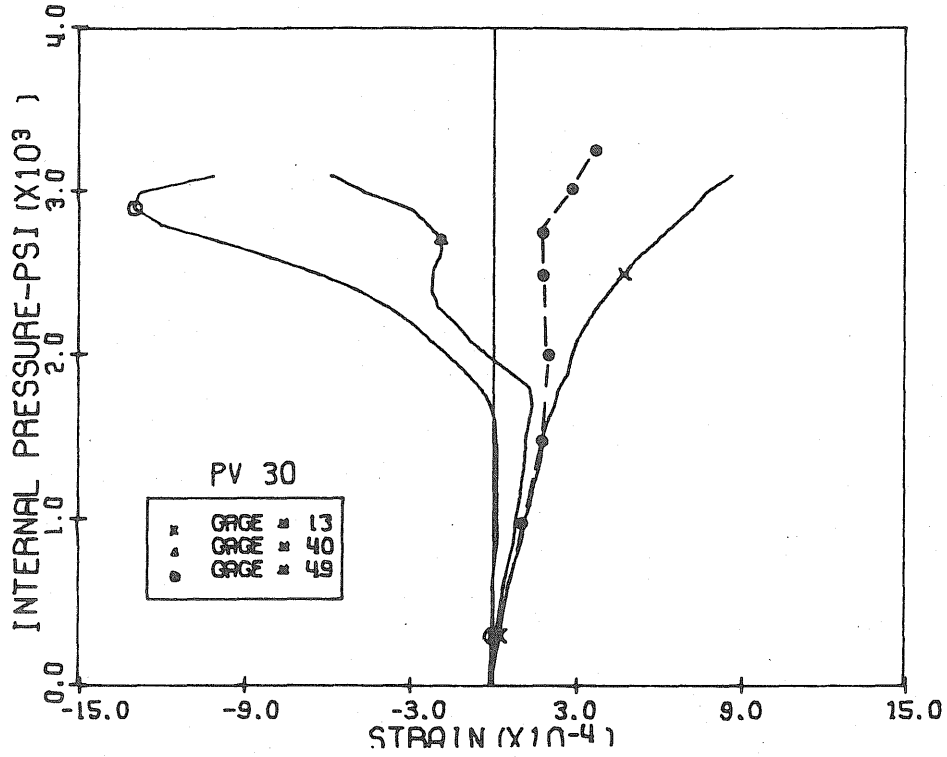

Fig. 5.9 Measured and Calculated Vertical Strains, Level 2 Penetrations 1 and 3, PV30

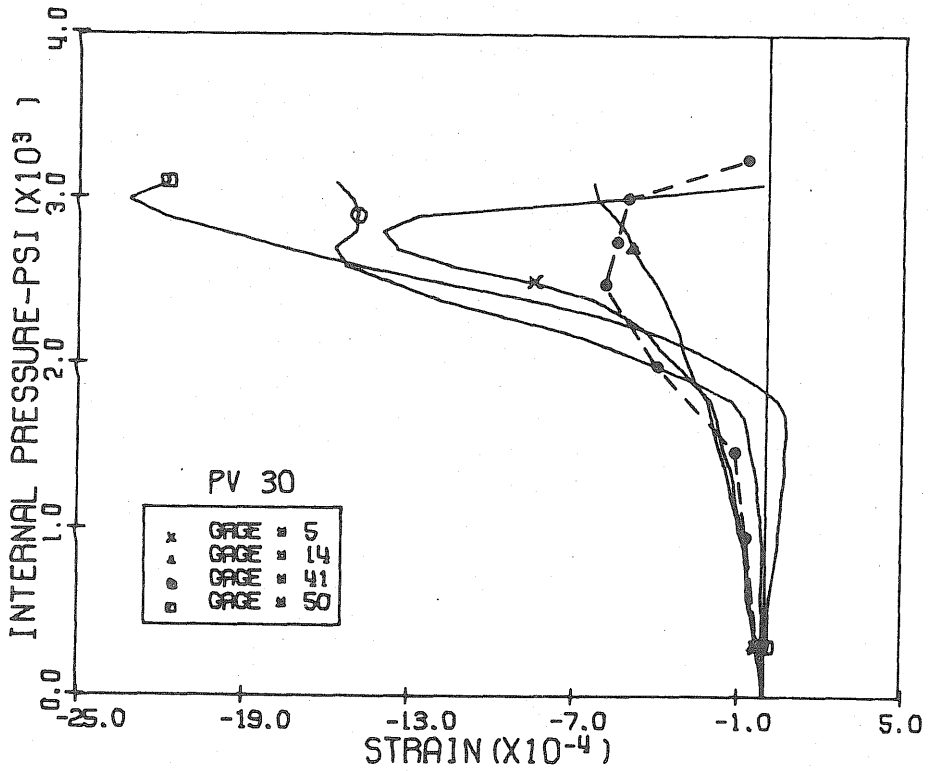

Fig. 5.10 Measured and Calculated Horizontal Strains, Level 2 Penetrations 1 and 3, PV30

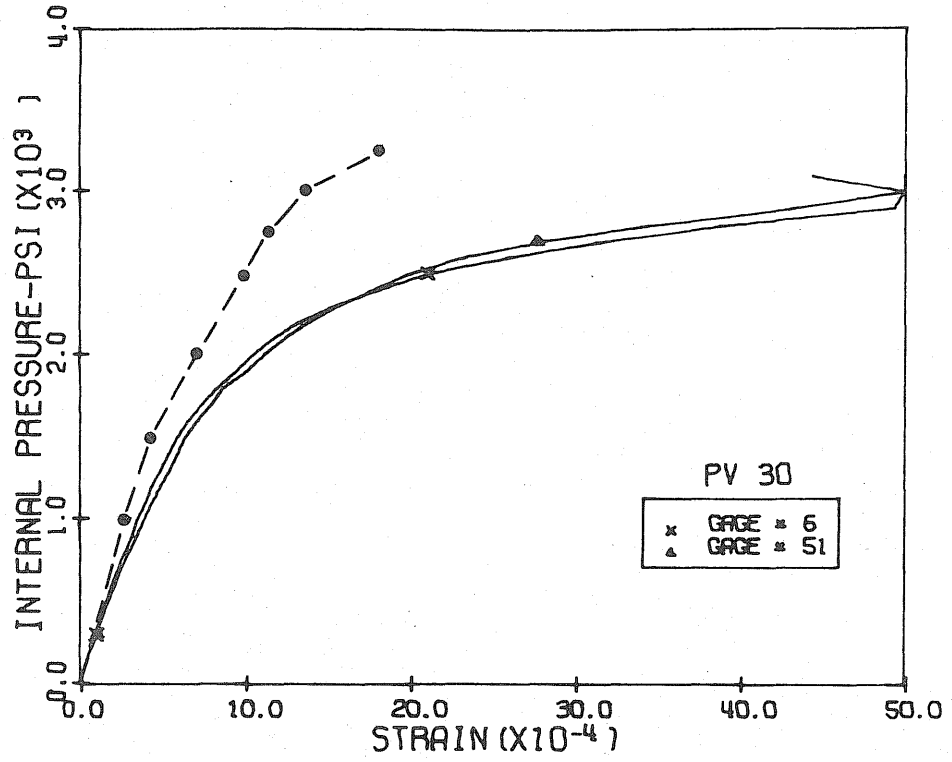

Fig. 5.11 Measured and Calculated Compression Diagonal Strains, Level 2 Penetrations 1 and 3, PV30

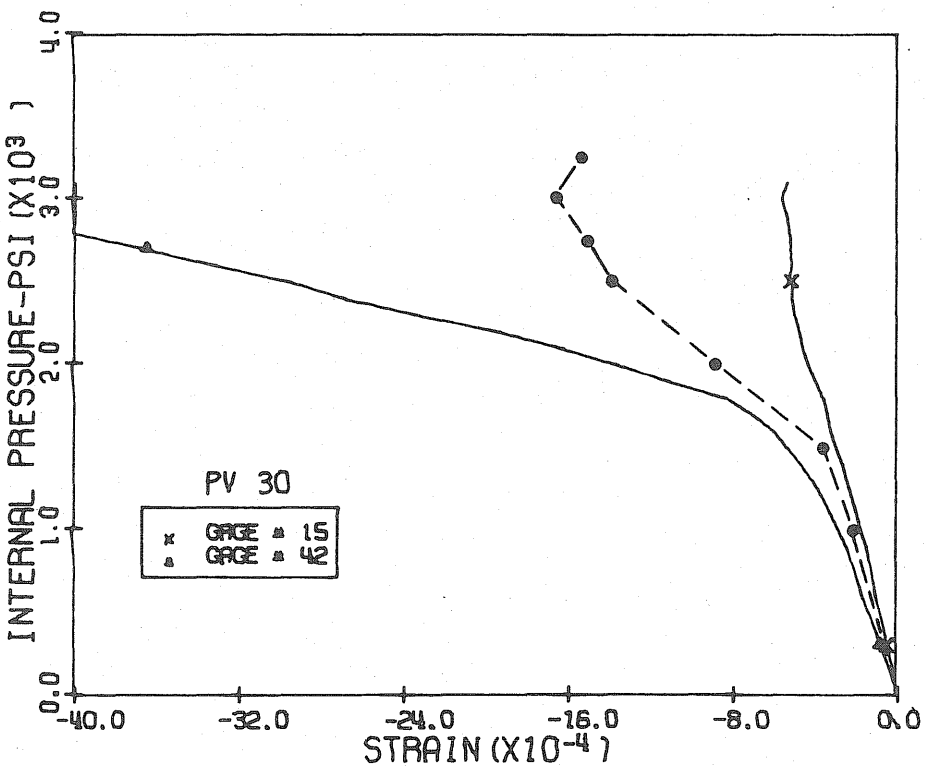

Fig. 5.12 Measured and Calculated Tension Diagonal Strains, Level 2 Penetrations 1 and 3, PV30

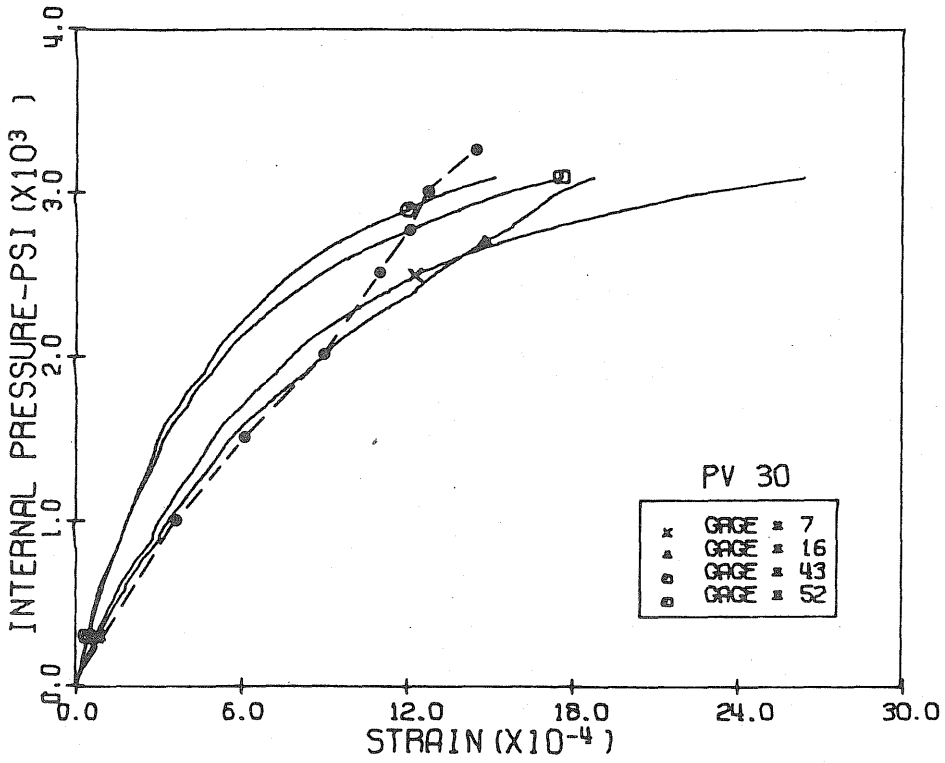

Fig. 5.13 Measured and Calculated Vertical Strains, Level 3 Penetrations 1 and 3, PV30

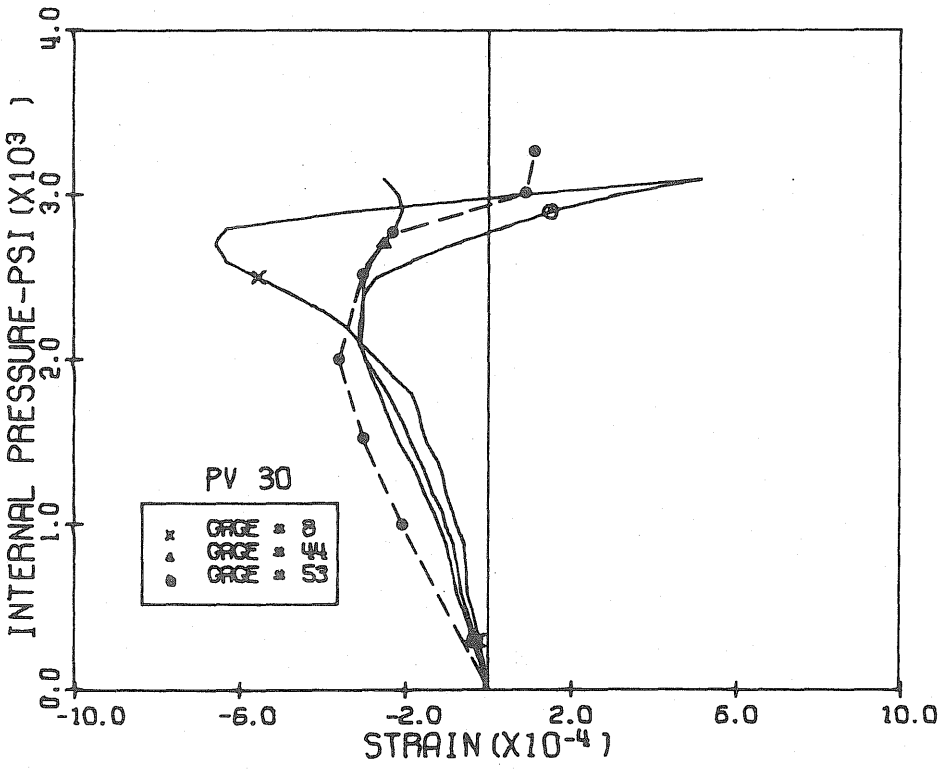

Fig. 5.14 Measured and Calculated Horizontal Strains, Level 3 Penetrations 1 and 3, PV30

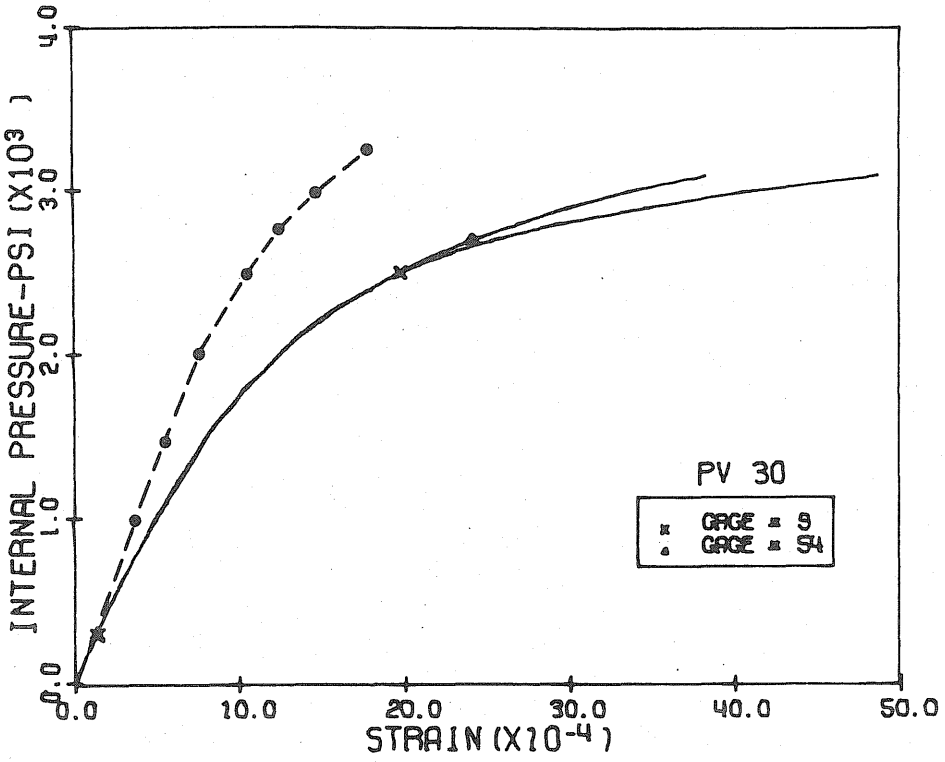

Fig. 5.15 Measured and Calculated Compression Diagonal Strains, Level 3 Penetrations 1 and 3, PV30

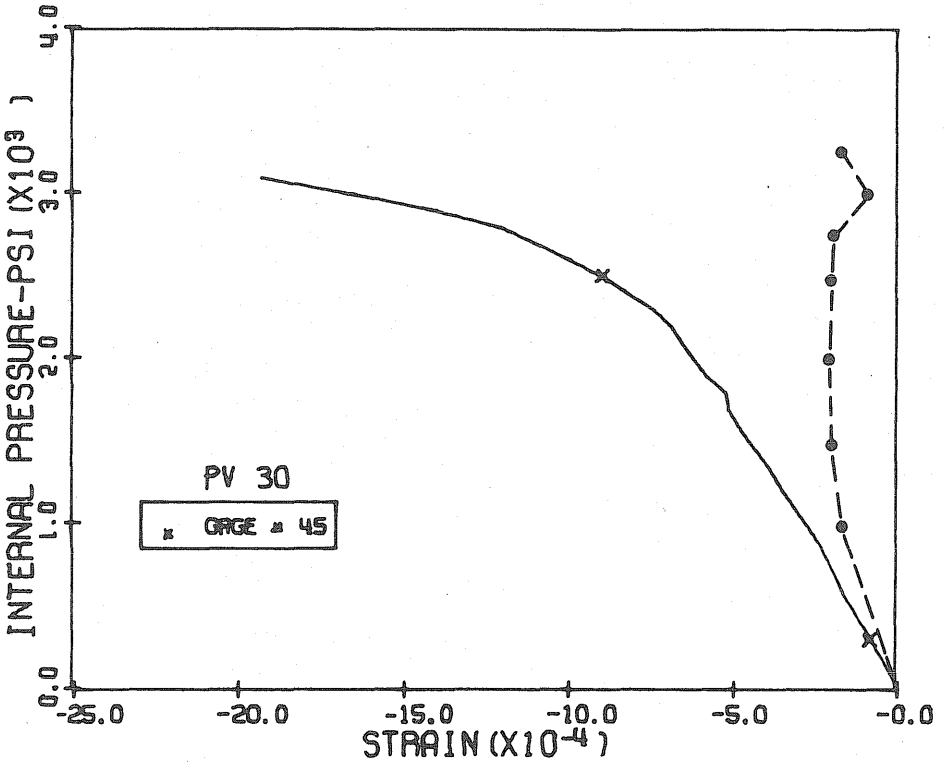

Fig. 5.16 Measured and Calculated Tension Diagonal Strains, Level 3 Penetrations 1 and 3, PV30

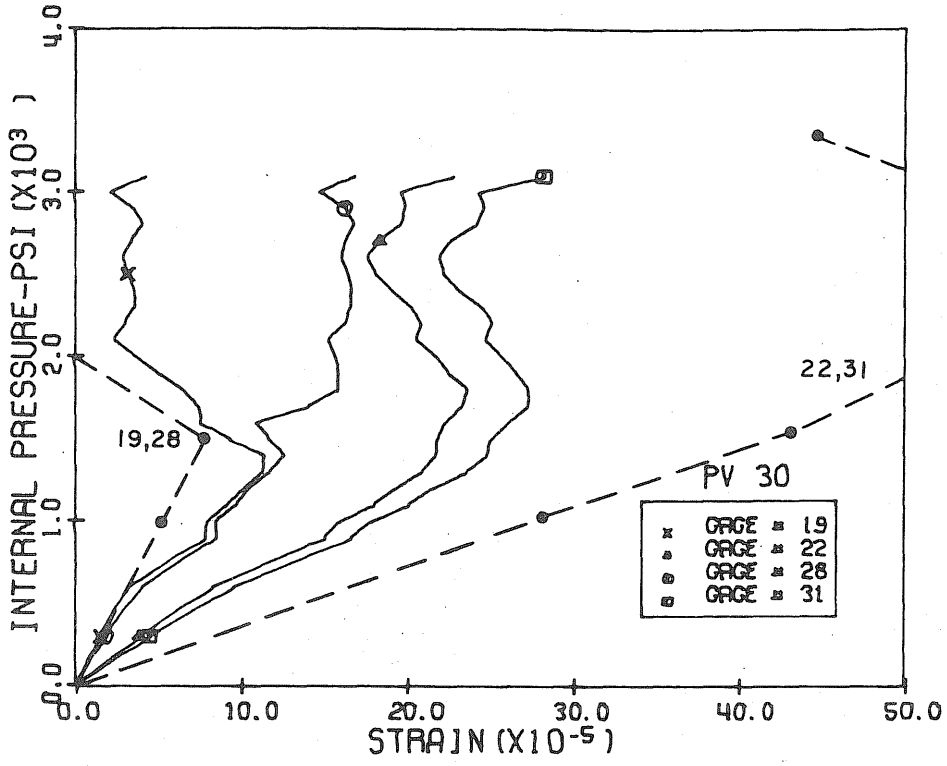

Fig. 5.17 Measured and Calculated Vertical Strains, Levels 1 and 2 Penetration 2, PV30

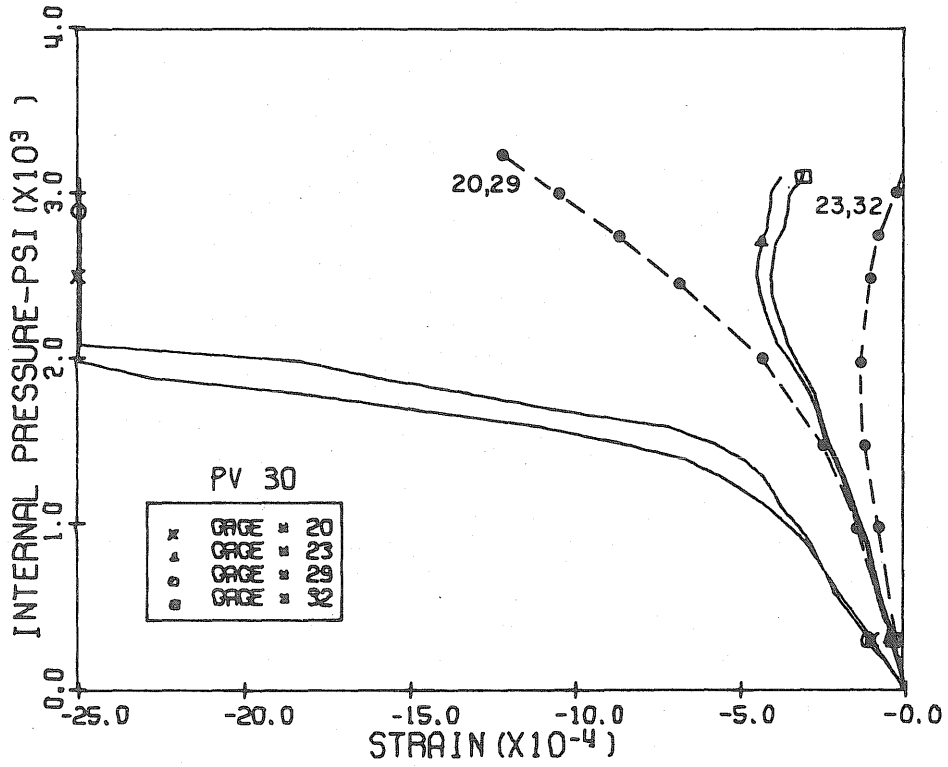

Fig. 5.18 Measured and Calculated Horizontal Strains, Levels 1 and 2 Penetration 2, PV30

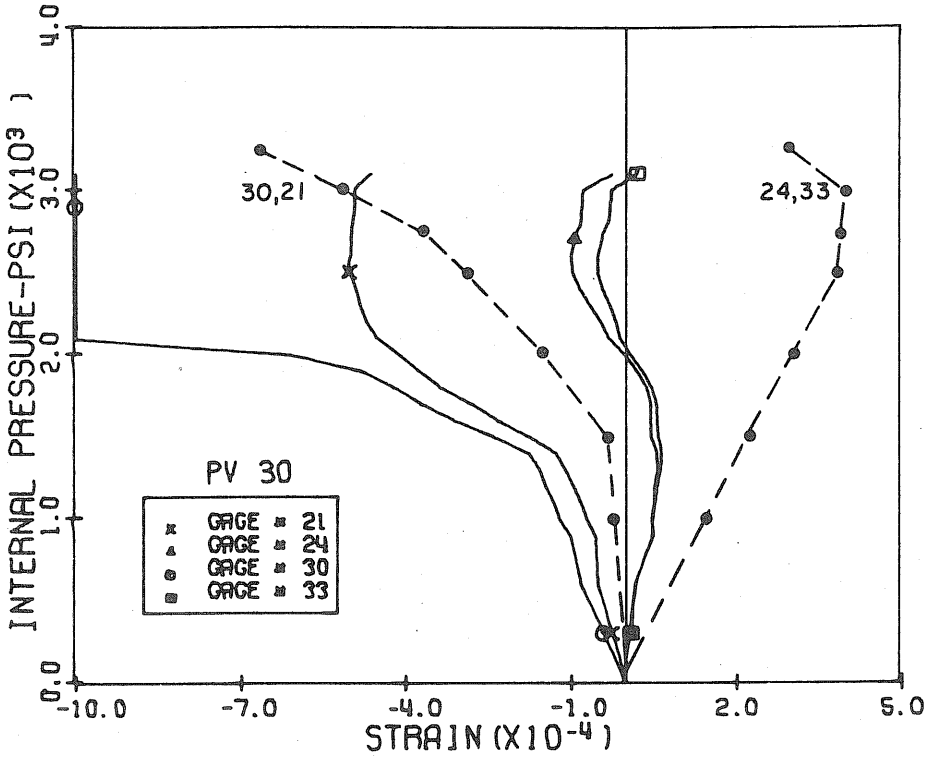

Fig. 5.19 Measured and Calculated Diagonal Strains, Levels 1 and 2 Penetration 2, PV30

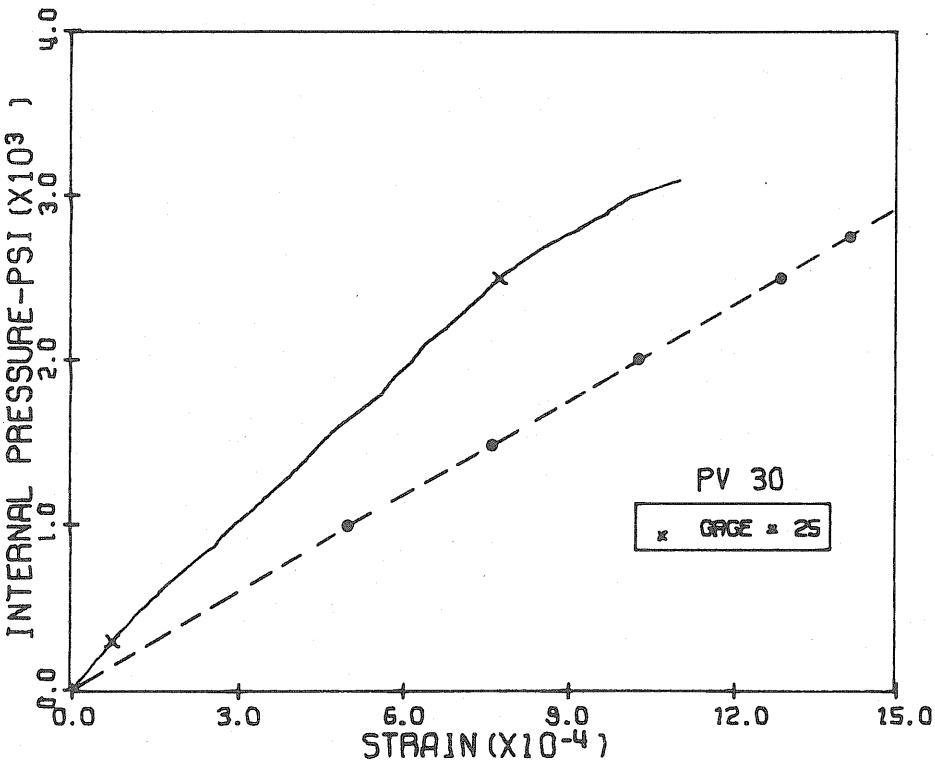

Fig. 5.20 Measured and Calculated Vertical Strain, Level 3 Penetration 2, PV30

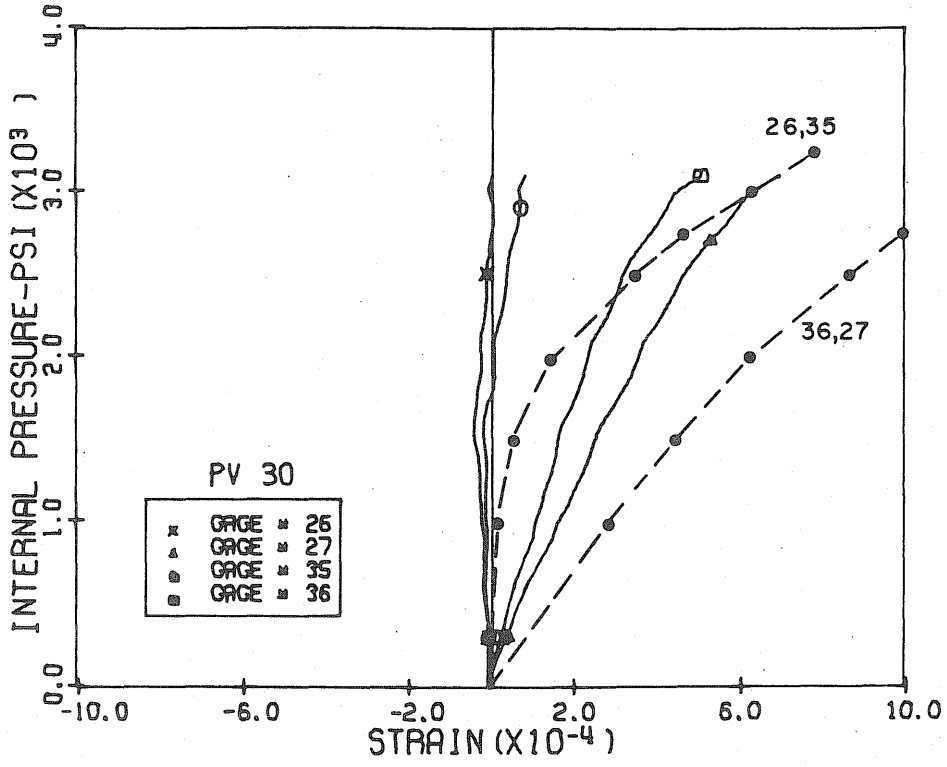

Fig. 5.21 Measured and Calculated Horizontal and Diagonal Strains Level 3 Penetration 2, PV30

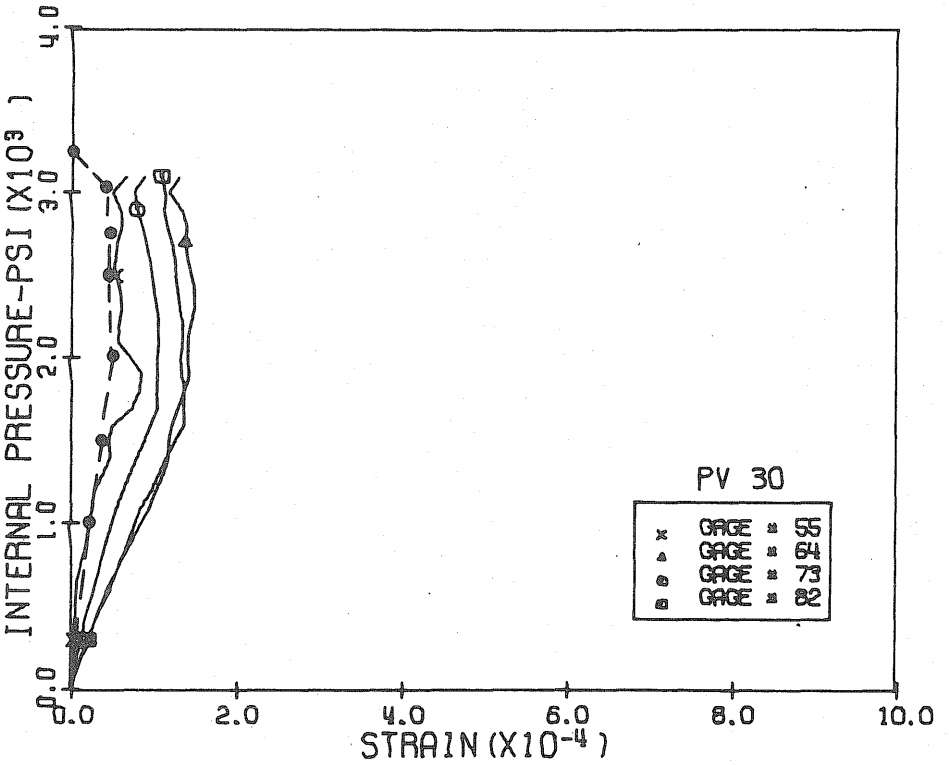

Fig. 5.22 Measured and Calculated Vertical Strains, Level 1 Penetrations 4 and 5, PV30

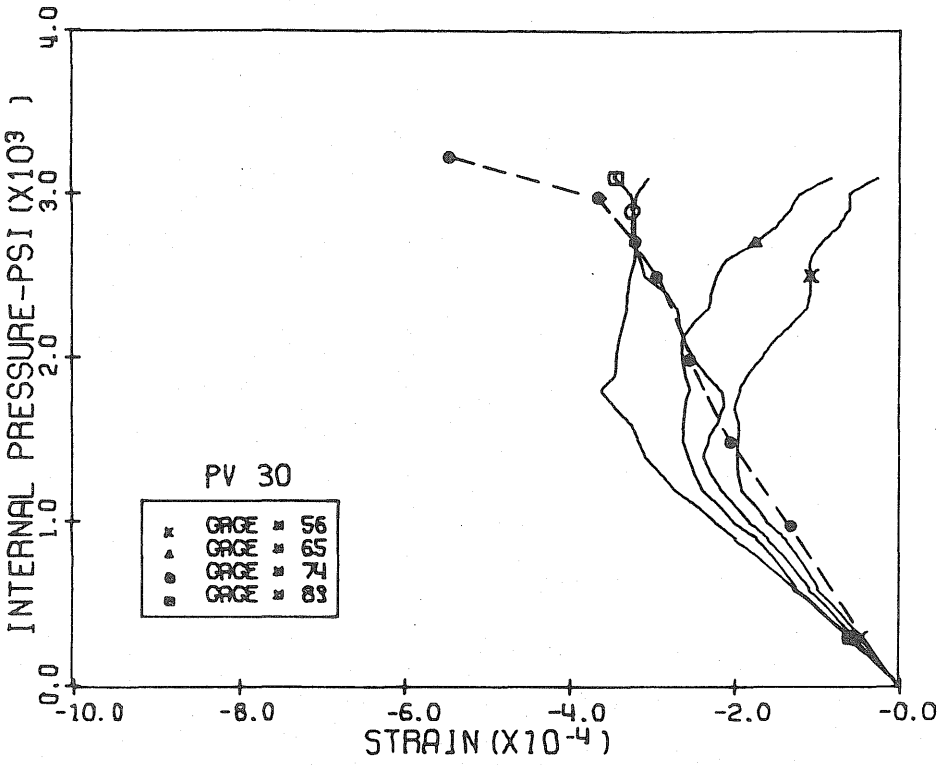

Fig. 5.23 Measured and Calculated Horizontal Strains, Level 1 Penetrations 4 and 5, PV30

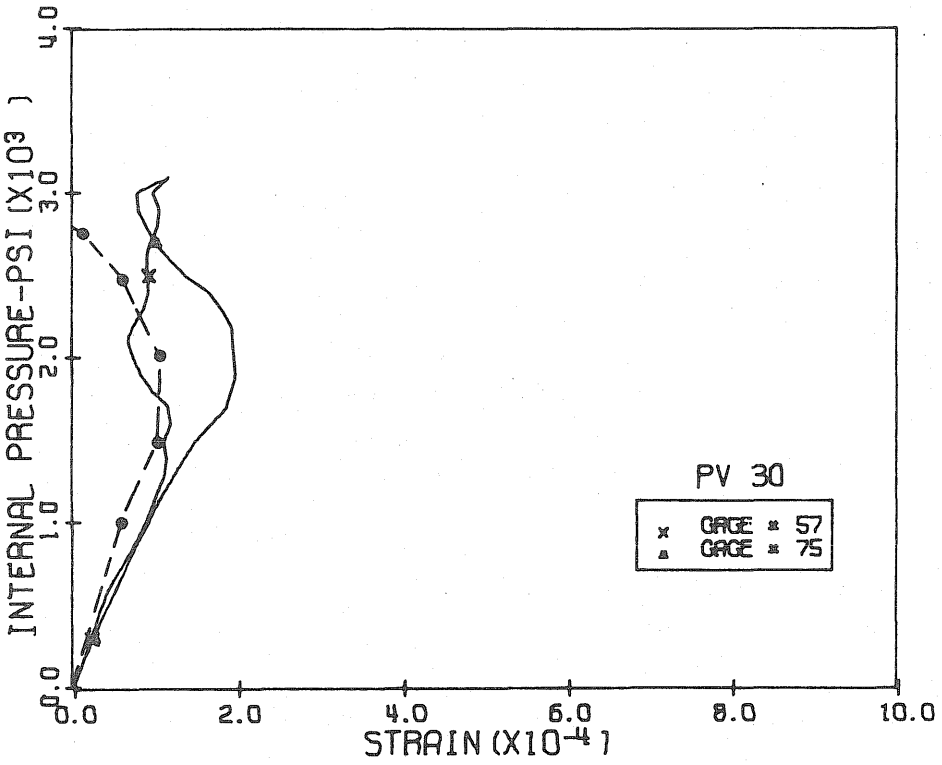

Fig. 5.24 Measured and Calculated Compression Diagonal Strains, Level 1 Penetrations 4 and 5, PV30

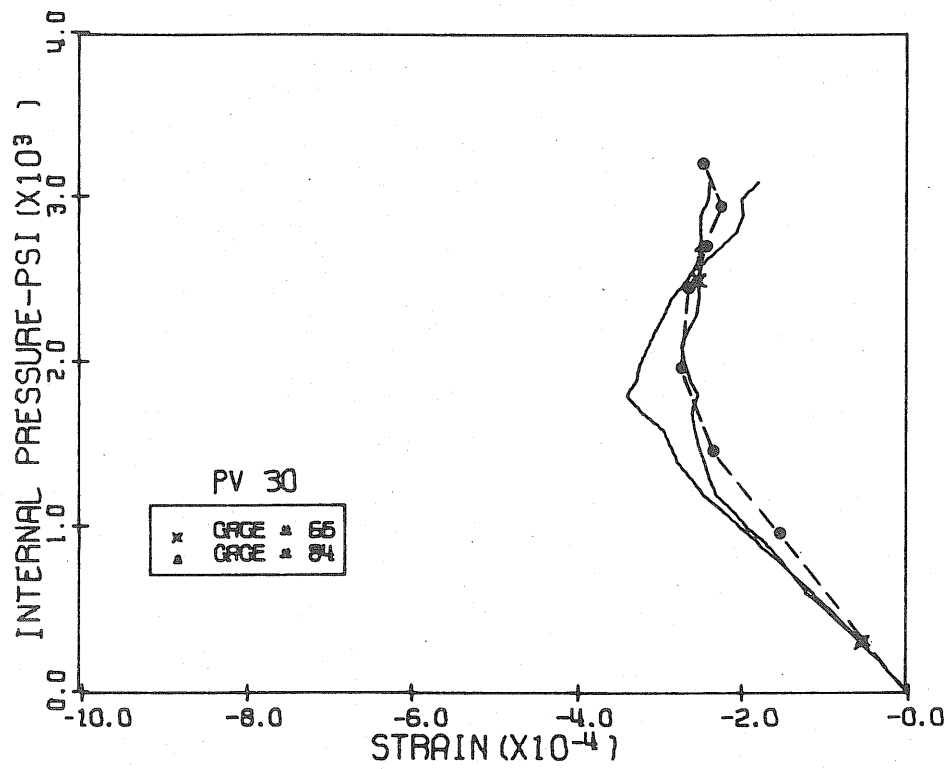

Fig. 5.25 Measured and Calculated Tension Diagonal Strains, Level 1 Penetrations 4 and 5, PV30

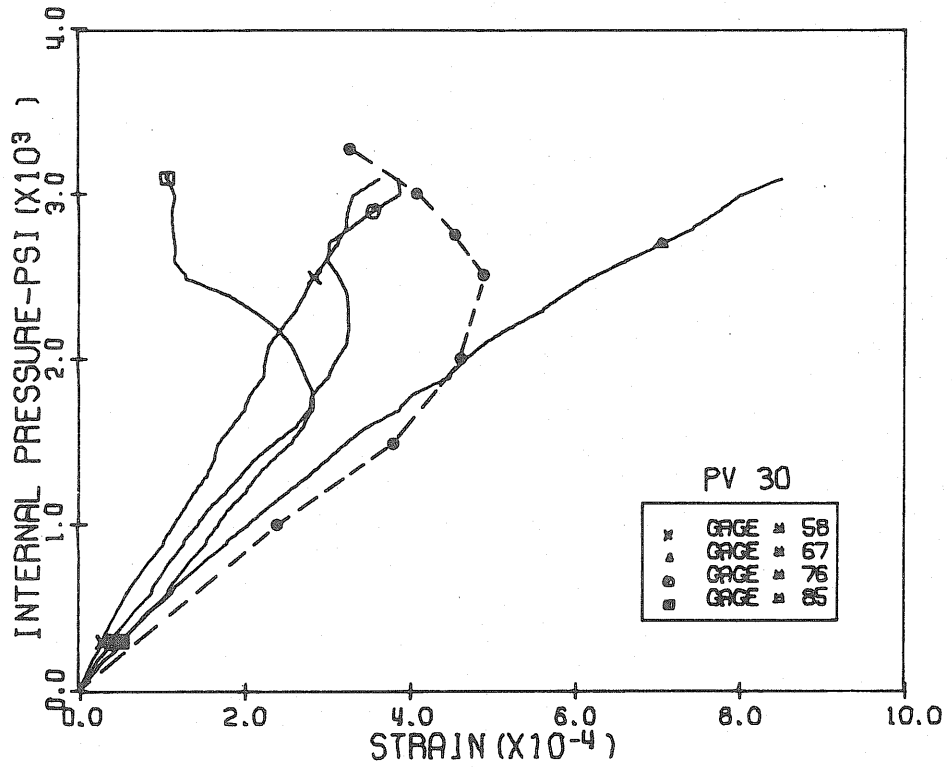

Fig. 5.26 Measured and Calculated Vertical Strains, Level 2 Penetrations 4 and 5, PV30

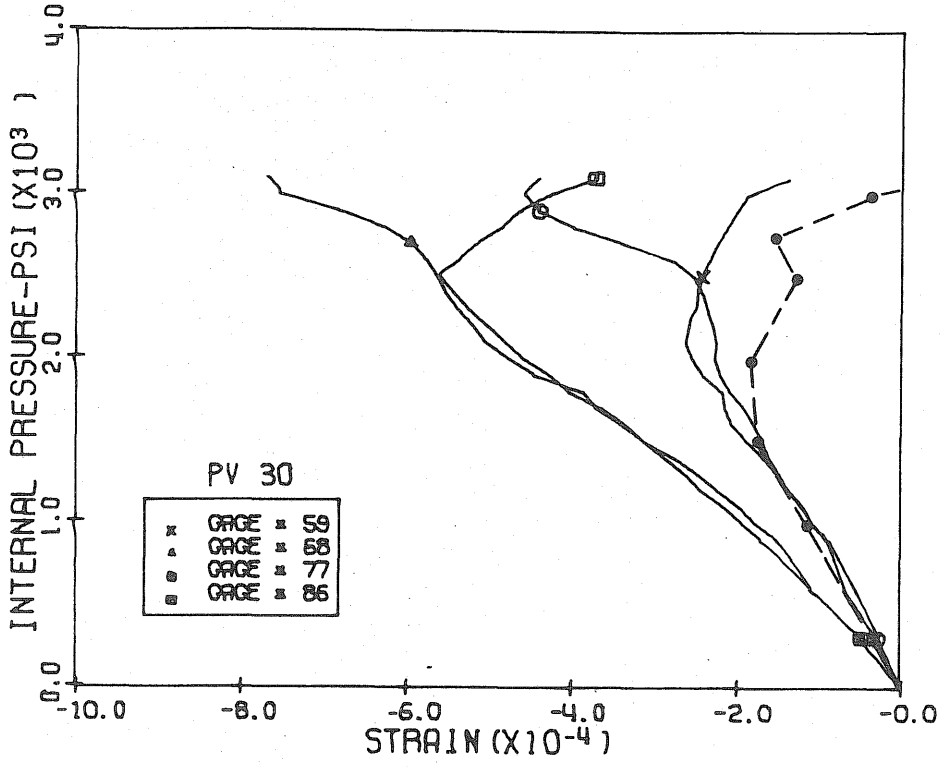

Fig. 5.27 Measured and Calculated Horizontal Strains, Level 2 Penetrations 4 and 5, PV30

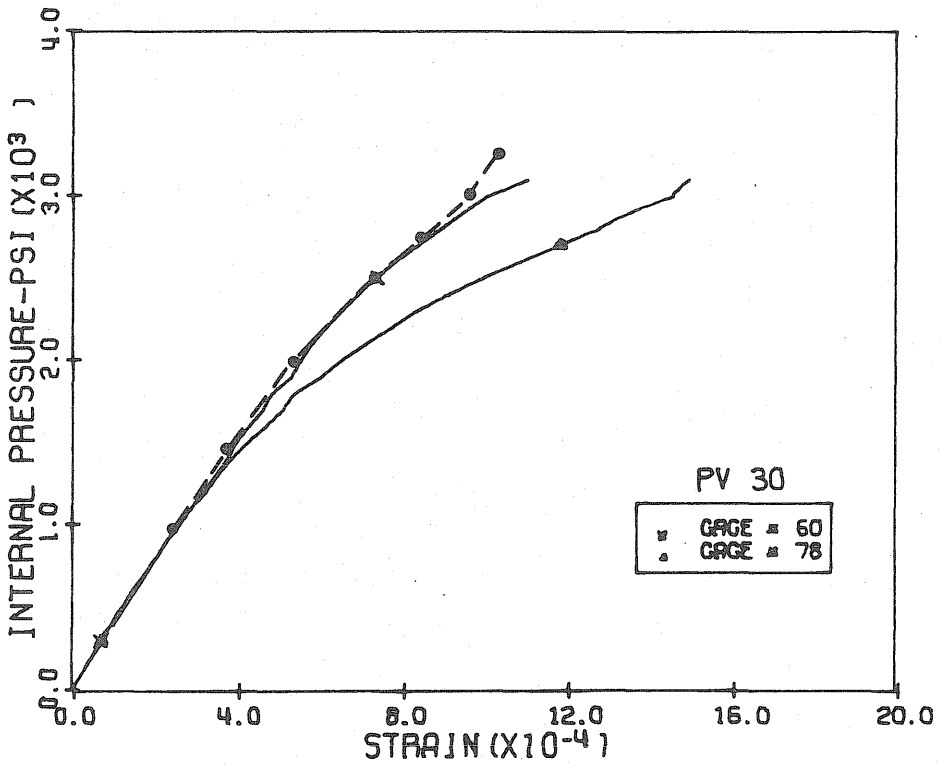

Fig. 5.28 Measured and Calculated Compression Diagonal Strains, Level 2 Penetrations 4 and 5, PV30

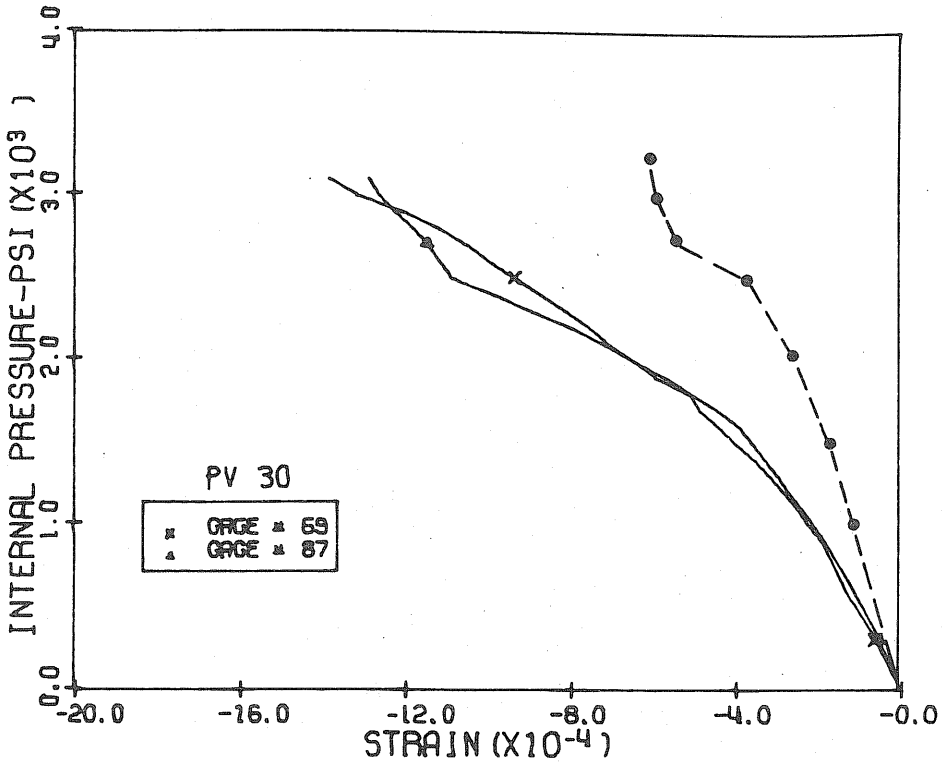

Fig. 5.29 Measured and Calculated Tension Diagonal Strains, Level 2 Penetrations 4 and 5, PV30

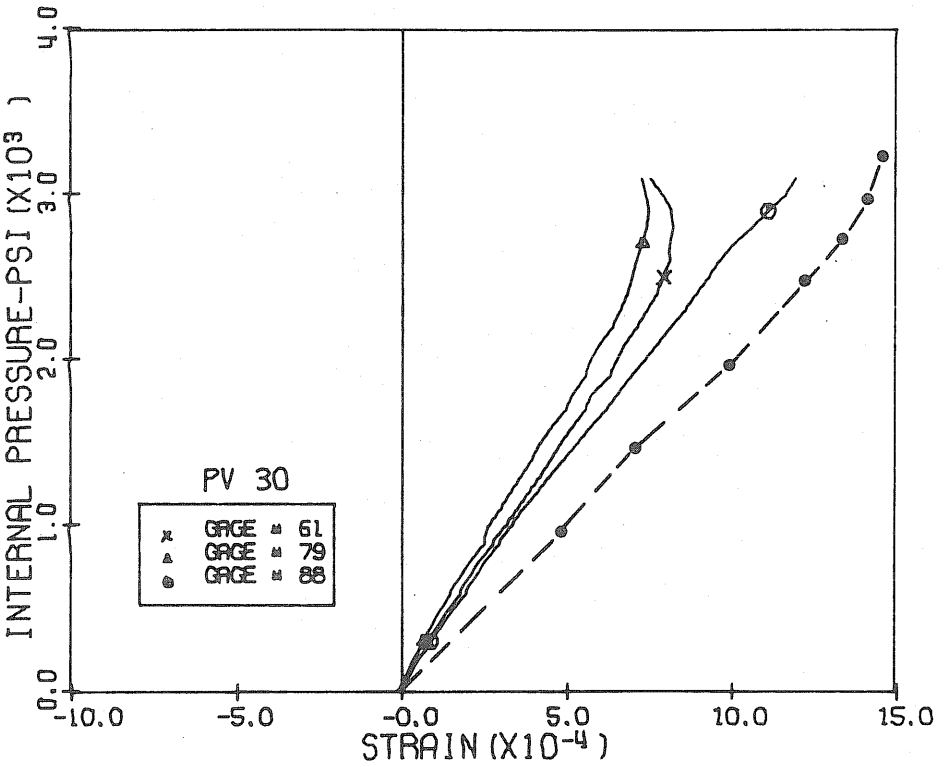

Fig. 5.30 Measured and Calculated Vertical Strains, Level 3 Penetrations 4 and 5, PV30

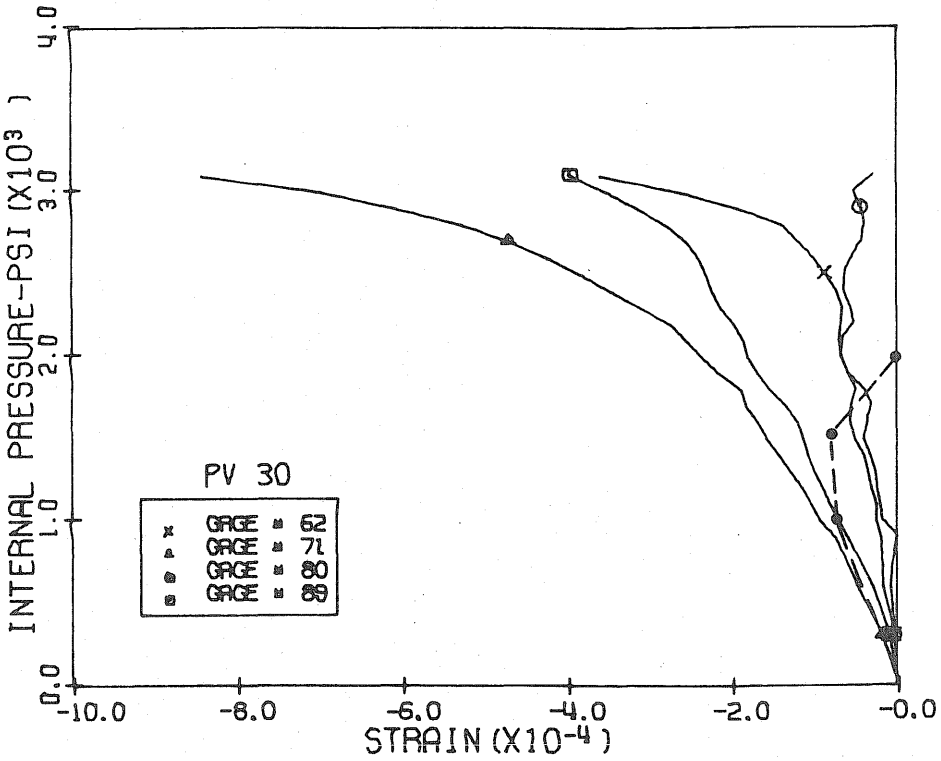

Fig. 5.31 Measured and Calculated Horizontal Strains, Level 3 Penetrations 4 and 5, PV30

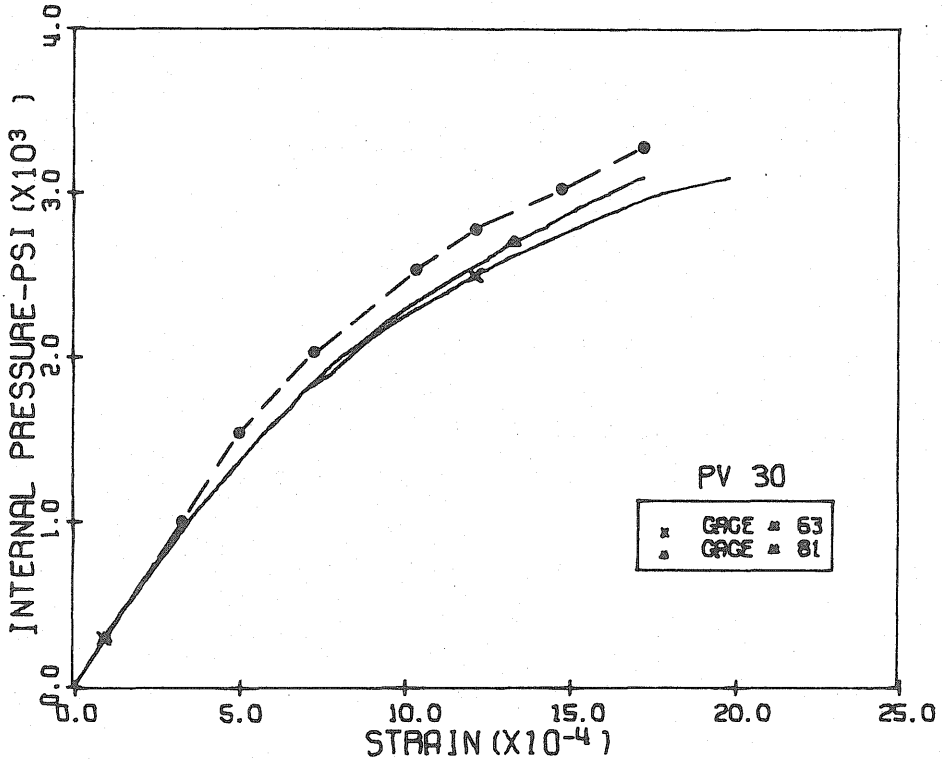

Fig. 5.32 Measured and Calculated Compression Diagonal Strains, Level 3 Penetrations 4 and 5, PV30

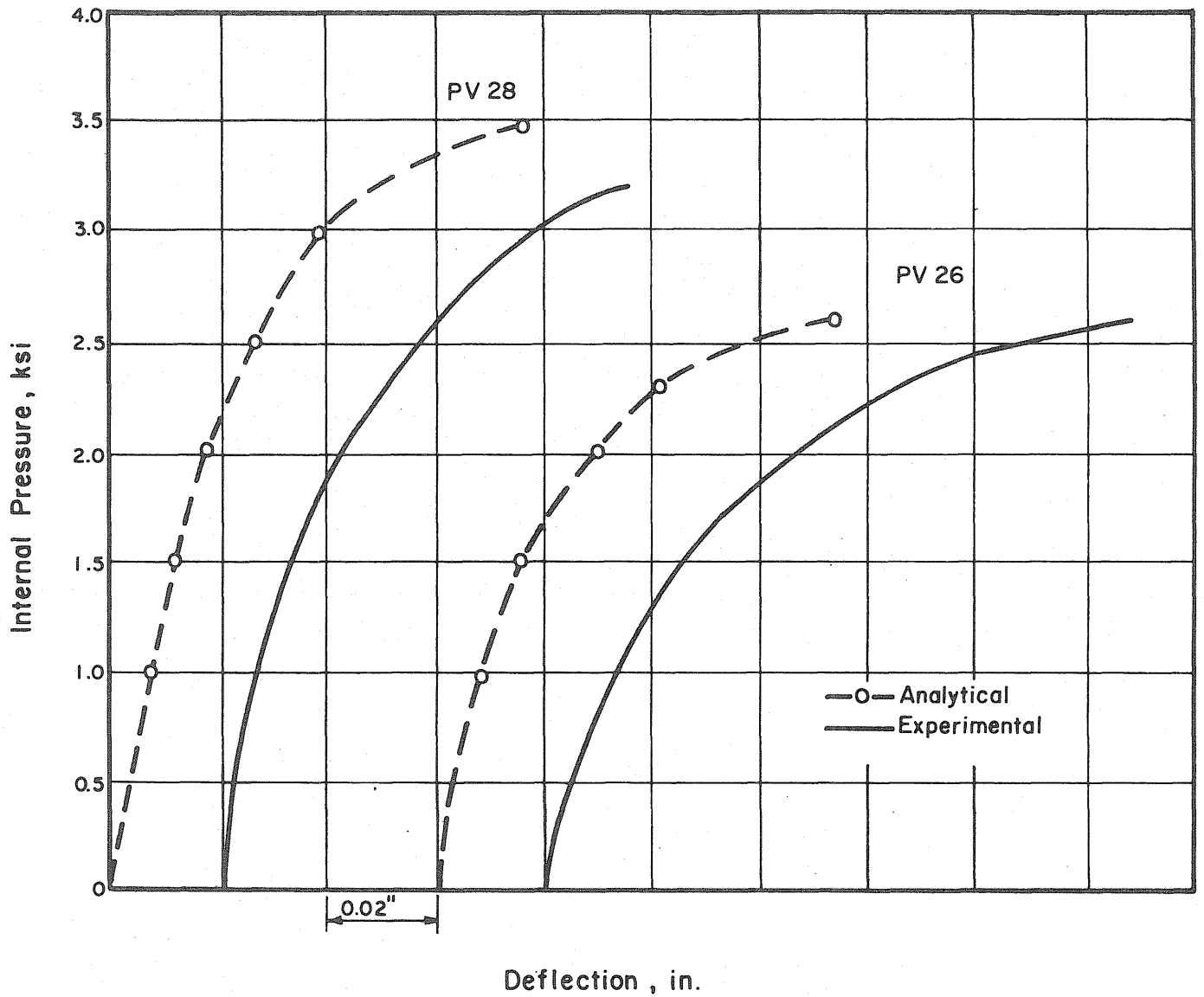

Fig. 5.33 Measured and Calculated Deflections at the Center of the End Slab for the Vessels with No Penetrations

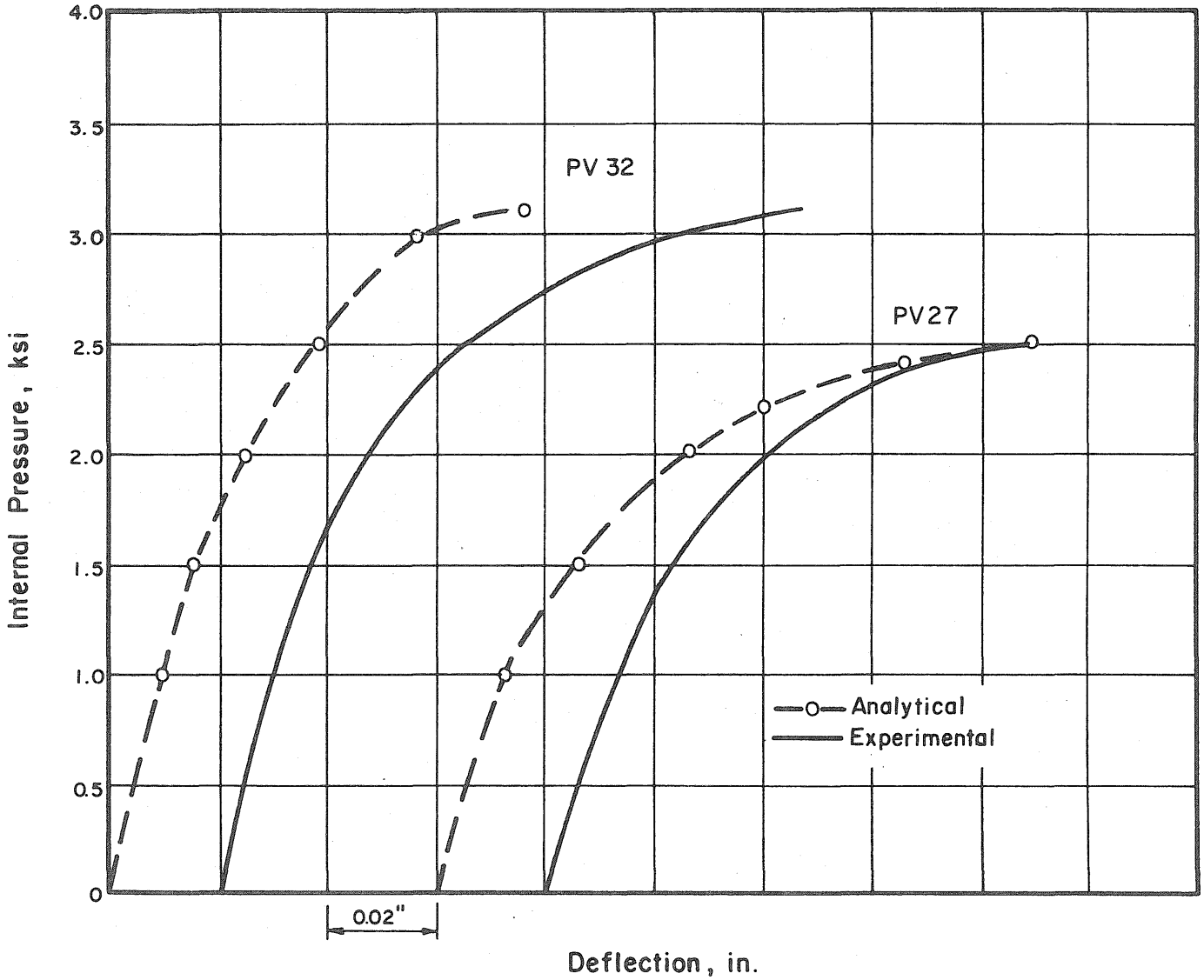

Fig. 5.34 Measured and Calculated Deflections at the Center of the End Slab for the Vessels with 5-in. Penetrations

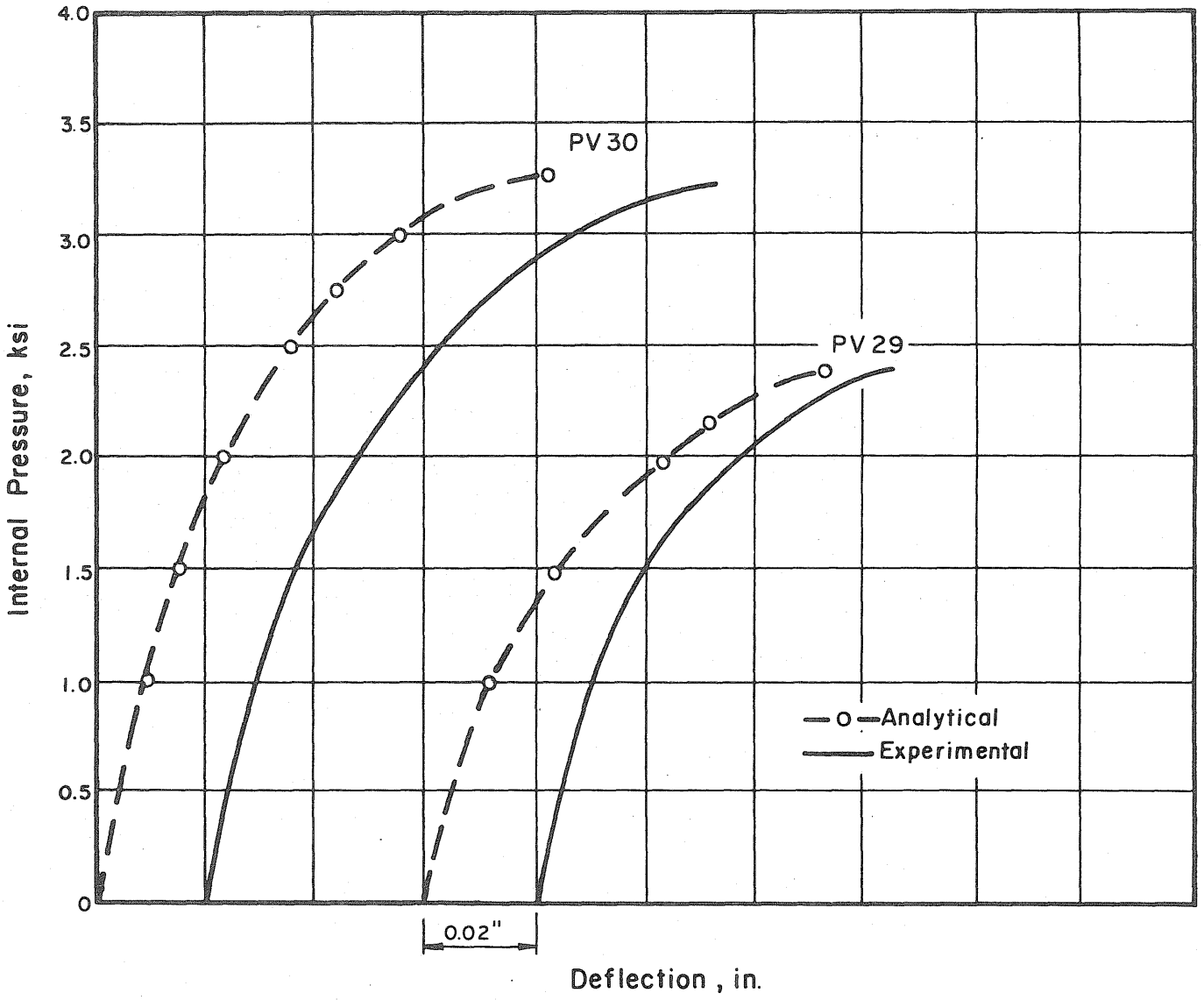

Fig. 5.35 Measured and Calculated Deflections at the Center of the End Slab for the Vessels with 2-in. Penetrations

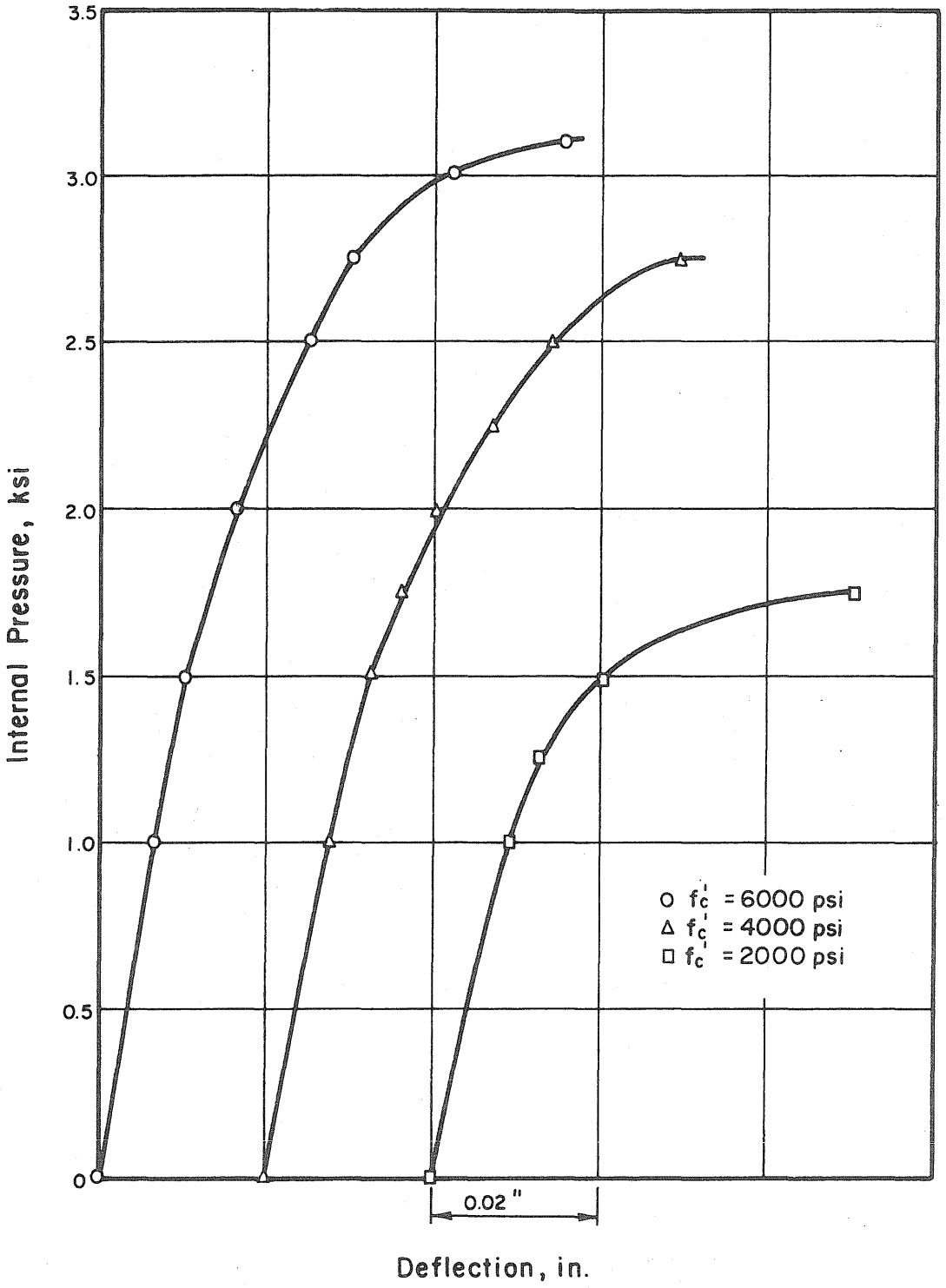

Fig. 5.36 Deflection at the Center of the End Slab for Three Values of Compressive Strength of Concrete, PV31

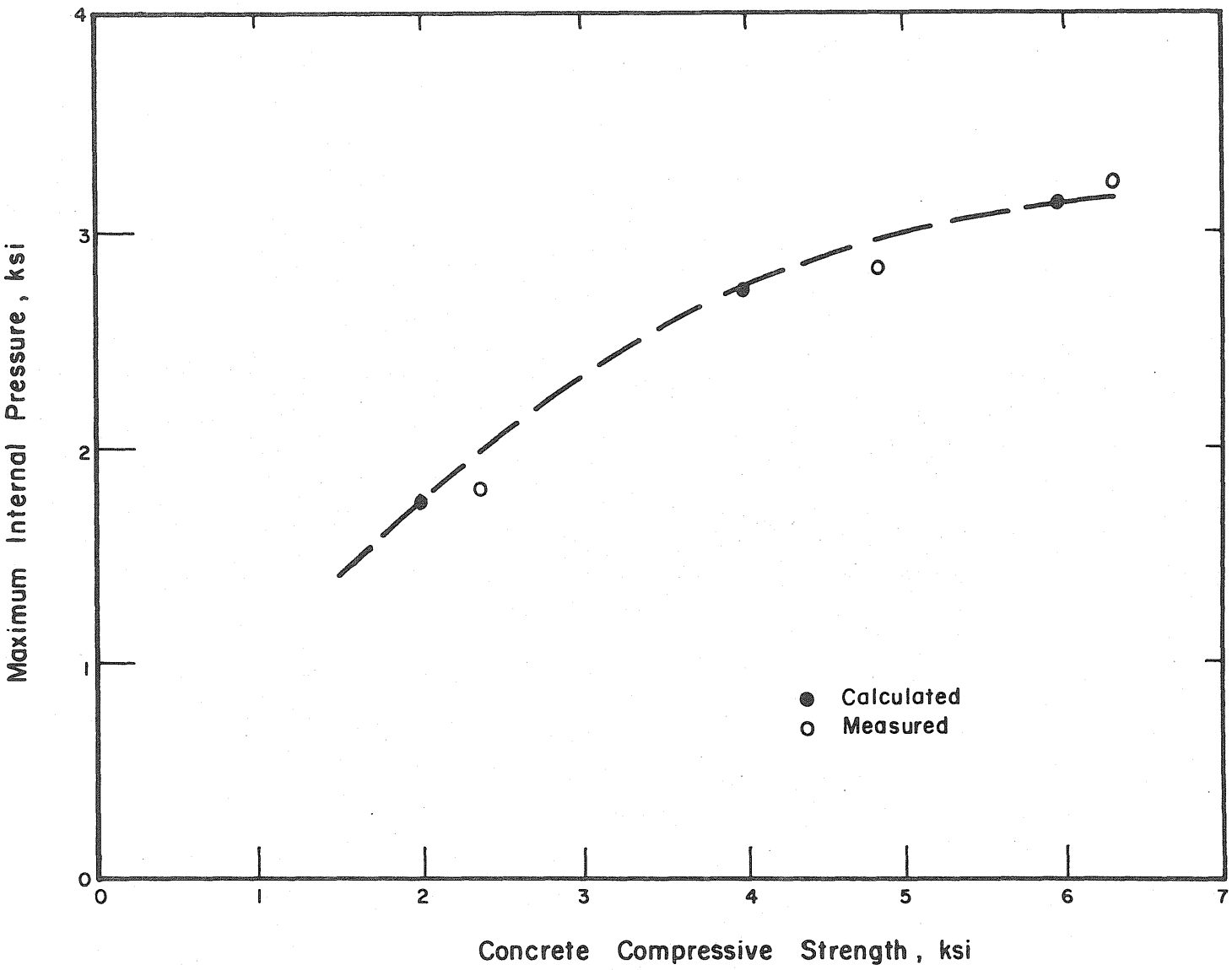

Fig. 5.37 Variation of End-Slab Strength with Compressive Strength of Concrete

APPENDIX A

A1 MATERIALS

A1.1 Concrete

The vessels were cast from concrete mixed in the laboratory. Two different mixes were used for each test vessel, one for the cylindrical skirt and one for the end slab.

The first mix was used for the skirt up to a level of 2-in. below the reentrant corner. Two batches of concrete were required to cast the skirt. The concrete contained pea-gravel aggregate, sand and type III cement. The proportions by weight of cement: sand: gravel were 1.00: 2.77: 3.07 and the water cement ratio was 0.67.

The second mix was used for the slab and the top 2-in. of the skirt and was made in one batch. The concrete contained crushed limestone aggregate, sand and type III cement. The proportions by weight of cement: sand: gravel were 1.00: 3.51: 3.40 for the first eight specimens and 1: 4.9: 4.7 for PV34 and PV35. Type III cement was used with a water cement ratio of 0.80 for the first eight specimens and 1.1 for the last two.

Five 6 x 12-in. cylinders were cast from each of the first two batches. Eight 6 x 12-in. cylinders and eight 6 x 6-in. cylinders were cast from the third batch used in the end slab of the vessels. The properties of the batches used in the end slabs of the vessels are shown in Table A.1.

A1.2 Longitudinal Reinforcement

PV26 was prestressed with the rods from the previous series of tests, namely 0.775-in. diameter Stressteel rods with an ultimate stress of

140 ksi. However, the threads on several of these rods stripped off during prestressing.

New rods and bolts were purchased and used in all of the subsequent tests. The results of a tensile test of a 30-in. Stressteel rod are plotted in Fig. A1. The strain was measured using an eight-in. extensometer. The ultimate stress in the rod, which had a measured cross-sectional area of 0.471 sq. in. was 140 ksi.

A1.3 Circumferential Reinforcement

The wire used to prestress the vessels circumferentially was obtained from ARMCO, Kansas City, Missouri. The wire was 0.08-in. diameter extra high strength high carbon rope. Two strain gages were attached on opposite sides of wire samples cut from the unstressed coils. These samples were subjected to tensile testing and the stress versus average strain was plotted. The Young's Modulus for the wire was found to be 30×10^6 psi. All of the samples failed at the grips of the testing machine. The failures occurred at an average load of 1400 lbs or approximately 280 ksi. The actual strength of the wire may be slightly higher.

A1.4 Liner Materials

The neoprene used to seal the pressure vessels was purchased in 100-ft rolls. The sheets were 36-in. wide and 1/16-in. thick. It was specified as "60 Durameter Shore A Black Neoprene Sheeting, Type #260."

The O-ring material was obtained in 100-ft lengths. The diameters of the 3/16-in. and 3/4-in. O-ring stock were 0.210 ± 0.010 in. and 0.750 ± 0.010 in. respectively. The material was specified as "70 Durameter Buna-N O-ring Cord Stock."

The caulking used to seal and hold the neoprene intact was specified as "General Electric Construction Sealant, SE-1204 Neutral in 1/12 U.S. Gallon Paper Tubes."

Sheets of 0.104-in. thick steel and 16 oz. soft copper were used on the sides and end slabs of the vessels.

A2 FABRICATION

A2.1 Casting and Curing

All pressure vessels in the current series, PV 26 through PV 35, were cast in the same outer steel form. This form was rolled from 5/16-in. steel plate and reinforced with rolled 2 x 2 x 1/4-in. angles. The inner form was basically a closed steel cylinder. Its height could be adjusted by adding 2 1/2-in. steel bands around the bottom or open end of the cylinder. This made it possible to vary the thickness of the concrete vessel head. Both the inner and outer forms were bolted to a 1/2-in. thick base plate. Sixty holes were drilled 3/8 in. into the base plate to receive the 7/8-in. diameter aluminum rods which form the openings for the longitudinal prestress rods. The tops of the rods were secured by a template of 1/2-in. steel which was attached to the outer form by sections of 4-in. wide channel. The center of the template was cut out to allow easier access when casting and trowelling. For the vessels which had penetrations in the head, holes were drilled and tapped in the top or closed end of the inner form. Steel pipes having the desired length and diameter were then bolted to the form.

All vessels were cast in three batches. The first two batches containing pea gravel aggregate, were used for the skirt of the vessel up to a level approximately 2-in. below the top of the inner form. The third batch, which contained a limestone aggregate, was used to complete the remaining skirt and head slab. The concrete was vibrated internally with an electric vibrator during casting. The sidewalls of the vessels were reinforced with 40 No. 4 rebars, providing a reinforcement ratio of approximately

one percent. The bars were placed longitudinally around the outside of the skirt with about a 1/2-in. cover provided.

After the concrete had been placed and vibrated, the surface was trowelled until the concrete had begun to set up. The oiled aluminum rods and penetration pipes were periodically twisted during this time until the concrete was firm enough to allow the pulling of the rods and penetration pipes. This was accomplished by first removing the 1/2-in. steel template and then very carefully rotating and lifting the rods and penetrations out.

The vessel and cylinders were then covered with wet burlap and plastic. On the second day after casting, the forms were struck and a grinder was used to smooth out any rough spots on the surface of the vessel head. The cylinders were removed from their forms and placed around the vessel and again covered with wet burlap and plastic. The wet curing process continued until the seventh day after casting.

A2.2 Circumferential Prestressing

The pressure vessels were circumferentially prestressed in the Civil Engineering Machine Shop on a specially built prestressing rig. The 0.08-in. diameter wire was applied in a series of five "belts" as shown in Fig. A.2. Each of the five "belts" contained between 290 and 300 wraps of wire applied in six layers of about 50 turns each. The wires in each band were kept from slipping out of position by a series of steel plates bolted into coupling nuts cast into the concrete. The coupling nuts were cast into the vessel by drilling holes in the outer form and bolting them from the outside against the inside of the form. A 0.5-in. washer bolted to the coupling nut provided

bearing for anchorage. When the forms were struck, the bolts were unscrewed and the forms removed, leaving the openings of the nuts exposed. Screw-in clamps on each of the bands served as tie-offs for the beginning and end of each band of prestressing wire.

The prestressing operation was initiated by securing the wire in one of these clamps. The first wrap of prestress was applied at a reduced load to facilitate the proper alignment of the wire on the vessel. Subsequent wraps of the 0.08-in. diameter wire were applied at a tension of between 700 and 730 lbs. Ten steel rods were used to bolt the vessel securely on the lathe.

A schematic diagram of the prestressing apparatus is shown in Fig. A.3. The extra high strength wire was shipped in coils weighing around 500 lbs. It was necessary to rewind the coils of wire on a large spool to provide a more uniform rate of feed. The spool of wire was then mounted on a stand at the rear of the prestressing rig. A rope was wrapped around the spool axle and kept taut during the entire operation. This prevented the feed spool from gaining momentum and letting out more wire than was needed. The wire was first passed around a friction pulley a total of five times and then pulled over the first of the mounted pulleys. The wire was then passed under the pulley mounted on the 1500 lb. weight and back up and over the second mounted pulley. Finally, the wire was passed under a smaller pulley attached to a dynamometer and secured on the vessel (Fig. A.4).

Two automotive brakes were mounted on the axle of the friction pulley and they ultimately controlled the rate at which the wire was fed from the spool. It was the brakeman's function to control the rate of feed so that it equalled the rate at which the rotating lathe wrapped the wire onto the

vessel. The brakeman was able to gage this proper rate by watching the suspended 1500 lb weight and its relative motion. If the weight was rising, that indicated that the lathe was taking on wire faster than the spool was feeding it. Thus, the pressure on the brake had to be reduced. Conversely, if the weight was descending, the brake pressure had to be increased. Once the wrapping operation was begun, the weight was kept suspended at all times to maintain full tension in the wire. Approximately two hours was required to wrap one "belt" of 295 turns.

After all five bands had been applied, the vessel was unbolted from the turret lathe and inspected for cracks. In each case, a series of two or three circumferential cracks was found on the inside walls of the vessel at a spacing of approximately nine in. from the open end.

The dynamometer or load cell attached to the last pulley was connected to a strip chart and continuous strain readings were taken during prestressing. From these readings, a value for the average tension in the wire was obtained.

The effective prestress was determined with the help of information on shrinkage and creep characteristics of the concrete used (Reference 1, Vol. II, Fig. A.3). The "anchoring" stress for each wrap was measured. The instantaneous stress reduction on each wrap caused by subsequent wraps was calculated using a linear elastic model of the vessel. The following expressions, based on experimental data, were used for time-dependent strain changes in the concrete:

$$\varepsilon_c = \frac{10^{-3}}{1250 + \frac{30{,}000}{t_p}} \qquad (A.1)$$

$$\varepsilon_{sh} = \frac{1}{1700 + \frac{30{,}000}{t_c}} \qquad (A.2)$$

where ε_c = creep strain per psi

ε_{sh} = shrinkage strain

t_p = time after prestress, days

t_c = time after casting, days

Both expressions are intended to apply to the concrete used and for values of t less than 120 days. The rate-of-creep method was used to determine the effective prestress with an integration interval of one day. The calculated reduction in stress for the prestressing bands near the end slab ranged from approximately 15 to 20 percent (Table A.2).

A2.3 Longitudinal Prestressing

Sixty Stressteel bolts were used to prestress all of the vessels. Strain gages were placed on 15 of the rods and were calibrated in the laboratory. Loading of the bolts was accomplished with a 30-ton Simplex jack with the scheme shown in Fig. A.5. A continuous steel plate 1 1/4-in. thick was used as a bearing plate. The fifteen gaged rods were pulled first, with strain readings taken before and after. The load in the bolts after the jack was released varied from 40 to 45 kips. After the rest of the bolts were prestressed the gaged bolts registered loads of less than 40 kips. This loss was attributed to the effects of creep and to the fact that the loading of a bolt adjacent to an already loaded bolt tended to reduce the force in the loaded bolt. To minimize this effect, the rods were pulled a second time in the

same manner. In this way, a force approaching 45 kips was attained in each of the rods. A final set of readings from the gaged bolts was taken immediately before the test so that the vertical prestressing force was known at the time of the test.

A2.4 Liner

A detail of the typical liner used for all the vessels is provided in Fig. A6. For the vessels having penetrations, steel plugs or plates were used to cover the holes on the inside of the vessel (Fig. A.7). A welded steel can, 0.104-in. thick, was then grouted into place with the use of an electric vibrator. The 16-oz. soft copper can was soldered in next with all copper to copper and copper to steel connections tinned and sweated. The vessels were then lightly prestressed longitudinally and pressurized to 50 psi gas pressure to check for leaks. A layer of 1/16-in. thick neoprene was placed over the copper and secured with rubber cement and General Electric Silicone Caulking. A 3/4-in. neoprene O-ring was also installed at the junction of the end slab and the sidewall. An aluminum expansion ring was used to hold the neoprene securely in place around the bottom of the sidewall. The seal between the steel base plate and the sealing ring was made by compressing a 0.210-in. O-ring into the groove in the base plate (Fig. A.8).

A3 TEST SETUP

All testing was conducted in the basement at the east end of the Civil Engineering Building. The vessels, having been lined and prestressed, were transported by crane and fork lift to the test room. On the day prior to testing, the vessels were filled with water to within approximately 1/2-in. of the end slab. An oil pump was used to pressurize the vessel to failure. This procedure greatly reduces the violent release of energy that occurs when using gas pressurization. However, it was still necessary to contain the explosion by the use of steel channels bolted across the top of the prestress rods in a criss-cross pattern (Fig. A.9).

During the tests, the door to the test room was barricaded and warning signs were posted in all adjacent corridors. All operations were conducted remotely in an area at the east end of the Crane Bay, directly above the test room located in the basement. Here strain measurements were taken and recorded on a teletype equipped with a paper tape, deflection readings were taken from the two television monitors, and the internal pressure of the vessel was monitored and controlled by the test personnel.

A4 INSTRUMENTATION AND TEST PROCEDURE

In general, the instrumentation of the vessels consisted of deflection dials across one diameter of the head and down the side on a line at one end of this diameter, strain gages on the inside surface of the head and the surfaces of the penetration walls and load cells on the fifteen prestressing rods.

Deflections across the head of the specimen and on the side wall were measured with 0.0005-in. Brown and Sharpe Dial Indicators. For PV 26 the dial gages were connected to push rod extensions in direct contact with the surface but due to the explosion at failure, all of the dials on top were destroyed. For PV 27, push rods were again used for the sidewall gages. However, the head dial gages were connected to piano wires which were strung over ball bearing pulleys and attached to metal tabs glued to the specimen. Tension springs connected to the back end of the dial gage plunger kept the piano wires taut. This system proved unsatisfactory due to the great amount of internal friction which markedly reduced the sensitivity of the gages. Thus, for PV 28, the head gages were mounted directly above the specimen and connected to piano wires running vertically down to the vessel head and attached to the metal tabs glued to the surface (Fig. A.10). The gages were protected from damage by a series of steel channels bolted over the head. This method proved satisfactory and was adopted for all subsequent tests. The dial gages were read with a closed circuit television hookup with the monitors situated on the first floor at the east end of the Crane Bay. Two television cameras equipped with telephoto lenses were used to read the deflection gages (Fig. A.11).

Strain gages were used on the inside surface of the concrete and in the penetrations were limited to two types: the BLH type A12 which has a one-in. gage length and 3/32-in. gage width, and the BLH type AR-2-S6 which is a rosette having a gage length of 3/4-in. and gage width of 9/64-in. Careful steps were taken to ensure a smooth surface and good bonding for all gages. The concrete surface was first sanded to a smooth finish. A hydrocal paste was then applied over the surface to fill in any holes or indentations. The surface was again sanded down and a layer of cement glue was placed on the concrete and allowed to set to a smooth, hard finish. The gages were then attached to this prepared surface with Eastman 910 cement (Fig. A.12). In addition, a soft rubbery protective coating was placed over all strain gages on the inside surface of the vessel. The wires from the inside gages were run down the inside wall of the vessel and out between the concrete skirt and the one-in. steel ring. Channels 1 in. wide by 1/8-in. deep were cast into the concrete to accommodate the gage wires.

Load cells were used to measure the changes in force in the prestress bolts. Four strain gages were cemented to the outside of these bolts and wired into a full bridge. Before they were used, the load cells were calibrated in a testing machine.

Strains were read by a Pivan switching strain indicator located at the east end of the Crane Bay in the Civil Engineering Building, directly over the testing room one floor below. The load cells were calibrated with a 10k ohm resistor while all others required a 60k ohm resistor.

Pressure was applied to the inside of the specimen by a high-pressure hydraulic pump with a maximum capacity of 10,000 psi. During a test the

gas pressure was increased in increments and once the pressure was set and became stable all measurements were taken. Approximately 3 to 4 minutes were usually required for each set of readings. The size of the pressure increments varied among the tests.

TABLE A.1

Concrete Properties

Mark	Age @ Test Days	Slump in.	Modulus of Elasticity psi x 10^6	Splitting Strength psi	Compressive Strength		
					Batch 1 psi	Batch 2 psi	Batch 3 (End Slab) psi
PV26	98	3 1/2	3.9	445	7320	7910	6710
PV27	102	4	3.8	460	7620	7610	6845
PV29	52	3/4	3.8	450	5760	6660	5480
PV28	117	2	3.9	440	7620	8120	6420
PV30	93	2 3/4	3.7	495	6350	5890	6300
PV31	85	2 1/2	3.7	380	4910	5890	4970
PV32	114	2 1/2	3.8	450	4940	5560	5720
PV33	95	1 1/2	3.7	375	5030	5670	4875
PV34	59	8	2.5	280	4950	4960	2440
PV35	84	8	3.0	380	6035	6530	3150

TABLE A.2

Longitudinal and Circumferential Prestress

Mark	Longitudinal Prestressing			Circumferential Prestress			
					Mean Force in Bands 1 & 2[b]		
	Age Days	Force per rod kips	Index[a] psi	Age days	Initial kips	Final kips	Final Index[c] psi
PV26.1	56	40.0	4890	19	199	159	1590
PV26.2	93	41.0	5010	--	199	155	1560
PV27	126	43.7	5340	27	194	156	1560
PV29	45	43.6	5330	29	199	171	1710
PV28.1	83	44.1	5390	56	203	175	1760
PV28.2	111	47.1	5760	--	203	170	1700
PV30	85	43.7	5340	30	206	169	1690
PV31.1	64	43.8	5350	30	201	171	1710
PV31.2	80	45.0	5500	--	201	168	1680
PV32	112	45.3	5540	83	203	178	1780
PV33.1	76	44.4	5430	34	205	173	1730
PV33.2	84	44.2	5400	--	205	170	1700
PV34	57	44.2	5400	36	202	170	1700
PV35	82	44.1	5390	44	201	168	1680

[a]Total force divided by horizontal cross-sectional area of cavity

[b]Mean force in bands 1 and 2 around end slab at time of prestressing

[c]Mean effective prestress in bands 1 and 2 around end slab at time of test

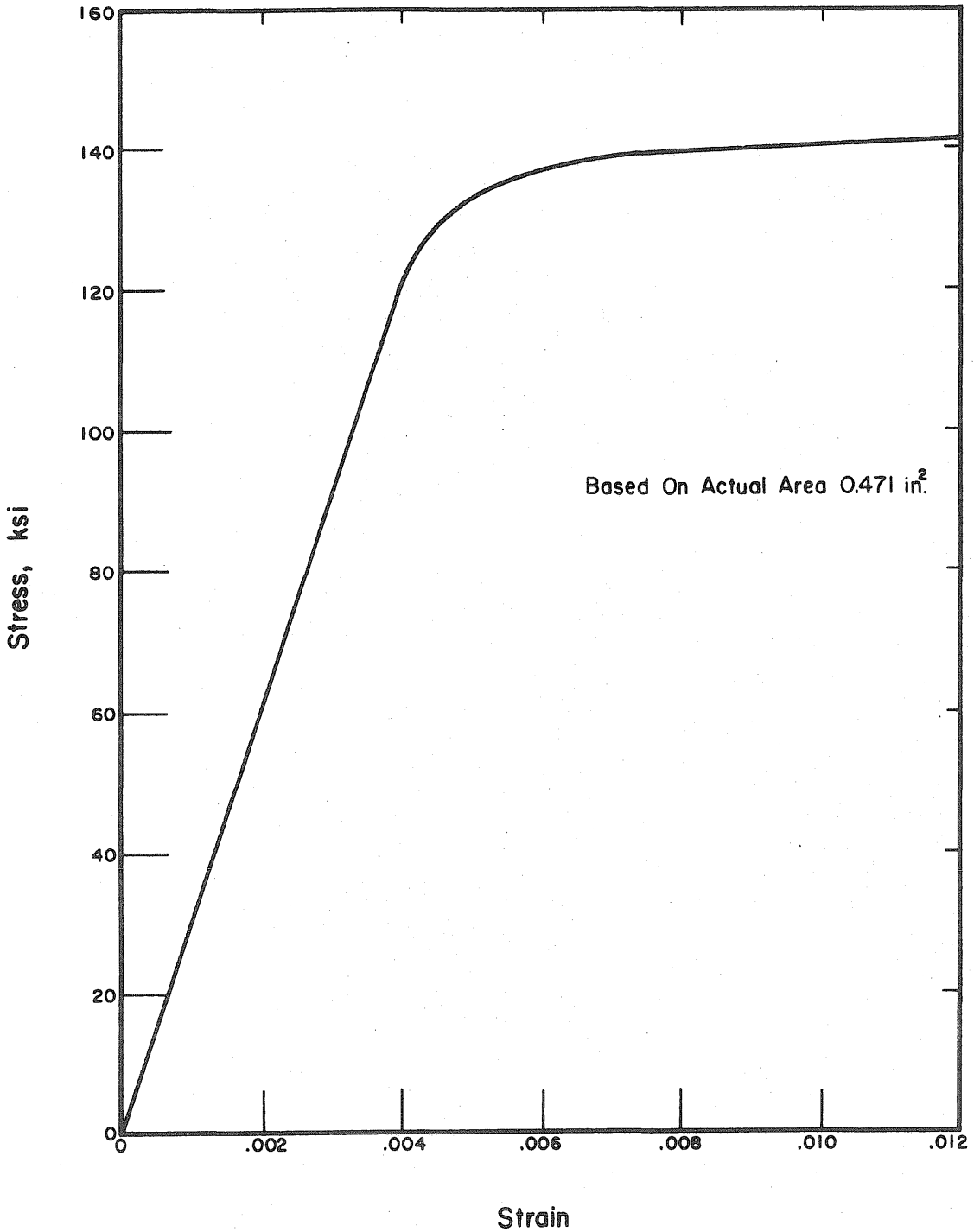

Fig. A.1 Stress-Strain Curve for Stressteel Rods

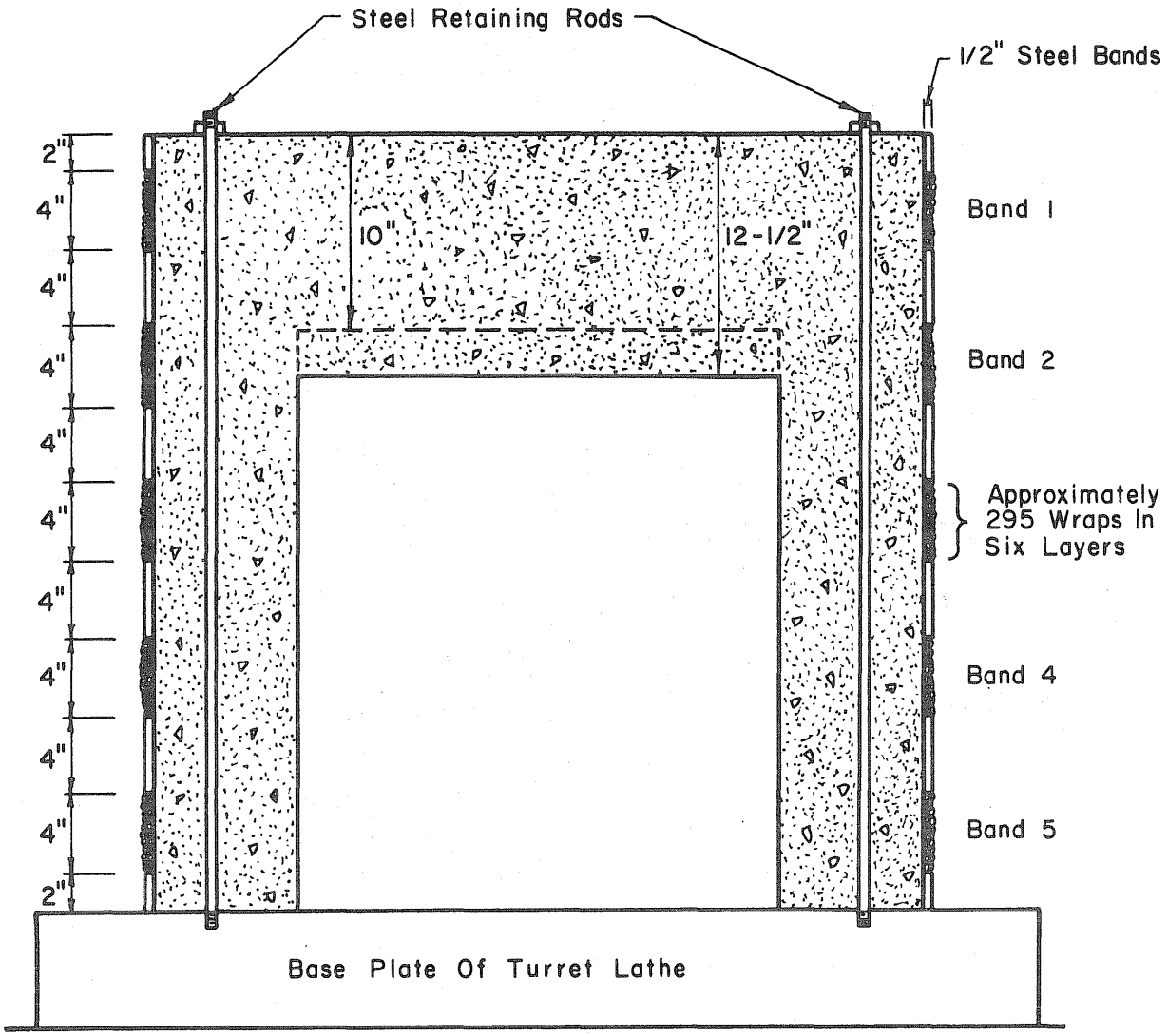

Fig. A.2 Locations of Bands of 0.08-in. Wire Used

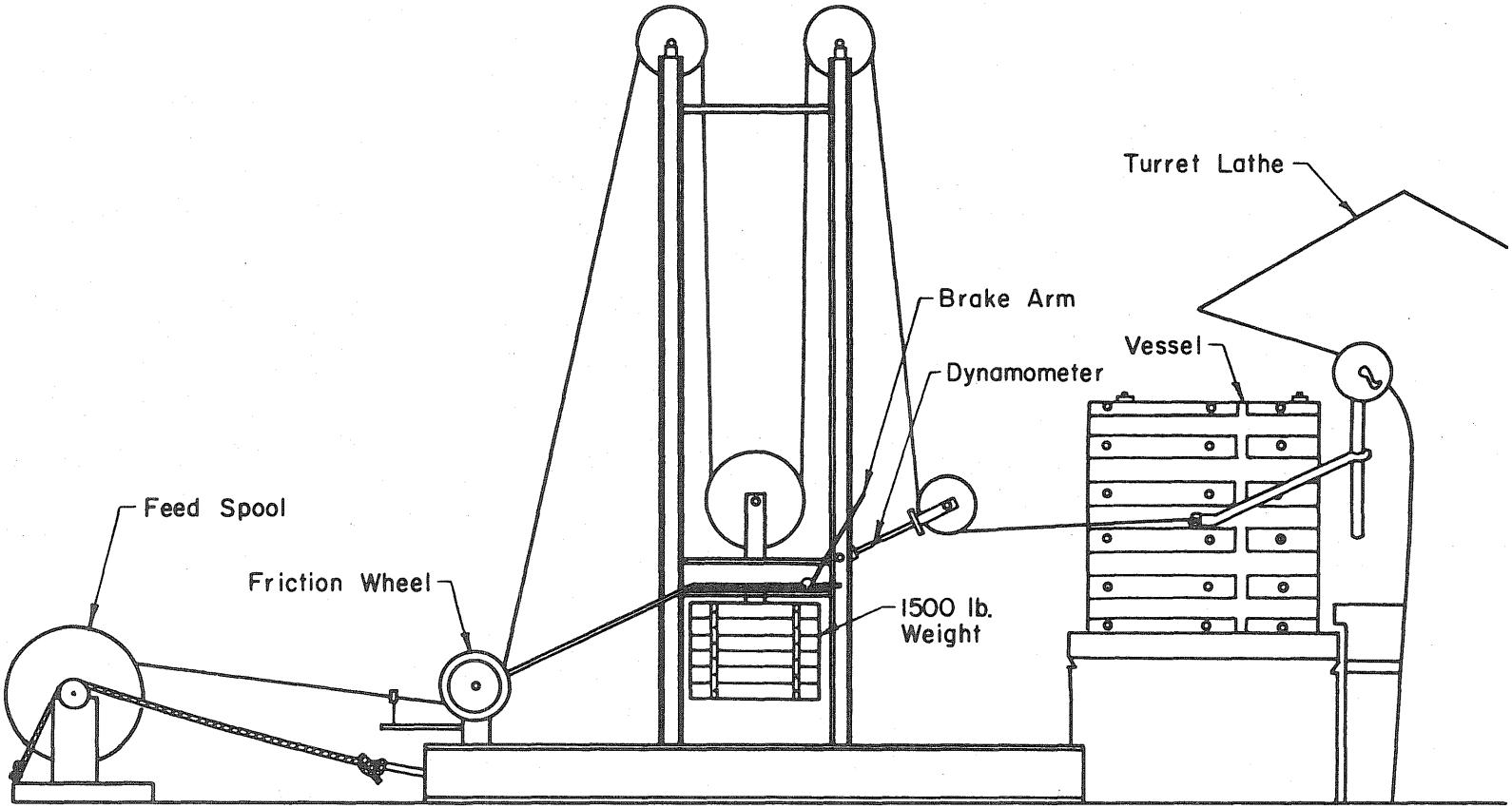

Fig. A.3 Schematic View of Circumferential Prestressing Rig

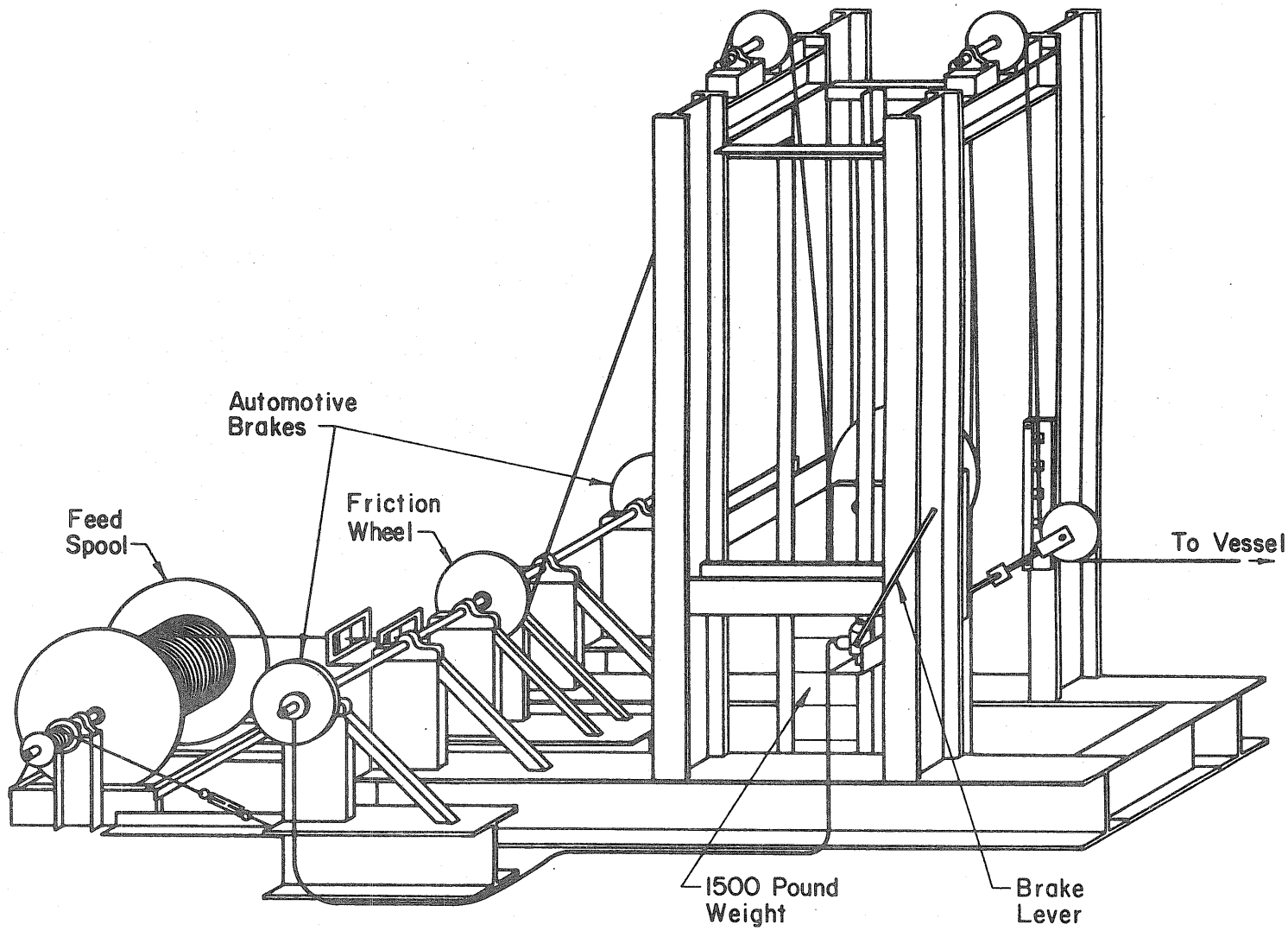

Fig. A.4 Isometric View of Prestressing Rig

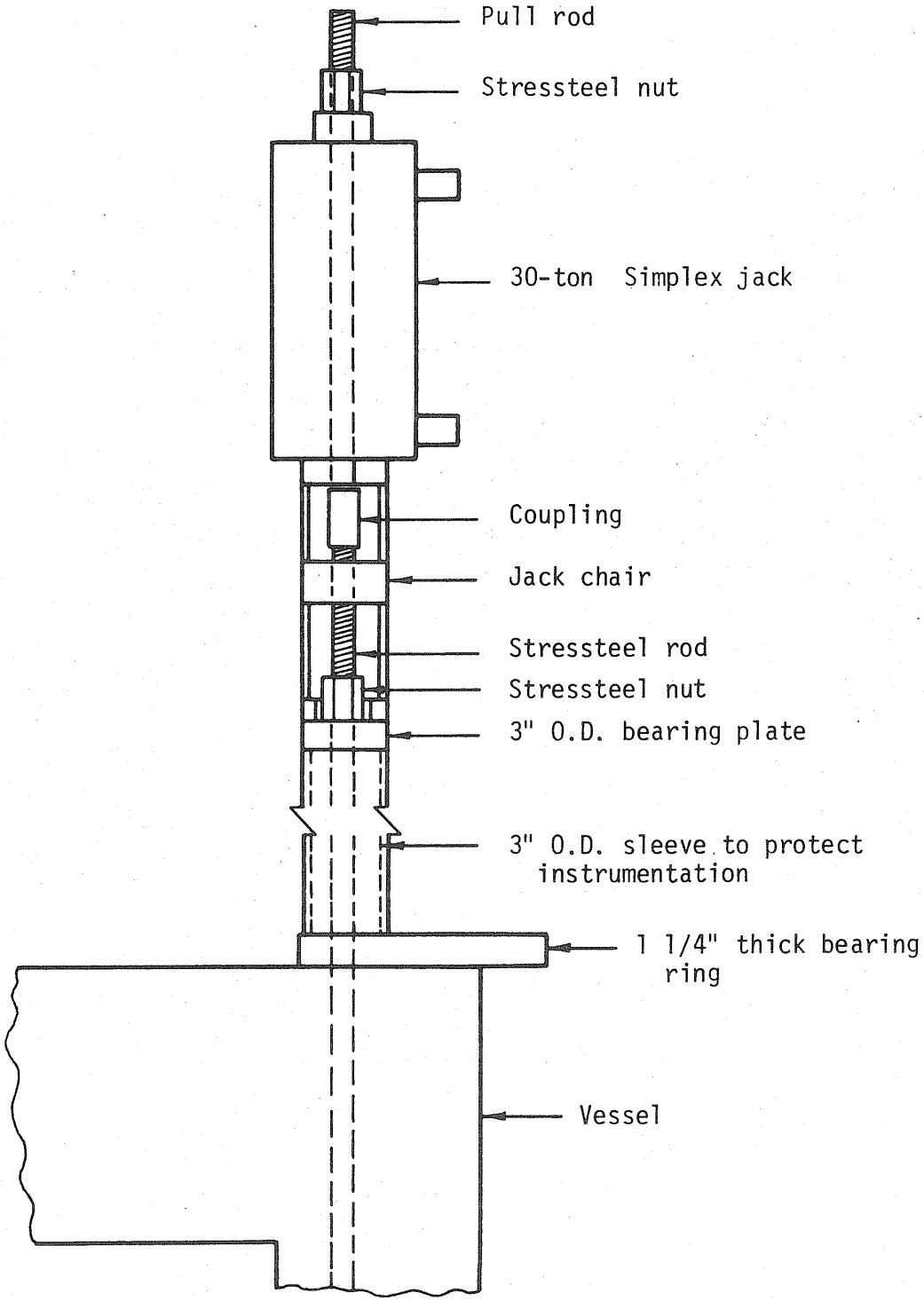

Fig. A.5 Apparatus Used for Longitudinal Prestressing

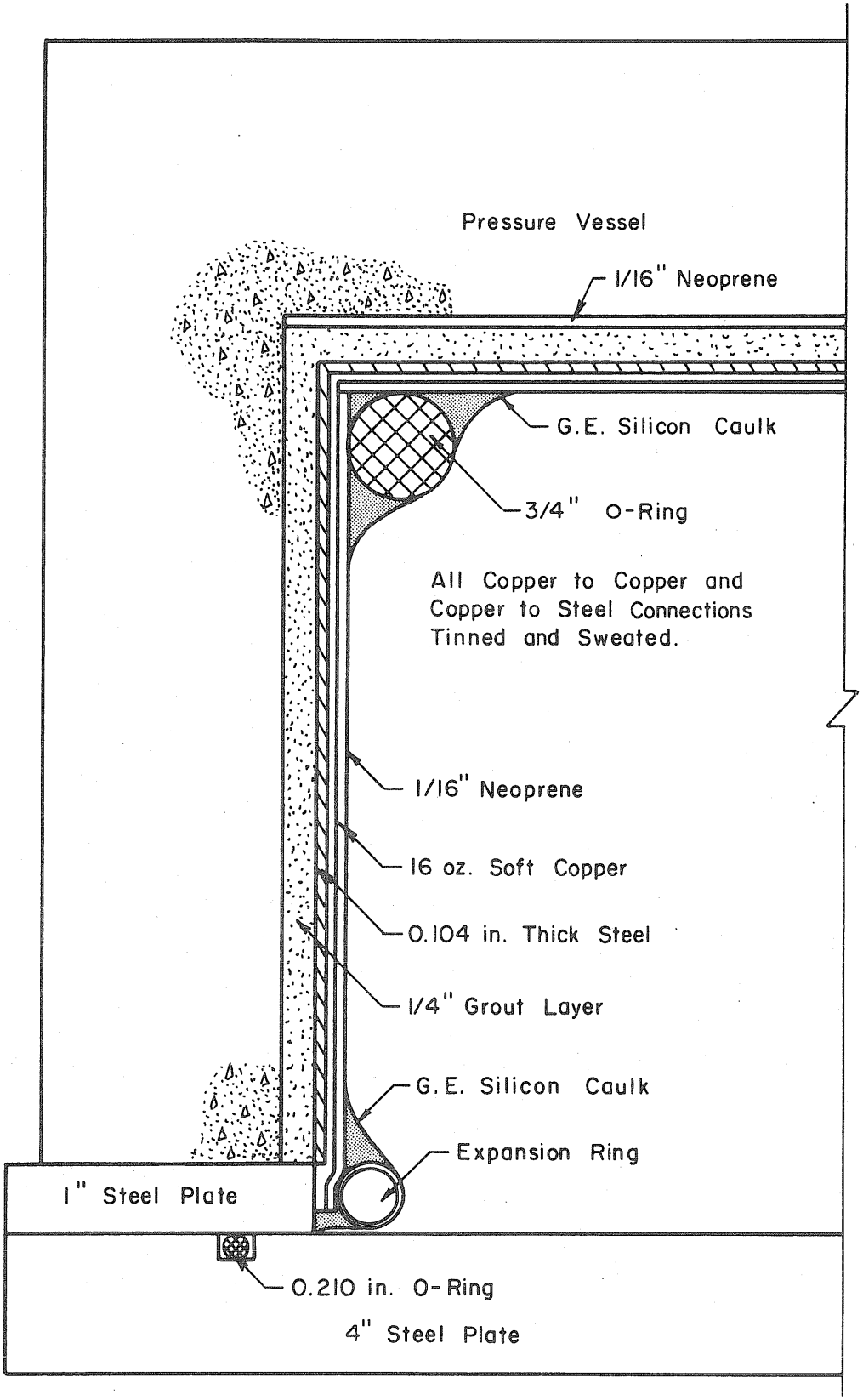

Fig. A.6 Typical Liner Details (not to scale)

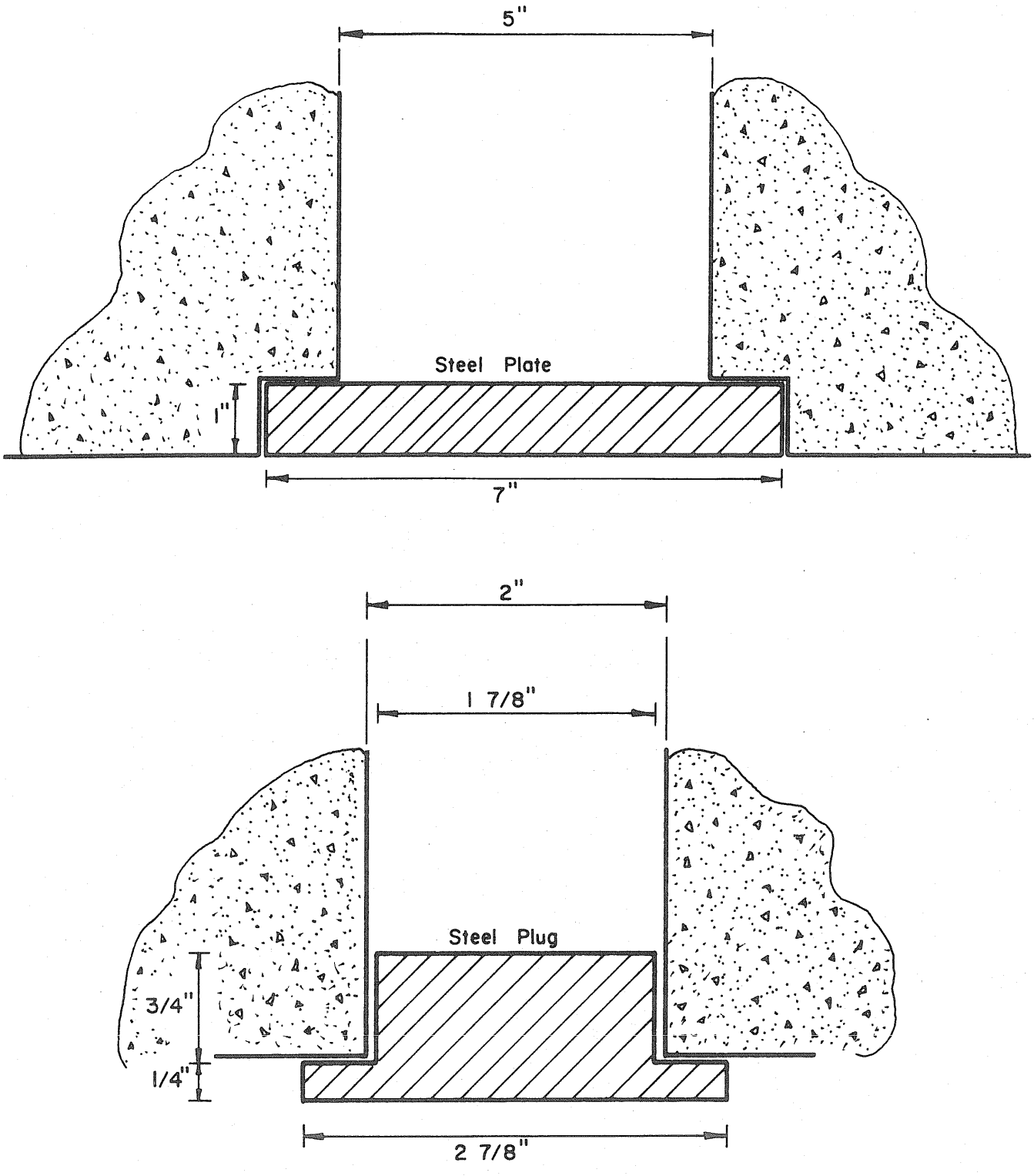

Fig. A.7 Steel Closure Plates

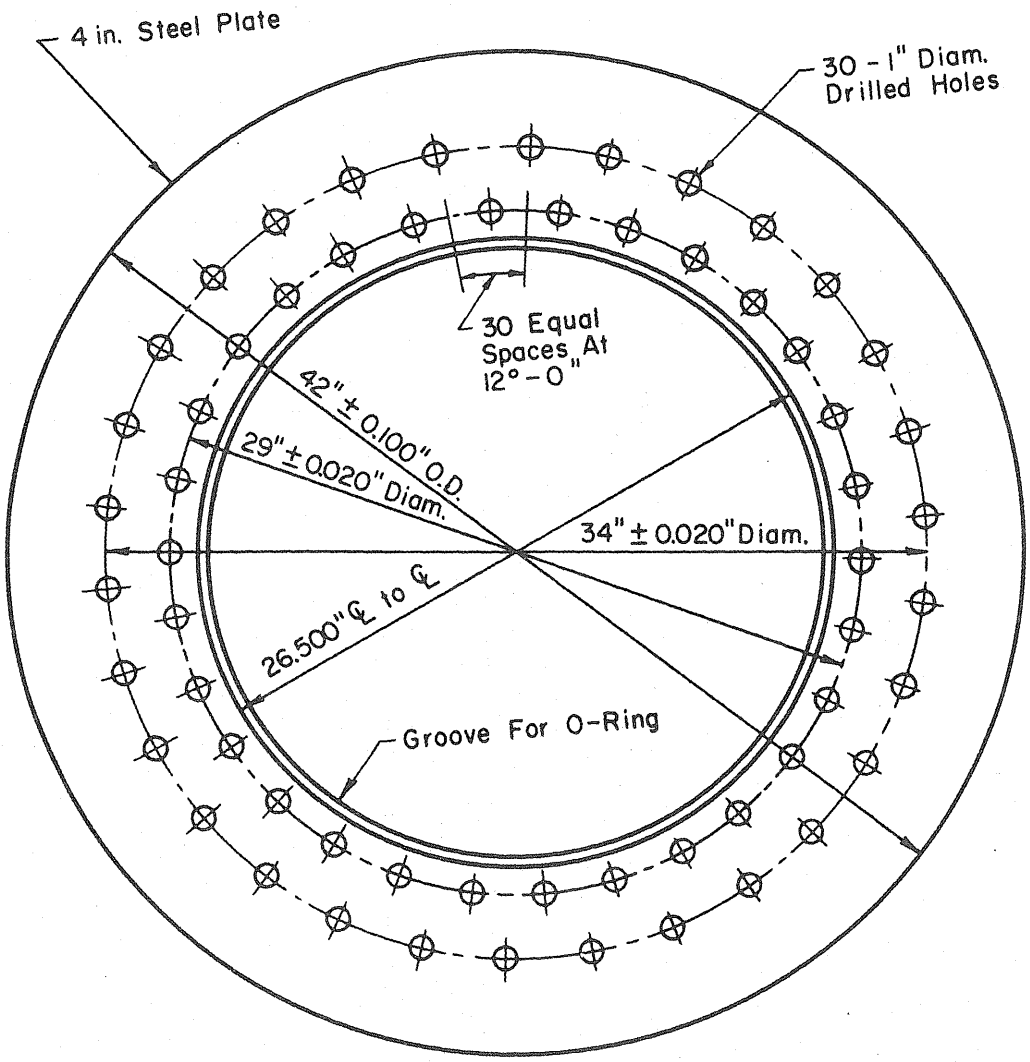

Fig. A.8 Steel Base Plate

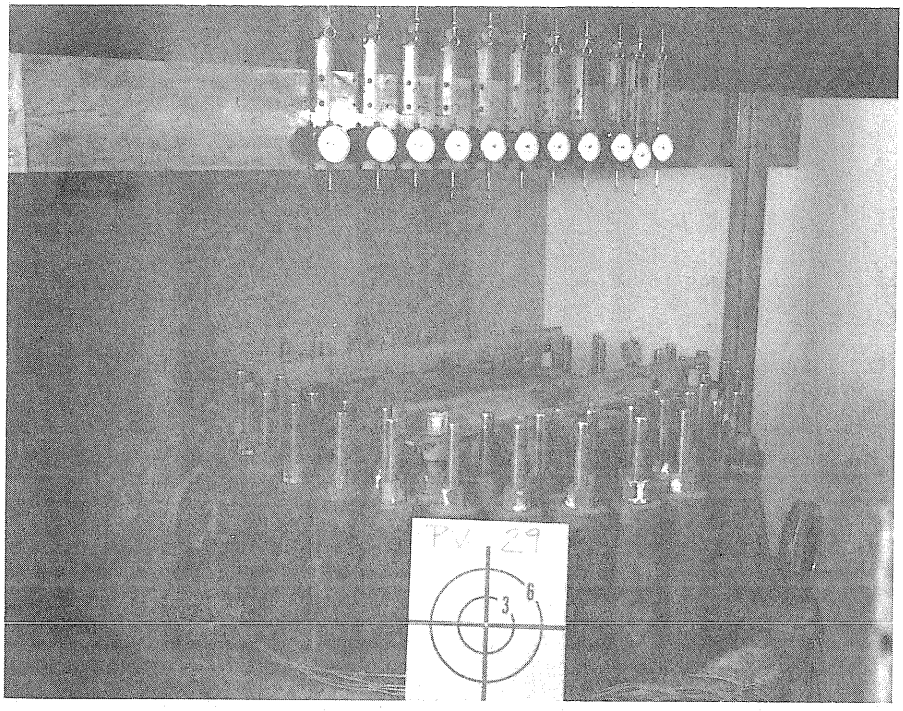

Fig. A.9 Protective Steel Channels Across Top of Vessel

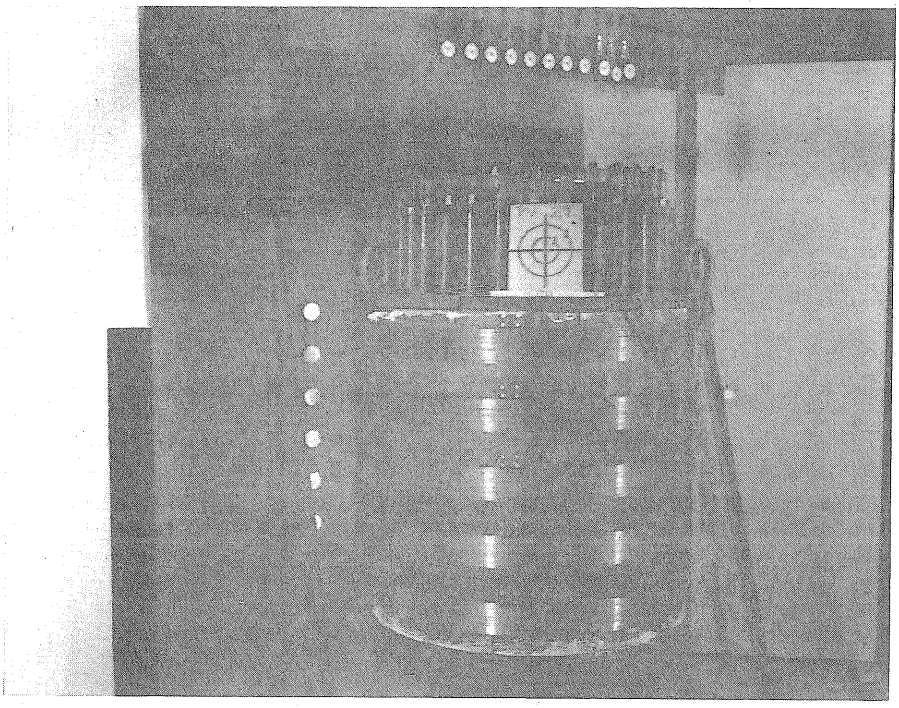

Fig. A.10 Dial Gages Measuring End-Slab Deflections

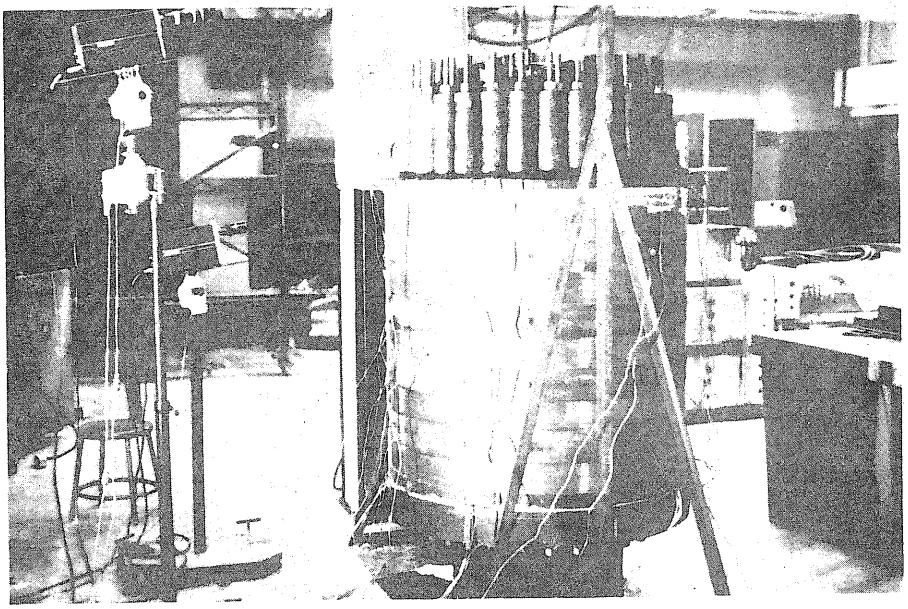

Fig. A.11 Closed-Circuit TV Cameras to Read Dial Gages

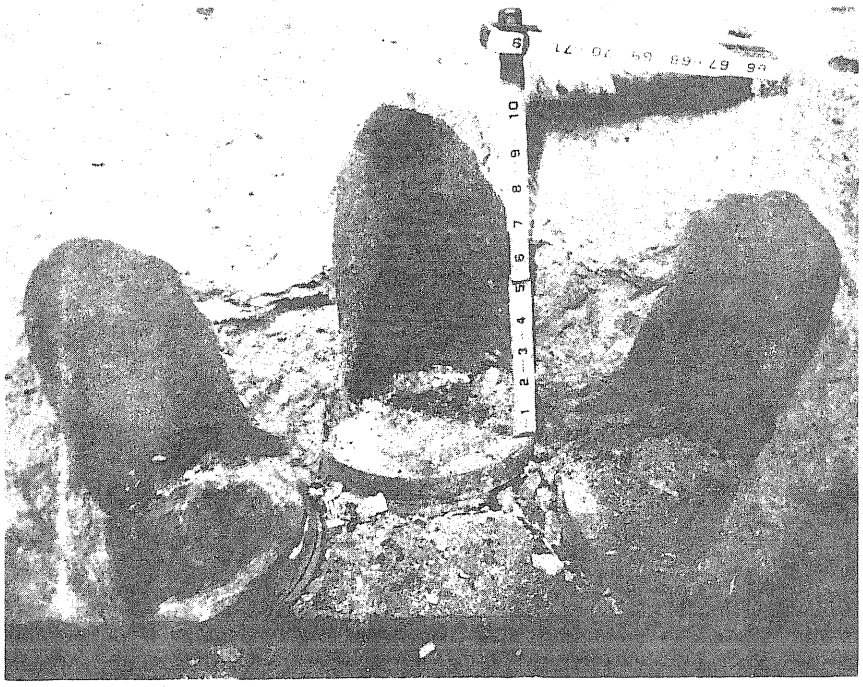

Fig. A.12 Strain Rosettes

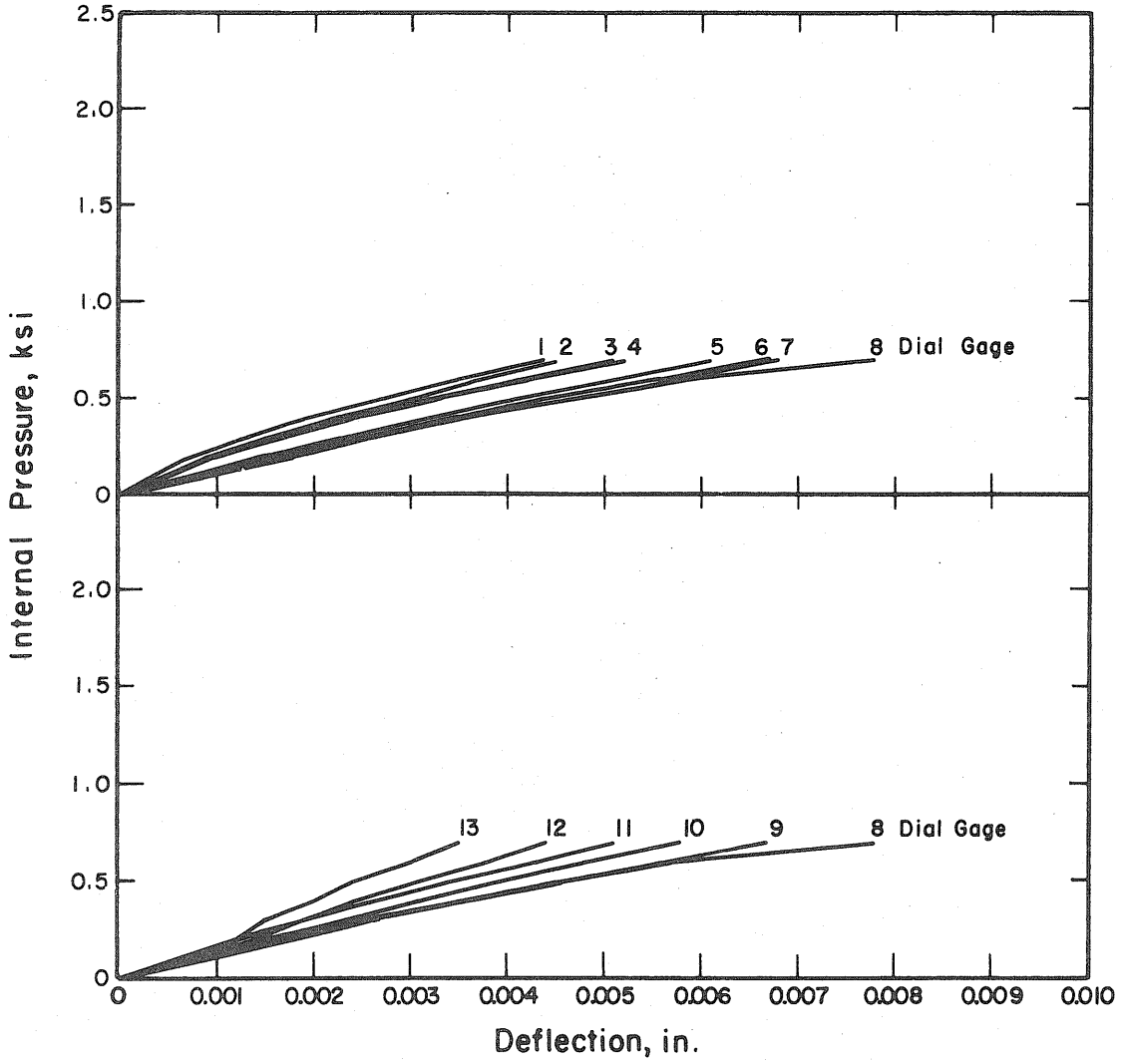

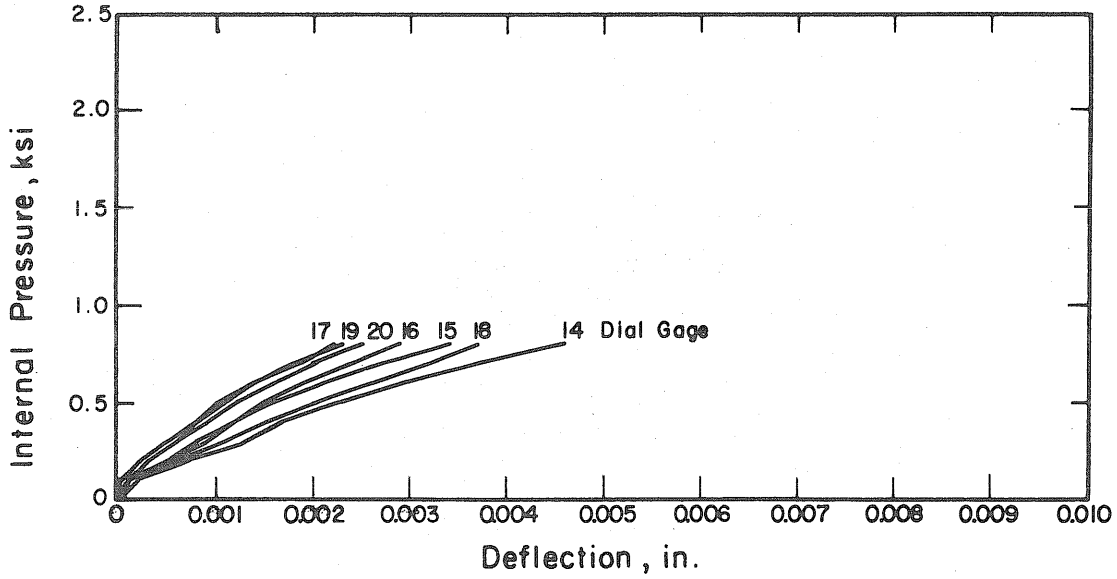

Fig. A.13 Measured Pressure-Deflection Curves, Test PV26.1

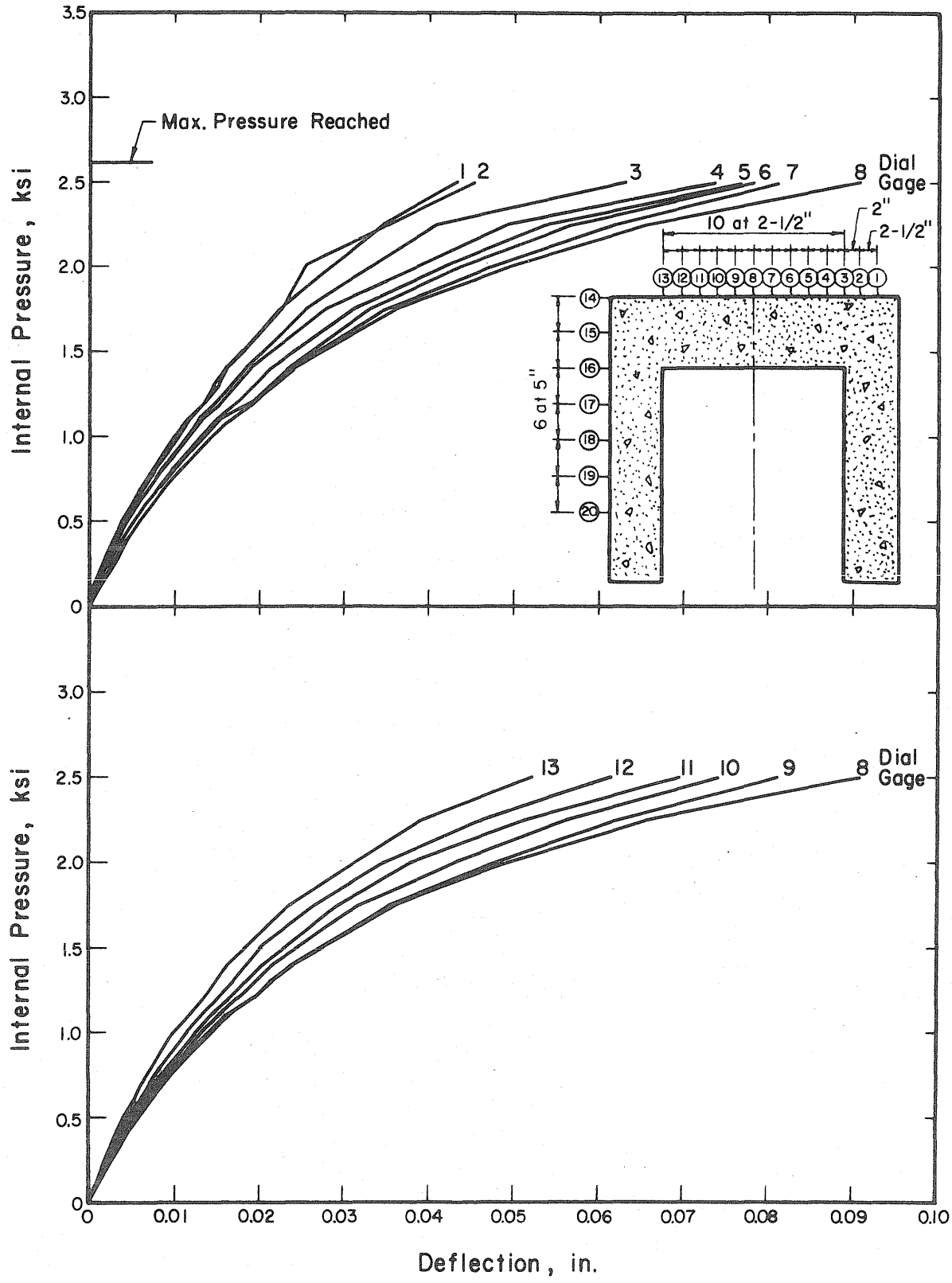

Fig. A.14 Measured Pressure-Deflection Curves End Slab, Test PV26.2

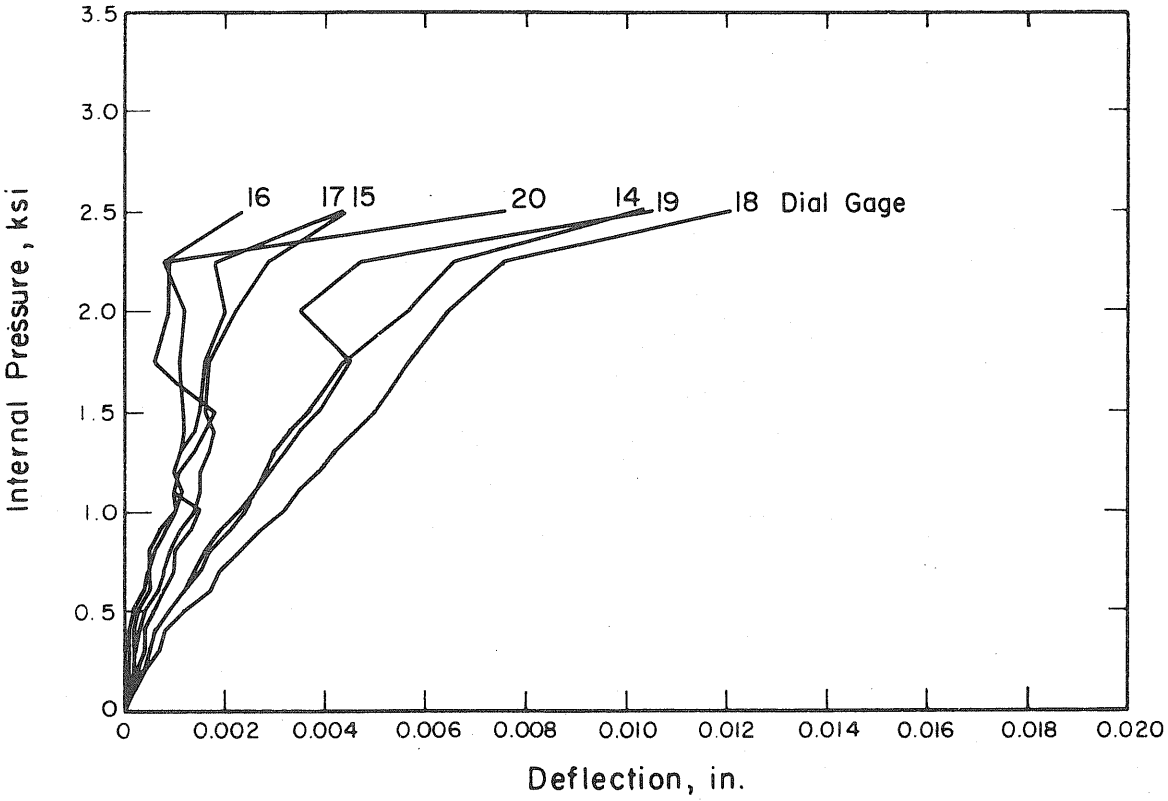

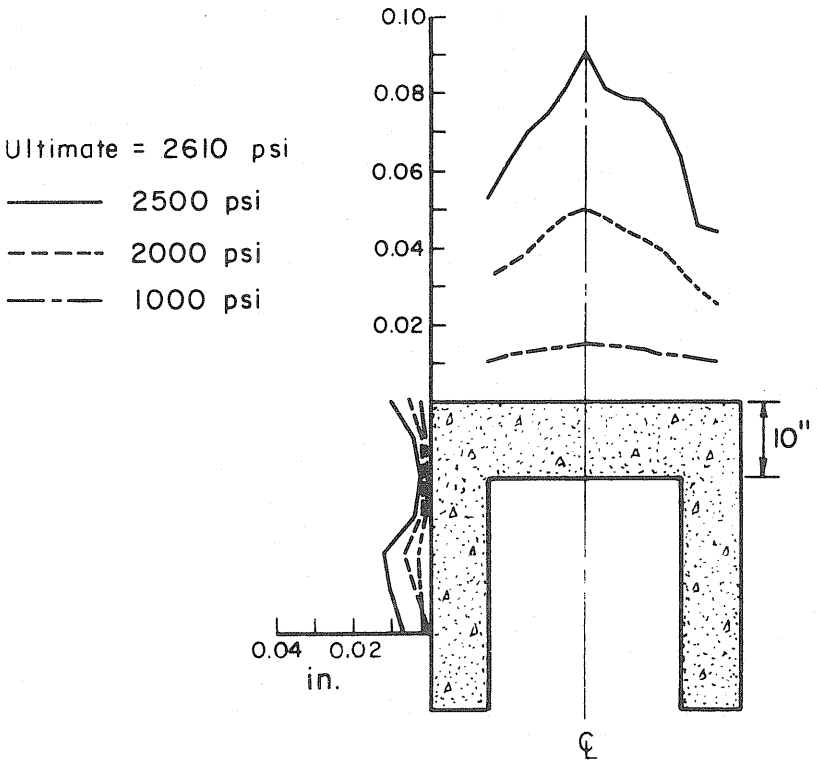

Fig. A.15 Measured Pressure-Deflection Curves Side Wall, Test PV26.2

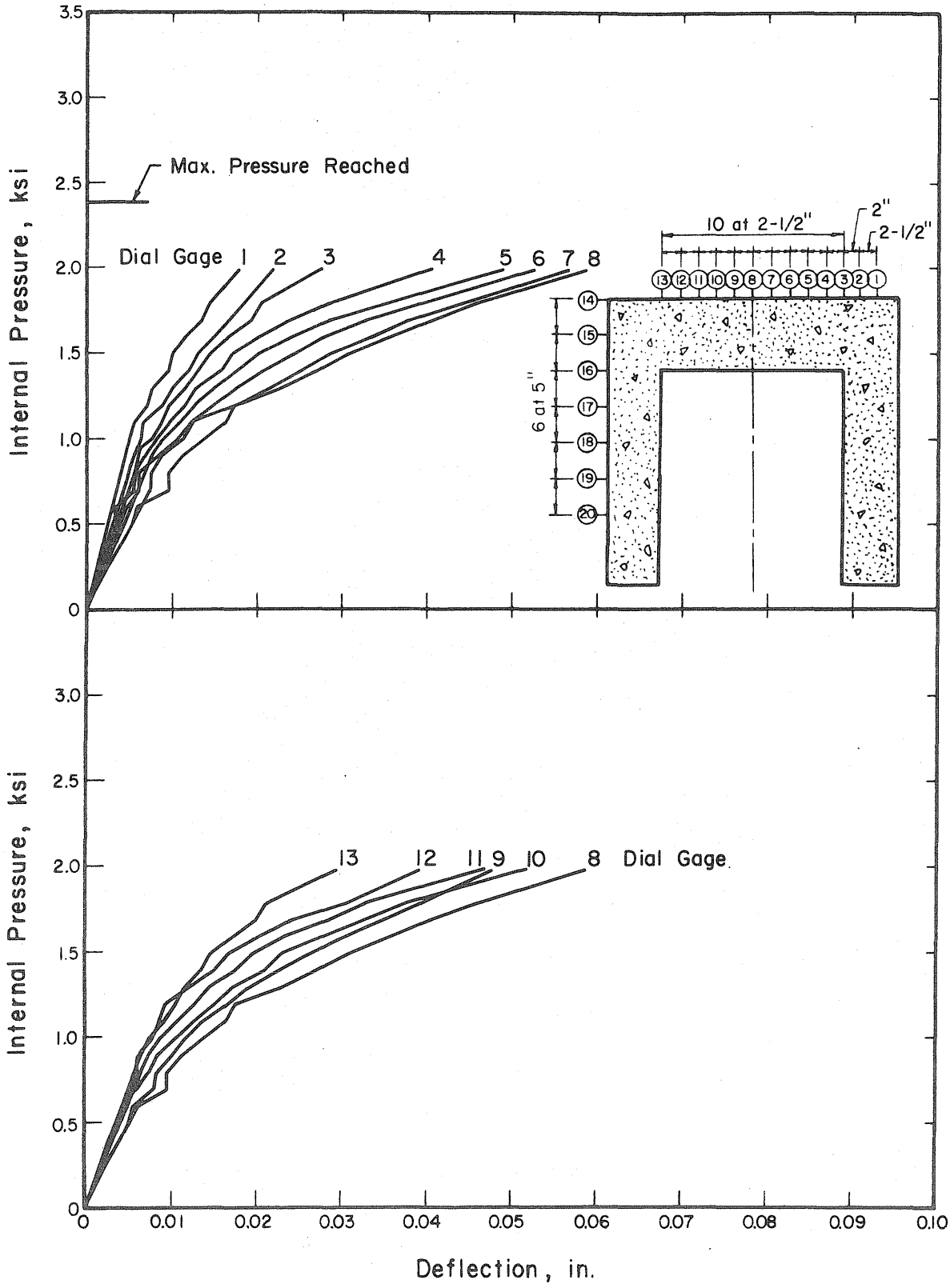

Fig. A.16 Measured Pressure-Deflection Curves End Slab, Test PV27

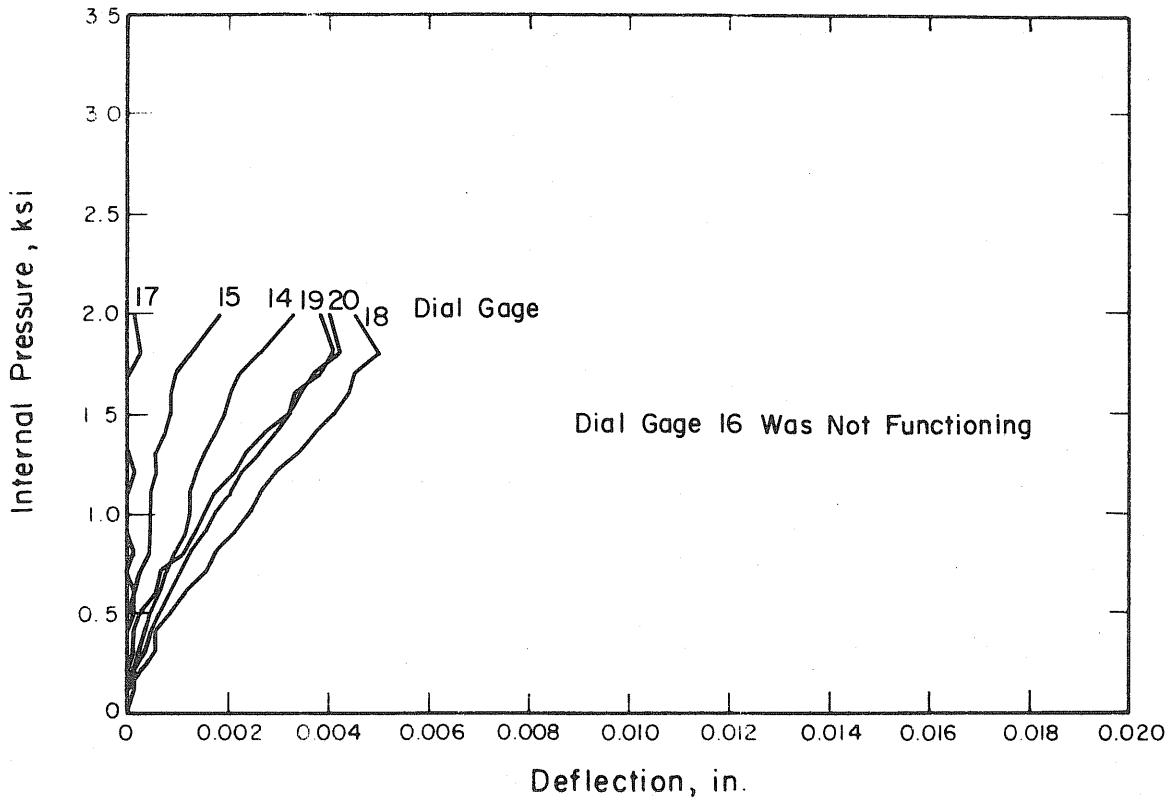

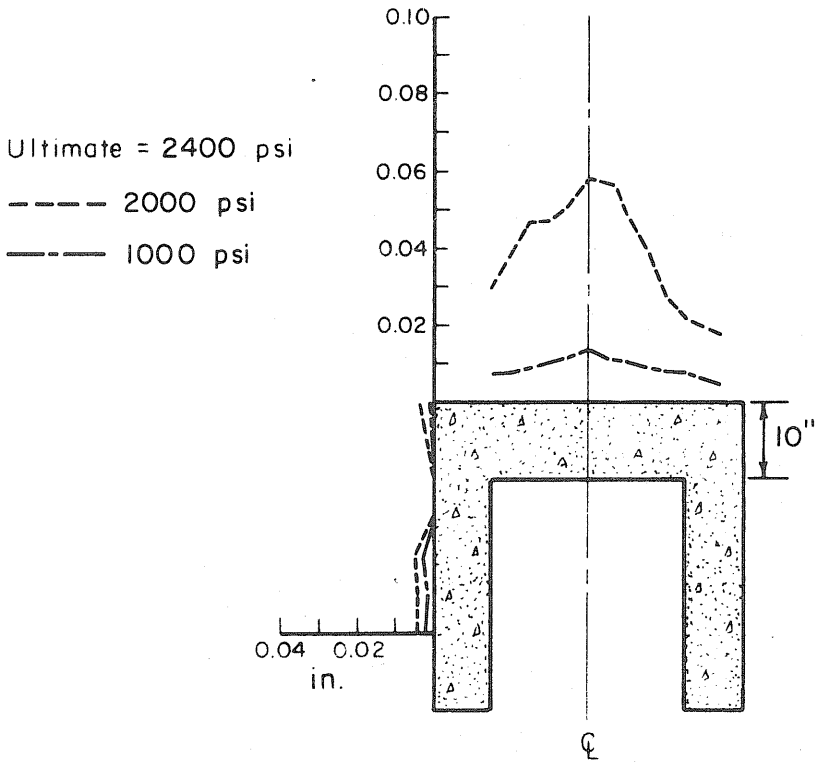

Fig. A.17 Measured Pressure-Deflection Curves Side Wall, Test PV27

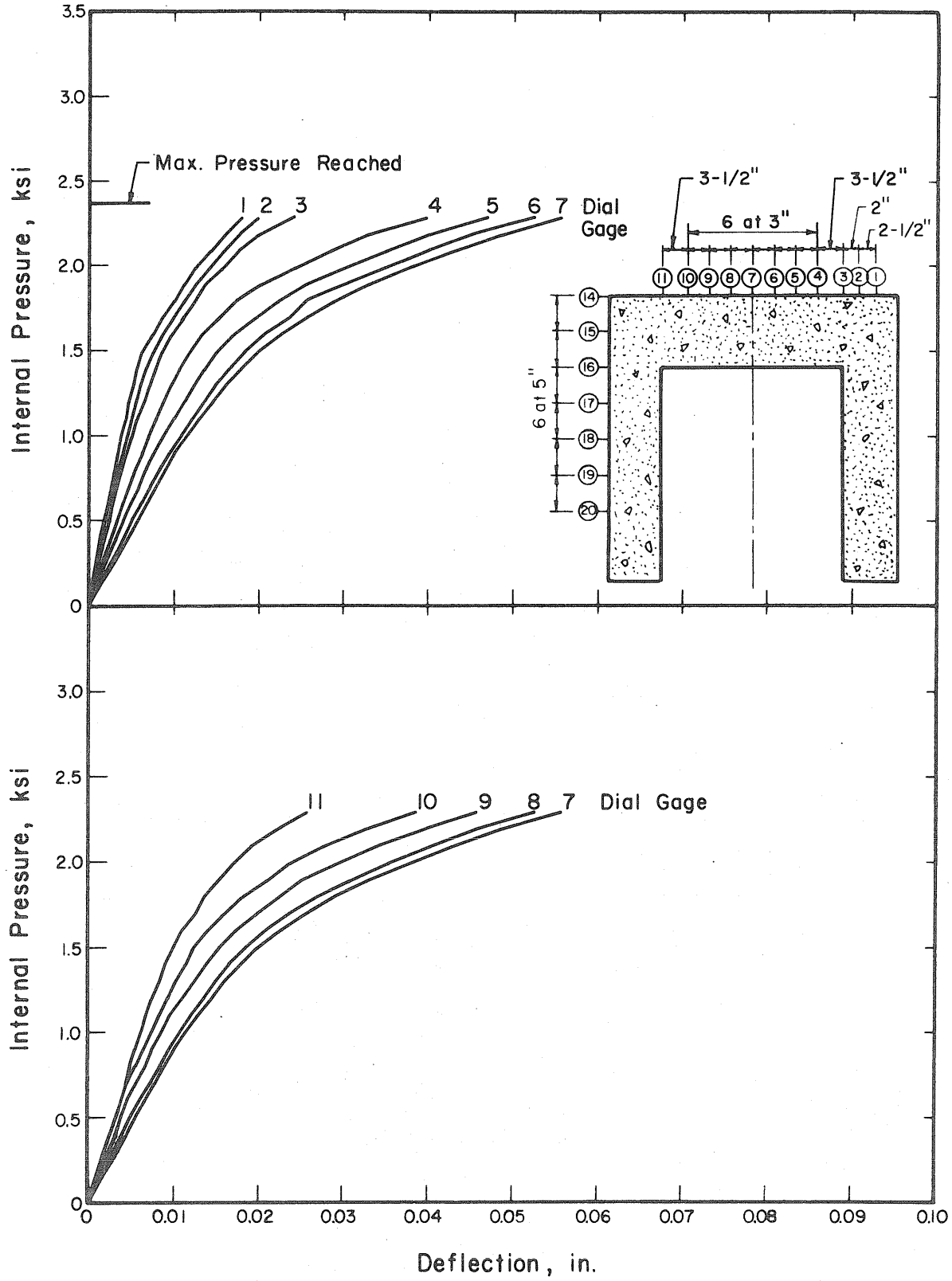

Fig. A.18 Measured Pressure-Deflection Curves End Slab, Test PV29

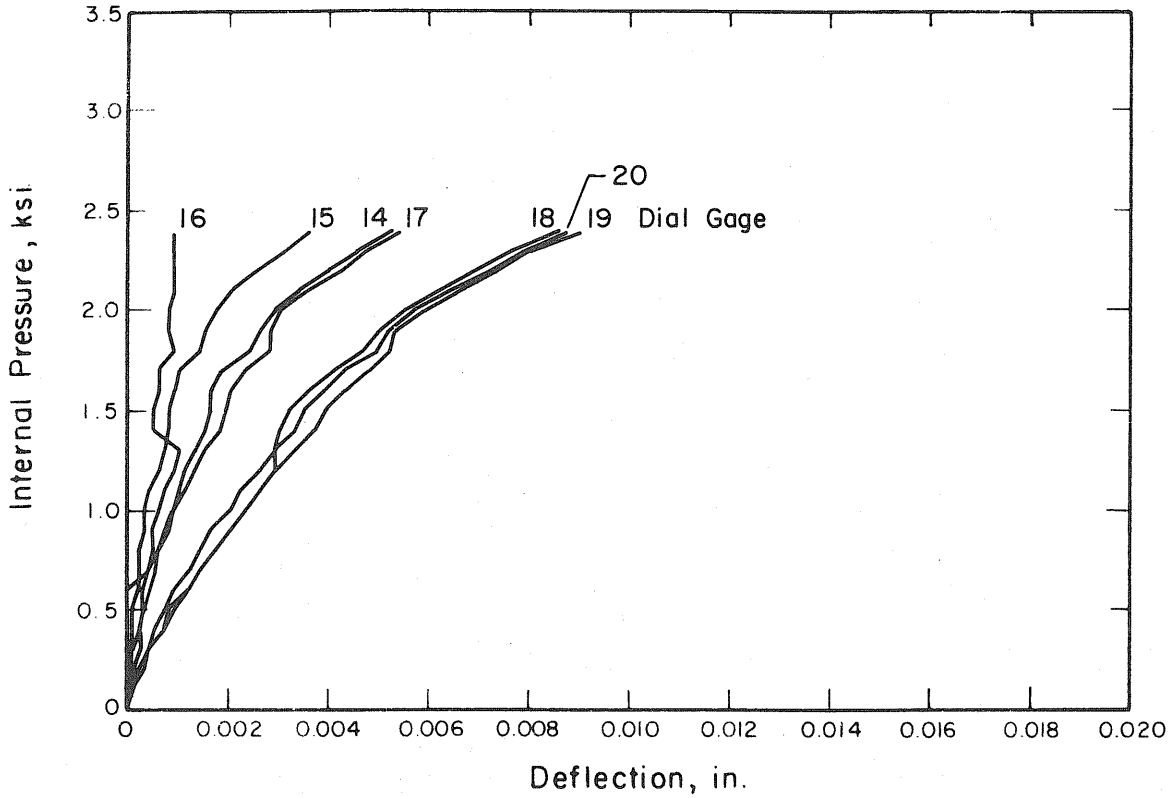

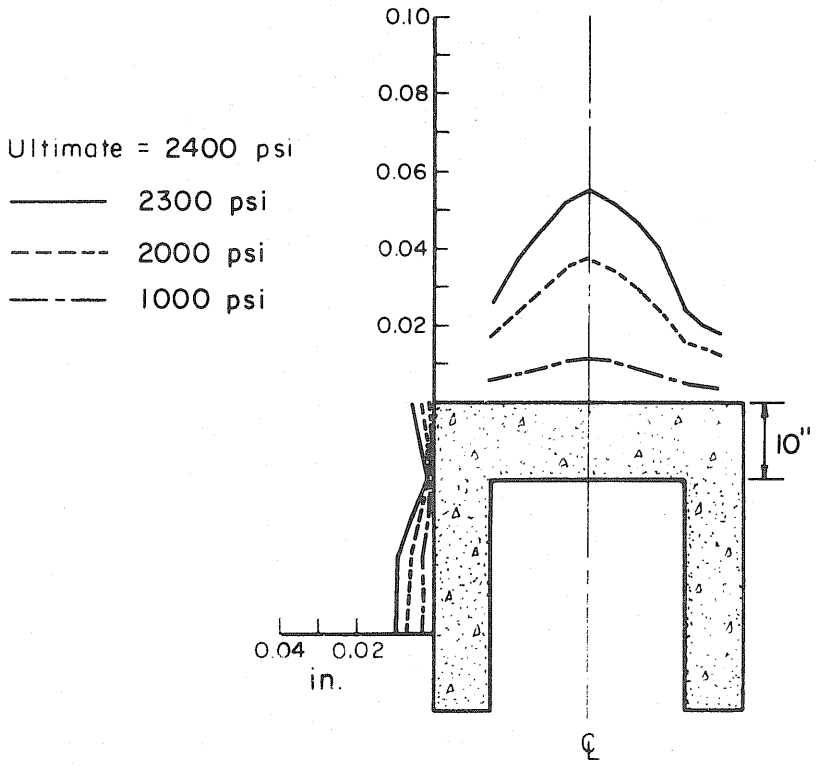

Fig. A.19 Measured Pressure-Deflection Curves Side Wall, Test PV29

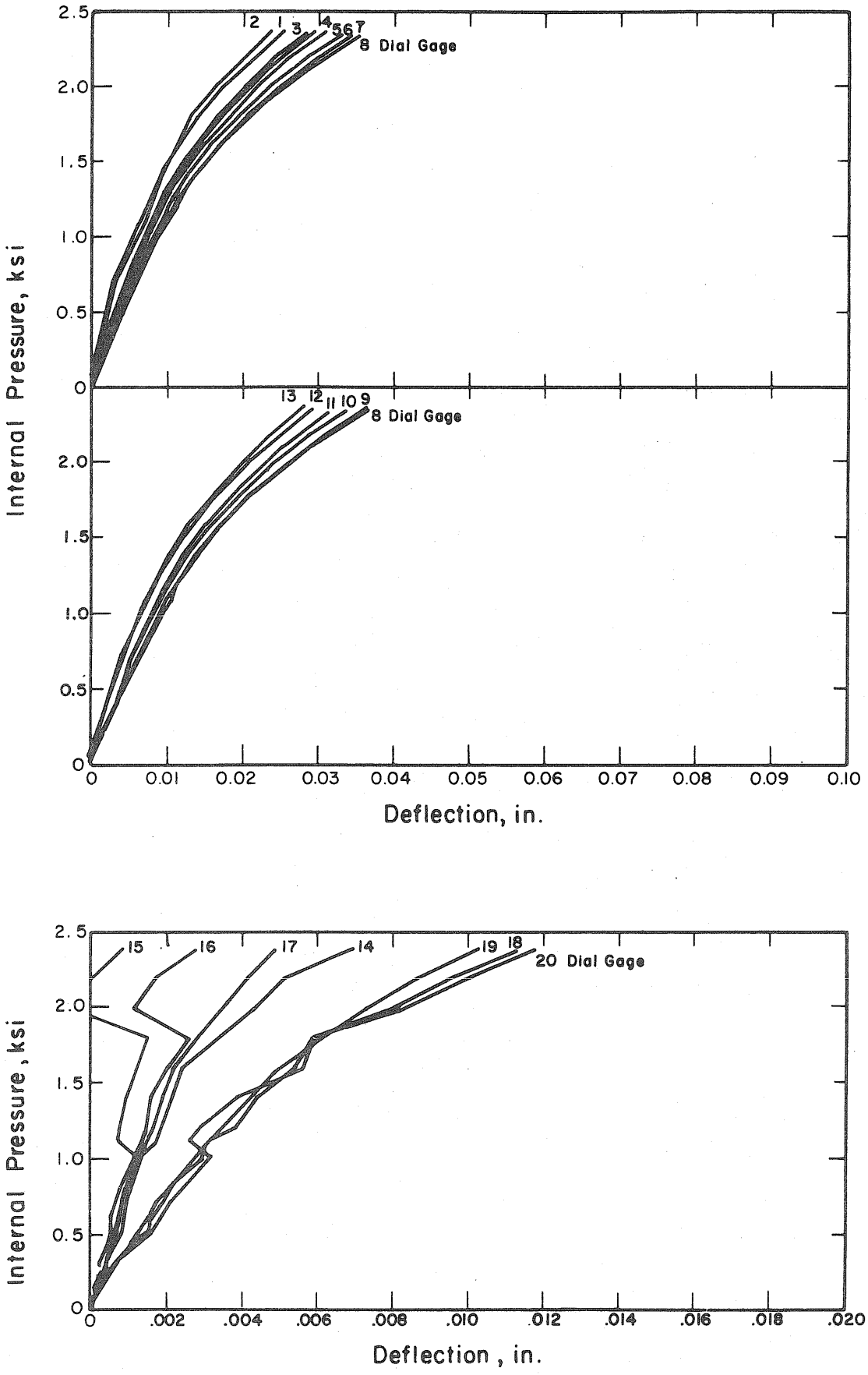

Fig. A.20 Measured Pressure-Deflection Curves, Test PV28.1

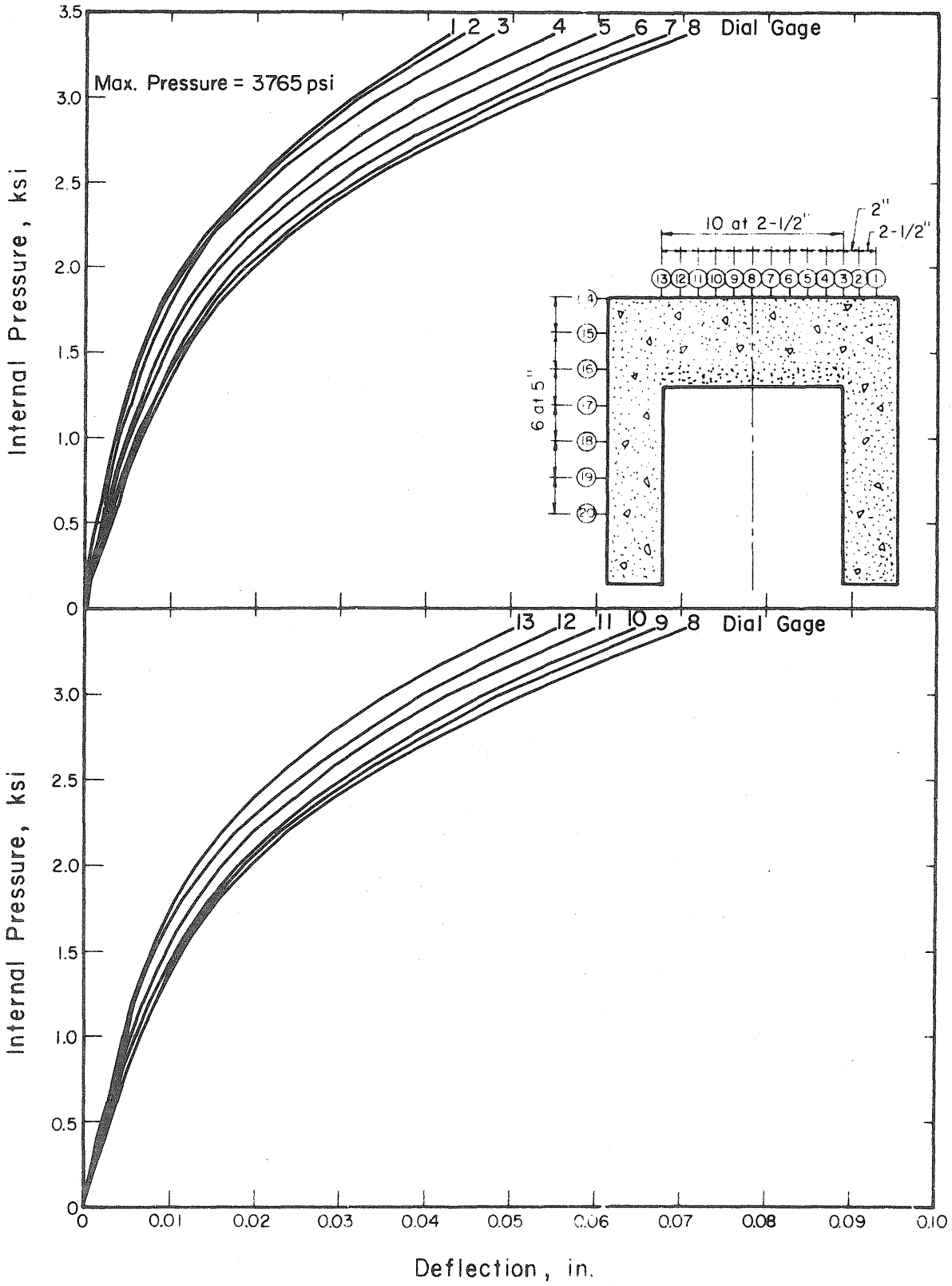

Fig. A.21 Measured Pressure-Deflection Curves End Slab, Test PV28.2

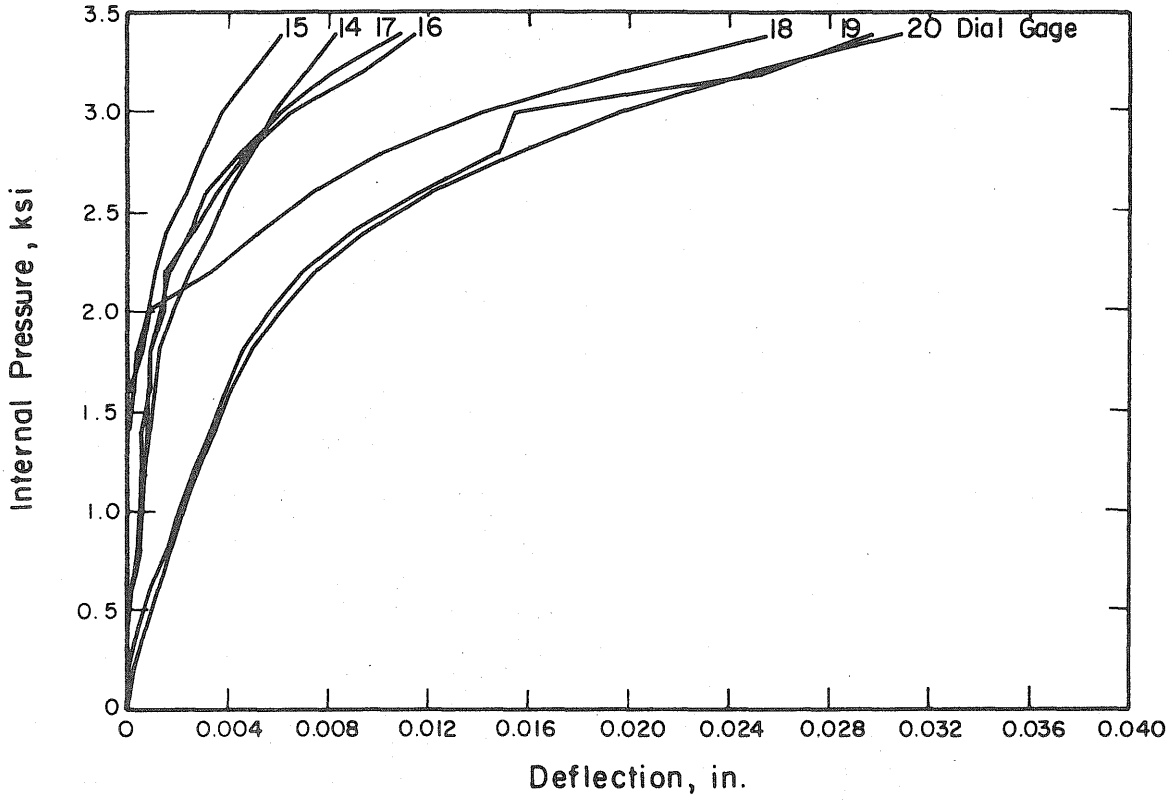

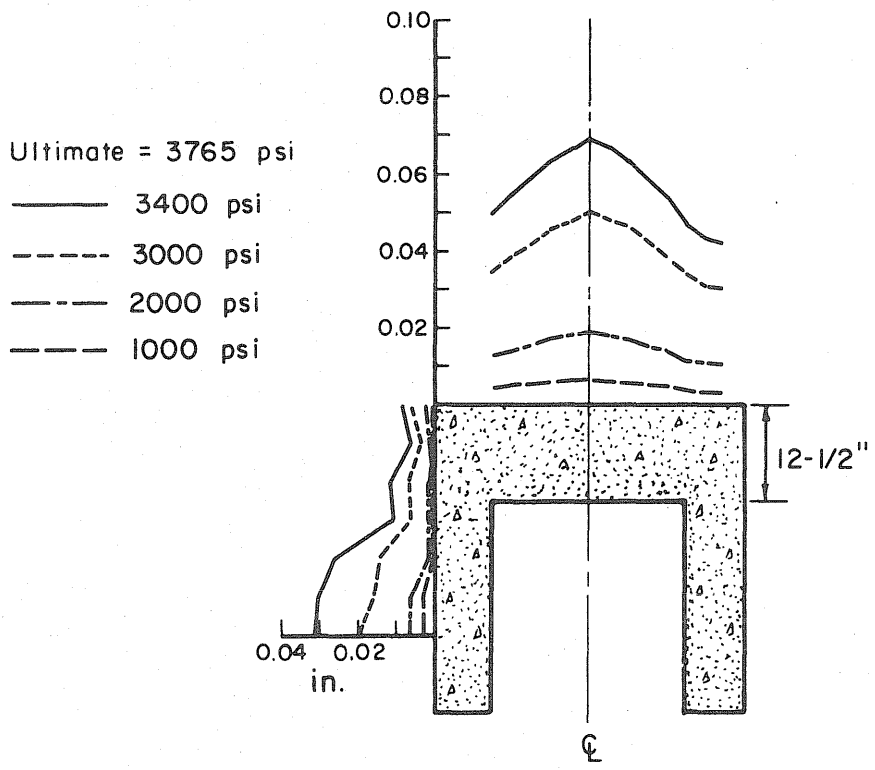

Fig. A.22 Measured Pressure-Deflection Curves Side Wall, Test PV28.2

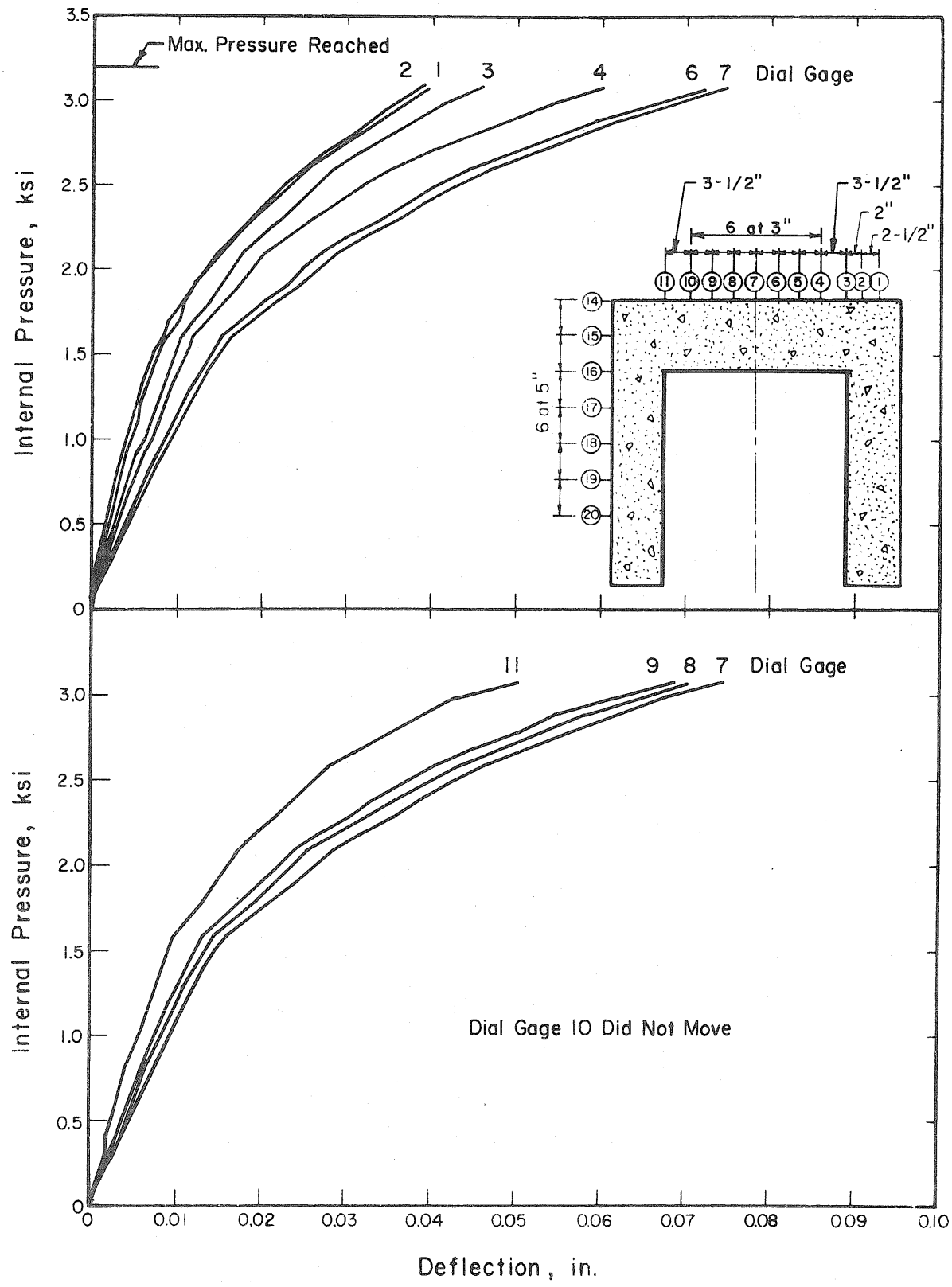

Fig. A.23 Measured Pressure-Deflection Curves End Slab, Test PV30

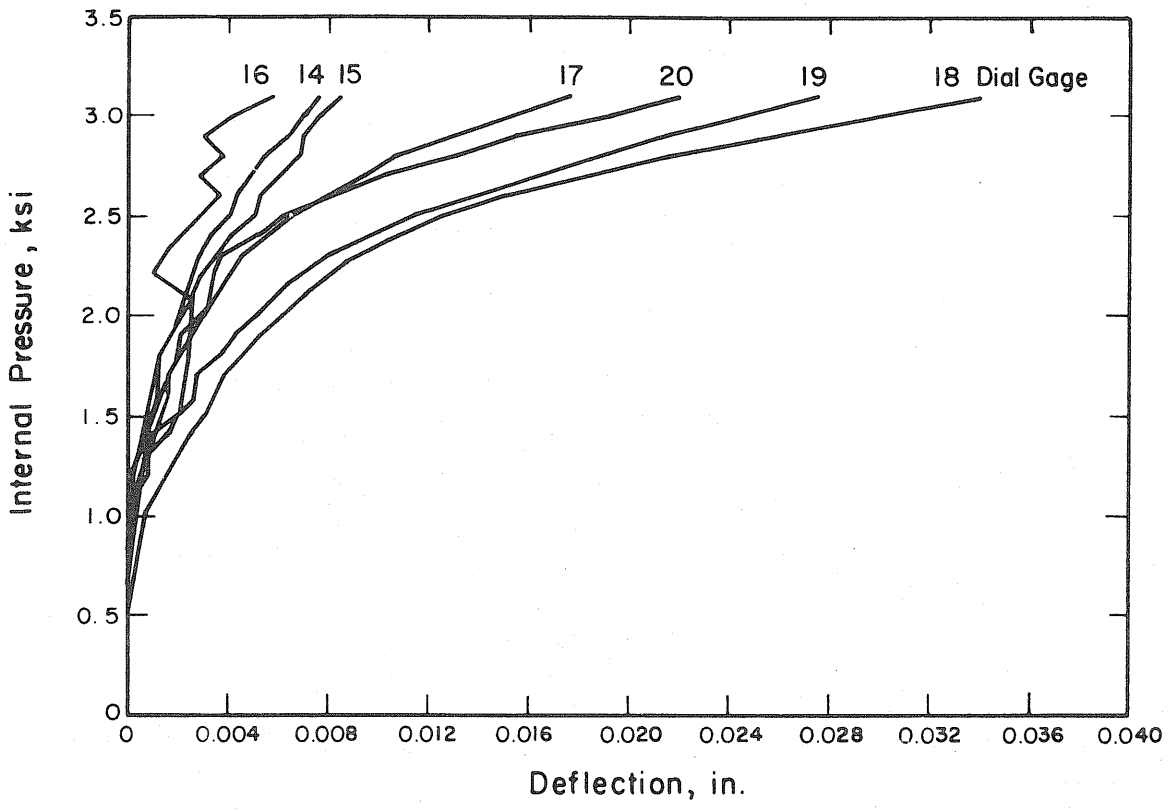

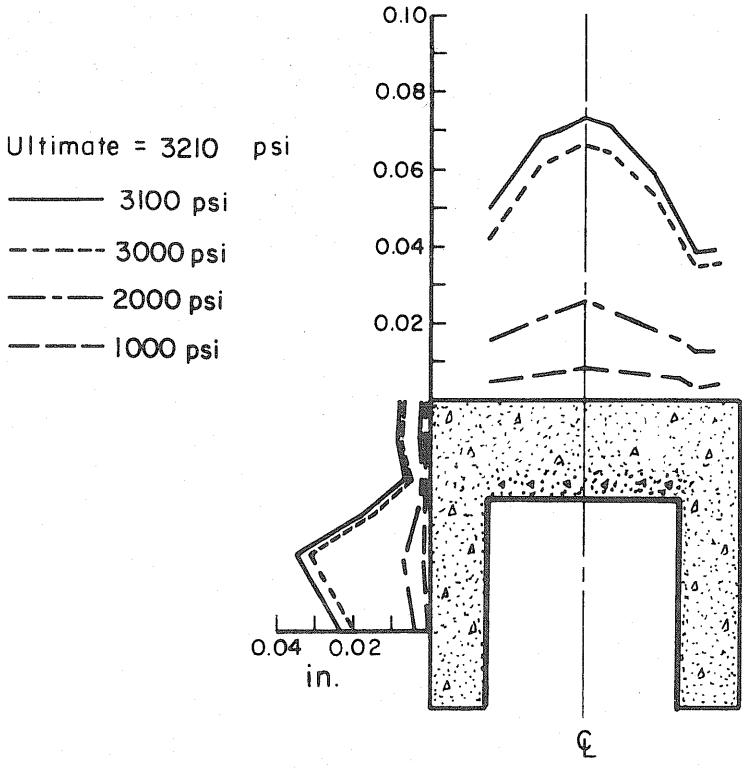

Fig. A.24 Measured Pressure-Deflection Curves Side Wall, Test PV30

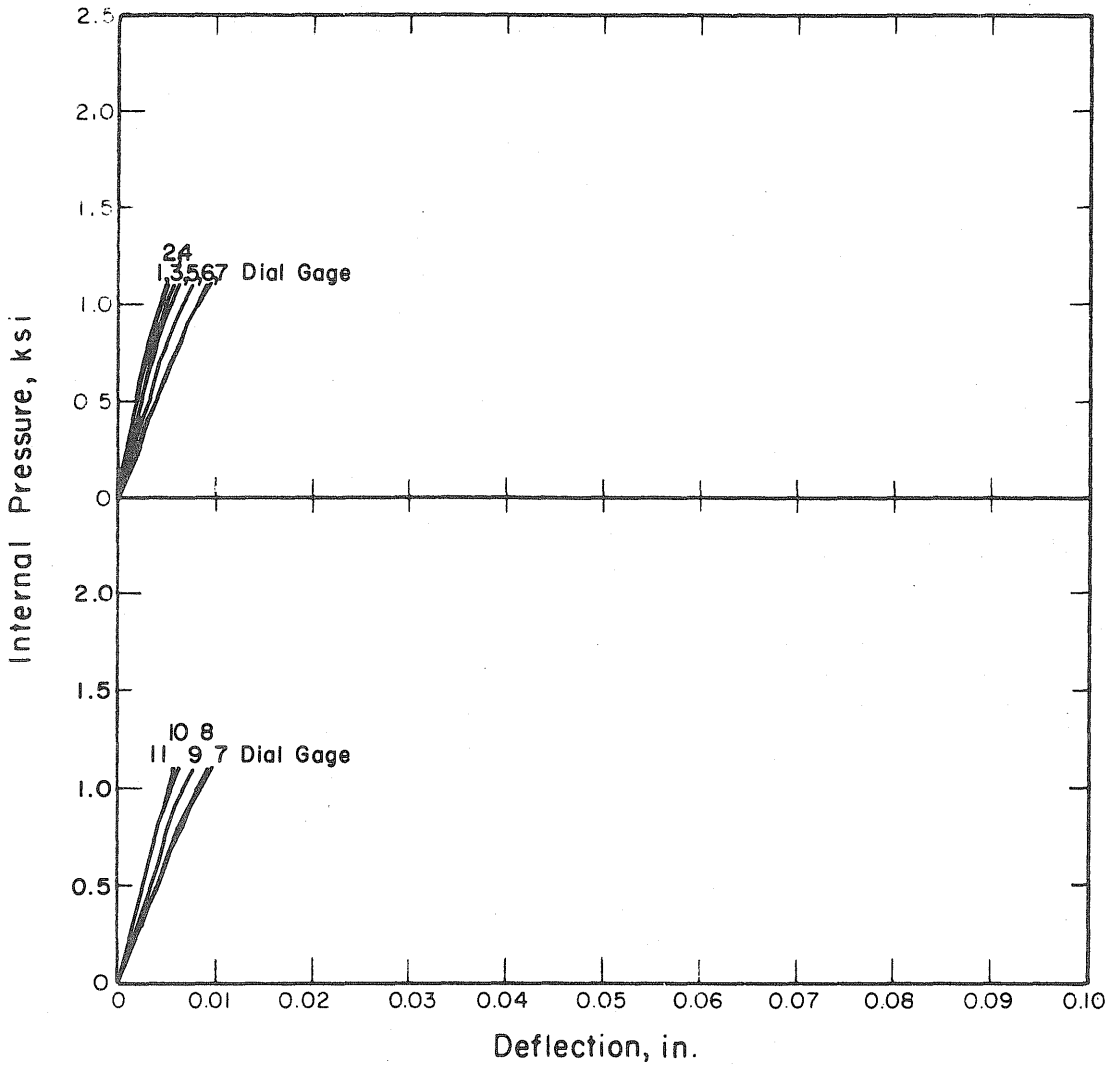

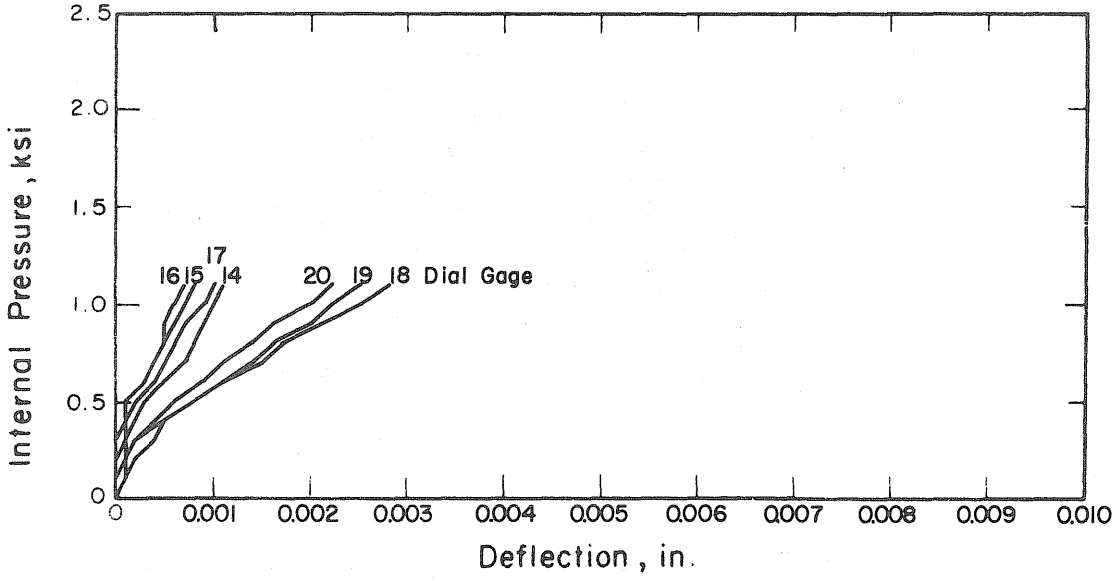

Fig. A.25 Measured Pressure-Deflection Curves, Test PV31.1

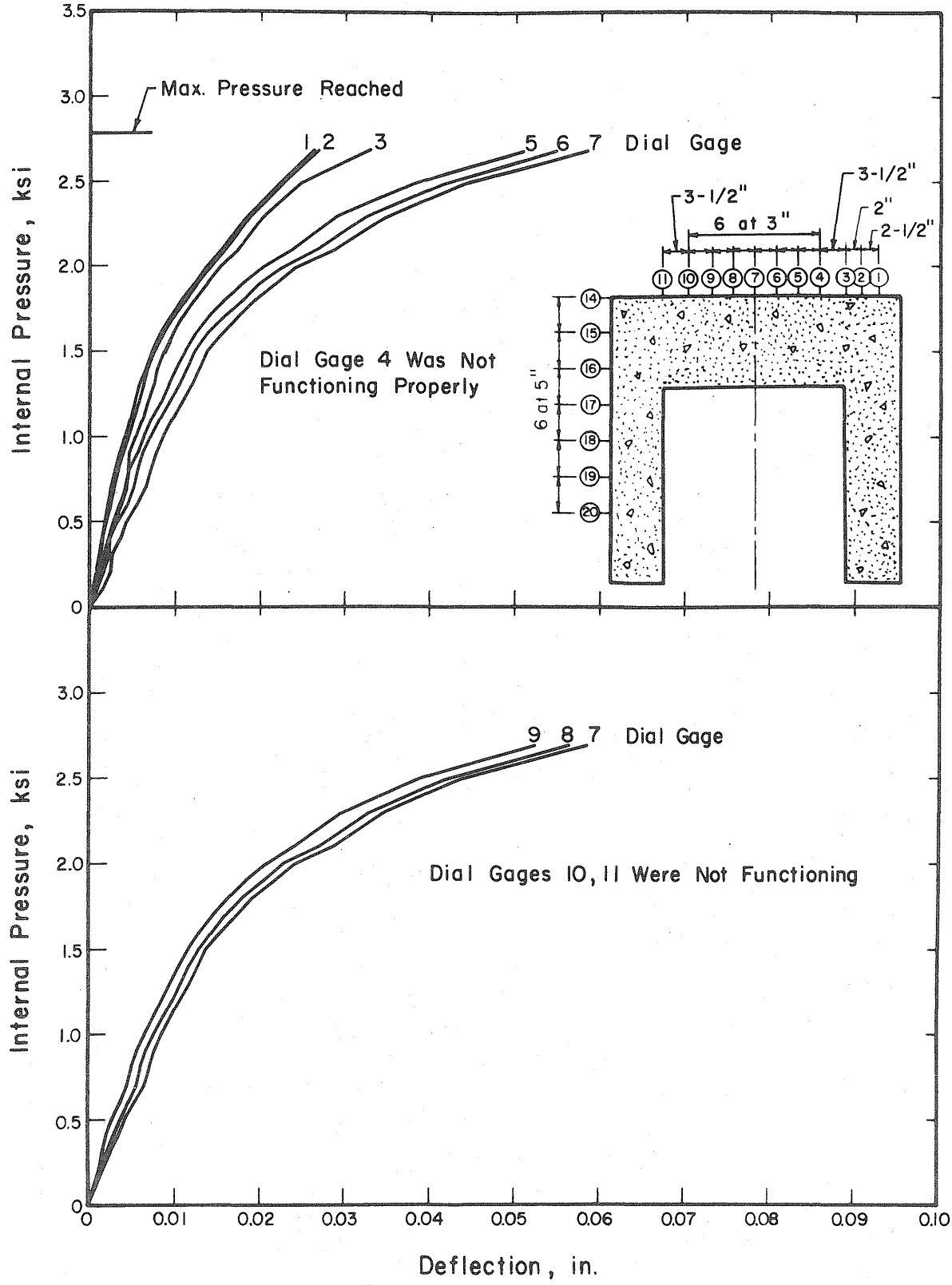

Fig. A.26 Measured Pressure-Deflection Curves End Slab, Test PV31.2

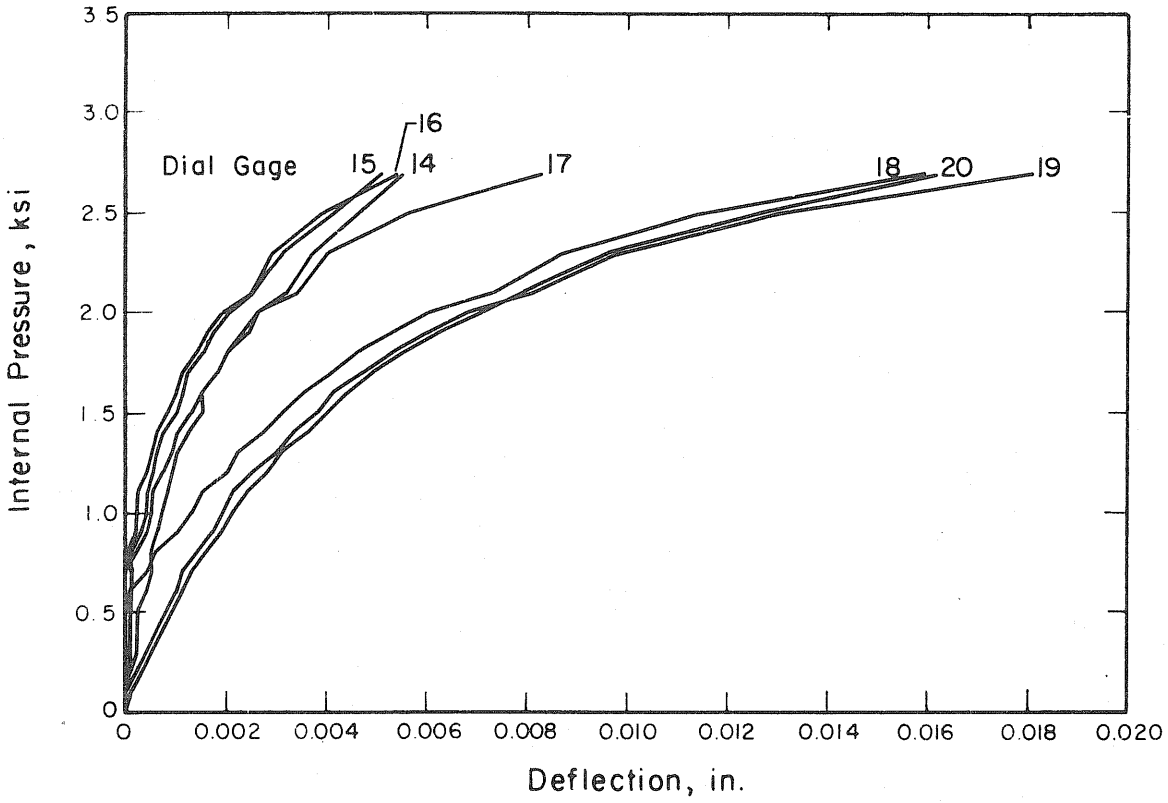

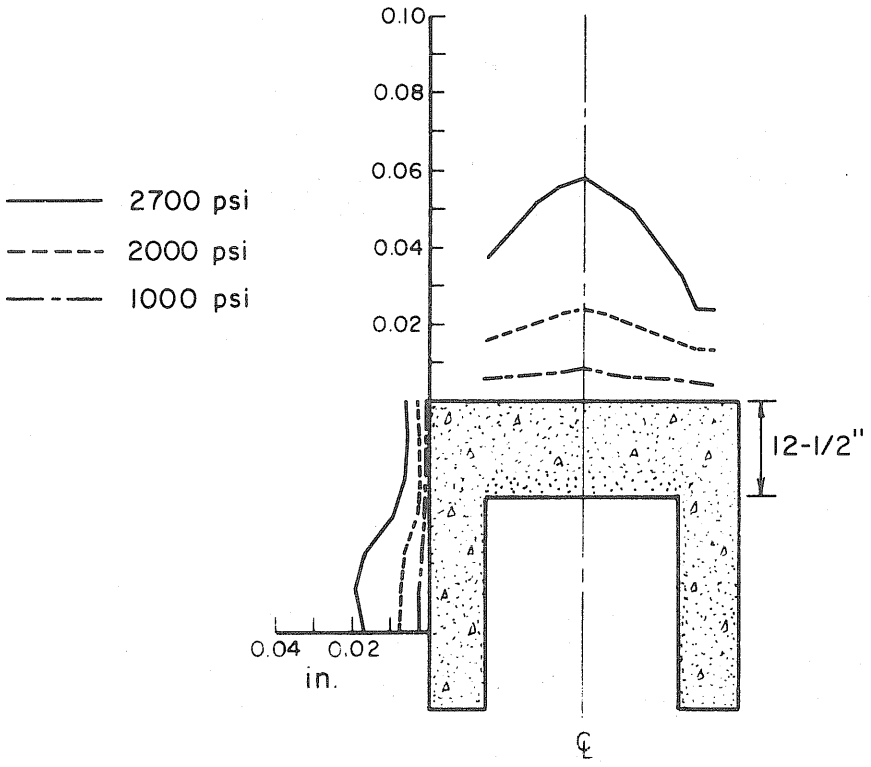

Fig. A.27 Measured Pressure-Deflection Curves Side Wall, Test PV31.2

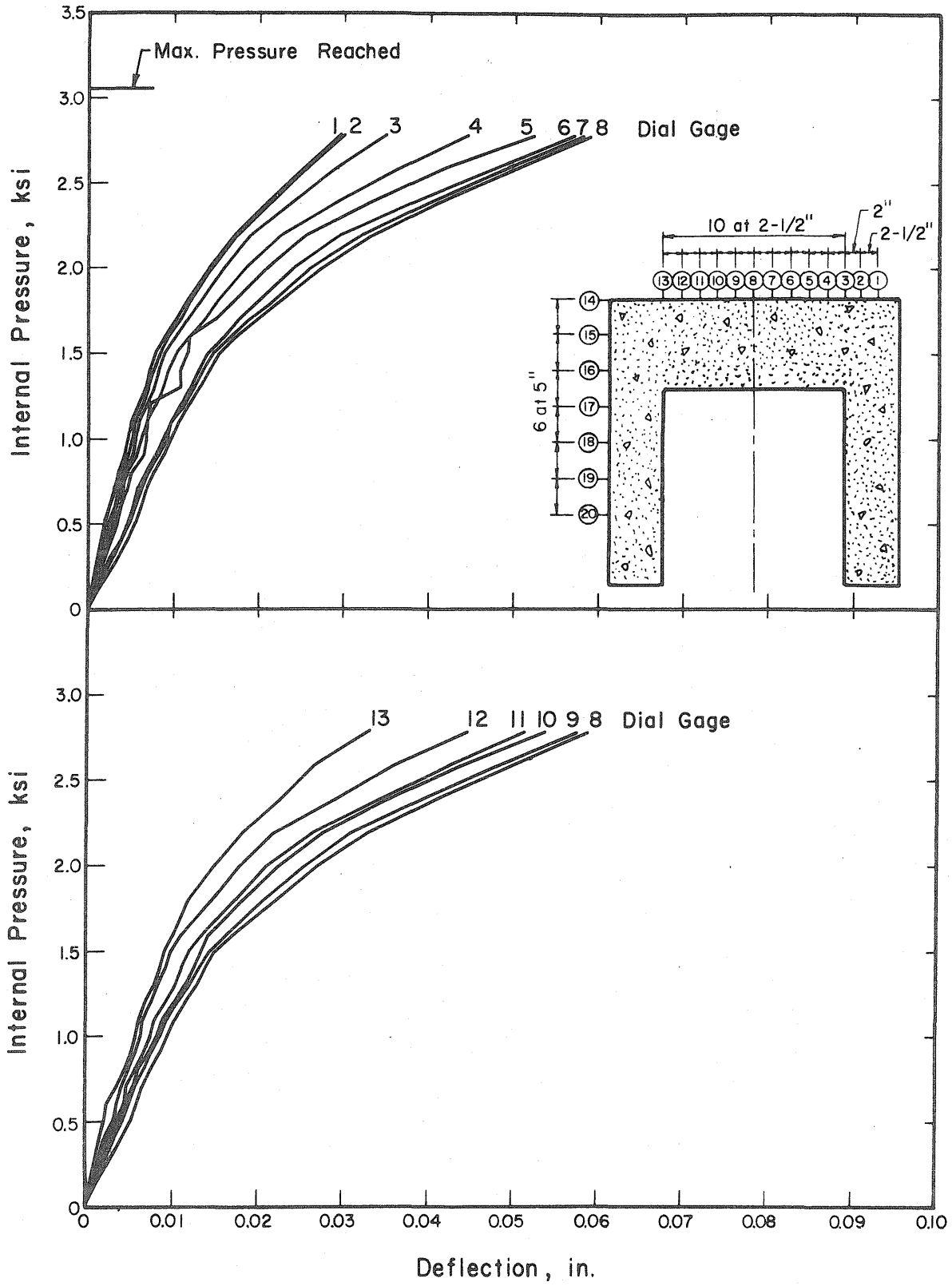

Fig. A.28 Measured Pressure-Deflection Curves End Slab, Test PV32

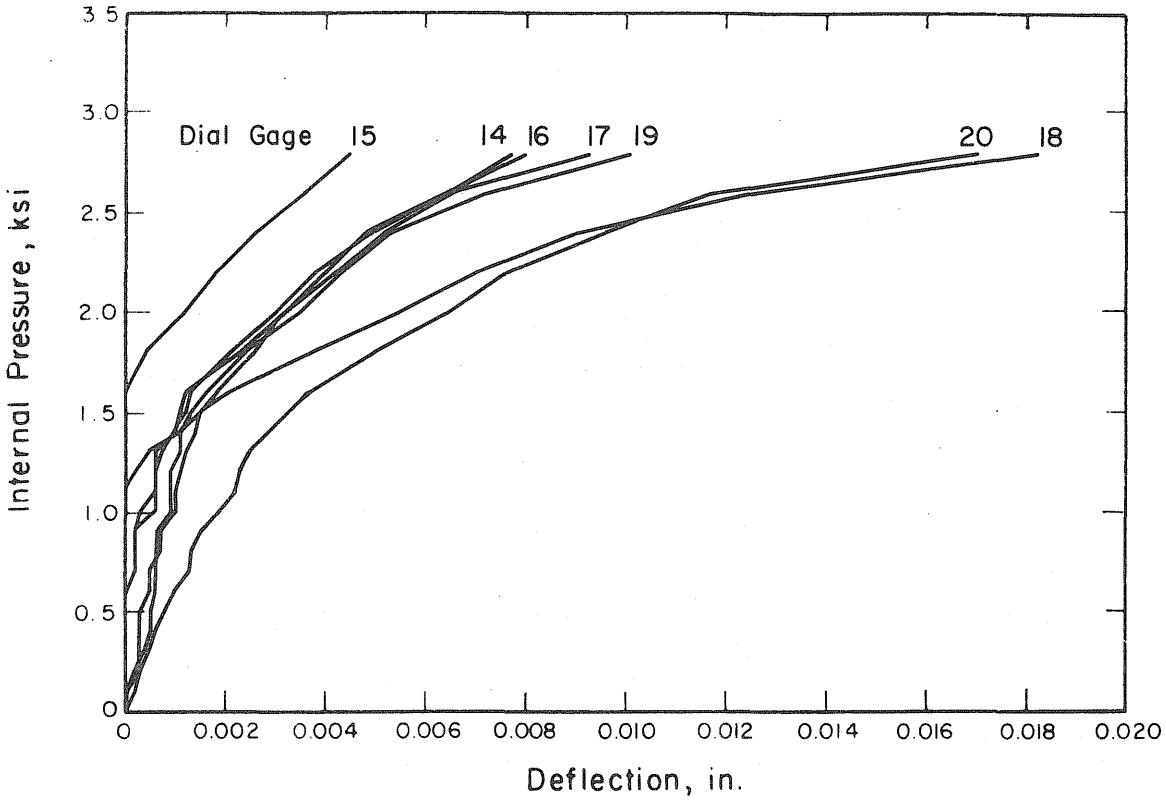

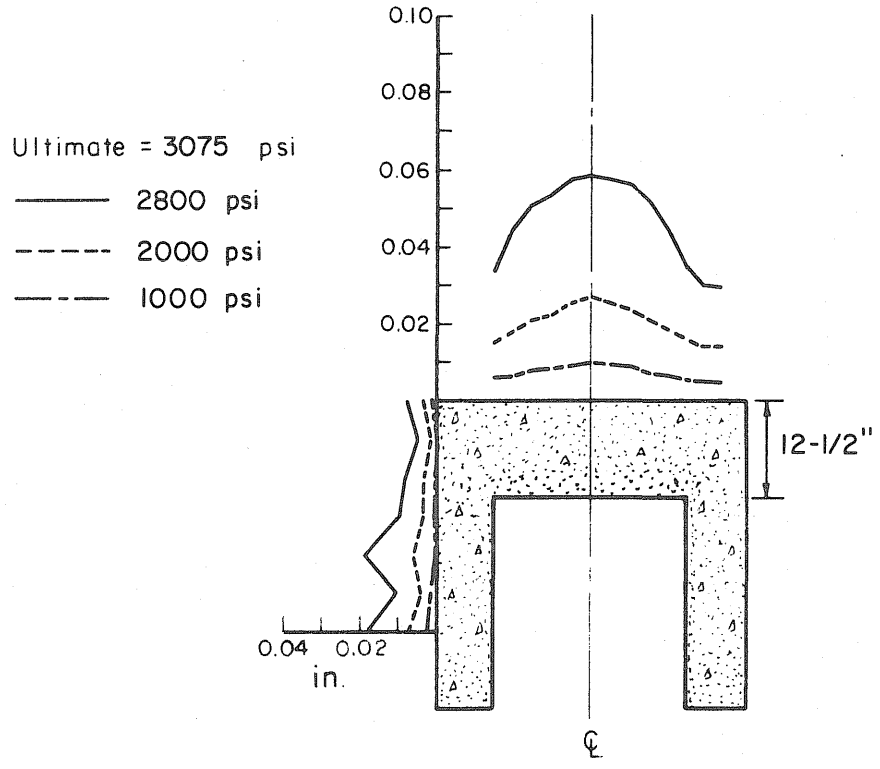

Fig. A.29 Measured Pressure-Deflection Curves Side Wall, Test PV32

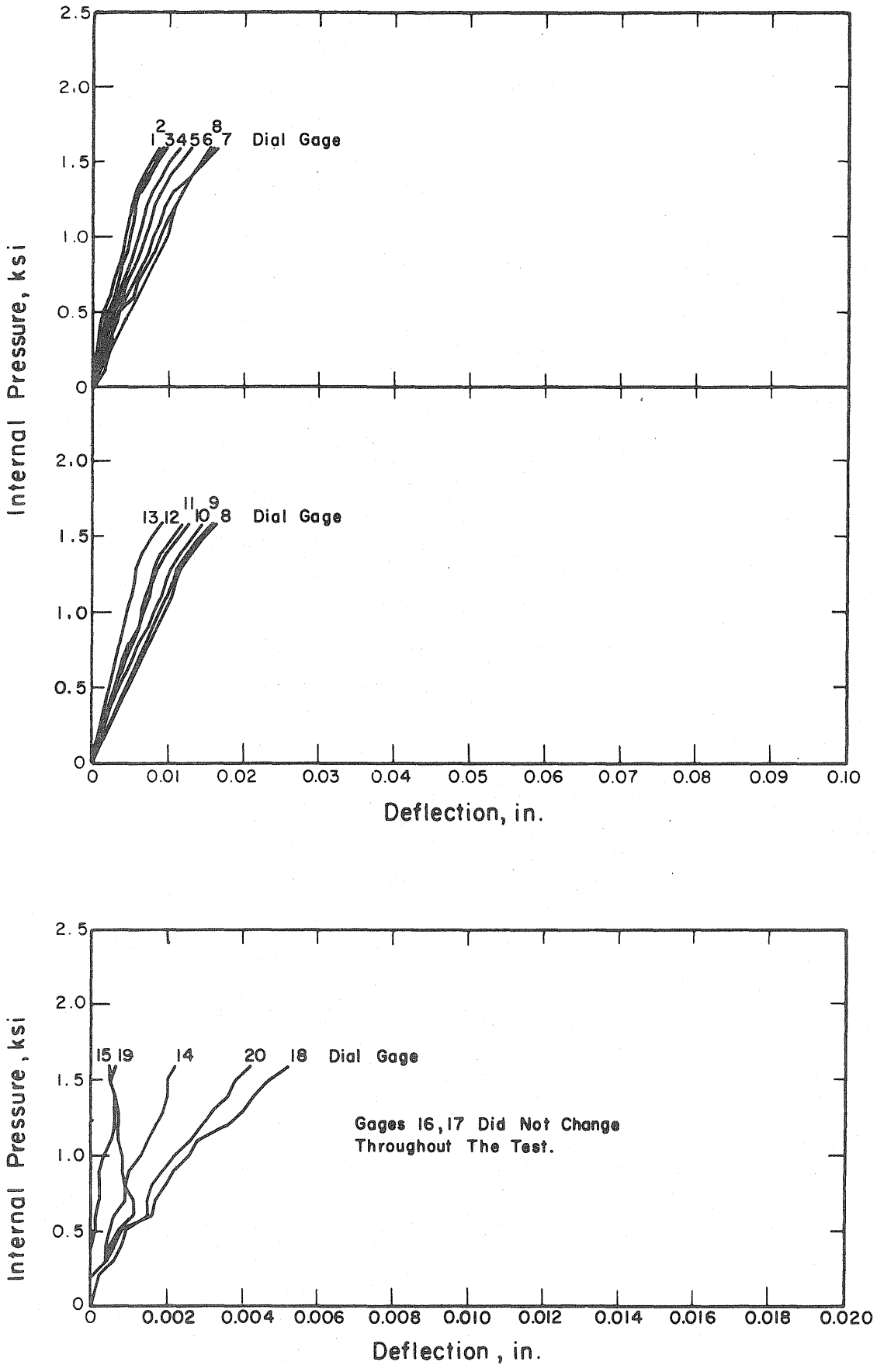

Fig. A.30 Measured Pressure-Deflection Curves, Test PV33.1

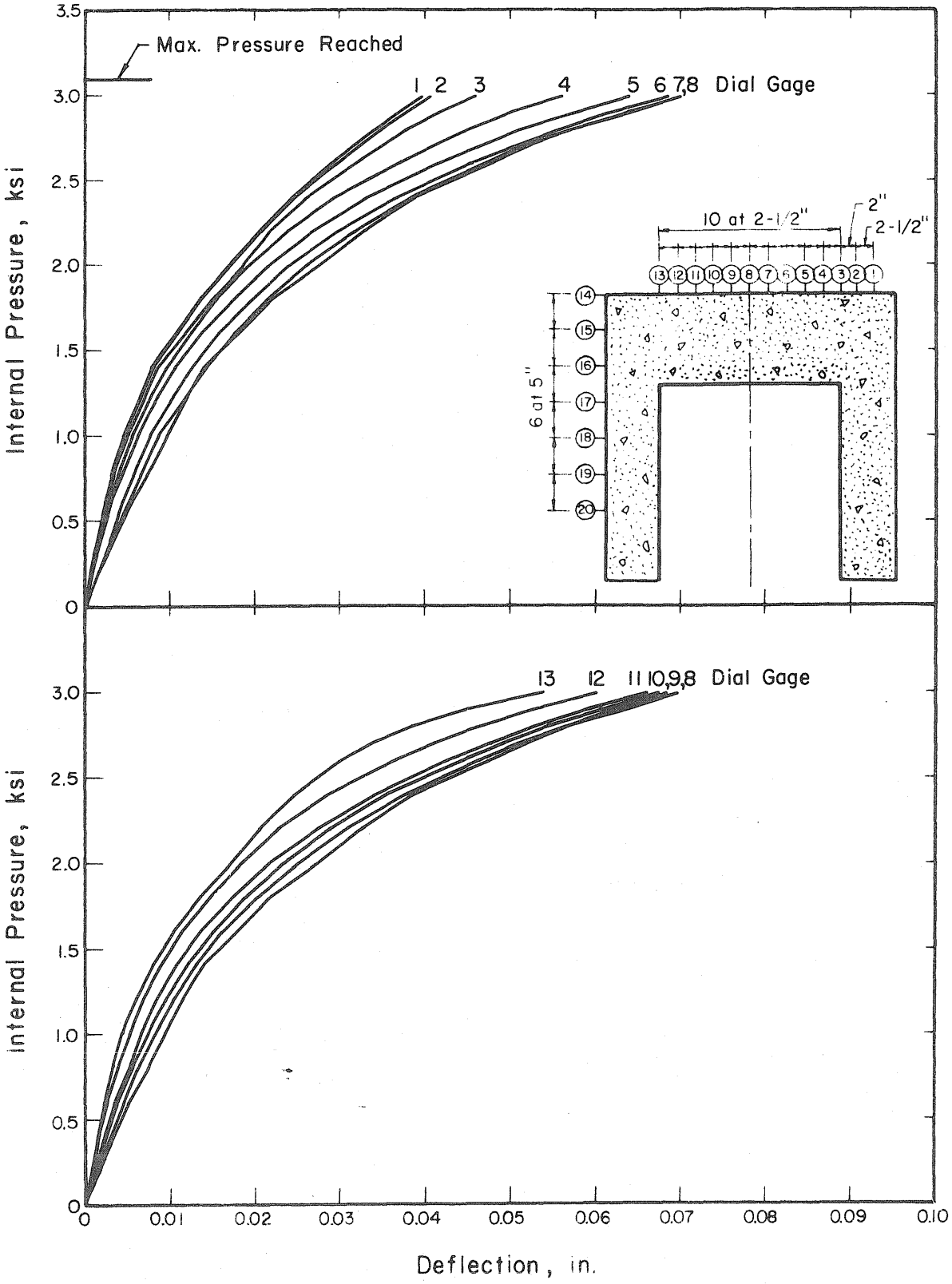

Fig. A.31 Measured Pressure-Deflection Curves End Slab, Test PV33.2

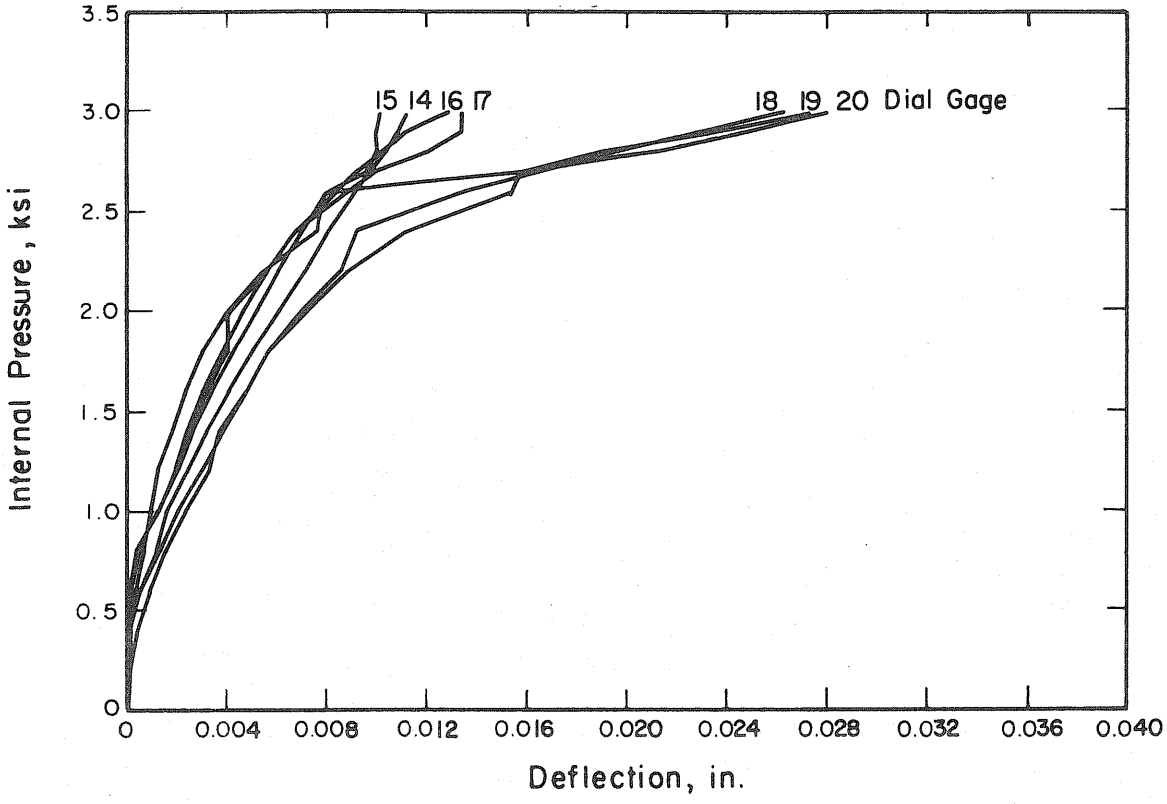

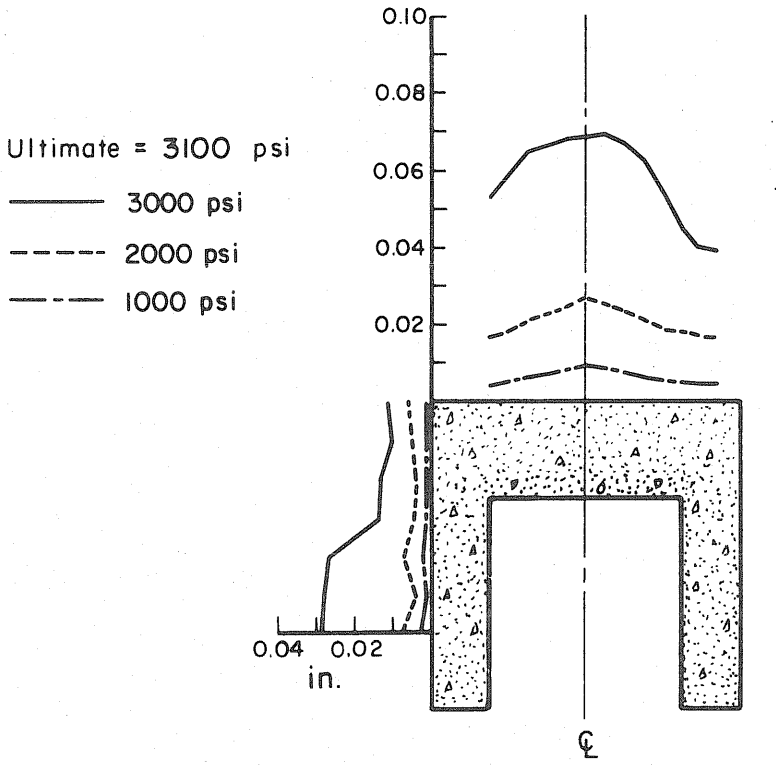

Fig. A.32 Measured Pressure-Deflection Curves Side Wall, Test PV33.2

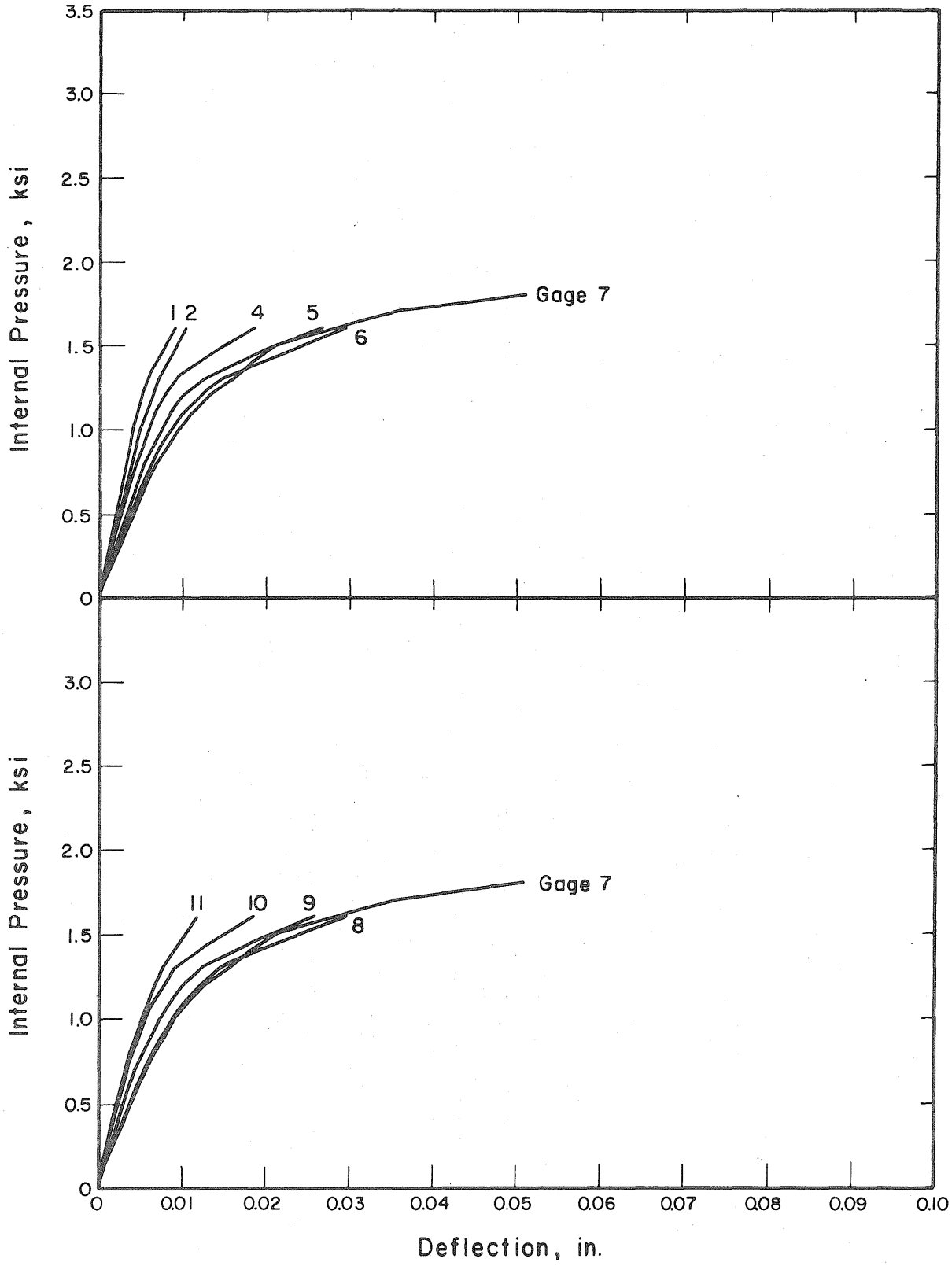

Fig. A.33 Measured Pressure-Deflection Curves, End Slab, PV34
(See Fig. A.26 for Gage Locations)

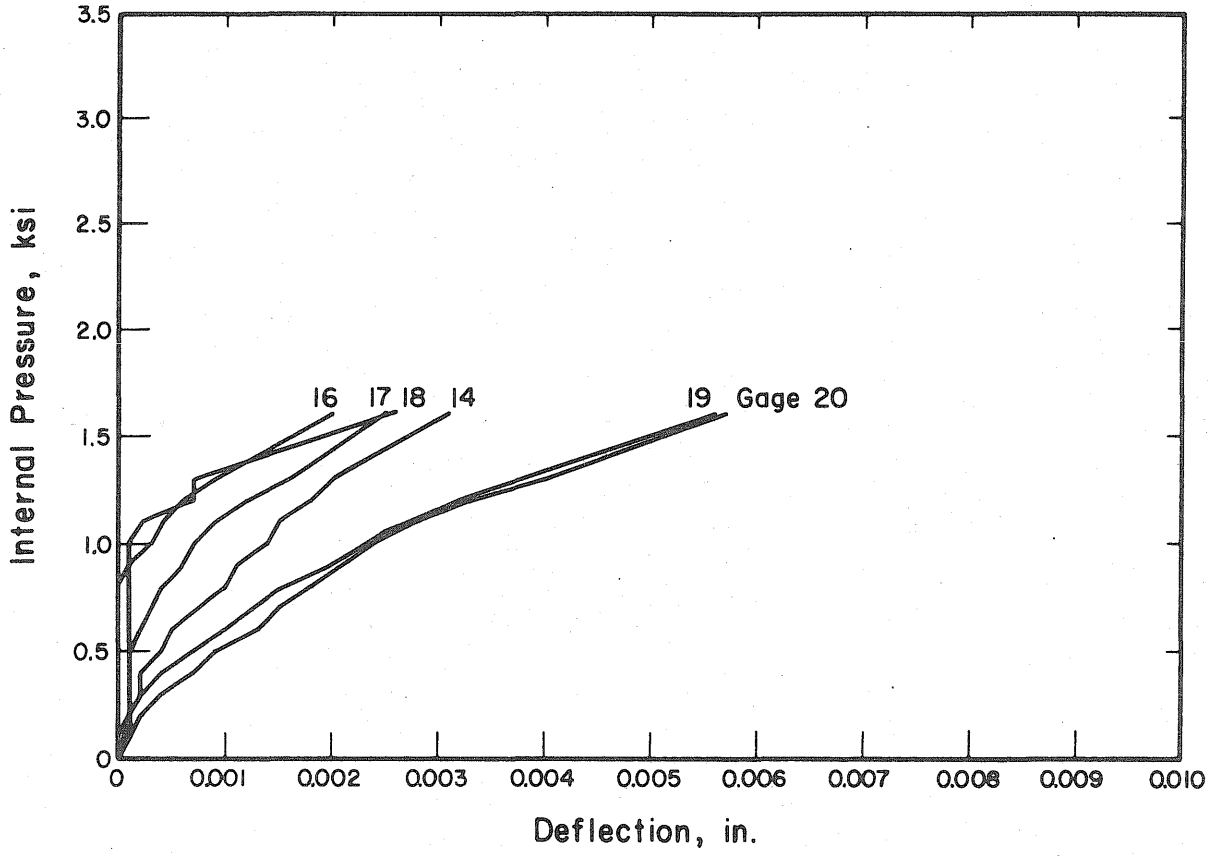

Fig. A.34 Measured Pressure-Deflection Curves, Side Wall, PV34
(See Fig. A.26 for Gage Locations)

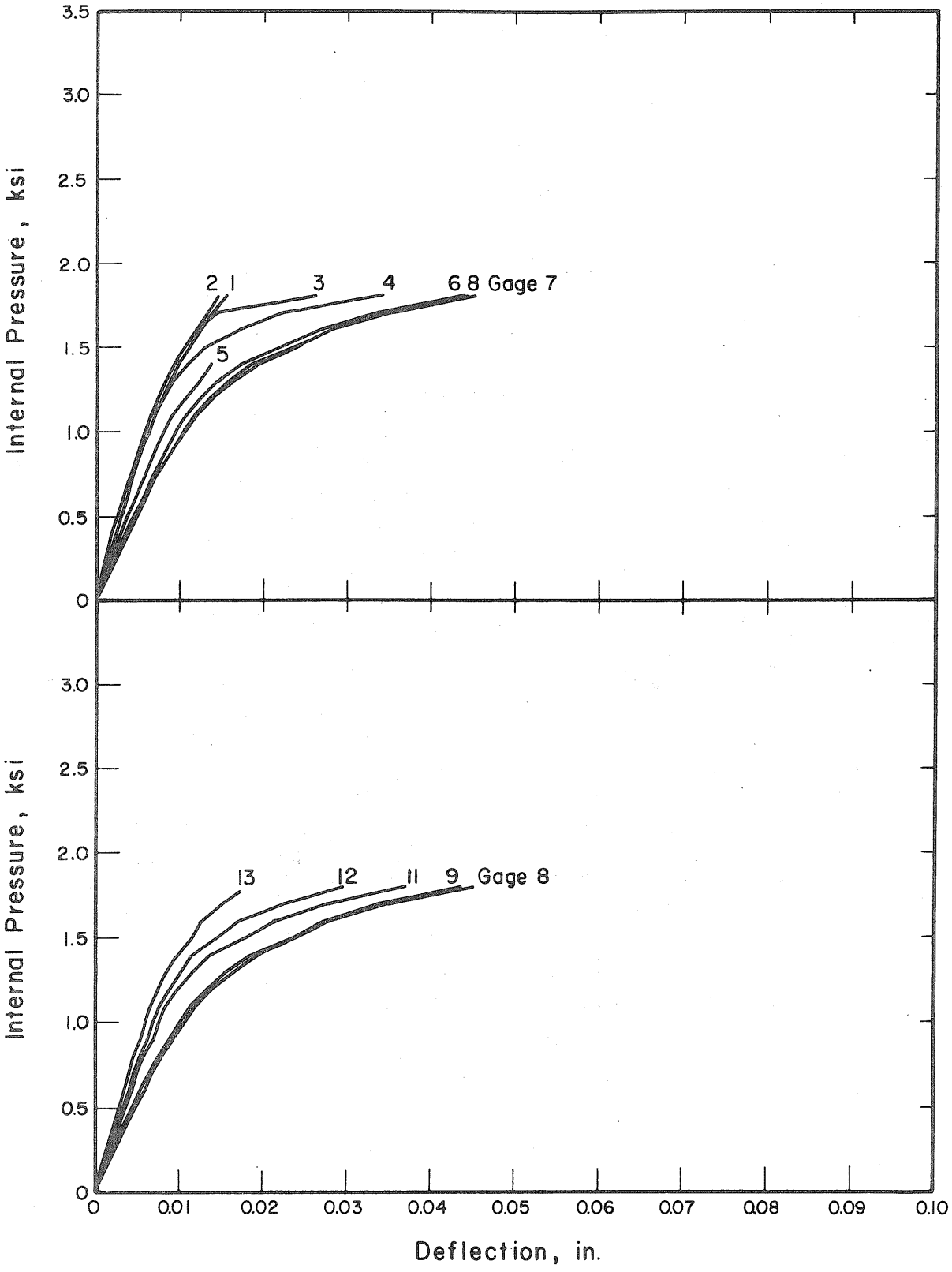

Fig. A.35 Measured Pressure-Deflection Curves, End Slab, PV35
(See Fig. A.28 for Gage Locations)

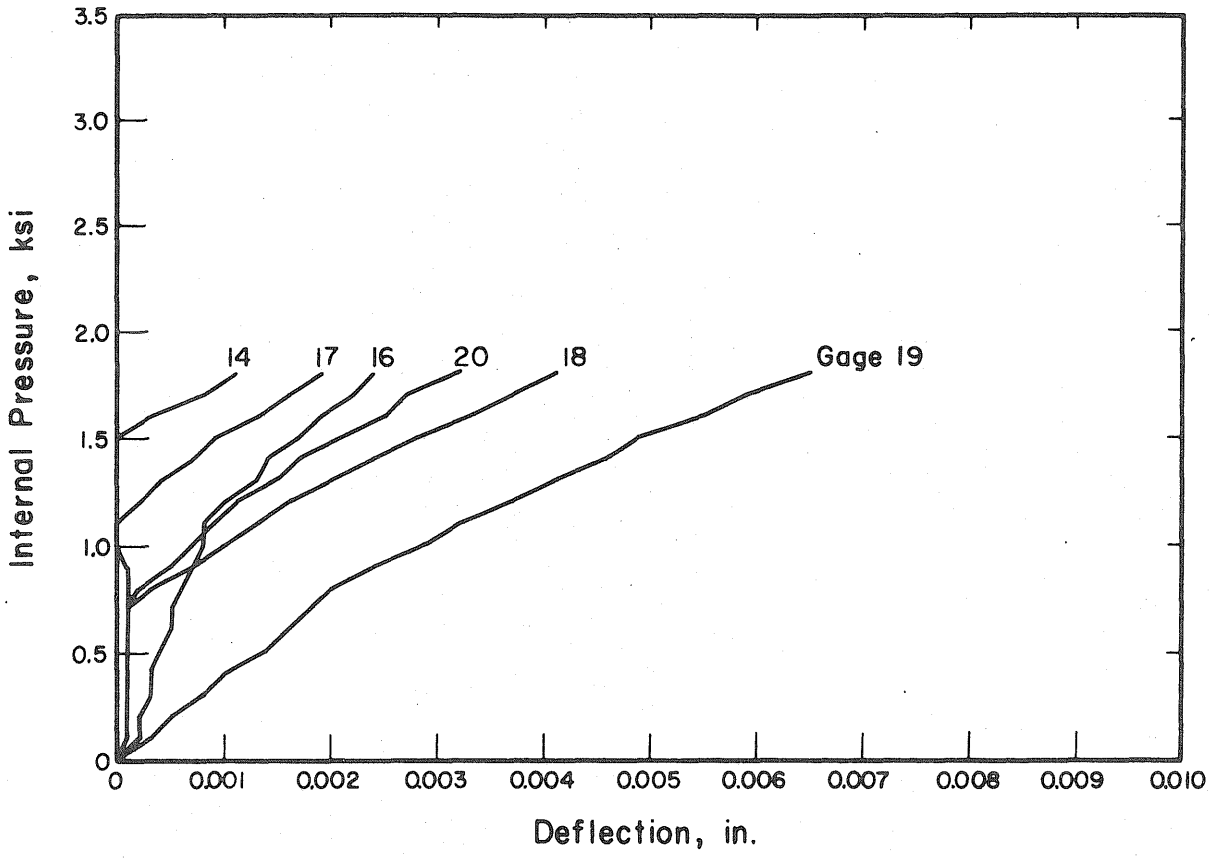

Fig. A.36 Measured Pressure-Deflection Curves, Side Wall, PV35
(See Fig. A.28 for Gage Locations)

APPENDIX B

TEST DATA

INTRODUCTION

This appendix contains specific information on the different characteristics of each of the ten vessels tested. The dates of casting, prestressing, and testing of each specimen are recorded in Table B.1

A brief description of each vessel is provided in this section. Since the basic materials and procedures used for each specimen were detailed in Appendix A, they will not be repeated in each vessel description. The graphs of pressure-deflection readings for each test are included at the end of Appendix A.

B.1. Test Vessel PV26 (Solid, 10-in. head)

Since PV26 was the first vessel tested in the current series it had many unique features which were later modified or eliminated from the other vessels. It was circumferentially prestressed going from the bottom to the top, an operation which resulted in radial cracks in the end slab after the bottom four bands were completely prestressed. These cracks closed upon prestressing the last band located around the slab.

PV26 was also the only vessel that was longitudinally prestressed using the rods from the previous series. The vessel was originally lined with only a welded steel can grouted into place. However, the first test of the vessel had to be aborted after reaching 800 psi due

to leaks through the welds of the steel can. The specimen was lined with copper and neoprene over the steel as described in Appendix A. This served as the liner for all subsequent tests with only minor changes. The second test proved successful with an ultimate pressure of 2610 psi obtained. The deflection readings of the head surface were obtained using push rod extension gages in direct contact with the concrete. The readings taken in the two tests were quite good using this setup. However the explosive manner of failure destroyed all of the head deflection gages and thus a new method had to be used for later vessels.

B.2 Test Vessel PV27 (six 5-in. penetrations, 10-in. head)

PV27 and all subsequent vessels were circumferentially prestressed going from top to bottom. In addition, new stressteel rods were purchased for the longitudinal prestressing. The vessel was tested successfully on the first attempt, reaching an ultimate pressure of 2400 psi. A new deflection gage system was designed for this vessel. The head dial gages were mounted to the side of the vessel out of the direct line of the explosive failure path. Metal tabs were glued to the specimen and piano wire was threaded into these tabs and tied off. The wire was then strung over ball bearing pulleys and across the head to the spring loaded gages on the side. This system was effective in protecting the gages from damage but the readings taken from these gages indicated a great amount of friction was present in the system. Thus, a new system was adopted for the next vessel.

B.3 Test Vessel PV28 (Solid, 12½-in. head)

The deflection gage system used for all remaining vessels was first used for PV28. The gages were mounted over the vessel, directly above the metal tabs glued to the surface. Piano wire was tied to the tab, stretched taut and attached to the spring loaded gages. Steel channels were run across the top of the vessel between the piano wires and bolted to the prestress rods. This system gave good readings and at the same time contained the explosion and protected the gages. An internal pressure of 3170 psi was reached during the first test of PV28 before the leaks in the vessel could not be outrun by the pump. The vessel was relined and tested successfully three weeks later to an ultimate pressure of 3765 psi.

B.4 Test Vessel PV29 (Thirty-seven 2-in. penetrations, 10-in. head)

Fabrication and testing procedures had become well established with the successful testing of three vessels. No major changes were made for PV29. It was cast and tested to failure in a relatively short period of time. No concrete strain gages were applied to the vessel.

B.5 Test Vessels PV30, PV31 (Thirty-seven 2-in. penetrations, 12½-in. head)

PV30 and PV31 were nominally the same in size and penetration pattern. However, there were several important differences in their physical properties and behaviors. The actual head thickness of PV30 was found to be 12.22-in. while PV31 had a thickness of 12.02-in. The compressive strength of the concrete head was 6350 psi for PV30 and 4950 psi for PV31. PV30 failed on the first attempt at 3210 psi in a

symmetric manner. PV31 developed a leak in the liner on the first test and reached an internal pressure of only 1200 psi. Upon retest PV31 failed at 2800 psi in a somewhat unsymmetric shear failure.

B.6 Test Vessels PV32, PV33 (Six 5-in. penetrations, 12½-in. head)

PV32 and PV33 were also designed and tested as a check against each other. Their properties were in closer agreement than were PV30 and PV31 and the results reflect this similarity. PV32 and PV33 had concrete compressive strengths of 5720 psi and 4875 psi respectively. The average head thickness of PV33 was 12.45-in. as compared to 12.30-in. for PV32. These two factors of concrete strength and slab thickness appear to have offset one another. PV32 failed at 3075 psi while PV33, after an aborted first test due to leakage, failed at 3100 psi. After PV33 developed a leak in its first test at 1700 psi, a new type of copper liner was used for the second test. A copper can was fabricated to fit into the steel liner grouted into the vessel. The use of a copper can provided a better fit in the reentrant corners and thus reduced the amount of expansion that high pressures would produce. PV33 was retested with this new liner and was pressurized to failure without a single leak.

TABLE B.1

Chronology

Mark	Casting	Circumferential Prestressing	Longitudinal Prestressing	Testing
PV26.1	1-29-75	2-17-75	3-26-75	4-16-75
PV26.2	--	--	5-2-75	5-8-75
PV27	3-13-75	4-9-75	7-17-75	7-25-75
PV28.1	6-5-75	7-31-75	8-27-75	9-4-75
PV28.2	--	--	9-24-75	9-30-75
PV29	9-15-75	10-14-75	10-30-75	11-6-75
PV30	10-20-75	11-19-75	1-13-76	1-21-76
PV31.1	12-9-75	1-8-76	2-11-76	2-17-76
PV31.2	--	--	2-27-76	3-2-76
PV32	12-17-75	3-9-76	4-7-76	4-9-76
PV33.1	2-20-76	3-25-76	5-6-76	5-11-76
PV33.2	--	--	5-20-76	5-25-76
PV34	4-12-76	5-19-76	6-8-76	6-10-76
PV35	7-6-76	8-18-76	9-23-76	9-28-76